Effect of high radiation doses (MGy) on light Emitting Diodes and optical glasses

Timothé Allanche

N°d'ordre NNT : **2020LYSES039**

THESE de DOCTORAT DE L'UNIVERSITE DE LYON

opérée au sein du
Laboratoire Hubert Curien

Ecole Doctorale N° 488
(SCIENCES, INGÉNIERIE, SANTÉ)

Spécialité / discipline de doctorat :
Optique-photonique

Soutenue publiquement le 09/11/2020, par :
Timothé ALLANCHE

Effect of high radiation doses (MGy) on Light Emitting Diodes and optical glasses

---

Devant le jury composé de :

Paillet, Philippe	Directeur de recherche	CEA DAM	Président
Bouazaoui ,Mohamed	Professeur	Univ Lille, PhLAM	Rapporteur
Van Uffelen, Marco,	Dr, Expert	F4E	Rapporteur
Rizzolo, Serena	Dr, Ingénieur R&D	Airbus Toulouse	Examinatrice
Virmontois, Cedric	Expert	CNES	Examinateur
Beaumel, Matthieu	Expert	SODERN	Examinateur
Ouerdane, Youcef	Professeur	UJM, LabHC	Directeur de thèse
Clerc, Raphaël	Professeur	UJM, LabHc	Co-directeur de thèse
Boukenter, Aziz	Professeur	UJM, LabHc	Invité
Girard, Sylvain	Professeur	UJM, LabHc	Invité

Table of Contents

Glossary

ANDRA	French National Agency for Radioactive Waste Management Agence Nationale pour la gestion des Déchets RAdioactifs
CEA	French Alternative Energies and Atomic Energy Commission Commissariat à l'énergie atomique et aux énergies alternatives
CFL	Compact Fluorescent Lamp
CID	Charge Injection Devices
CIGEO	Industrial Centre for Geological Disposal Centre industriel de stockage géologique
CIS	CMOS Image Sensors
CMOS	Complementary Metal Oxide Semiconductor
COTS	Components Off The Shelf
EDF	Electricity of France Électricité de France
EQE	Eternal Quantum Efficiency
ESA	European Space Agency
GaAs	Gallium arsenide
GaN	Gallium nitride
Gy	Gray: $1\ \mathrm{Gy} = {}^{\mathrm{J}}/_{\mathrm{kg}}$, 1 Gy = 100 rad
IR	Infrared
IRMA	IRradiation of MAterials is a panoramic irradiation cell for studying how materials or equipment react to the effects of dose and dose rate due to exposure to gamma radiation IRradiation de MAtériaux
IRSN	Radioprotection and Nuclear Safety Institute Institut de radioprotection et de sûreté nucléaire
ISAE- SUPAERO	National Higher French Institute of Aeronautics and Space Institut Supérieur de l'Aéronautique et de l'Espace
ITER	International Thermonuclear Experimental Reactor
LabHC	Laboratoire Hubert-Curien (Saint-Etienne, France)
LED	Light-emitting diode

LFL	Linear Fluorescent Lamp
LMJ	Laser Megajoule
Online measurement	Used for measurement performed during the irradiation (and optionally during the recovery) contrast to Post-Mortem measurement
OS	Optical System
PIA	Investment program for the future Programme d'investissement d'avenir
After irradiation measurement	Used for measurement performed after the end of irradiation in contrast to Online measurement
RadHard	Radiation hardened
Recovery	Refer to the time after the end of the irradiation during which a part of the radiation effects disappear
RGB	Red, Green and Blue
RIA	Radiation Induced Attenuation
RIE	Radiation Induced Emission
RIRIC	Radiation Induced Refractive Index Change
Standard glasses	Refer to a glass that is not designed to be radiation hardened
TID	Total Ionizing Dose
UJM	Jean Monnet University (Saint-Etienne, France) /Université Jean Monnet
UV	Ultraviolet

Introduction

This PhD work was carried out as part of the CAMRAD project funded by the French-PIA (*Programme d'investissement d'avenir*). It is a collaborative work involving several partners such as: ANDRA, CEA DAM, ISAE SUPAERO, IRSN, Optsys, Orano and the Laboratoire Hubert-Curien. The objective is to develop a HD color camera able to withstand at least a cumulative irradiation dose of 1 MGy and to become a commercial product (manufactured by Optsys). Thanks to its capacity to tolerate a total dose ten times higher than other existing radiation hardened cameras it will fit the need of the geological storage of nuclear waste (CIGEO managed by Andra) and the ones of customers that deal with high irradiation doses. The work will focus on the effect of radiation on commercial Light Emitting Diodes and optical glasses.

After a review of the radiation hardened camera market and some CAMRAD project specifications, we will remind LEDs basics and their responses in gamma-ray environment. I carried out both after irradiation and online experiments. Thanks to the after irradiation analysis, we measured the optical power evolution, spectral and angular luminous intensity after gamma and X-ray irradiations. The online ones were carried out to highlight the temperature influence as well as the potential transient radiation effects on the LEDs operation. In addition, these different irradiation types allow us to compare X-rays and gamma ray effects on LEDs at the MGy dose level.

The third chapter addresses the radiation effects on optical glasses for the optical system. After a reminder on the materials optical responses as well as their combination to design an optical system, I presented some optically active defects generated in a radiative environment and which are harmful for our application. I have paid particular attention to the optical responses of several hardened glasses manufactured by Schott. This highlights the positive effect of Ce-doping via the darkening reduction level of the studied materials during the irradiation. The last two sections focus on the description and the validation the optical set-up we developed to measure the spectral darkening of glasses during the irradiation. We performed online measurement on both Cerium doped materials and on their standard counterparts. In the end we showed that well-chosen standard glasses can be equivalent or better than "radiation hardened glasses" in radiation environments.

Introduction

Le travail présenté dans cette thèse de doctorat a été effectué dans le cadre du projet CAMRAD financé par PIA (*Programme d'investissement d'avenir*) pour lequel ANDRA, CEA DAM, ISAE SUPAERO, IRSN, Optsys, Orano et le Laboratoire Hubert-Curien ont collaboré. Son objectif est le développement d'une caméra HD couleurs gardant ses performances jusqu'à une dose cumulée minimum de 1 MGy. Cette caméra deviendra un produit commercial fabriqué et vendu par Optsys. Grâce à sa résistance à une dose dix fois supérieure aux autres caméras du marché, elle conviendra notamment aux besoins particuliers liés au stockage géologique profond (Projet CIGEO) et aux projets faisant face à la question des hautes doses. Les recherches menées étudient les effets des radiations sur des LEDs et les verres optiques.

Après une étude du marché des caméras résistantes aux radiations et une description du projet CAMRAD, nous rappelons quelques connaissances de base sur les LEDs et leurs comportements sous rayonnement gamma. J'ai réalisé des mesures pendant et post-irradiation : les post-irradiations pour déterminer les modifications spectrales de puissances et de direction d'émission causées par les rayons-X et gamma ; et les mesures pendant les irradiations pour quantifier les modifications de température et les potentiels effets transitoires pouvant affecter le fonctionnement des LEDs. Ces différentes expériences nous ont permis de comparer les effets des rayonnements gamma et X sur les puissances émises et les cônes d'émissions après 1 MGy.

Le troisième chapitre est dédié à nos travaux sur les verres optiques. Après des rappels sur la combinaison des verres pour la conception de systèmes optiques, je présente certains défauts optiques causés par les radiations pouvant affecter notre application. J'ai concentré mes travaux sur les verres dits « durcis » fabriqués par SCHOTT pour mettre en avant leur résistance aux radiations. Nous détaillons les mécanismes qui permettent à ces verres de moins se noircir sous radiation grâce à leur dopage au Cérium. Les deux dernières parties se concentrent sur le montage optique que nous avons conçu pour mesurer le noircissement des verres pendant l'irradiation et les mesures réalisées sur les verres durcis et leurs équivalents standards. Enfin nous

montrons que la transmission de certains verres standards est équivalente ou meilleure en milieux radiatifs que celle des verres dit « durcis ».

Chapter A. Project's framework

A.1 Project description

In France, 25 nuclear plants are currently being in dismantling including power and reseach reactors, 16 belonging to the CEA (*French Alternative Energies and Atomic Energy Commission* / *Commissariat à l'énergie atomique et aux énergies alternatives)* and 9 to EDF (*Electricity of France* / *Electricité de France*) [1]. At the end of 2017 in Europe there were 46 nuclear power plants in dismantling or decontamination [2] and in the future more will follow at least in France as its Government decided to decrease the part of the nuclear in the energy mix [3]. Between 2022 and 2030 the CIGEO (*Industrial Centre for Geological Disposal* / *Centre industriel de stockage géologique*) project should receive its first nuclear wastes [4]. These activities and others (such as nuclear safety) require the use of radiation resistant imaging systems and sensors to monitor the radioactive wastes, remote handling operations such in ITER [5],[6], to inspect reactors, plants or laboratories and to control robots. Tube based cameras currently offer the highest radiation hardness but are fragile, bulky and limited in terms of performances and image resolution [7]. Other types of sensors as *CID* (Charge Injection Devices) or CMOS (*Complementary Metal Oxide Semiconductor*), CIS (*CMOS Image Sensors*), are limited to a maximum TID (*Total Ionizing Dose*) of 100 kGy(SiO_2) when no shielding and no thermal annealing techniques are used to extend their lifetimes. Fig. 1 illustrates one of the radiation effects on the image quality. More images illustrating the various possible failures of COTS (*Components Off The Shelf*) cameras under radiation can be found in [8].

Fig. 1: Typical image degradation observed on COTS camera at low TID (<10 kGy). Figure from [9].

CAMRAD is a mixed project between academics and industrialists aiming to define a prototype of a camera resistant to severe environments that will then be manufactured at a larger scale by Optsys [10], with the ambition to lower the prices compared to existing radiation tolerant products. Therefore we had to adapt our strategie and choices to fit this context. The CIS is the only part of the camera that will not be COTS, it is developed by the ISAE- SUPARERO (*National Higher French Institute of Aeronautics and Space / Institut Supérieur de l'Aéronautique et de l'Espace*). By using radiation hardening techniques at the device and system levels, they greatly enhance the capacity of CIS to withstand high doses, up to several MegaGray (MGy). A preliminary design of the CAMRAD camera is presented in Fig. 2 with its synoptic diagram in Fig. 3.

As it will be more developed in this PhD thesis, there is a tremendous lack of data about radiation effects on LEDs and optical glasses at relatively high irradiation dose levels (MGy). So, an important part of the work was to select and characterize LEDs and glass materials especially their optical responses at high doses and ensure that their performances fulfill the target dose levels.

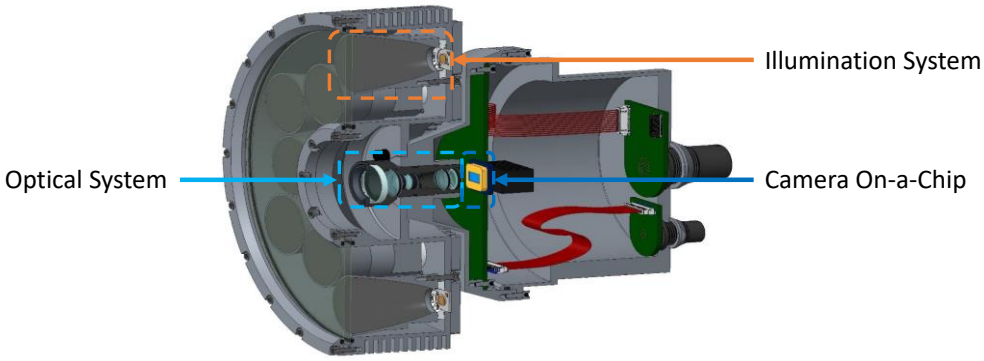

Fig. 2: CAMRAD camera prototype preliminary design made by Optsys.

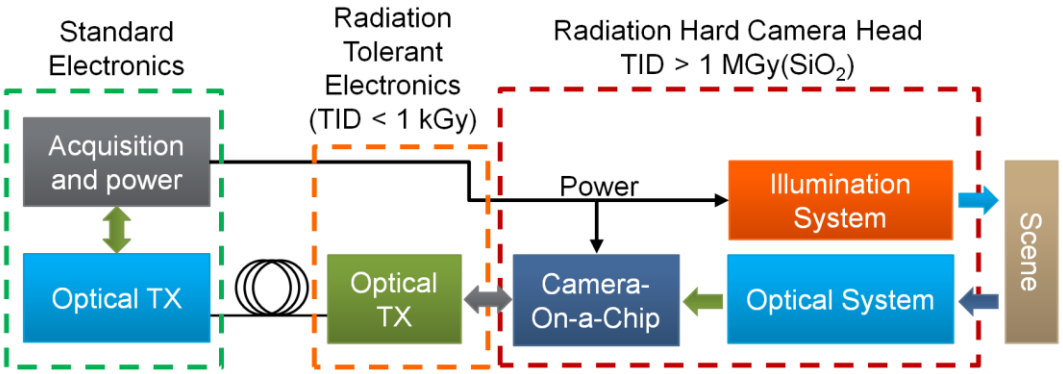

Fig. 3: CAMRAD camera prototype synoptic diagram.

CAMRAD's goal is to develop a CIS-based camera autonomous in terms of light sources and able to sustain at least 1 MGy(SiO_2) dose of ionizing radiation. Moreover this project will extend the knowledge on radiation effects over all the camera's components to higher dose levels with publications in the open literature [11], [12], [7], [13], presentations and posters in conferences (DEM, ANIMMA, RADECS, NSREC and IISW see references flowed by ⁂ in the list of related conferences), one patent [14] and two PhD thesis (this one and [15]). Ultimately, the final camera prototype will be evaluated at the IRMA (*IRradiation of MAterials* / *IRradiation de MAtériaux*) [16] irradiation facility (Fig. 4) of IRSN (*Radioprotection and Nuclear Safety Institute* / *Institut de Radioprotection et de Sûreté Nucléaire*). This final test has been designed as a worst-case scenario compared to the real conditions encountered for example by Orano company.

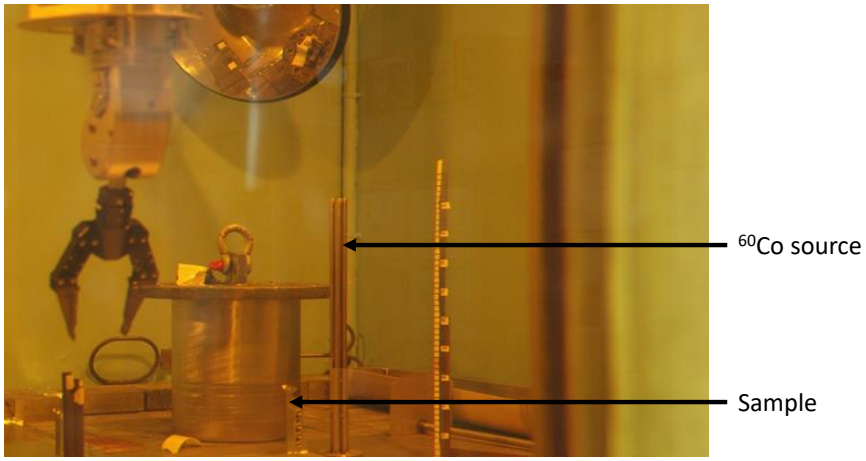

Fig. 4: IRMA irradiation room. Figure adapted from [17].

For the final test, at IRMA, the camera will be positioned, in active mode, close to the ^{60}Co source without any shielding. It will operate for nearly two weeks until all the

camera's head (red rectangle of Fig. 3) will be exposed to 1 MGy dose of gamma irradiation. At this position, the expected maximum dose rate will be close to 3 kGy/h (or 0.8 Gy/s). The radiation tolerant electro-optic conversion will be located further from the source and exposed to an accumulated dose limited to around 1 kGy. The experimental run will be performed at room temperature with online image acquisitions. After the test, images will be analyzed to determine the color rendering and contrast variation as a function of the dose.

A.2 CAMRAD organization

CAMRAD organization is described in Fig. 5. Work packages were shared between the different institutions of the consortium. This PhD work focuses on both the illumination system and the optical materiel exploration while another PhD student, Cyprien Muller, mainly worked on the photometry budget simulation and the optical system design [15].

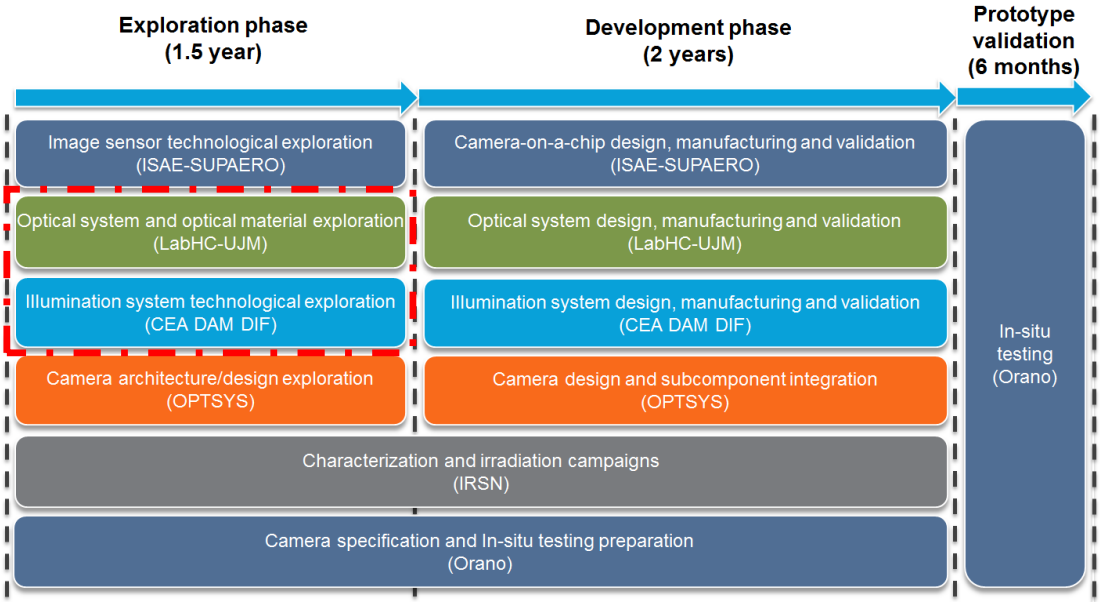

Fig. 5: CAMRAD project organization overview. The red square highlights the work packages on which this PhD focuses.

A.3 State of the art

Table 1 reviews the major brands selling cameras adapted for radiation environments and pointed out, for each company, the characteristics of their products. We chose to

select for each company the reference that presents the highest radiation tolerance and is using an electronic image sensor. Products from the major radiation camera suppliers are reported while Dekra products are not listed as the datasheet of their best reference (VT XLRAD-10PTZ) in term of total dose is unclear on the maximal dose. Public data are not exhaustive and do not show cameras performances close to their maximal TID. To the best of our knowledge there is no public demonstration of a camera's capacity to really sustain 1 MGy dose, manufacturers demand to the buyer an act of faith. The only public demonstration we found was realized by Thermo Scientific [18] up to 10 kGy.

Table 1: Radiation resistant camera available on the market information are based on camera makers' datasheets.

	Mirion technologies	Thermo Scientific	Ermes-electronics	Ahlberg cameras	Diakont	CAMRAD
Product	Hyperion	CID8825D	Viza	Z160	Proton	**CAMERA protype**
Radiation Tolerance	1 MGy	3×10^{-2} MGy	0.5MGy without shielding	0.2 MGy	2×10^{-3} MGy	**>1 MGy**
Radiation Dose Rate	1 kGy/h	2.8 kGy	Unknown	10 kGy/h	50 Gy/h	**1 kGy/h**
Resolution	960*540	710x484	1280*960	720x1280 progressive scan	1080p	**720p**
Image sensor	solid-state 1 megapixel sensor	Charge Injection Device	CMOS	Unknown	CMOS	**CMOS**
Color	No	Yes	Yes	Yes	Yes	**Yes**
Public demonstration	No	Yes	No	No	No	**Yes**

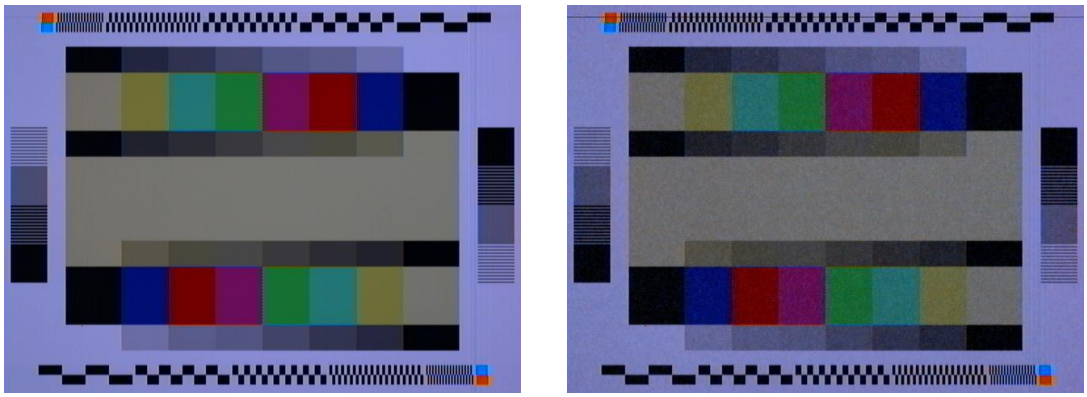

Dose : 0 Gy | Dose : 10 kGy, dose rate 2.2 kGy/h

Fig. 6: CID8825D camera response by Thermo Scientific before and under gamma irradiation (^{60}Co) at 10 kGy. Figure adapted from [18].

The only camera that claim to resist to 1 MGy without thermal annealing is the Mirion Tech one whose weight is 23.5 kg (that is probably due to a shielding) and Mirion Tech did not published a test report.

All the performances of the cameras which exist on the market are below that aimed in this CAMRAD project

Conclusion Chapter A

The "radiation hardened camera" market is heterogeneous. These cameras really differ in terms of radiation resistance and image quality. There is nearly no information in open literature to confirm the datasheets information. While in a near future, there will be more and more nuclear plants that will need to be dismantled and a lot of nuclear waste to inspect. For these operations, cameras able to sustain high doses and dose rates will be required as the one developed during our CAMRAD project. In addition to providing an industrial camera with the best performances on the market, with the publication of our results, CAMRAD will help the community to move forward.

Chapter B. LEDs selection for the illumination system

CAMRAD camera must be able to operate autonomously in an extreme environment comprising radiations and eventually in complete darkness. So, it is necessary to include an illumination system powerful enough to acquire images using low integration times (to reduce the image radiation induced degradation). The study of radiation effects on LEDs, carried out within the framework of CAMRAD, aimed to provide a database of usable commercial LEDs with the necessary information for both photometric calculations and the design of the illumination system for our targeted application. Two examples of these calculations can be found in [12] and [19], this part of the project will be discussed in details in Cyprien Muller's the PhD thesis [15].

Since the beginning of the project, LED technology had been considered as the most promising solution for the building block of the illumination system. There are several reasons for this choice: their easy integration thanks to their small size and volume, their luminance efficiency, their reduced cost and, of course, their already reported good resistance to ionizing radiations such as gamma-rays at moderate dose levels. As it will be developed later in this chapter, the LEDs are indeed intrinsically quite resistant to energetic radiations and their responses are marginally affected by γ-rays.

In order to respond to the different configurations suggested during the CAMRAD project, we tested both RGB and white LEDs. We were interested in the modification of the three following LEDs parameters:

- The emitted light power, and its evolution versus irradiation dose (whether after irradiation or during the irradiation runs).

- The spectrum shape.

- The LED emission cones (LED intensity diagram).

This chapter provides the necessary information to address the emission properties of white and colored LEDs. After that, the literature regarding the impact of radiation, and in particular gamma rays, will be discussed. Finally, it describes the

selected characterization methods used, the obtained results and outcomes for CAMRAD.

Project requirement for the illumination system

As it will be developed in Chapter C, the transmission of glass lenses will decrease under irradiation. Indeed, even with a set of the most adequate glasses, the optical system without anti-reflection coating will feature non-negligible losses, close to 3 dB @ 800 nm [12]. However, the major constraint is associated with the CIS which should be used at low integration time (between 1 and 3 ms) to keep at reasonable levels both the dark current [9] [20] [21] (see Fig. 7) and the photo-induced current [22] [23] (see Fig. 8).

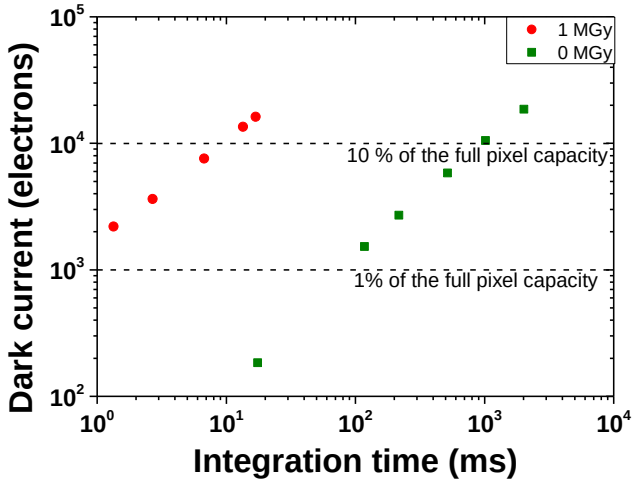

Fig. 7: Evolution of the dark current as a function of the integration time: before and after gamma irradiation (at a cumulated dose of 1 MGy) in a RadHard CMOS with a full capacity of 10^5 electrons. Figure adapted from [12][1].

[1] *Appendix A details the different notations "**Redrawn from**", "**Adapted from**", "**Created from**" and presents an example for each case.*

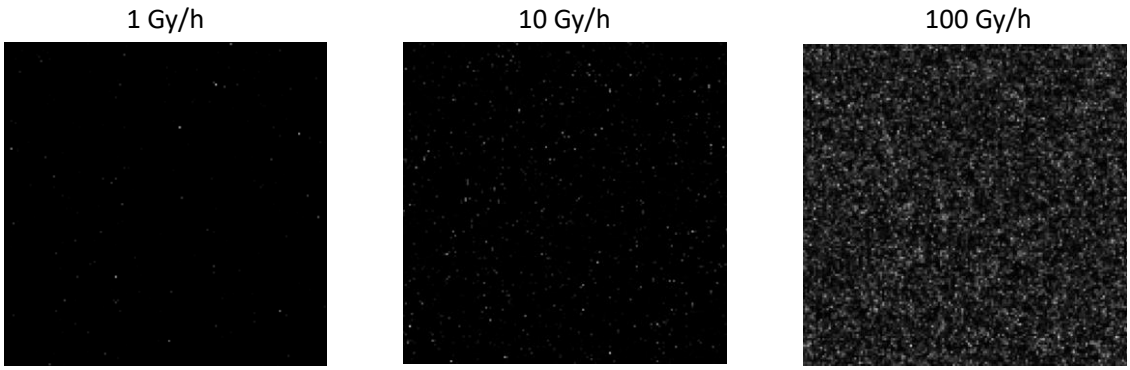

Fig. 8: Photo-induced current in a CMV2000 image sensor (CMOS) exposed to radiations at different dose rates (^{60}Co). Images recorded at the very beginning of the irradiation run with an integration time of 20 ms. Images are 1/3 of the sensor. Figure adapted from [24].

A mock-up, reported in Fig. 9, was developed to highlight the effects of camera's aperture, the field of view, the light power and especially the integration time on the image brightness. We used a camera with a tunable integration time, objects with different albedos (proportion of reflected light) and one LED with an output power of 1.1 W / 93.9 lm (object distance and camera's aperture are the same as for the final camera test). We kept all parameters constant and we have varied the integration time (which is equivalent to the exposure time in photography). When the integration time is doubled the sensor will receive two times more photons for one image. It is nearly equivalent to double the quantity of light on the scene.

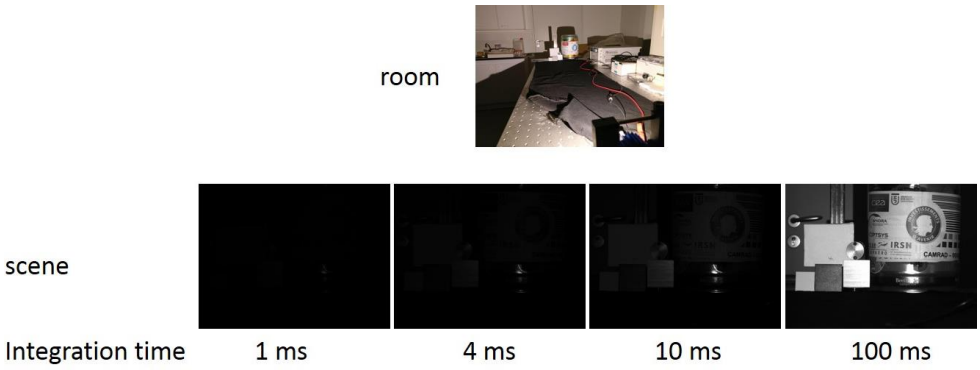

Fig. 9: Mock-up of the CAMRAD final test at 1:1 ratio. The image on the top is a picture of the room only enlighted by the one LED. Images below are camera pictures made with the same aperture than the final camera at different integration times. The scene is at ≈1.5 m from the first optical lens. The used LED is a XPEBWT with an output power of 1.1 W or 93.9 lm.

Fig. 9 shows that for a camera – with the same opical parameters as the ones expected for CAMRAD final test, and even in the case where the scene seems well enlightened (Fig. 9 room) – integration time around a hundred ms is required to obtain an image. Of course it is possible to increase the gain (ISO in photography) to obtain a

brighter picture, but it will also increase the noise. Another possibility is not to use all the sensor dynamics and scale it on the display/screen. Nevertheless, the photometric calculations were made in the hypothesis that the illumination system will be able to entirely fill the sensor pixels without additional gain. So in Fig. 9 we have chosen not to modify the gain and to use all the sensor dynamics to highlight the effect of the integration time. However, this remains useful to adapt the image display during the operating time where other parameters could vary such as the illumination.

Considering all camera parameters and an exposure time of 1 ms, we should use a power of around 90 W for the scene lighting [15]. Consequently, we will study the responses of LEDs with more than one thousand lumen flux.

B.1. LEDs basics

The mechanism of light emission significantly differs between the LEDs (*electroluminescence in a solid-state semiconductor material*) and the more conventional light sources such as halogen lamps (incandescent lamp, black body radiation), or discharge lamps (LFL (*Linear Fluorescent Lamp*), CFL (*Compact Fluorescent Lamp*) …). As shown in Fig. 10, LED is composed of a P-N junction obtained by doping a III-V semiconductor crystal, the P zone is an electron acceptor (therefore in excess of holes) while the N zone is an electron donor (therefore in excess of electrons). The light is emitted by radiative recombination of a hole-electron pair, when the device is biased in direct, in the central area, called the depletion zone, where the carriers will be able to meet and recombine.

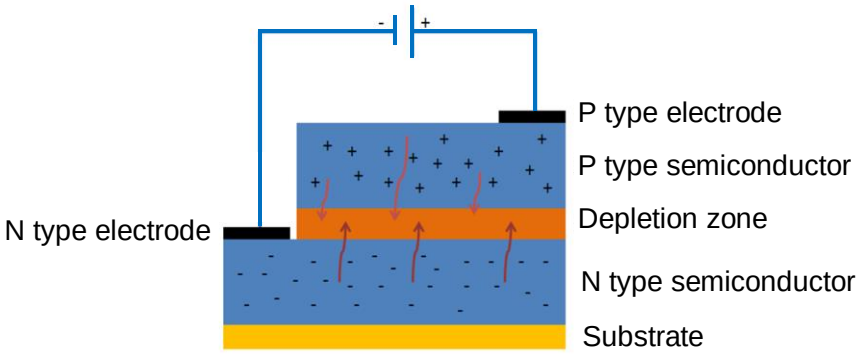

Fig. 10: Diagram for a P-N junction for a LED. Figure redrawn from [25].

For the emission, the LED must be polarized directly to its operating voltage (this concept will be discussed in the section B.1.3) and the process is controlled by the injected current level. This current is driven by the free carriers in motion (electrons in the N-zone and holes in the P zone). To return to a state closer to equilibrium, recombination of excess holes and electrons will spontaneously occur. In the case of LEDs, the materials and their arrangement in layers have been designed to promote radiative recombination, to the detriment of other non-radiative recombination (such as trap assisted recombination and Auger recombination [26], discussed in the section B.1.5). This is achieved by using direct gap materials (where radiative recombination is favored), and by judiciously introducing electron barriers and multiple quantum wells to promote radiative transitions.

B.1.1. Colored LEDs

LED is essentially a quasi-monochromatic light source, the emission wavelength depends on the energy gap value of the material where the emission takes place. In order to obtain polychromatic sources, it is therefore necessary to precisely adjust the gap value, which is achieved by changing the composition of the emission material. There are two main families: the family commonly named GaN (*Gallium nitride*), where the emission occurs in an $In_XGa_{1-X}N$ heterostructure sandwiched with GaN, and a family commonly named GaAs, where the emission occurs in a $(Al_XGa_{1-X})_{0.52}In_{0.48}P$ heterostructure sandwiched with GaAs. The first GaN family allows an emission from blue to amber, while the second GaAs from amber to infrared. There is also a third family for ultraviolet emission. Some examples are given in Table 2.

Table 2: Semiconductor associated to LEDs colors. Table from [25].

Color	Emission peak (nm)	Structure
Red	660	GaAlAs/GaAlAs
Yellow	585	GaAsP/GaP
Green	555	GaP/GaP
Blue	430	GaN/SiC

Spectral bandwidth of LEDs spectrum is driven by the thermal agitation that causes dispersion centered in the band gap value. The full width at half maximum stays within [20 - 80] nm range [25].

B.1.2. White LEDs

LEDs do not directly emit white light. To design a white source using LEDs, a first approach, leading to the best efficiency in lm/W, consists in combining several monochromatic LEDs (the simplest set being RGB (*Red, Green and Blue*) LEDs). However, this solution is also the most expensive and raises several issues. First, it is necessary to use an optical system to mix the emissions of the different LEDs, second, it is necessary to manage the drifts of the characteristics of each LED with heating and ageing, in order to maintain the same “white” color.

The second and more common approach, consists in depositing a fluorescent material (as in Compact Fluorescent CFL lamps), commonly called “phosphor” (phosphor-converted white LED), such as for instance Cerium-doped Yttrium Aluminum Garnet (Ce^{3+}:YAG). This material converts high energy photons (blue in practice, but also UV (*Ultraviolet*) in some cases) into lower energy photons (by fluorescence). Since this conversion is not ideal (because of heat loss from the Stokes shift), some blue photons are absorbed without being converted into photons of lower energy. Consequently, this solution degrades the quantum efficiency (emitted photons divided by injected electrons) of white LEDs compared to blue ones. The typical appearance of a white LED emission spectrum obtained by a phosphor conversion is reported in Fig. 11. One challenge is to decrease the size of the spectral gap between the blue LED and the converted light.

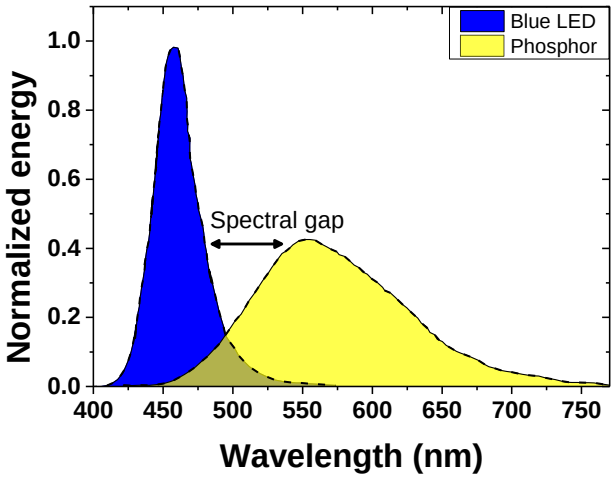

Fig. 11: Typical white LED spectrum by phosphorus conversion. Figure adapted from [25].

The spectrum emitted by fluorescence depends on the type of phosphor material, its thickness, its grain size distribution, and the shape given to the deposit. Of course, the composition of the phosphor and its deposition technique are manufacturer dependent. One of the issues penalizing the quality of the white light is the spectral gap (between 470 and 520 nm) between the emission spectrum of the blue LED and the fluorescence spectrum. Techniques based on UV LEDs to excite the fluorescence of phosphors have been suggested (that suppress the spectral gap in the visible range), but the low efficiency of UV LEDs remains an issue [25]. Examples of phosphor emission spectrum used in LED are given in Fig. 12 and examples of white LED spectrum are reported in Fig. 13. It is possible, by combining several phosphors, to create white LEDs with several emission peaks, adjusting color rendering, at the expense of a decrease in luminous efficiency (lm/W) and of a cost increase.

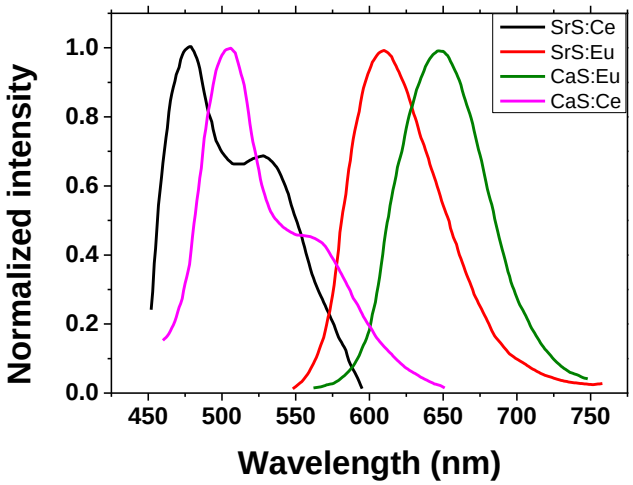

Fig. 12: Emission spectrum of phosphors. Figure adapted from [25].

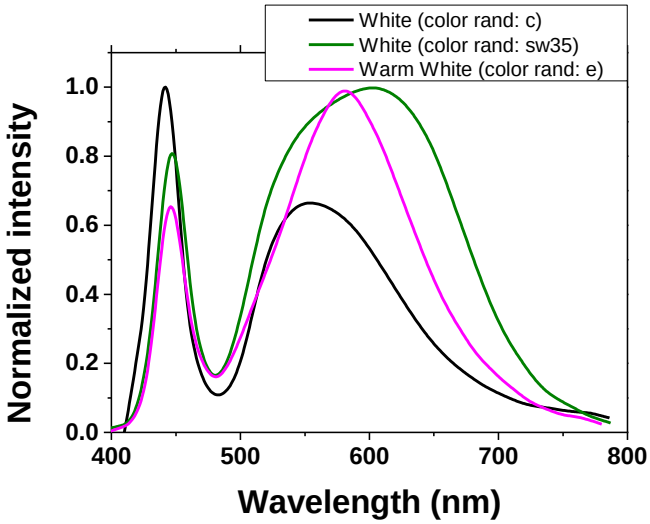

Fig. 13: Examples of white LEDs emission spectrum, with different phosphors to optimize the color rendering depending on the application. Figure adapted from [25].

B.1.3. Power supply

Most of LEDs operate with direct current (DC), there are also LEDs operating on alternating current, but their efficiency and life span are lower [25]. This PhD thesis presents only LEDs operating with direct current. Fig. 14 shows the classical I-V characteristic of a LED.

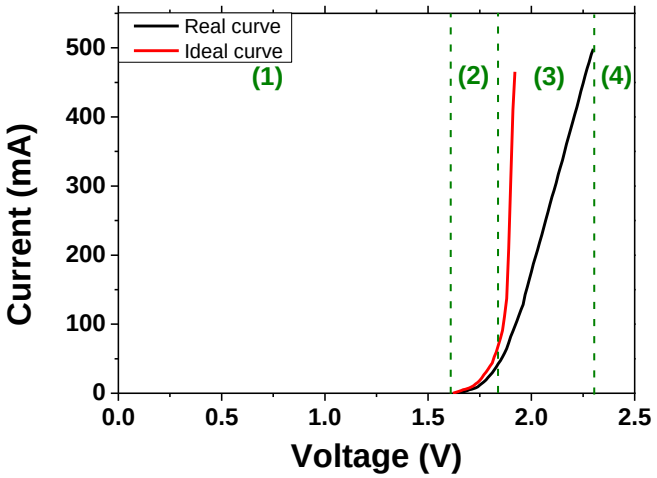

Fig. 14: Typical Current-Tension (I-V) diagram of a LED in linear regime. Figure adapted from [25].

This characteristic response can be divided in four zones:

- (1) From 0 to the threshold voltage (here approximately 1.6 V), nearly no current passes through the LED (it is in reverse regime),
- (2) Just above the threshold, the current appears: the LED I-V response is strongly non linear (exponential),
- (3) The third zone is characterized by a linear response which is the operation regime (probably due to series resistance),
- (4) At higher current, the LED would be damaged (not shown in Fig. 14).

LEDs have to be driven in current (and not in voltage) because a small increase in applied voltage generates a large increase in current. As the threshold voltage varies with temperature (it decreases as the temperature increases), in the case of voltage control, the increase in temperature will generate a higher current supply than necessary and cause heating. This impacts the emission spectrum and can possibly damage the LED.

B.1.4. Temperature

The emission spectrum, efficiency and lifetime of LEDs strongly depend on temperature. The impact of temperature slightly differs between LED technologies due to difference in used materials, in manufacturing processes, and thermal properties of the

LED packaging. This is one of the main differences between LEDs and other lighting sources, such as incandescent lamps for instance, that are relatively insensitive to temperature variations.

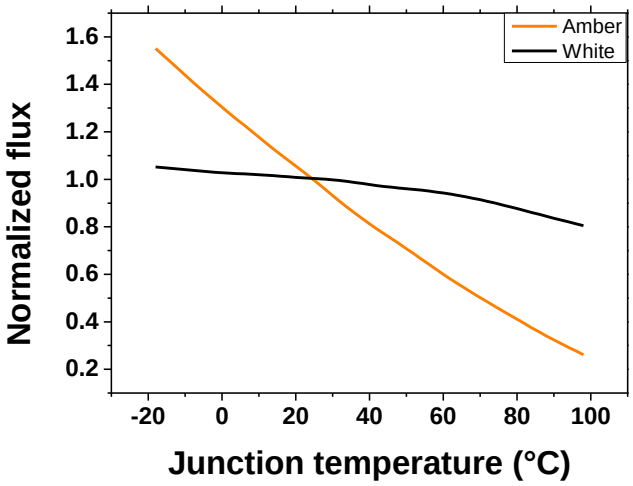

Fig. 15: Temperature effect on the LED light flux (reference temperature is 25°C). Figure adapted from [25].

The operating temperature of LED is not a priori know, since the LEDs heat up during operation. It also depends on their environment, particularly their packaging. It is sometimes necessary to thermally control – to cool – them to stabilize their performance. To have an idea of the LED internal temperature, it is mandatory to measure its junction temperature [27].

As far as the emission spectrum is concerned, an increase in temperature leads to a global shift of the spectrum toward higher wavelengths (“red shift”) up to ten nanometers for amber LEDs (with a variation of the temperature junction from 25 to 125°C), which is mostly due to the decrease of semiconductor bandgap with temperature.

Regarding the efficiency, an increase in temperature will promote non-radiative recombination and joule effect, and will reduce the emitted light power, as shown in Fig. 15. This effect is more pronounced for low-power LEDs. The blue LEDs used as a "pump" for the white LEDs are among the ones that lose the least amount of flux with increasing temperature.

A high temperature will also shorten the LEDs lifetime. However, the overall lifetime remains good compared to the lifetime of most lighting device (Fluorescent tubes typically are rated at about 10,000 to 25,000 hours, and incandescent light bulbs at 1,000 to 2,000 hours), even at high temperatures (above 100°C), as shown in Fig. 16.

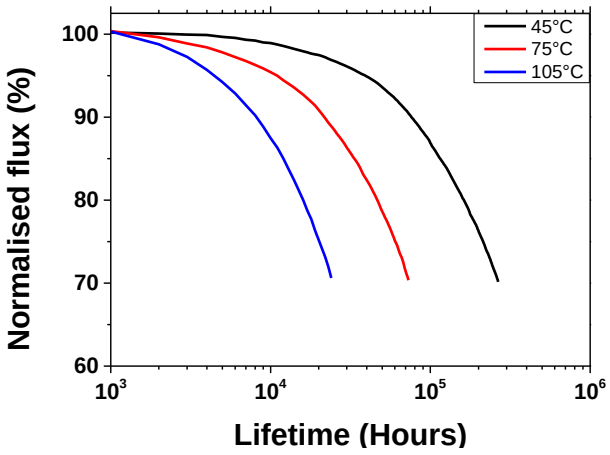

Fig. 16 Lifetime and loss of luminous flux for different junction temperatures for CREE Inc. LEDs. Figure adapted from [25].

B.1.5. Efficiency droop and ABC model

LEDs and especially InGaN blue emitting LEDs are known to be affected by the phenomena of "efficiency droop," i.e. a detrimental decrease of quantum efficiency at high injected current [28], observed mostly for GaN LED and attributed to Auger recombination [26]. The phenomenon of efficiency droop is visible since the efficiency (radiation flux divided by electrical power) tends to decrease when increasing the drive current. To clarify the notion of external quantum efficiency, we first have to define different LED figures of merits. Fig. 17 is used to illustrate them.

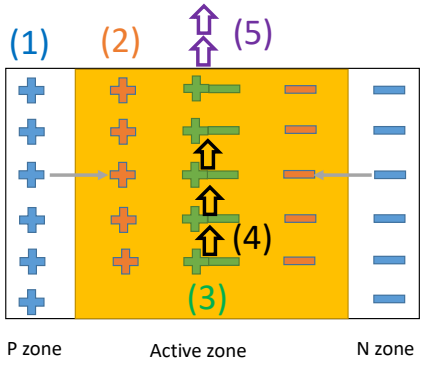

Fig. 17: Illustration of the different steps between charge injection and the emitted photons

- The injection efficiency (η_{inj}) is the ratio between the number of electron reaching the LED's active zone per second by the total number of electron injected in the LED per second (current / e) → $^{(2)}/_{(1)}$

- Radiative efficiency (RE). It is the ratio of radiative recombination by the total number of recombination within the LED's active zone during per second → $^{(3)}/_{(2)}$

- Internal Quantum Efficiency: IQE is the ratio between the number of radiative recombination by the number of charges per second → $^{(4)}/_{(3)}$

$$IQE = RE * \eta_{inj} \quad (1)$$

- Extraction efficiency (η_{opt}): It is the ratio between the number of photons per second extracted and the number of photons generated per second → $^{(5)}/_{(4)}$

- External Quantum Efficiency (EQE): is the number of extracted photons per second by the number of injected electrons in the LED per second. → $^{(5)}/_{(1)}$

$$EQE = \eta_{inj} * RE * \eta_{opt} \quad (2)$$

As a consequence, EQE results from a trade-off between charge injection, radiative recombination efficiency and light extraction. The EQE is the quantity that can be measured with the flux measurement, see section B.2.3.

An example of efficiency droop from [29] is presented in Fig. 18. At low level of current, the efficiency increases with the current, then decreases at high level of current.

This effect is usually explained by the competition between several recombination mechanisms impacting the radiative efficiency: non-radiative recombination Shockley-Read-Hall (trap assisted), radiative recombination and Auger recombination.

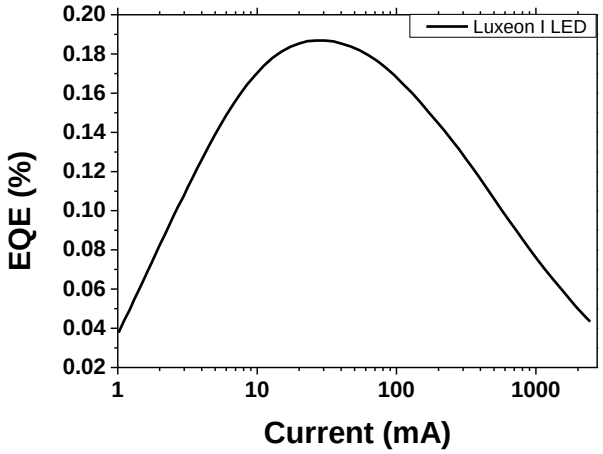

Fig. 18: External quantum efficiency of commercial green LEDs @530 nm (Philips Lumileds'Luxeon line) as a function of operating current. Figure adapted from [29]

The Auger recombination is not the only effect that may cause non-radiative recombination and decrease the LED efficiency, there also is the non-radiative recombination Shockley-Read-Hall (trap assisted). The Fig. 19 illustrate the different types of recombinations.

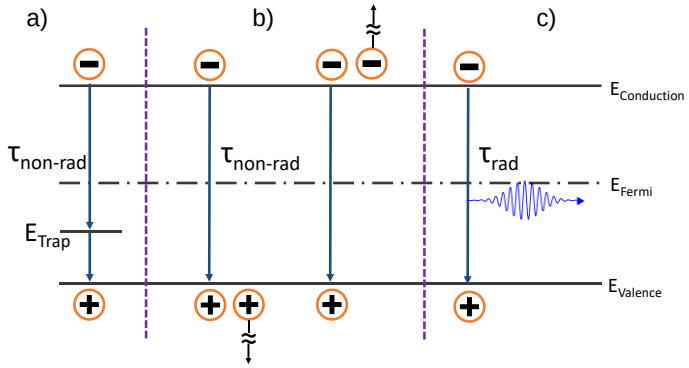

Fig. 19: Band diagram illustrating recombination mechanism in LED: a) via Shockley-Read-Hall (trap assisted), b) via Auger process, c) radiative recombination. Figure adapted from [27].

A simple model can capture the impact of traps and Auger recombinations on the quantum efficiency. Indeed, the radiative efficiency (RE) is by definition equal to:

$$RE = \frac{\int_0^W R_{rad}(x)\,dx}{\int_0^W R_{trap}(x)\,dx + \int_0^W R_{rad}(x)\,dx + \int_0^W R_{auger}(x)\,dx}$$

Where R_{trap} (resp. R_{rad}, R_{auger}) is the trap assisted (resp. radiative, auger) recombination rate within the active layer of thickness W.

Replacing the recombination rates by their standard expressions, and assuming that the injected electron n and holes concentrations are equal and uniform within the active layer (a reasonable assumption for quantum well LEDs), the internal quantum efficiency reduces to:

$$IQE = \frac{Bn^2}{An + Bn^2 + Cn^3} \quad (3)$$

Where A represent the Shockley-Read-Hall, B the radiative recombination and C the Auger coefficient. Finally, the current flowing through the LED can be expressed as:

$$i = i_0(An + Bn^2 + Cn^3) \quad (4)$$

Where i_0 depend on the LED dimensions (quantum well thickness and current section). Combining these two equations, it is possible to compute the IQE vs current curves.

Fig. 20 shows a comparison from the literature between experimental data and the model. In this paper [30], the ABC model is used to analyze the impact of lateral recombinations on LEDs pixels of different sizes. Indeed, the ABC model has been modified to account for an hypothetical dependency of trap assisted recombination with the perimeter / area ratio, according to :.

$$IQE = \frac{Bn}{A\frac{P}{S}n + Bn^2 + Cn^3} \quad (5)$$

Where P is the perimeter of the LED and S its surface. Model and experiments are in qualitative good agreement, even though less accurate for smaller pixel.

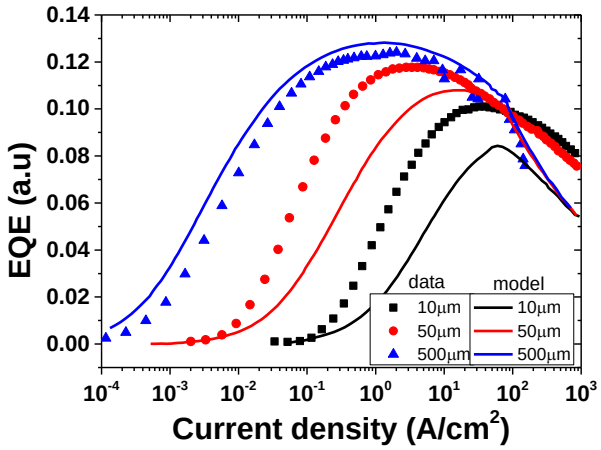

Fig. 20: External quantum efficiency versus current density for different LED sizes. Some difference are yet observable between measurement and simulation, due to the ABC model approximation on the LED current modeling. Figure adapted from [30]

This model will be used in the section B.3.3 to give an understanding of the radiation effects in LEDs.

B.1.6. Emission angle

In absence of additional optical elements or surface texturing, the light emission from a high refractive index medium to the air (planar diopter) follows a light intensity (cd or W/str) distribution of the Lambertian type, i.e.:

$$I = I_0 \cos(\theta) \tag{6}$$

With I_0 the intensity in the normal direction to the LED and θ the angle between I_0 and I as shown in Fig. 21. The half of the normalized intensity is obtained for a particular value of θ ($\theta_{1/2}$) given by:

$$\frac{I}{I_0} = \frac{1}{2} = \cos(\theta_{1/2}) \tag{7}$$

For a Lambertian source, $\theta_{1/2} = 60°$. Manufacturers often report, in their datasheet, $2\theta_{1/2}$, (120° for a Lambertian source). The intensity $I(\theta)$ indicates how the luminous flux is dispersed in the 2π solid angles of the half-space, it can often be

interesting to concentrate this flux in a given direction, which can be done by means of a lens (often in silicone) placed on the top of the LED or by using a reflector.

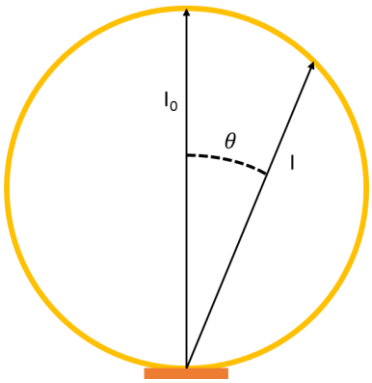

Fig. 21: Normalized intensity diagram of a Lambertian source.

B.1.7. Radiation effect on LEDs

The effects of radiation on LEDs have already been studied in the literature, particularly for low-dose space applications (a few tens of kGy) and mainly under ionizing particles [31] [32]. In addition, CERN is currently working on the effects of high proton flux on LEDs in order to optimize the lighting in its accelerator tunnels [33] [34]. It is admitted that the degradation of LEDs by irradiation is mainly due to atomic displacements caused by particles such as protons or neutrons [13], [16], [17]–[23]. Gamma radiation is mainly associated with ionization processes but can possibly cause rare atomic displacements by side effect (Compton electron). Johnston (who wrote two major reviews on radiation effect in optoelectronic devices [35] [36]) attributed LEDs degradation “to displacement damage from Compton electrons produced by gamma rays, not ionization damage”, [36] nevertheless many authors attributed a part of the degradation to ionization process. We will compare both hypothesis with our results. In the context of CAMRAD, we limited our study to gamma radiation effects and focused our attention on the articles dealing with this type of radiation.

It is known that LED technologies have greatly improved in past decades. So we decided to not review papers older than the ones quoted in the 2013 review [41]. In it two articles address gamma effects on LED, the first one [42] focused only on the electrical modifications of n-GaN LEDs irradiated at 0.21 MGy. The second one [43] studied the optical power loss of InGaN/GaN LEDs in the 410-510 nm spectral range irradiated up to

20 MGy. To the best of our knowledge, since 2013, just few studies have been published on the modification of the optical power emitted by high-dose gamma irradiated LEDs: one on 590 nm AlGaInP LEDs irradiated at 0.3 MGy [44], the second [45] on red LEDs for signal transfers and the last [33] on luminaire, which have a packaging that mainly explain their degradation. Main optical characteristics from these articles are reported in Table 3.

Table 3: Main characteristics of gamma irradiated LEDs in the literature

Ref	Type	Spectral range (nm)	Maximum dose	Power change (%)	Year	Silicon lens
[43]	InGaN	410 to 510	7.5 MGy	-80	2005	With and without
[44]	AlGaInP	590	0.3 MGy	- 35	2013	unknow
[45]	AlGaInP	575	1 MGy	- 90	2016	with
	AlGaInP	609	1 MGy	- 80	2016	with
	AlGaInP	635	1 MGy	- 40	2016	with
[33]	Cree XP-G	white light (phosphors converting)	100 kGy	-79	2016	Full illuminator packaging
	Cree XP-E	white light (phosphors converting)	100 kGy	-73	2016	Full illuminator packaging

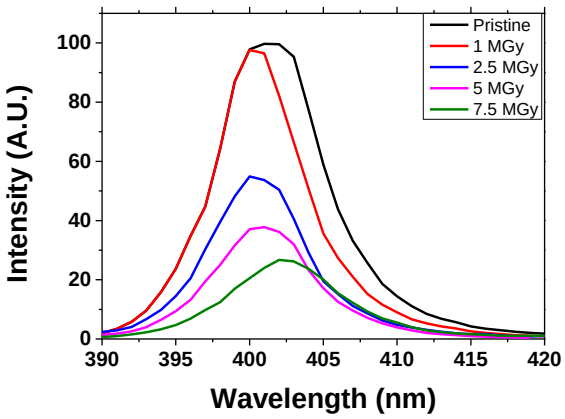

Fig. 22: Emission spectra evolution at different gamma ray (^{60}Co) doses. The 410 nm (InGaN/GaN) LED was biased during irradiation. Figure redrawn from [43].

All the LEDs from Table 3 present non-negligible losses. So, their intrinsic resistance to gamma radiation is not perfect at high doses. The loss of emission power is most often attributed to the creation of recombination centers that will cause non-radiative effects. An example, from [43], is reported in Fig. 22, showing the spectral flux degradation of a blue LED at 410 nm (without lenses) at different gamma radiation doses. Despite irradiation up to 7.5 MGy, the authors didn't find any visible degradation of the LED appearance. Fig. *23* shows the time dependency of the forward voltage before and after irradiation. The small voltage increase may be due to a higher number of traps in the p-side leading to a decrease of the hole concentration.

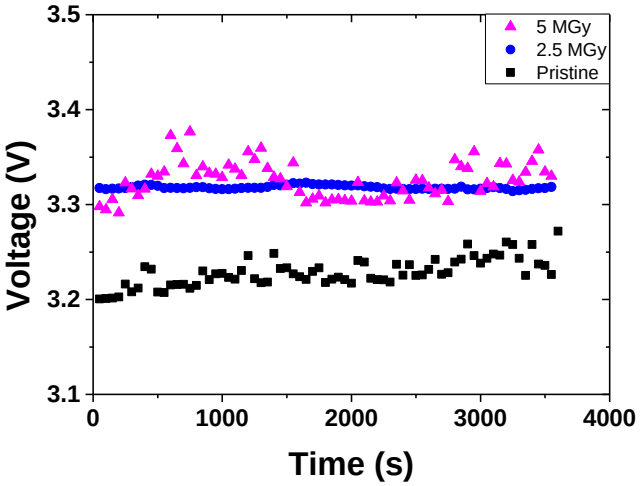

Fig. 23: LED's voltage time evolution before and after irradiation (gamma). Figure adapted from [43].

The studied LED is a blue one, similar to that typically used in white LEDs to pump the phosphor materials. It should be noted that for radiation dose lower than 1 MGy, the degradation of the light flux remains limited, but can reach ~ 80 % for the high dose of 7.5 MGy. In this paper, the LED was driven at a constant current: a decrease of the applied voltage and more importantly a significant instability over time were observed with radiation, even at low doses. This phenomenon was not discussed in the article, and no recovery phenomena was neither reported nor discussed.

An interesting conclusion from [44] is that if the LED is driven with high current, less degradation seems to occur. According to the authors, it is attributed to the operating current density. This effect is highlighted in Fig. 24.

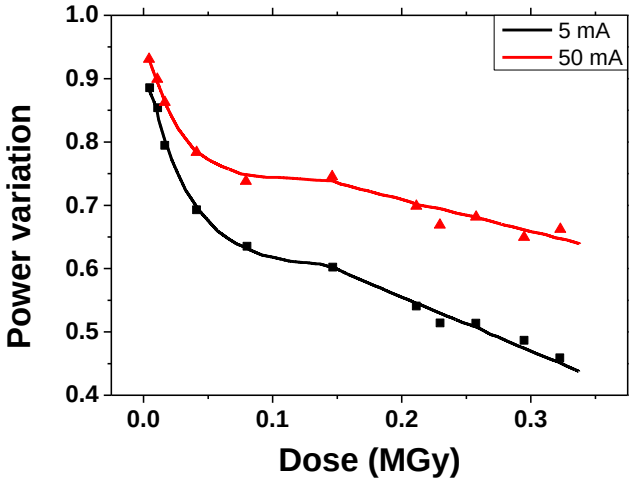

Fig. 24: Power variation @ 590 nm at different gamma doses for 2 currents. Figure redrawn from [44].

Authors analyzed their results as follows:

- First the degradation is driven by the conversion of the existing defects (precursors) into non-radiative centers. This effect saturates at a cumulative gamma dose of about 0.15 MGy,
- Then the degradation slows down and is driven by the creation of traps without precursors.

In Fig. 25, the power of the blue LED, reported in Fig. 22, has been plotted versus dose, illustrating this slowdown of the degradation.

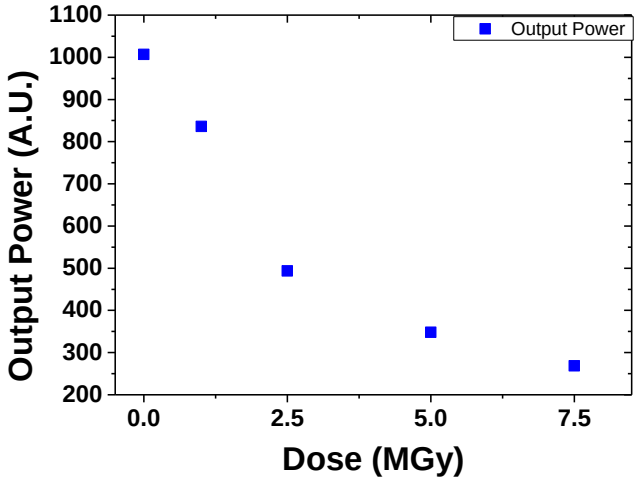

Fig. 25: Output power evolution as a function of the dose for a blue LED. Figure created from [43].

In a previous study [46] (founded by F4E), our consortium studied the effects of gamma radiation on white and amber LEDs of low and medium output powers (0.22 to 1.73 W before irradiation for white LEDs). The results can be summarized as follow.

First, by removing silicone lens before irradiation and comparing the same LED with and without its lens, the impact of irradiation on the output power was monitored. We showed that even if the transparent silicon lens turns to brownish color during the irradiation, the LED output power is higher with the lens than without (see Fig. 26). Consequently, it may not be mandatory to remove the LED's lens for its use in a harsh environment.

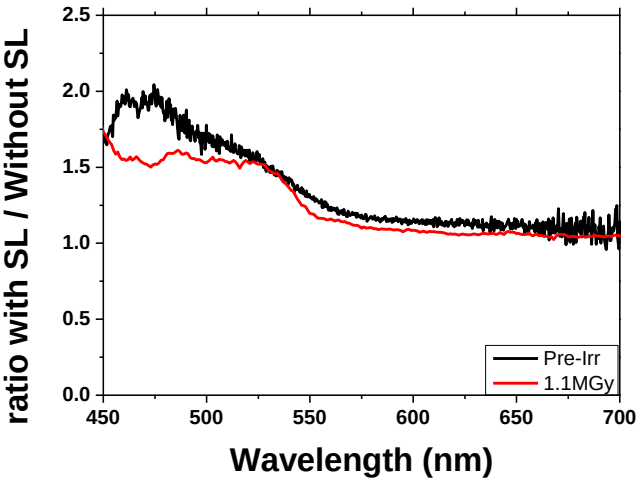

Fig. 26: Flux ratio between the same white LED with and without a silicon lens before and after gamma irradiation up to a cumulative dose of 1.1 MGy. Figure from [46].

Second, we showed that high-power LED (supplied with high DC electrical power) seems less impacted by radiation, in agreement with [44].

Third, we investigated the "efficiency droop". This phenomenon consists in a penalizing decrease of quantum efficiency at high injected current [28] observed mostly for GaN LED, attributed to Auger recombination [26]. The phenomenon of efficiency droop is expected in all tested samples, since the efficiency (radiation flux divided by electrical power) tends to decrease when increasing the driving current. However, if the irradiation indeed decreases the output power, it does not significantly affect the slope of the efficiency versus current curve, suggesting that the efficiency droop remains

unaltered [20]. Regarding AlInGaP amber devices (Fig. 27), an efficiency droop is observed in the unirradiated device, however, its amplitude is less pronounced than in InGaN white devices. In the literature, this phenomena is usually not observed for AlInGaP, except in [47], but only at low temperatures. Indeed, after irradiation, contrary to the case of InGaN (Fig. 28), the efficiency droop in AlInGaP amber devices almost disappears. One possible explanation for this unexpected observation is that recombination may be so enhanced by radiation that the level of electrons and holes concentrations required for Auger recombination to occur is no longer achieved, removing efficiency droop. The overall low efficiency level and strong impact of radiation on AlInGaP amber devices are in favor of this hypothesis.

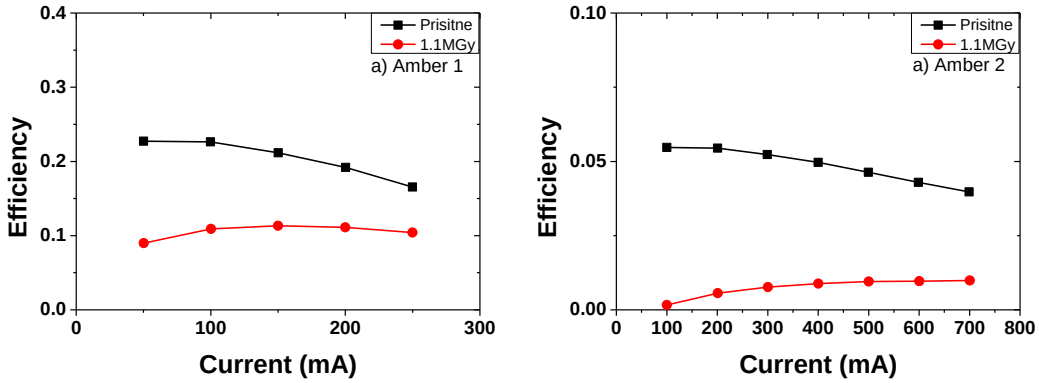

Fig. 27: Impact of radiation on the "efficiency droops" (Efficiency=photons emitted/electrons injected) for amber LEDs. Amber 1 is an AlInGaP LED and Amber 2 is a InGaN one. Figure adapted from [46].

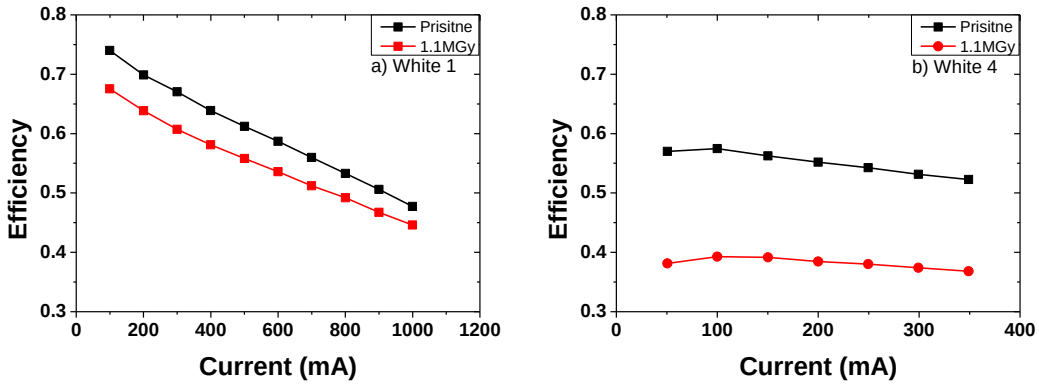

*Fig. 28: Impact of radiation on the "efficiency droops" (Efficiency=photons emitted/electrons injected) for 2 different white LEDs (*White 1 *and* White 4*). Both LED are InGaN devices. Figure adapted from [46].*

Finally, even if LEDs are considered to be intrinsically resistant to gamma radiation, which is true for some references, we also measured losses up to 58% @ 1.1 MGy for amber LEDs and up to 33% @ 1.1 MGy for white LEDs (our results are

presented in Table 4). So it's still mandatory to test COTS LEDs before using them in a radiation-rich environment, as it is also the case for integrated circuit in general.

Table 4: Evolution of some LED output powers after 1.1 MGy, data from [46]

LED reference	Amber 1	Amber 2	Amber 3	White 1	White 2	White 3	White 4	White 5
Power before irradiation (W)	0.07	0.12	0.46	1.73	0.33	0.22	0.39	0.51
Power after 1.1 MGy (W)	0.04	0.05	0.44	1.65	0.24	0.15	0.26	0.36
Change after 1.1 MGy (%)	- 43	- 58	- 4	- 4	- 27	-32	- 33	- 29

Conclusion Section B.1

In this chapter, we explained how the constraints on the image sensor impact the requirements for the illumination set up for CAMRAD system (which was set to 90 W).

Then, we gathered LEDs basic knowledge to give the reader all the needed information to understand the two next chapters about LED characterization set up and results. In particular, it may be useful to keep in mind that LEDs output power decreases when the LEDs temperature increases.

Finally, we presented a literature review on the effect of gamma radiation on LEDs. LEDs are known to be intrinsically resistant to gamma radiation, so there are only a few papers dealing with it especially for commercial LED. Nevertheless, we can estimate that LEDs may lose more than half of their output power after 1 MGy. Hence, they have to be tested before being implemented in a radiation environment. Gamma radiation affects more the output power of the LEDs than their electrical responses. In the next chapter we will describe our protocol to measure this parameter on the selected CAMRAD LED references.

B.2. Materials and methods for LED characterization

B.2.1. Gamma irradiation (color & white LEDs)

In the CAMRAD project, we had access to gamma irradiation campaigns (^{60}Co) at IRMA [16] (IRSN, Saclay, France) the first at the end of 2017 and the second at the end of 2018. LEDs from Table 5 and Table 6[2] have been irradiated at three dose levels: 0.1, 0.5 and 1 MGy (the irradiation campaign was ≈2 weeks long). All LEDs were unbiased during the gamma irradiation runs by material constraint (we used X-ray to compare biased and unbiased cases)

Table 5: Product number of RGB and RGB White LEDs irradiated at the first IRMA campaign (2017), all data come from manufacturer specification sheets

Product number	Manufacturer	Color	Nominal current (mA)	Nominal voltage (V)	Maximal optical power	Dissipated power (W)
RTDUW	OSRAM	Red Green Blue White	700	2.50 3.60 3.45 3.45	112 lm 180 lm 900 mW 224 lm	N.C
F50360	Seoul Semiconductor Inc	Red Green Blue	350	2.0 ~ 3.0 3.0 ~ 4.2 3.0 ~ 4.1	35 lm 57 lm 13 lm	1.68 W
Z power F50360RLS	Seoul Semiconductor Inc	Red Green Blue	800	2.3 3.25 3.25	48 lm 70 lm 22 lm	2.4 W 4.0 W 4.0 W
SML LX1610	Lumex	Red Green Blue	300 350 350	2.1 3.5 3.5	25 lm 25 lm 8.0 lm	3.5 W

[2] The full reference of each LED is available in Appendix B.

Table 6: Product number of White LEDs irradiated at the first IRMA campaign (2017), all data come from specification sheets

Product number	Manufacturer	Nominal current (mA)	Nominal voltage (V)	Optical Power (lm)
CXA3590	CREE	1100	34	9 000
CXA2590	CREE	1200	36	7 945
MKRBWT	CREE	400	36	870
MKRAWT	CREE	1400	11.7	840
MCE4WT	CREE	700	3.1	260
XMLAWT	CREE	700	2.9	220
XPEBWT	CREE	700	3.05	93.9
XPEWHT	CREE	350	3.05	93
LHC1-3090	LUMILED	1200	36	3 750
SDW84F1C	SEOUL SEMICONDUCTOR	700	35.6	3 000

After the first set of measurements which was not consistent with the literature (cf. B.3.1.1 & B.3.1.2), we performed new tests in the same conditions. Products numbers irradiated during the second campaign are listed in Table 7.

Table 7: Product number of White LEDs irradiated at the second IRMA campaign (2018).

Product number	LCH1 3090	MKRBWT	SDW84FC	MKRAWT	XPEBWT

B.2.2. X-ray irradiation (White LEDs)

For radiation tests, we used the *LabHC MOPERIX* machine (100 kV X-ray tube with W-target filtered by 4 mm thick of Beryllium material) that delivers X-rays beam, spectrum Fig. 29. All doses and dose rates measured under X-ray are converted in SiO_2 equivalent. Irradiations were performed at room temperature. Product number and irradiation condition are in Table 8.

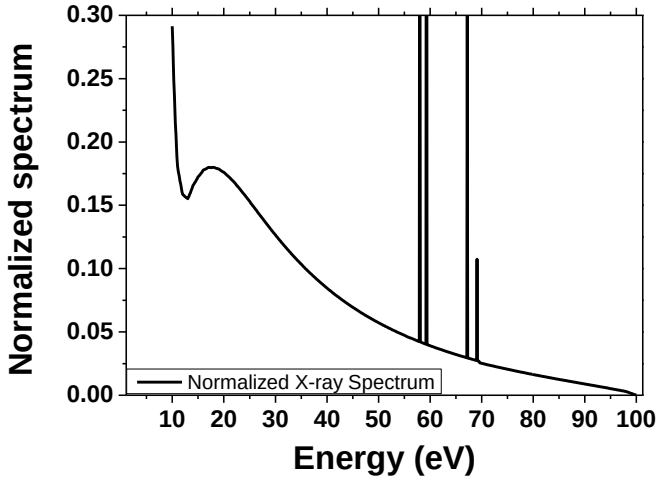

Fig. 29: Emitted X-ray spectrum with an accelerating voltage of 100kV, computed with SpekCalc [48]–[51] with the following parameters: Beryllium thickness = 4 mm, air thickness = 0 mm and theta = 30°(X-ray emission angle).

Table 8: LEDs irradiated with X-ray up to a cumulative dose of 1 MGy

Product number	LCH1 3090	MKRBWT	SDW84FC
Irradiation conditions	Biased and Unbiased	Biased and Unbiased	Biased and Unbiased

We also made radiation characteristics measurement on the LEDs of Table 9

Table 9: type and conditions of irradiated LEDs which radiation characteristic was measured.

Product number	LCH1 3090	MKRBWT	SDW84FC
Type and Irradiation conditions	1 MGy ϒ Unbiased 1 MGy X Unbiased 1 MGy X Biased	1 MGy ϒ Unbiased 1 MGy X Unbiased 1 MGy X Biased	1 MGy ϒ Unbiased 1 MGy X Unbiased 1 MGy X Biased

B.2.3. Flux measurement with an integrating sphere

First step is to measure the total flux emitted by each LED (W or lm). We used a *Labsphere Ltd LCS-100* allowing an accurate measurement of the LED optical power. An integrating sphere was chosen for two main reasons:

- It collects the entire flux emitted by the LEDs (independently of their directions of emission);

- The illumination at any point on the surface of the sphere is identical and Lambertian, thanks to the sphere internal coating made of white barium sulfate ($BaSO_4$). This coating presents the advantage of scatter in an isotropic way almost all the radiations in the visible domain, regardless its wavelength. That means that the position of the detector in the sphere does not need to be finely controlled.

Accurate measurement using an integrating sphere requires a calibration of the "sphere→ optical fiber→ spectrophotometer" response to a calibration lamp. Thank to this calibration, we directly obtain results in Watt/nm after correction of the signal deformations induced by the fiber and the spectrometer/detection spectral response. The calibration process and associated calculations are explained in more details in [46]. In addition, this calibration allows us to compare the measurements even after an assembly and disassembly of the experimental bench. The principle of the integrating sphere is illustrated in Fig. 30. Following the first measurement campaign at the end of 2017, results showed a surprising slight increase of the emitted light after irradiation for some LEDs (see section B.3.1). So, we carried out a second measurement campaign. To avoid the difficulties encountered previously, we improved the measurement method by leaving one minute between each current level and making five measurements per step (≈ 1 every 10 seconds) to ensure similar thermal effects from LED to LED. This method was used to perform the repeatability tests (see below) and measurements shown in section B.3.2. The sphere allows recovering a constant part of the LED flux: this is shown in Fig. 31 which was obtained by removing and replacing the LED in the sphere and then performing new measurements at three different currents (100, 500 and 1000 mA). The coefficients of variation are then given by:

$$c_v = \frac{\sigma}{\mu}. \qquad (8)$$

with σ the standard deviation, μ the average power.

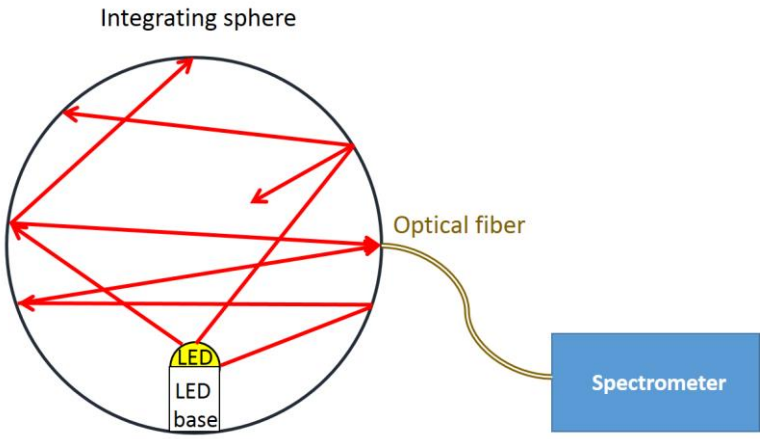

Fig. 30: Representation of a LED in an integrating sphere and its spectral power measurements

.

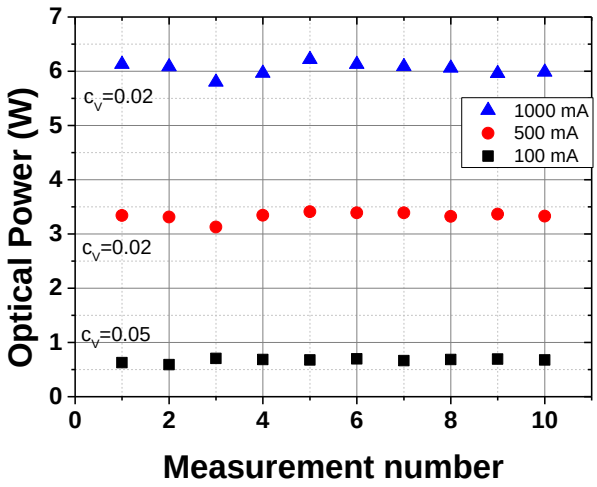

Fig. 31: Repeatability of the LED positioning in the sphere and power steps. Between each measurement, the LED was shut down, removed from the sphere then replaced again. The power measurement was made at three different current levels.

Fig. 31 also shows the repeatability between each current rise (*the LED is placed unbiased in the sphere, then the current is rising step by step leaving the voltage free*). We can note that for all tests, values at each step are really close. Nevertheless at 1000 mA the emitted power decreases from measures 5 to 10, which can be related to the increase of the LED temperature that did not decrease exactly back to initial room temperature between each measurement. As shown in Fig. 49 temperature stabilization can take up to 1 hour. This duration will make the measurement quite time consuming. But above all we were concerned by the risk that the temperature damages the sphere coating, because of the radiator temperature (see Fig. 35) that rises up to 70°C at the

end of the measurement run. So I choose to wait 5 minutes after each current step, then to make 1 measurement each 10 second during 1 minutes before moving to the next current step. I also waited for 10 minutes after the end of each measurement to let the radiator temperature decrease.

We also verified that each LED of the same family gives the same response, one example is presented in Fig. 32. We tested every LED before irradiation to check that they have identical responses.

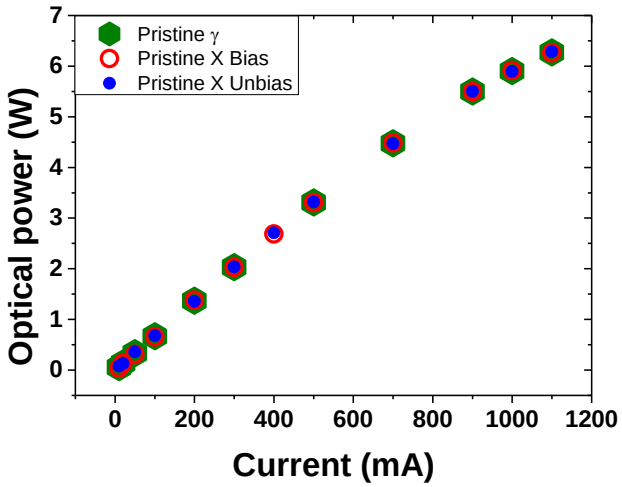

Fig. 32: Response of 3 different LEDs from the same family (LCH1 3090) before irradiation. Their names correspond to the type of irradiation each one will be subjected to.

B.2.4. Angular luminous intensity measurement by goniometer

Typical photometric calculations of the imaging and lighting system [12] take into account the angular distribution $I(\theta)$ of the LED luminous intensity and assume that it remains unchanged during irradiation. To the best of our knowledge, there is no bibliographical reference to confirm this assumption. To validate this hypothesis, we therefore carried out angular luminous intensity measurements in a few LEDs before and after irradiation. To this aim, we used a 1D goniometer, i.e. a rotating arm at the end of which we placed a lens that injects the light from the LED into an optical fiber connected to a spectrometer. The measurement principle is shown in Fig. 33, as this bench is quite rudimentary, we do not claim to make measurements as precisely as manufacturers, In consequence, we focus our attention only on pre- / post-irradiation comparisons. A

typical measurement is shown in Fig. 34, where the offset on the measurement is a systematic positioning error, so the radiation characteristic is not symmetrical with respect to 0°. For each indicator, the LED is removed and replaced again 4 times, the result is an average of these successive measurements.

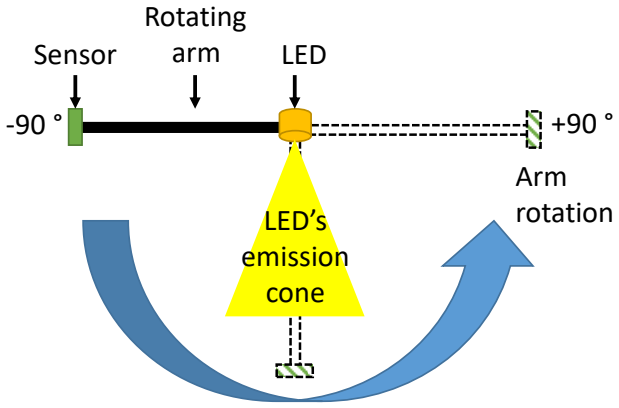

Fig. 33: Radiation characteristic measurement setup.

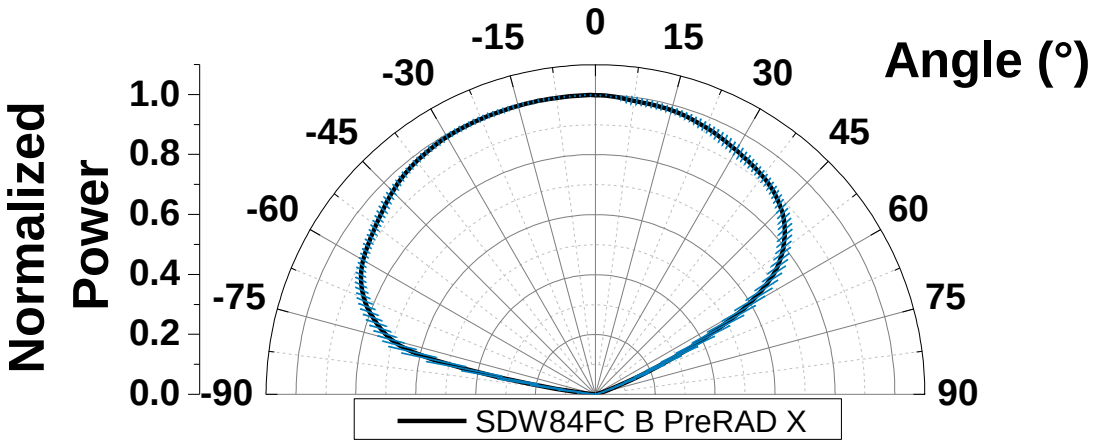

Fig. 34: Typical measurement of radiation characteristic on an unirradiated LED. Error bars are the standard deviation.

B.2.5. Setup for LED online characterization under X-rays

Online measurement of the radiation effects on the LEDs optical performances is one of the novelties of this PhD thesis. The advantages of the in-situ characterization are:

- To detect any abnormal phenomena such as: transient effect, thermal, power or supply fluctuations or interactions between high energy photons and phosphor,
- To compare the radiation effects for biased and unbiased LEDs,
- To compare between X-ray (in situ) and gamma-ray (after irradiation) radiation effects.
- As the X-ray facility is easy to access, it's interesting to know if it's relevant to use X-ray instead of gamma, to simplify and decrease the cost of LEDs future radiation testing.

For this experiment the LED is placed as shown in Fig. 35 while the setup is described in Fig. 36.

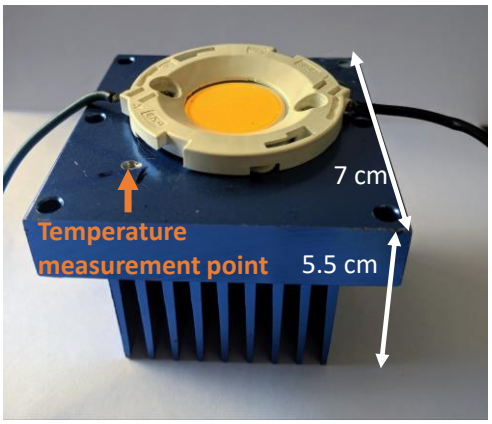

Fig. 35: LED is fixed on its radiator for online measurements.

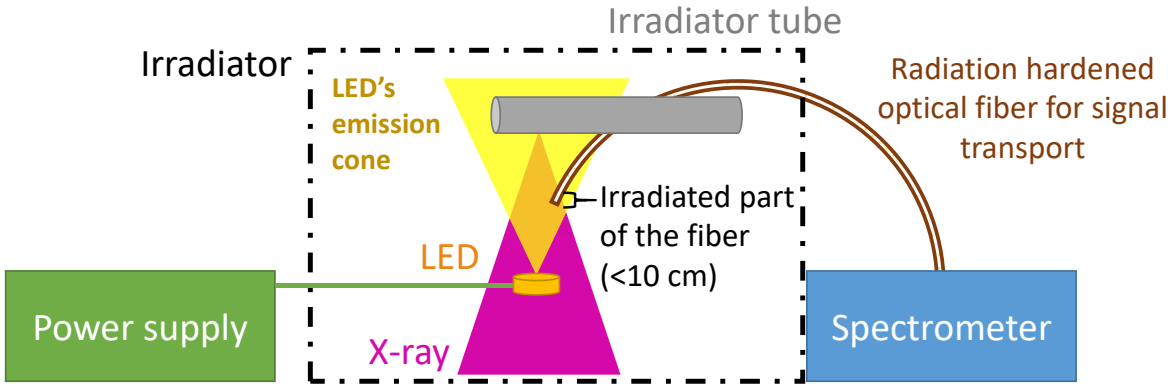

Fig. 36: Schematic representation of online characterization of LEDs under irradiation. Both power supply and spectrometer (spectral detection analysis) are located out the X-ray irradiation chamber.

The LED is mounted on a passive radiator, it is powered at nominal voltage and current by a *KEYSIGHT E36312A* (that can record the time evolution of both the voltage and current), a multimode optical radiation hardened fiber (*Draka MM SuperRadHard*) is placed in the LED's emission cone and protected from the radiation beam (over its exposed part) by an additional shielding (≈1.5 cm of aluminum). This fiber will collect a part of the emitted light, with the hypothesis that the emission cone is stable during the irradiation run[3]. This fiber is connected to a spectrometer (*QE from Ocean Optics*) for signal analysis. The refractive index of the fiber is not altered or modified by the small X-ray dose received. The light intensity collected by the optical fiber is driven by its numerical aperture ($N.A.$) given by:

$$N.A. = \sqrt{n_{core}^2 - n_{cladd}^2} \quad (9)$$

With n_{core} and $n_{clad}$the refractive index of the fiber core and the cladding respectively. $N.A.$ is only function of both refractive index, so it will be kept constant during irradiation. Finally, the quantity of light in the fiber will only depend of the variation of the output power of the LED and irradiation conditions.

Conclusion Section B.2

Here we presented the different techniques used to measure the LEDs emitted spectrum for both online and post-irradiation runs. We also measured the angular luminous intensity that is an important parameter for both online measurement and especially the photometric calculation that is needed to design the LEDs reflector and determine the number of LEDs required to fulfill the camera illumination system requirements.

Then, we reported the main parameters of the tested LEDs and detailed the irradiation conditions. They allow us to compare unbiased gamma irradiation, unbiased X-ray and biased X-ray effects.

[3] We verified (see B.3.4) that the emission cone is the same before and after the irradiation run.

B.3. LEDs results

To facilitate the reading of this PhD thesis, this section will first show an example of LEDs that have undergone a significant flux modification, for both RGB and white LEDs. Then all the results for each LED type will be summarized. This will be followed by a comparison between the measurements under X-rays (biased or not) with those under gamma-rays (2018 IRMA campaign) on white LEDs. Thanks to the ABC model, we will suggest an analysis of LEDs degradation process. Then radiation characteristics and online irradiation results will be discussed.

B.3.1. Spectral measurements after the first (2017) gamma irradiation

During this first campaign, we proceeded only to post-irradiation analysis. Even if LEDs are standardized components, their responses were tested and compared before and after the irradiations. These measurements showed, especially for white LEDs, a slight increase of the output power after the irradiation. This unexpected result is not consistent with the literature, unless considering experimental issues leading to larger measurement uncertainties on devices that are almost not affected by the received radiation dose levels.

In a former study [46], this problem was not observed (or at marginal level) probably because these LEDs were more affected by radiation, less powerful (so less affected by heating processes) and had a lower nominal current. Because of the really good resistance of several LED references to gamma radiation, for some of them the radiation-induced changes are smaller than the measurement uncertainties. M in this section present a strong dispersion. I did not performed them. We may attribute this dispersion to:

- The positioning method of the LED in the sphere,
- The measurement duration that should be reproducible between LED: if not slight variations could lead to a difference of the junction temperature at the measurement that will more affect the device than radiation.

To overcome these issues, we improved our test method, allowing us to obtain repeatability results shown in Fig. 31 & Fig. 32. We then repeated the measurements during the IRMA-2018 campaign on a selected set of samples. All results reported in the following tables are given at nominal current and voltage.

B.3.1.1 RGB LEDs

Figures below show the acquired results on the F50360 LED. This reference is composed of three independent LEDs (Red, Blue and Green), assembled on the same chip. Each color is tested separately. Fig. 37.a) highlights spectral differences before and after irradiation at a cumulated gamma ray dose of 1 MGy, Fig. 37.b) shows these spectra after a normalization to highlight the radiation effects on the spectral shape while Fig. 38 shows the output power variation as a function of current at 1 MGy. This figure shows that the red LED is the most affected of the three colors, but from the results presented in Table 10, it is not a general result.

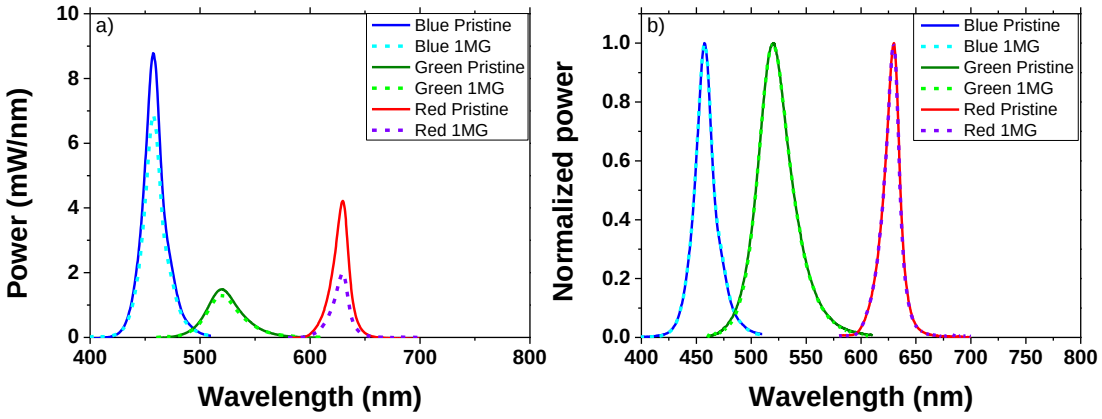

Fig. 37: a) Emission spectra of the F50360 LED before and after gamma irradiation at a cumulated dose of 1 MGy.b) Normalized emission before and after gamma irradiation at a cumulated dose of 1 MGy.

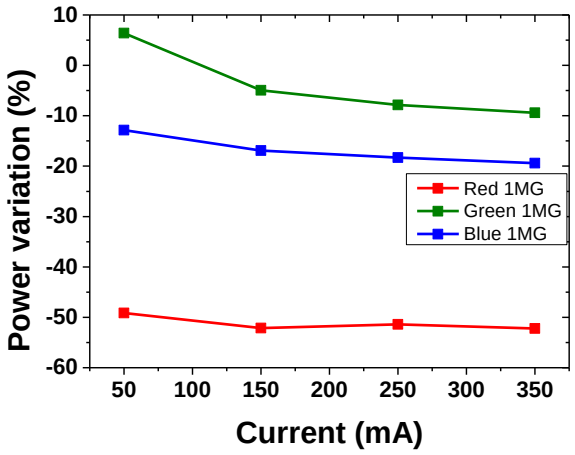

Fig. 38: Power variation as a function of current supply for the F50360 LED after 1 MGy.

After the irradiation at a dose of 1 MGy, the power variations are within -50 % (for the red), -5 % (for the green) and -15 % (for the blue) respectively. After normalization, we can note that there is no modification of the spectral power shape, suggesting that there is no additional absorption band created within the LED. Regarding their power evolution as a function of the current intensity, it remains relatively constant with no huge differences between low and high currents.

Similar results were obtained for the other RGB LEDs, they are summarized in Table 10.

Table 10: Outup powers of pristine and 1 MGy irradiated color LEDs at nominal current. Colors in the Table are associated with LED colors (red, green, blue), in the case of the RTDUW, black corresponds to the white LED.

Product number	F50360	RTDUW	Seoul Z power	SML-LX1610
Power before irradiation (W)	0.23 / 0.17 / 0.57	0.63 / 0.41 1.14 / 0.87	0.44 / 0.54 / 2	0.50 / 0.41 / 0.37
Power @ 1 MGy (W)	0.11 / 0.15 / 0.46	0.51 / 0.34 / 0.64 / 1.0	0.30 / 0.73 / 2.6	0.26 / 0.27 / 0.40
Variation	-52 % / -11 % / - 19 %	-19 % / -17 % / - 43 % / +14 %	-31 % / 35 % / +30 %	- 48 % / -34 % / +8%

B.3.1.2 White LEDs

Fig. 39.a) and Fig. 39.b) show results on the CXA2590 white LED. This device is interesting for a potential use in the final camera as it delivers a relatively high-power with respect to its size. This device is composed of a grid of LEDs on the same chip.

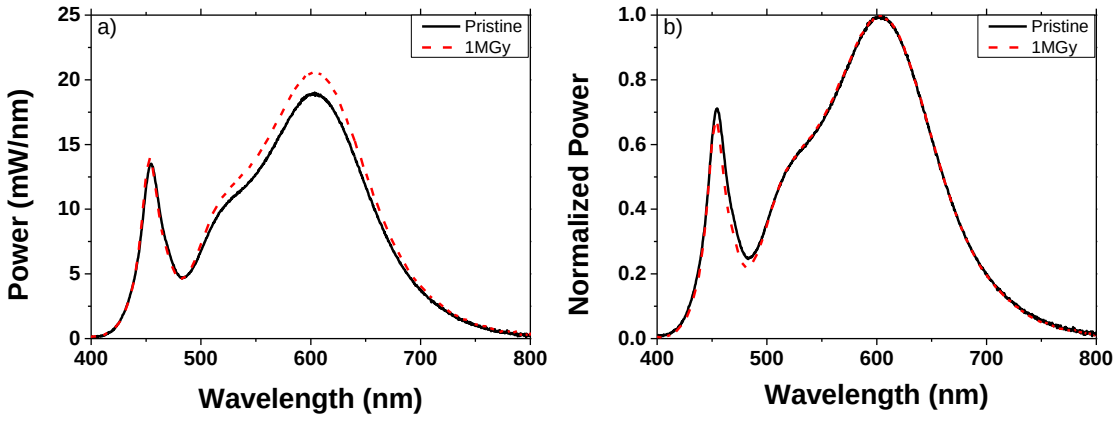

Fig. 39: a) Emission spectra of the CXA2590 LED before and after an irradiation dose of 1 MGy, b) Normalized emission spectra before and after an irradiation dose of 1 MGy.

This LED is one of the cases where the measured power is slightly higher after irradiation. As already discussed we attribute this effect to an experimental inaccuracy but this also indicates a very small (if any) effect of radiation on the LED spectral optical

power. We did not find a convenient way to estimate the inaccuracy and add error bars. The results of the different LEDs tested are summarized in Table 11.

Table 11: Power of pristine, 1 MGy irradiated and variation of white LEDs, after the first campaign (IRMA 2017).

Product Number	Power before irradiation (W)	Power after @ 1 MGy	Variation (%)
CXA2590A	9.3	9.3	0
CXA3590	13	11	-15
MKRBWT	6.8	9.2	35
MKRAWT	5.0	5.5	10
MCE4WT	0.75	0.59	-21
XMLAWT	1.3	1.8	38
XPEBWT	1.1	1.4	27
XPEWHT	0.75	0.90	20
LHC1-3090	15	16	6
SDW84F1C	9	9.1	1

It seems difficult to draw conclusions from these results other than a change in power within the measurement error of our initial setup. This explains the work done to improve our measurement technique before the second gamma irradiation campaign.

B.3.2. Spectral measurements after the second gamma irradiation run (2018) and comparison with X-ray measurement

Following the analysis of the results extracted from the first campaign, we decided to take advantage of the October 2018 irradiation campaign at IRMA to make additional measurements in order to compare them with X-ray ones. Two examples of the acquired results are shown in Fig. 40 and Fig. 41.

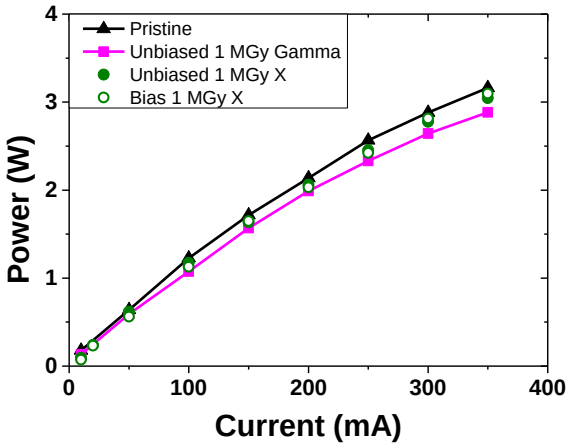

Fig. 40: Output powers of the MKRBWT LED as a function of the current for different irradiation conditions. Here the "Pristine" is an average of the measurement of the 3 LEDs before irradiation.

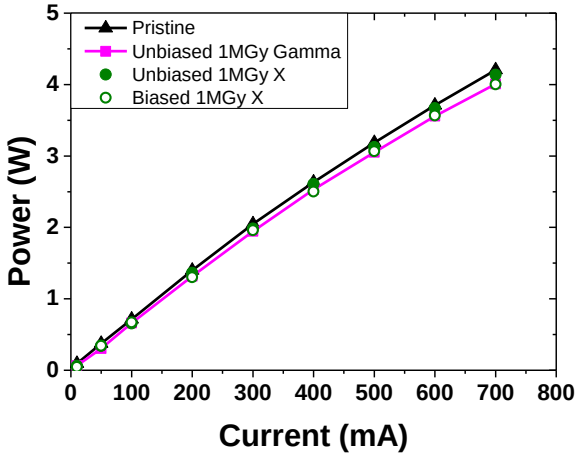

Fig. 41: Output powers of the SDW84F1C LED as a function of the current for different irradiation conditions. Here the "Pristine" is an average of the measurement of the 3 LEDs before irradiation.

First of all, all power curves as a function of current illustrate the "efficiency droop effect", i.e. the efficiency (optical power / electrical power) of blue (and therefore white) LEDs is lower at high current than at low current. As mentioned, this is currently attributed to the non-radiative recombination of the Auger type, which is stronger at high currents.

In the three tested cases, the degradations measured after X-irradiation are at best similar to or even lower than those measured after gamma irradiation. It is consistent with the Johnston statement [36], X-rays have a lower probability to generate Compton electron [52] and to cause displacement damage. Consequently, power losses in LED are more probably caused by displacement damages rather than by ionization processes. Whether the LED is polarized or not has a negligible effect. It would be interesting to verify if this remains true under gamma irradiation. With this measurement

protocol, after 1 MGy gamma, we measured low degradations for 4 of the 5 white LEDs while for the 5th the increase is only of 4 % (see Table 12). This strongly supports our assumption that the previous measurements showing an improvement following irradiation are likely to be due to measurement uncertainties.

Table 12: Comparaison of the power variation at nominal current of white LEDs gamma irradiated during the second campaign (2018) and with X-rays.

Product Number	Unbiased variation @ 1 MGy γ	Unbiased variation @ 1 MGy X	Biased variation @ 1 MGy X
LCH1 3090	-8.2 %	+3.9 %	not tested
MKRAWT	-1 %	not tested	not tested
MKRBWT	-8.8 %	-3.7 %	-2.1 %
SDW84F1C	-4.6 %	-1.6 %	-4.8 %
XPEBWT	+2.6 %	not tested	not tested

B.3.3. Analysis of the impact of gamma irradiation using the ABC model

The previously described experiments allow to extract the evolution of external quantum efficiency versus applied current for pristine and irradiated samples.

According to the ABC theory for radiation efficiency, the EQE of GaN blue LED should increase at low current (at low injection, an increase of current improves radiative recombination over trap assisted recombination), and should decrease at high current (at high injection, an increase of current improves auger recombination over trap radiative recombination). Model and experiments are thus compared in the following section, considering single device LED (and not LED array, where the comparison with theory is not possible, by lack of information about the way LEDs are connected in array). Comparison between theory and experiments is shown in the following figures (Fig. 42 & Fig. 43).

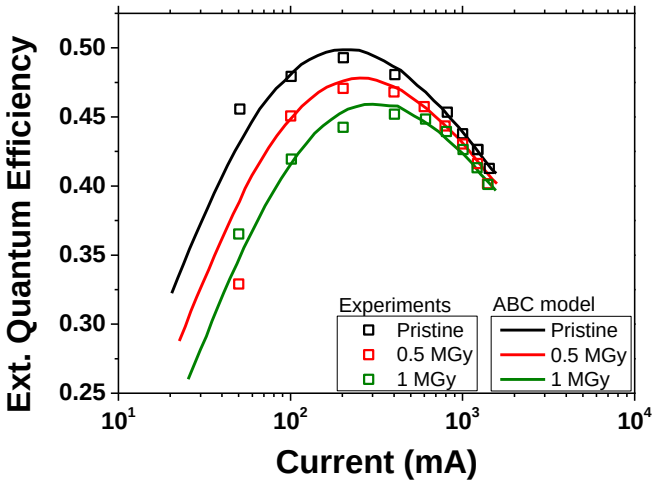

Fig. 42: EQE versus current for pristine and gamma irradiated MKRAWT LED device. ABC model = solid line, experiments = symbols

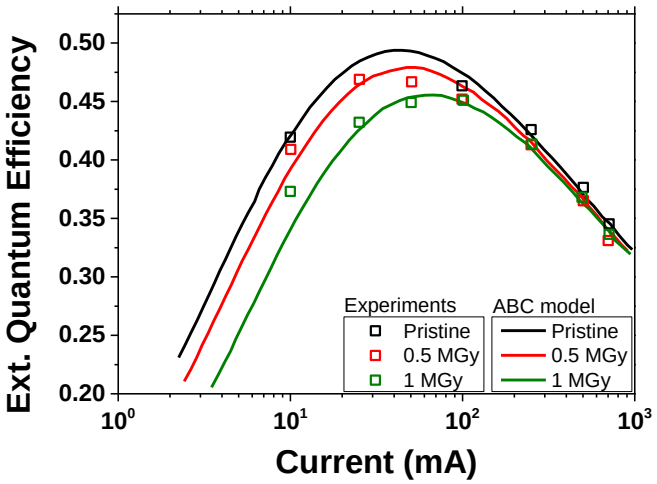

Fig. 43: EQE versus current for pristine and gamma irradiated XPEBWT LED device. ABC model = solid line, experiments = symbols.

Model and experiments have been found in qualitative good agreement, indicating that the ABC model is able to reproduce both pristine and irradiated devices performances.

Let us discuss in more details the fitting procedure. The model requires a minimum of four parameters: the A, B, C constants and the i_0 pre-factor. Only A and i_0 are technology dependent: i_0 depends on the LED dimensions, and A depends on the concentration of recombination centers within the active area. Indeed, according to Shockley Read Hall theory, in a LED direct operating conditions:

$$R_{traps} = \frac{\sigma_n \sigma_p v_{th} N_T (np - {n_i}^2)}{\sigma_n (n + n_1) + \sigma_p (p + p_1)} \approx \frac{\sigma_n \sigma_p v_{th} N_T}{(\sigma_n + \sigma_p)} n \quad (10)$$

Leading to:

$$A = \frac{\sigma_n \sigma_p v_{th} N_T}{(\sigma_n + \sigma_p)} \quad (11)$$

Where σ_n (resp. σ_p) are electrons (resp. holes) trap cross sections, v_{th} the thermal velocity and N_T the trap concentration. In consequence, A increases with the trap concentration.

As B and C are only temperature and material dependent parameters, we used the same data taken from literature for the two devices [53]. The fitting of experiments has been done only using i_0 and A as fitting parameters. In addition, as i_0 depends only on LED dimensions, it has been kept equal for each dose (pristine or not).The extracted parameters are reported in the following tables:

Table 13: MKRAWT LED fit parameters

Parameters	Pristine	0.5 MGy	1 MGy
A	5.1 10^7 /s	6 10^7 /s	7 10^7 /s
B	10^{-10} cm^3/s		
C	5.10^{-29} cm^6/s		
i_0	10^{-24} A cm^3/s		

Table 14: XPEBWT LED fit parameters

Parameters	Pristine	0.5 MGy	1 MGy
A	5.3 10^7 /s	6 10^7 /s	7.2 10^7 /s
B	10^{-10} cm^3/s		
C	5.10^{-29} cm^6/s		
i_0	2.10^{-25} A cm^3/s		

These results suggest that irradiation impacts only the A parameter (B, C, i_0 being radiation independent). On both pristine devices, A has been found of the same order of magnitude (~ 5. 10^7 /s), and has been found to increase almost linearly with the irradiation dose. In other words, as one may expect, gamma radiation is found to create recombination traps, without impacting the radiation and auger recombination properties of III V semiconductor materials. Because at high current traps effect is negligible in comparison with other recombination processes (see equation (3)), radiation less affect the EQE at high current.

This conclusion has an impact on the selection of LED for irradiated ambient. Indeed, current LED systems are composed of several mid power LED operating at low current, close to the maximum of quantum efficiency, in order to maximize the overall luminous efficiency (and minimize the power consumption). According to previous conclusions, such system is expected to be significantly impacted by gamma radiation. An alternative to produce the same amount of luminous flux consists in using one (or a lower number) of power LED operating at high current. If this second solution is usually avoided (it has a higher power consumption), these results suggest that for irradiation purpose, this second option would be less sensitive to damage produced by gamma radiation. Even if LEDs have a longer lifetime than other light sources, close to 50 000 hours [54], their output power will decrease in the time as presented Fig. 16. This decrease will be faster at a higher temperature. LED lifespan is a complex question that is not only determined by the LED chip but also by its environmental conditions (pressure, humidity...), its hardware (circuit, weld, AC/DC converter) and its utilization profile [33], [55], [56]. So the use of LEDs operating at high nominal current have to be a balance between radiation effects and reliability. This question is out of the scope of this study but all these constraints will require special attention during the integration phase.

B.3.4. Angular luminous intensity results

We had the possibility to perform radiation characteristic measurements on three LEDs, irradiated in three different conditions:

- Unbiased gamma irradiated at a cumulative dose of 1 MGy,
- Unbiased X-ray irradiated at a cumulative dose of 1 MGy,

- Biased X-ray irradiated at a cumulative dose of 1 MGy.

These tested LEDs are: MKRBWT, SDW84FC andLCH1 3090. The two first are made with LEDs grid under the phosphor without any lens, while the last reference is made with only one LED under a silicon lens. Results are reported on Fig. 44, Fig. 45 and Fig. 46 respectively.

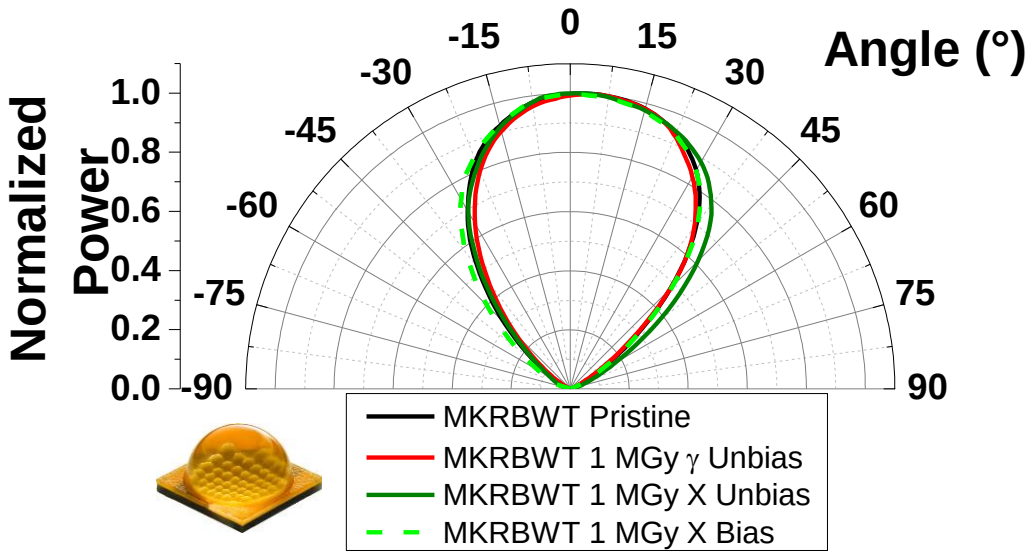

Fig. 44: Angular luminous intensity measurement of the MKRBWT LED before and after irradiation in several conditions and a picture of the LED. Here the "Pristine" is an average of the measurement of the 3 LEDs before irradiation.

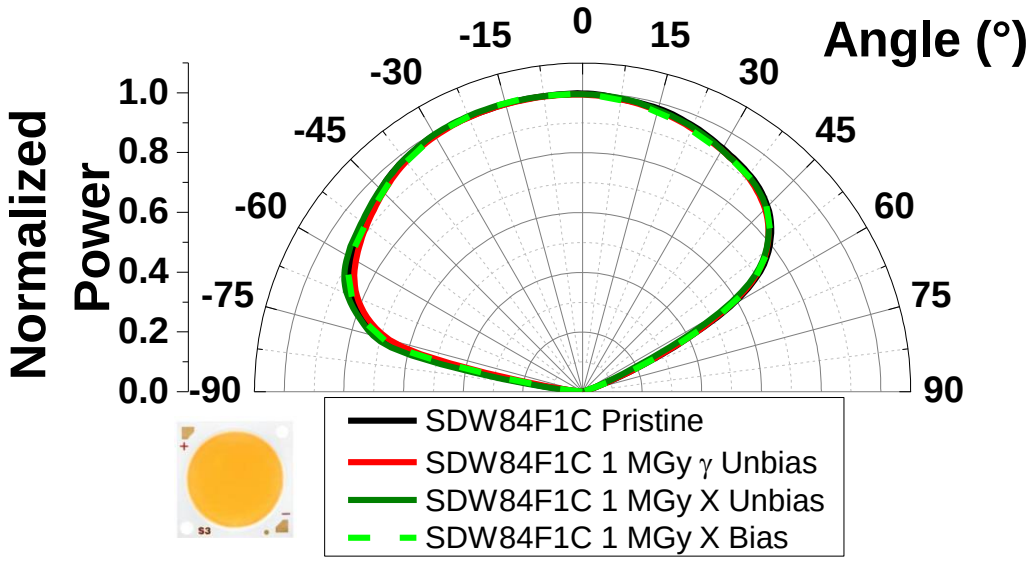

Fig. 45: Angular luminous intensity measurement of the SDW84F1C LED before and after irradiation in several conditions and a picture of the LED. Here the "Pristine" is an average of the measurement of the 3 LEDs before irradiation.

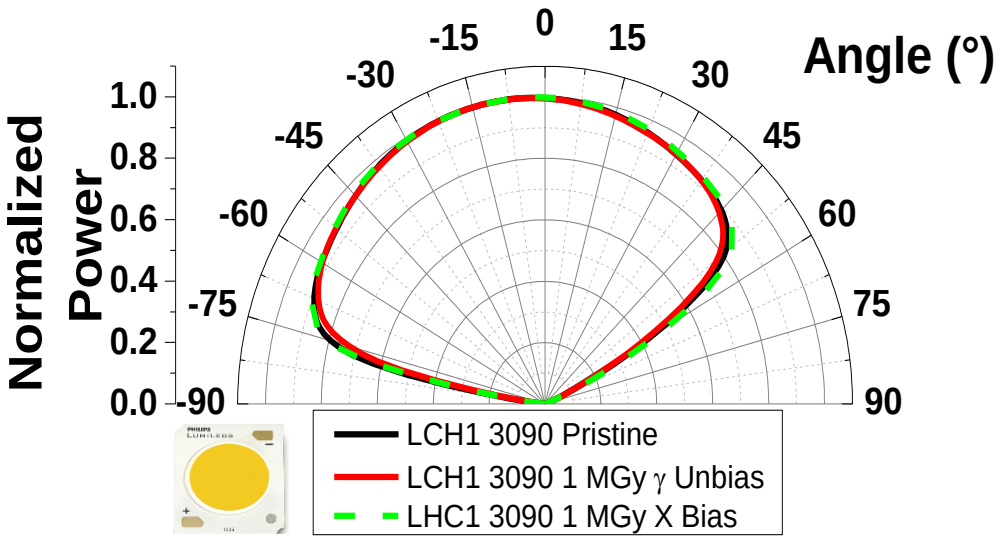

Fig. 46: Angular luminous intensity of the LCH1 3090 LED before and after irradiation in several conditions and a picture of the LED. Here the "Pristine" is an average of the measurement of the 3 LEDs before irradiation.

These experiments did not highlight significant differences in the angular luminous intensity before and after irradiation for the three tested LEDs. This was expected for the LEDs without a silicon cone to concentrate the flux but it was not the case for a LED such as the MKRBWT for which we could expect that radiation would modify the cone refractive index. Those results are encouraging to integrate LEDs in applications at MGy dose levels. To go further we used Zemax [57] to simulate the effect of a refractive index change of the lens. We considered a PMMA lens and we increased value by a factor 10 the refractive index change given in [58] (10^{-2}) to offset the PMMA refractive index. The used geometry is presented in Fig. 47 and the simulation result in Fig. 48. From this simulation, shape of LEDs emission cone seems quite constant even with a huge refractive change.

This results are particularly significant to validate the assumptions used for the CAMRAD camera photometric calculations and the pertinence of our online measurement technique.

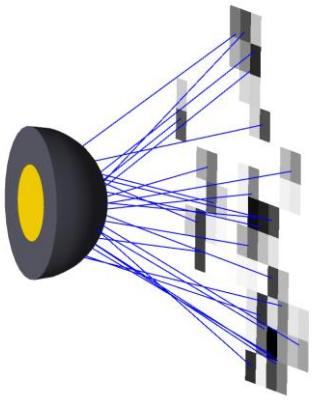

Fig. 47 : Geometry of the simulation. The yellow circle represent the LED, the dark dome is the the silicone lens and squares are the detector.

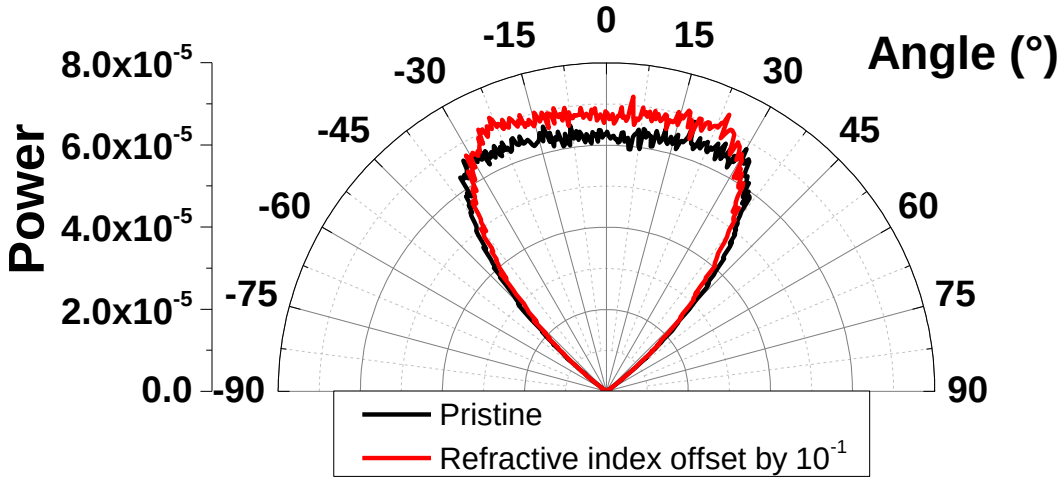

Fig. 48 Angular luminous intensity of the simulated LED before and after lens refractive index change (increase by 10^{-1}).

B.3.5. Online measurement results under X-rays

One of the main difficulties to have reliable results relies on the management of the LED temperature during the radiation test. In the irradiation machine, the temperature increases because of the heating of the X-ray tube and the fact that the chamber is a closed space without air circulation. This thermal effect is reported in Fig. 49 and Fig. 50. Fig. 49 shows the temperature evolution of the LED LCH1 3090 with and without X-ray exposure. Fig. 50 presents the temperature increase of the radiator alone. As presented in Fig. 35, the temperature measured is that of the LEDs' radiator.

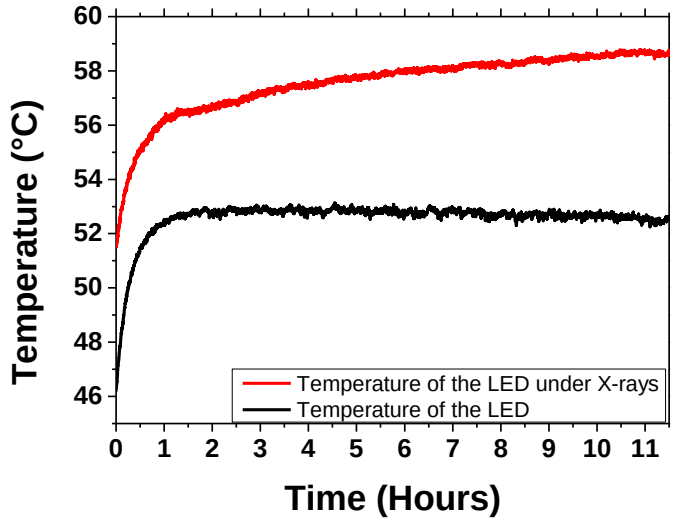

Fig. 49: Comparison between LED LHC1 3090 radiator temperature with the LED on, as a function of time in absence or presence of irradiation (25 Gy/s). The LED is powered at nominal current and voltage.

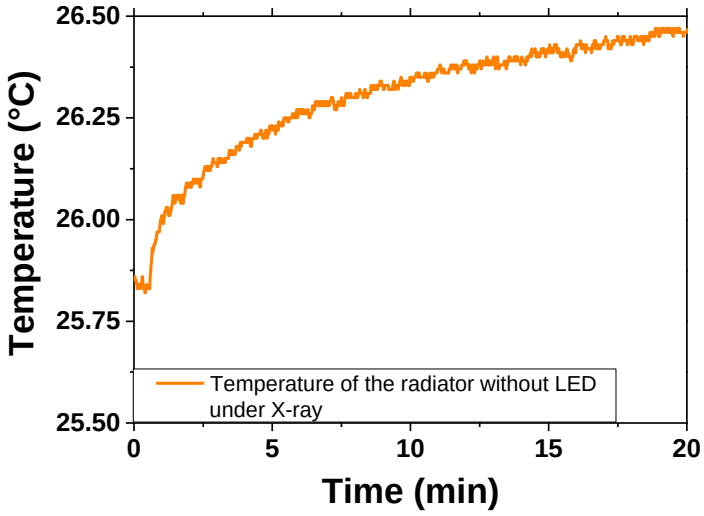

Fig. 50: Growth of the radiator temperature under X-rays without LED, (25 Gy/s)

This temperature increase, as explained in B.1.4, reduces the efficiency of the LEDs and causes a redshift of their spectrum. It would therefore be necessary to differentiate between the efficiency loss caused by heating and that caused by radiation. Since the effect of temperature is not linear, we cannot make a correction of its impact afterwards. So, we made an online measurement of the LED power with and without irradiation. Fig. 51 compares the losses on the pump (blue peak) and the entire spectrum with and without irradiation (when measuring the LED without radiation it was placed under a polystyrene enclosure to simulate the irradiator chamber). Fig. 51 shows that if there is an effect of radiation, it remains moderate in terms of optical power loss. Fig. 51

also highlights that, without irradiation, the power loss stabilizes after a certain time, while it continues to increase under irradiation. However, it is possible that this effect is mainly due to the heating of the chamber, since the temperature of the exposed LEDs is higher than the one not exposed to X-rays (4 to 6°C). This temperature difference cannot be fully attributed to the heating of the radiator as its temperature increases by less than 0.75°C see Fig. 50. This may show that radiation increases the self-heating of the LED.

On the other hand, the kinetics under irradiation seem to undergo greater fluctuations (Fig. 51), whereas the evolution of the power consumed over time remains similar between with and without radiation cases (Fig. 52). As a reminder, the LED is driven in current and the voltage is free. These fluctuations are following the ones of the blue LED (Fig. 51) so they are not related to the phosphor conversion.

Fig. 53 compares the spectral losses after the same operating time in the absence and presence of radiation. There is no appearance of a specific absorption signal, so irradiation does not create discernible absorption bands in the LED materials and does not cause any conversion phenomena. This is quite reassuring for the expectations of the CAMRAD project. The negative loss corresponds to a shift in the spectrum. This is probably a combined effect of temperature and radiation.

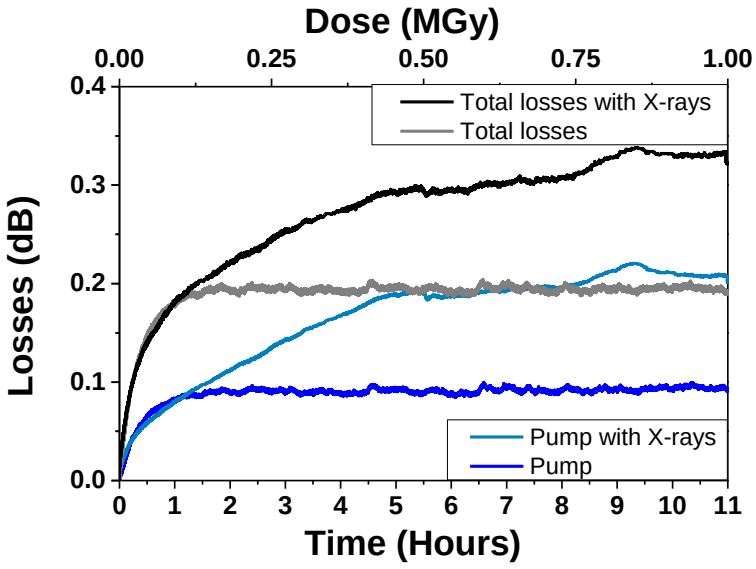

Fig. 51: Comparison between LED LCH1 3090 Losses as a function of time (& dose) with and without X-rays (25 Gy/s). Pump refers to the losses from 382 to 426 nm.

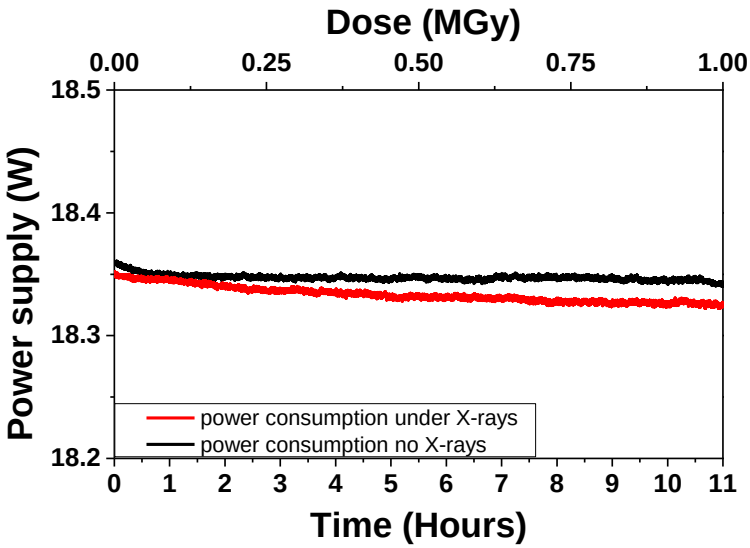

Fig. 52: Comparison between LCH1 3090 power consumption as a function of time (& dose) with and without X-rays (25 Gy/s).

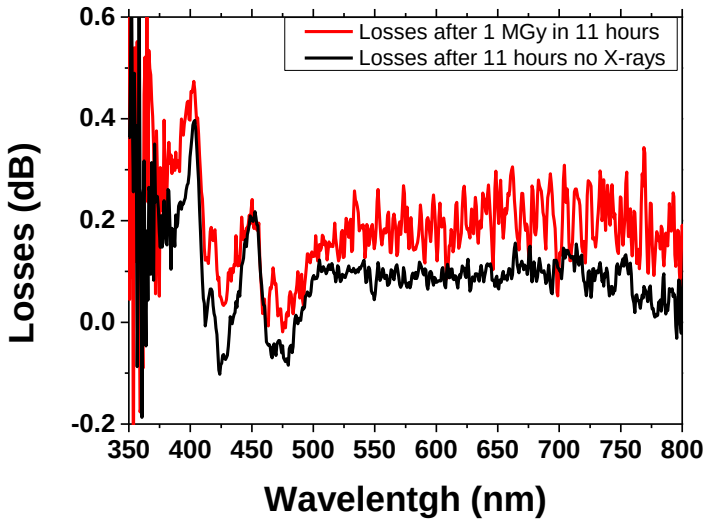

Fig. 53: Comparison of spectral losses between one LHC1 3090 irradiated up to a cumulative dose of 1 MGy (SiO_2) in 11 hours and one LED after 11 hours of operation.

Same measurements have been made on the SDW84F1C and are illustrated in Fig. 54, Fig. 55 and Fig. 56.

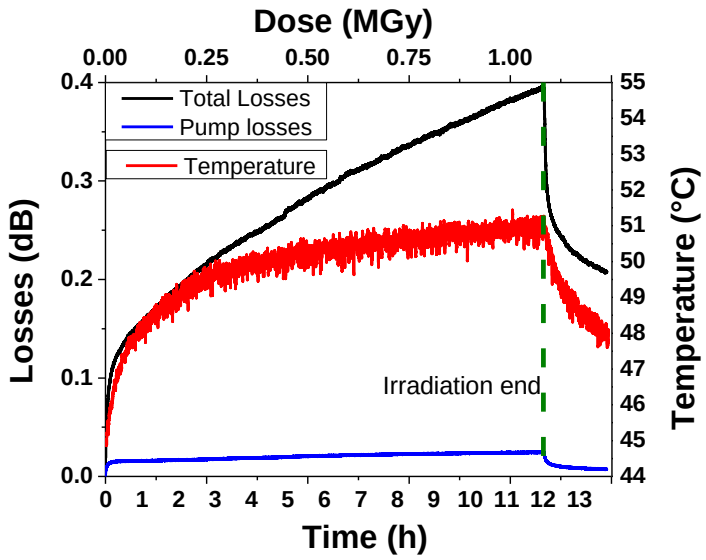

Fig. 54: Temperature and losses as a function of time (& dose) of pump [420 to 475 nm] and full spectrum of the SDW84F1C LED under X-rays (25 Gy/s) and during the recovery.

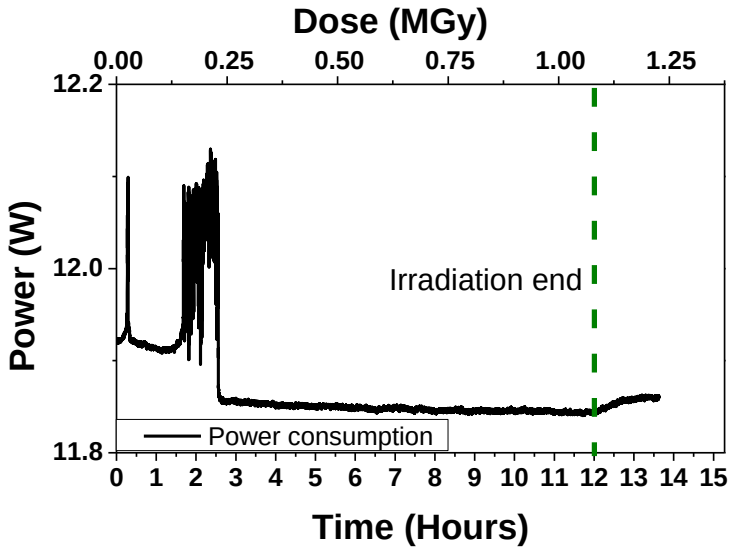

Fig. 55: Power consumption of the SDW84F1C under X-ray (25 Gy/s). Current is limited at the nominal value and voltage is free.

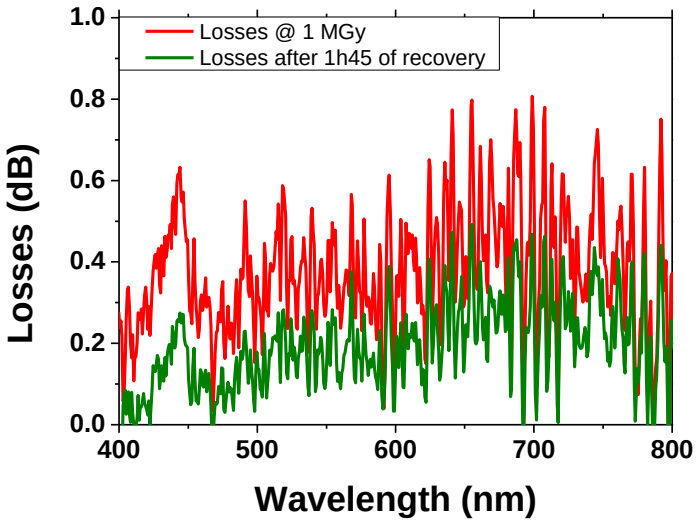

Fig. 56: Comparison of spectrum losses of the SDW84F1C after 1 MGy and 1h45 after the irradiation end.

Unlike the LCH1 3090 LED, the SDW84F1C does not show any sign of instability in the emitted spectrum (Fig. 54), despite the instability of the power consumption (≈ 2.5%) during the first hours of irradiation that did not affect the output power, which finally stabilizes at 11.8 W (due to a decrease of the voltage from 33.8 to 33.6 V) below its initial value (see Fig. 55). After the end of the irradiation, the consumption rises slightly. The emitted power decreases during the irradiation. However, in view of the post-irradiation recovery phenomena, the nearly half of losses can be attributed to thermal effects. Losses represent at the end of the irradiation -8.6 % (or 0.4 dB on the entire spectrum) of the initial power and -4.6 % after the recovery phase (Fig. 56) and -4.8 % on the after irradiation measurement. The small difference between losses after the recovery and the after irradiation one may be attributed to a temperature difference close to 20°C (the temperature of the radiator after the post irradiation measurement was ≈70°C). The LED temperature is probably higher in the integrating sphere than in the irradiator chamber (because of the smaller volume of the sphere). The fact that these two measurements are close to each other is a good argument to validate this measurement technique. These measurements let us make the following assumptions on biased LEDs under X-rays:

- Their output power is weakly affected.
- There is no interaction between high energy photons and phosphors conversion.

- Their electrical consumption is quite stable and its fluctuation doesn't affect the output power.
- High dose rate radiation could slightly increase the LED operating temperature.

Conclusion Section B.3

In this last chapter devoted to LEDs, results obtained during the different irradiations campaigns have been presented. The experimental difficulties met during the first gamma campaign forced us to improve our methodology for after irradiation measurements. At least with this first campaign, we have shown that most of white LEDs are quite resistant to gamma radiation up to 1 MGy dose, red and green LEDs, made of different materials, seem more sensitive.

The second gamma campaign allows us to measure some degradation of the emitted power down to -10 %. For the tested LEDs, we measured stronger degradations after gamma irradiation than after X-rays ones. That is consistent with the Johnston statement that most of damages are caused by displacement processes and not by ionizations. So X-rays up to 100 keV are not energetic enough to perfectly reproduce gamma effects, nevertheless they can be used as a loss-minimizing approximation. Maybe X-rays of higher energy will be a better compromise to model gamma effects.

Thanks for the ABC model, we explained why GaN LED operating at high currents are less degraded by radiation as it was shown in [44] and [46], at lower drive current. So we can draw the conclusion than contrary to the usual use of LED (many LED at low current) in a radiation environment it is better to use less LED at high currents even if they are less efficient from a power consumption perspective. This choice may affect the LED reliability and have to be take in account for the LEDs integration.

We also demonstrate that LEDs angular luminous intensity is not modified by the irradiation even for a LED with a silicone lens. That validated an important assumption used in the photometric calculations and allow us to develop a procedure for online LED characterization under X-rays.

The online measurements confirmed that LEDs did not present any failure and specific transient response during the irradiation. Nevertheless, the LEDs operating

temperature is higher under radiation. This observation has to be confirmed, because the combined effect between radiation and temperature may cause a decrease of the output power stronger than the ones measured after irradiation.

Now we will move to the study that we carried on radiation effects on optical glasses.

Chapter C. Glasses for optical system in radiation environment

CAMRAD optical system requirements are detailed in [15].

It is well known that energetic radiation modifies the structural properties of glasses with drastic consequences on their optical properties. This will play an important role in our case because our ultimate goal is to obtain good quality images in severe environments. In fact, the properties of the glasses, used to design the lenses of our optical system, will evolve during the irradiation exposure of the system and the degradation of their transmissions will affect the image quality of the camera. The radiation effects will be of great importance as they are known to have a higher impact in visible domain covered by our camera than the IR (*Infrared*) wavelength range.

The responses of the selected glasses in a radiation environment depend on several parameters. The most impacting ones are: the glass chemical composition, its manufacturing process, its profile of use and the targeted environment (radiation type, dose rate, cumulative dose, temperature...). This set prefigures the complexity of the study to be conducted to ultimately design a radiation hardened camera.

Pure silica glass transmission is less affected by radiation than multicomponent ones, particularly in the visible domain [6], [19], [46], [59]. We can consider pure silica as a key material for our application. Nevertheless as the CAMRAD project considers polychromatic systems, the use of a unique glass type is not possible, implying to combine different glasses with various chemical compositions (some of them are less-studied in radiation environments) to achieve the required performances in terms of image resolution.

We will first remind some basics about optical systems and their properties such as the chromatic aberrations to explain why we cannot easily elaborate a low-cost polychromatic optical system with only one glass type (more expensive solutions as freeform may need only one glass [60]). Then we will describe the different macroscopic and microscopic radiation effects on glasses and their impacts on the image quality. In the third part we will briefly describe some of the intrinsic radiation-induced defects

involved in the silica-based materials introducing their optical signatures. In the last part we will focus on the effects of Cerium doping on the defects' generation that opens the way to the design of glasses radiation hardened against darkening.

C.1. Basic properties of optical systems in absence of radiations

This section focuses on the chromatic aberration to explain why it is usually required to use at least two different glasses with appropriate refractive indices and chromatic dispersions in a color imaging optical system. The adjustment of these parameters is obtained by modifying the glass compositions.

C.1.1. Chromatic aberration

The chromatic aberration is a consequence of the refractive index spectral dependence (see Fig. 57). As a consequence, when using a single lens the rays at different wavelengths do not focus at the same position and generate blurry pictures as illustrated in Fig. 58.

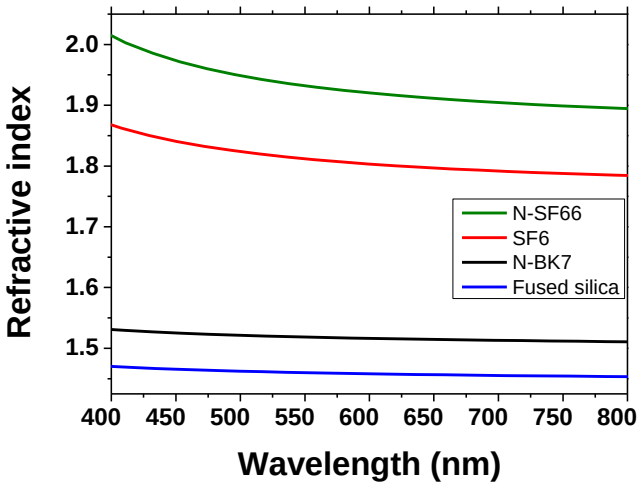

Fig. 57: Spectral dispersions of different glasses. Figure created with data respectively from [61]–[64]

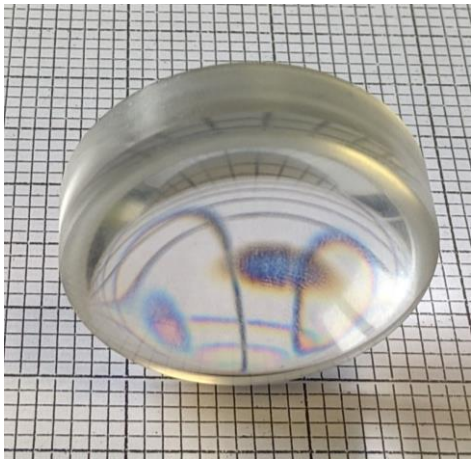

Fig. 58: Chromatic aberration through a lens creates rainbows that blur the image.

C.1.2. Abbe number and chromatic correction

Optical glasses properties are usually presented on an Abbe diagram, their names corresponding to their compositions. An example of Abbe diagram for SCHOTT glasses is plotted in Fig. 59 and highlights the evolution of the refractive index with the Abbe number for a variety of glasses. We will explain how this number is used by optical designer to choose appropriate glasses for an optical system.

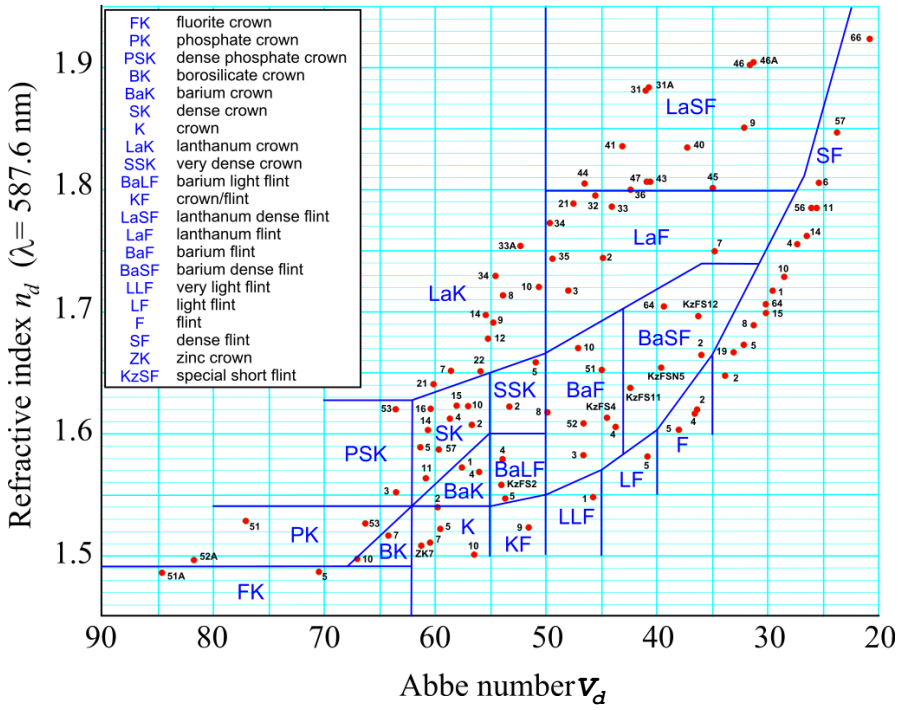

Fig. 59: SCHOTT's Abbe diagram. Figure from [65]

Abbe number V or V_d (depending on the chosen reference wavelength) is used to classify materials in terms of chromaticity in the visible spectral domain [66]. It also allows separating glasses in two categories, Flint (V <50) and Crown (V >50) [66]. It is defined as:

$$V = \frac{n_d - 1}{n_F - n_C} \tag{12}$$

Where n_d is the refractive index of the material at 587.6 nm, n_F at 486.1 nm and n_C at 656.3 nm. The physical signification of the Abbe number is illustrated Fig. 60 for two extreme cases.

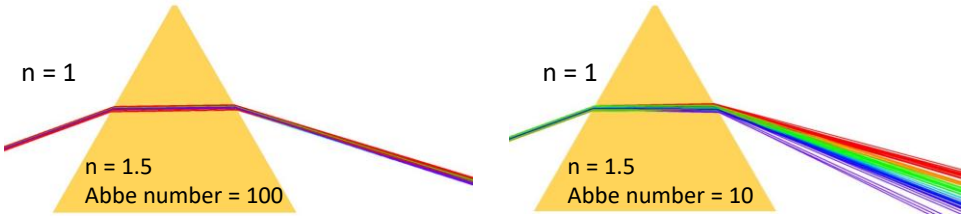

Fig. 60: Zemax simulation to highlight the difference between high and low Abbe number at constant refractive index in air.

This number is used to select glasses for an achromatic doublet (an optical system with two lenses) by solving the two following equations (13) & (14) [66]:

$$\phi_{sys} = \phi_1 + \phi_2 \tag{13}$$

Where $\phi = {}^{1}/_{f}$ with f the focal length, ϕ_1 and ϕ_2 are the powers of the first and the second lenses, respectively. For an achromatic doublet, the lens powers and Abbe numbers have to respect:

$$\phi_2 = -\frac{\phi_1 V_2}{V_1} \tag{14}$$

Where $V_1$and $V_2$are respectively the Abbe numbers of the first and the second lens. The combination of two lenses with adequate Abbe numbers and focal lengths will decrease the maximum focusing spatial shift as illustrated in Fig. 61.

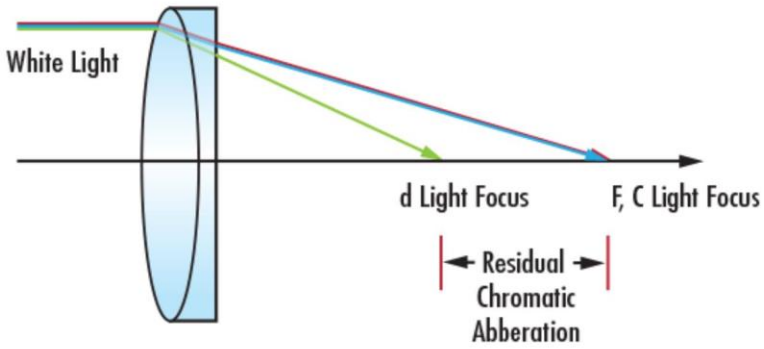

Fig. 61: Illustration of an achromatic doublet on the light path. d F and C correspond to 587.6, 486.1 and 656.3 nm respectively. These wavelengths are the ones used for Abbe number calculation. Figure from [67]

Better correction of chromatic aberrations are possible based on apochromat or superachromat approaches [66], but these approaches require to increase the number of the lenses and then the total thickness of the optical system. To enlarge the set of possible combinations, glass manufacturers create many different glasses with distinct properties [68]. Nowadays glasses based on ten or more different oxides are common [68] and glass properties modeling is used [69] to answer the complexification of formulas. This has to be kept in mind to understand the CAMRAD chosen glasses set and experiments.

These reminders help to understand why different glasses are needed to design an optical system and why these glasses have complex formulations that will lead to complex radiation responses. The next part will describe the effects of radiations on those glasses.

C.1.3. Radiation effects on optical glasses

The effects of radiation on glasses have been investigated for a long time. For example, we can refer to the Manhattan project which has made significant progress in this area [70]. At that time one research challenge concerned optical devices to examine reactor components and to monitor radioactive substances. To perform these measurements, several types of glasses as windows or lenses were used [70]. The darkening of these materials under irradiation, explained by the generation of microscopic point defects by ionization or knock-on processes, was expected and experimentally confirmed. The researchers also quickly understood that introducing rare

earth elements inside the glass matrix can strongly change the nature, growth and decay kinetics of the point defects [70].

In the early 60s, studies about defects, commonly called color centers, were continued because of the needs for lead glass “hot-cell” windows that did not darken under irradiation [70]. This period was really prolific and increases the knowledge regarding the basic mechanisms at the origin of defect generations in many different materials [70]. This research topic was also pushed with the development of space-related devices such as imaging optical systems or solar panels with good optical transparency even in the UV range [70]. Later, this research field was driven by the interest in laser material, optical fibers and detectors for plasma diagnostics [70]. Between 1998 and 2002, the ESA (*European Space Agency*) initiated a series of studies on both the optical properties and refractive index characterizations [71]–[74] of both radiation-hardened and standard glasses [75] (but at low doses and dose rates) to predict their radiation responses [76] [77] [78]. The last period was essentially driven by ITER needs for windows and diagnostic elements [6] [79] [80]. This presentation is not intended to be exhaustive in terms of state of the art, but gives a global survey of the performed studies in the past decades.

As it was discussed in Chapter A, to the best of our knowledge, the CAMRAD project is at the new frontiers for radiation effects, as it is targeting ionizing dose levels up to the MegaGray and beyond, which have not been previously reported in open literature concerning optical glasses.

Before studying radiation effects related to particular classes of glasses we will briefly present the three main radiation induced modifications and their potential consequences for the CAMRAD project. In this perspective we will especially use the N-BK7 glass (or BK7 for older studies, the difference between both glasses is explained in section C.1.4.3) as a reference glass. This material is one of the most studied optical glasses in literature and being quite radiation sensitive, it is convenient to emphasize radiation effects.

C.1.3.1 Radiation Induced Attenuation (*RIA*)

The RIA corresponds to the darkening of the glass. RIA is caused by the generation of optically active defects, either through ionization or knock-on processes [81]. These centers are at the origin of the appearance of absorption bands in the UV to IR domains. Fig. 62 illustrates the RIA impact at a macroscopic level for BK7 glass samples exposed to various gamma irradiation doses: while this material is transparent before irradiation it strongly darkens after a cumulated irradiation dose of 0.1 MGy. The RIA amplitude and kinetics are affected by both glass composition and irradiation conditions [82] (radiation type, energy, dose rate, dose, temperature…). The impacts of dose and radiation types are reported in Fig. 63, which shows that the same glass may have different responses to different kinds of irradiations. It is important to note that the RIA level is spectrally dependent and that RIA can recover after irradiation. Indeed for some glasses, the RIA amplitude decreases with time after irradiation even at room temperature as shown in Fig. 64.

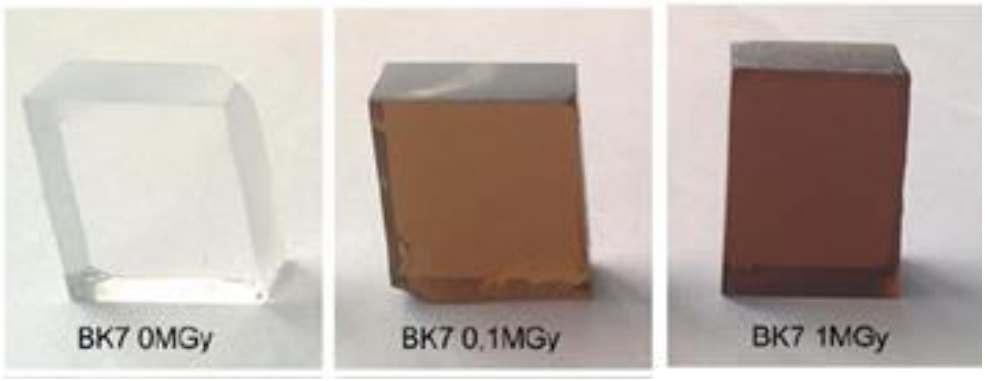

Fig. 62: Illustration of RIA on BK7, gamma irradiated at the IRMA facility [16] at 2 doses (room temperature)

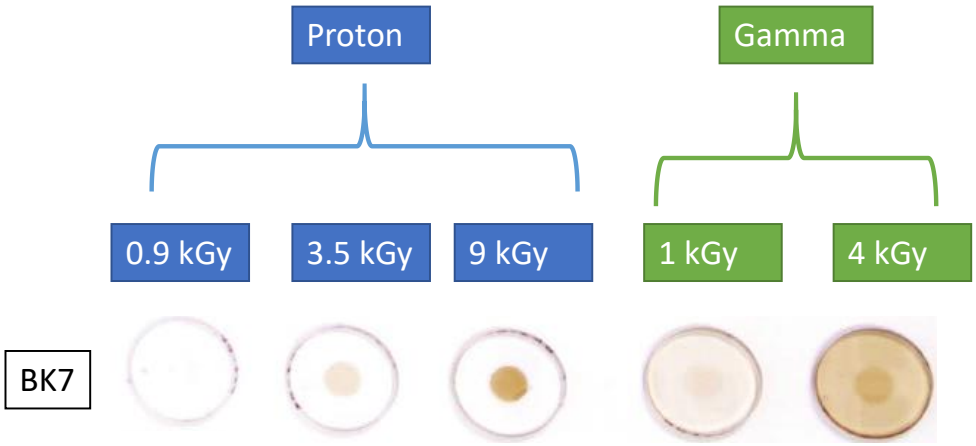

Fig. 63: Illustration of irradiation test results on BK7. In the case of the proton irradiation, only the central part of the glass is irradiated. For gamma-rays the whole glass samples are submitted to radiation and the dose on the periphery is half of the indicated dose. Figure adapted from [59]

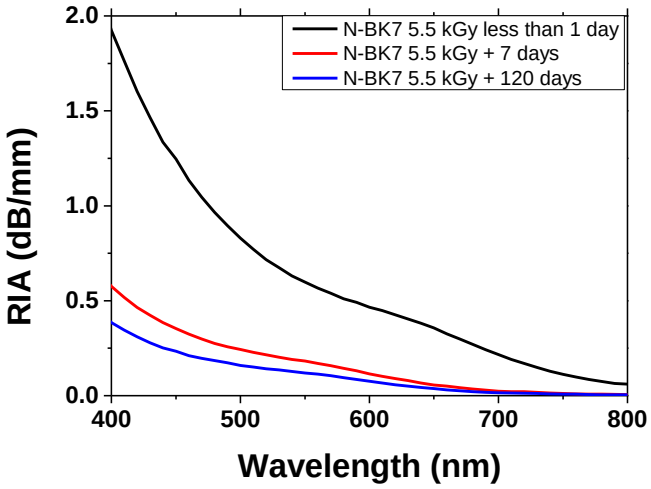

Fig. 64: RIA spectral dependence and its recovery after a Gamma irradiation up to 5.5 kGy of a 5 mm thick N-BK7 sample stored at room temperature after irradiation end. Figure created from [59]

C.1.3.2 Radiation Induced Emission (*RIE*)

The RIE or scintillation is the emission of light generated in a media by radiation. It is caused by either defect luminescence or Cerenkov emission [83]. RIE in different optical glasses was reviewed by CEA to evaluate this risk for the plasma diagnostics of LMJ (*Laser Megajoule*) in France [84]. An example of results obtained at the ELSA facility [85] (CEA, DAM, DIF, Arpajon, France) is represented in Fig. 65.

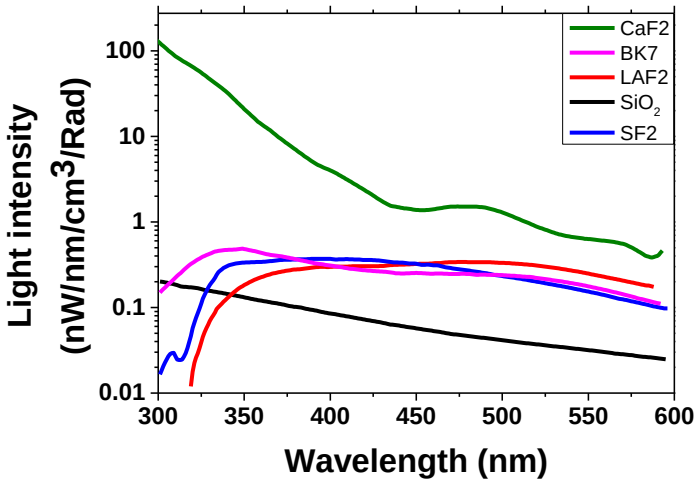

Fig. 65: Scintillation spectrum measured on ELSA accelerator with 18 MeV X-ray and normalized to dose and glass volume. Figure adapted from [84].

C.1.3.3 Radiation Induced Refractive Index Change (*RIRIC*)

The RIRIC is related to the RIA through the Kramer-Krönig relation:

$$\Delta n(\lambda) = \frac{1}{2\pi^2}\int_0^{\infty} \frac{\Delta\alpha(\lambda')}{1-(\lambda'/\lambda)^2}\,d\lambda' \qquad (15)$$

Where $\Delta n(\lambda)$ is the RIRIC at λ and $\Delta\alpha(\lambda')$ the RIA at λ'. To evaluate and to compute the RIRIC, at a given irradiation dose, we should have the spectrum evolution before and after irradiation over a quite large spectral domain. Such measurements are difficult to perform especially in the UV domain which is strongly affected by the RIA. The RIA in the UV region may affect the refractive index in the visible range [71]. However when these data are available such as for fiber Bragg gratings they can be used to explain the Bragg wavelength shift [86]. Some authors showed that the limited accuracy of absorption measurements at short wavelengths leads to overestimate the computed RIRIC values on optical glasses [71].

There is also a dependence of the refractive index change as a function of the density change trough the Lorentz-Lorenz equation [87]:

$$\Delta n = \frac{(n^2+2)\times(n^2-1)}{6n} \times \left(\frac{\Delta\rho}{\rho} + \frac{\Delta R}{R}\right) \quad (16)$$

Where n is the refractive index, ρ is the density and R the molar refractivity.

One example of glass density change with the gamma dose can be found in [88] and main results are summarized in Fig. 66. The authors attributed density changes to metallic and hydroxyl impurities introduced by the manufacturing process. Pure silicas presented in Fig. 66 have a quite simple composition, even in these cases the density changes are not simple to model.

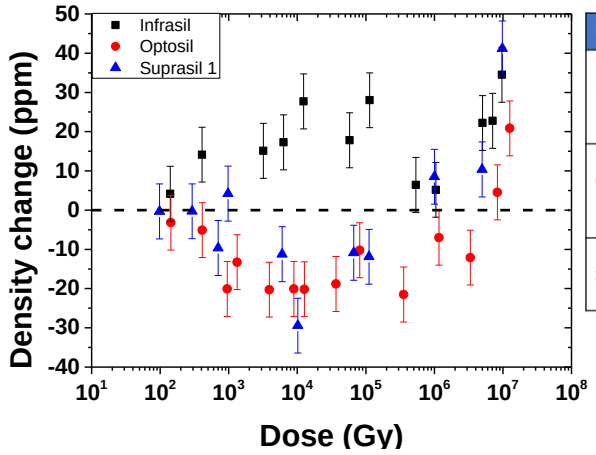

Name	Description	Impurety content
Infrasil	Natural quartz fused in an electric arc	[OH] < 5ppm [Al] = 10-50 ppm [Na] = 1-4 ppm
Optosil	Natural quartz fused in a flame	[OH] < 150 – 400 ppm [Al] = 0.1 ppm [Na] = 1-4 ppm
Suprasil 1	Synthetic, flame hydrolysis of $SiCl_4$ direct deposit	[OH] = 1200 ppm [Al] = 0.1 ppm [Na] = 0.04 ppm

Fig. 66: Density change of different silica types after gamma ray irradiation. Authors claimed a precision of ± 7 ppm reported in the figure. They made an average of at least two different samples, each measured two to five times. Figure created from [88].

There are also RIRIC computations from the measurements of wavefront aberration changes before and after irradiation as in [71] [73] [74]. One typical example of such measurements is shown in Fig. 67, the optical path difference is measured between the plate's periphery (gamma irradiated @ 4 kGy) and its center (gamma irradiated @ 8 kGy). Authors shielded the periphery to obtain this dose difference. From this measurement, RIRIC dose coefficient (refractive index variation / dose) can be computed with the method given in [74] and some examples from [71] are presented in Table 15.

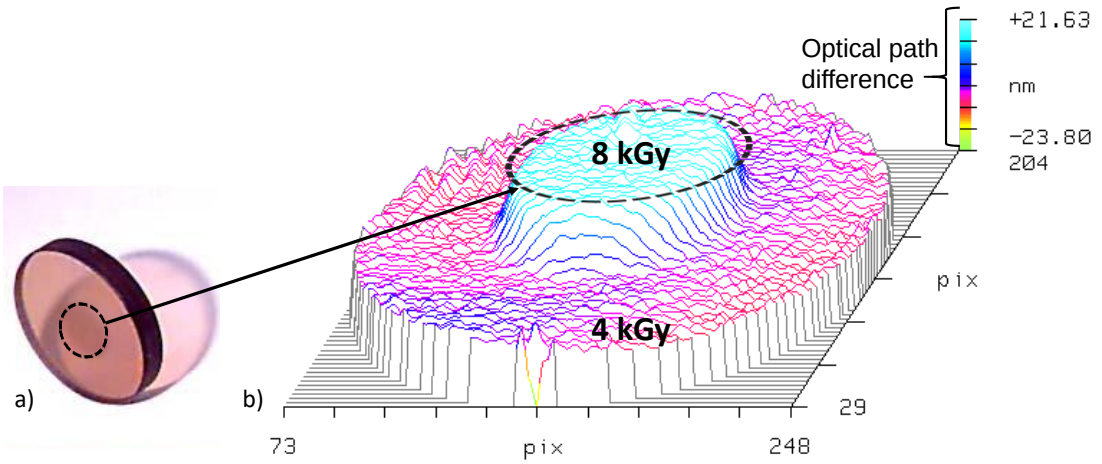

Fig. 67: a) Picture of a BK7 irradiated sample, the center of the glass received 8 kGy while the periphery received 4 kGy b) Fizeau interferometer wavefront measurement of the sample made at 633 nm. Figure adapted from [59], this reference is a presentation that reuse figure from [71] in a better quality.

Table 15: Radiation induced refractive index change coefficients in different glasses calculated from wavefront measurement recorded by Fizeau interferometer made at 633 nm such as the one presented in Fig. 67, data from [71]

Glass	RIRIC dose coeff ($\Delta n \times 10^{-9}$ /Gy)
LaK9	<0.15
BK7	-0.74
Fused silica	<0.15

These coefficients are evaluated via a linear approximation between 4 and 8 kGy and cannot really be used outside this small dose interval. We also found RIRIC in [89] calculated from Twyman-Green interferograms (this interferometer is a variant of the Michelson one). Authors used X-ray irradiation and measured the RIRIC at different depths in the glasses to obtain RIRIC at different doses. Their RIRIC data are summarized in Fig. 68.

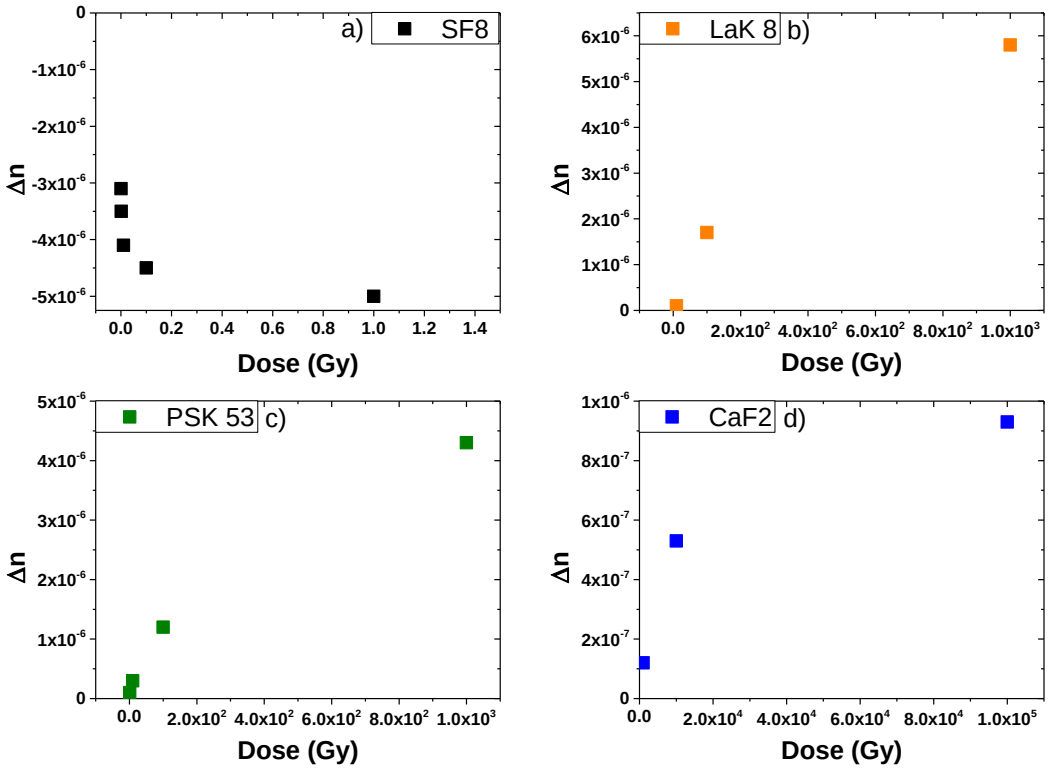

Fig. 68: RIRIC measurements in different glasses at 533 nm as a function of the dose computed from Twyman-Green interferograms. Figure created from [89]

It is important to note that all measured RIRIC saturate more or less quickly, but at doses lower than the 8 kGy from [71]. So even between 4 and 8 kGy it is questionable to use a linear approximation of the RIRIC as it was done in [71].

C.1.3.4 Consequences for CAMRAD

These three radiation induced effects will have different consequences on the camera performances. From the less to the most problematic for our application:

RIE: depending on the application and the design of the optical system, a part of this parasitic light generated in the bulk material of the lenses can be guided to the imager. Most of the light remains emitted at wavelengths below 450 nm. As it will be detailed in section C.1.5 and in C.3, radiation-hardened glasses present a strong absorption in this spectrum part, so they will act as a filter for most of the RIE.

RIRIC, is a tricky problem for optical designers because of the lack of available data in literature, explained by the difficulty to experimentally measure these changes.

We estimated by a Zemax [57] simulation that a modification of some 10^{-4} will not affect the image quality of our systems [90] and our RIRIC measurements are in this order of magnitude [46] (see Fig. 117 in C.3). Moreover a refractive index can either increase or decrease with the dose depending of the glass, so there could exist some possible compensation at the optical system level [90]. Facing the small amount of available glasses adapted for radiation environment (see section C.1.5.4 and Fig. 92) a compromise has to be found between the risk of using a glass without RIRIC data and the intrinsic optical system quality. In order to minimize this risk, more RIRIC data have to be produced, the possible RIRIC have to be considered during optical system design and studies have to be made on the possibility to use a zoom at high doses. In CAMRAD we are using a hardening-by-design approach to make the optical system intrinsically robust against RIRIC. As an example, we made a simulation on the impact of a RIRIC on a silica Cooke triplet. As shown in Fig. 69, we optimize the optical system through Zemax and then we modified the silica refractive index, considering a $\Delta n = +5\times10^{-5}$ caused by the radiation. In this case, it is enough to blur the image's details but this system is not designed to be tolerant to the refractive index change.

a) b)

*Fig. 69: Zemax simulation of the RIRIC effect on a monochromatic image made with a pure silica Cook triplet. Optical system parameters are: working distance: 100 mm, aperture: 5, wavelength: 595 nm. a) without RIRIC b) with Δn = +5*10-5. Figure from [9]*

The RIRIC cannot be neglected, we are still working on this issue through CAMRAD to acquire data at high doses on the main glasses used for our optical systems.

RIA was our major concern because it's meaningless to discuss other issues if there is not enough light after the optical system to make an image. The effect of RIA is illustrated in Fig. 70 showing pictures of the mire that will be used during CAMRAD final

test through 5 and 10 mm of N-BK7 windows both irradiated at 1 MGy (X-ray). The total thickness of the various lenses of the CAMRAD optical system will be close to 20 mm.

Fig. 70: The three images were made with a Galaxy S8+ cell phone and: Integration time: 50 ms, Aperture Number: 1.7, ISO 50. a) No N-BK7 window. b) One window of 5 mm of N-BK7 X-ray irradiated at 1 MGy (SiO_2). c) Two windows of 5 mm of N-BK7 X-ray irradiated at 1 MGy (SiO_2).

So to minimize as much as possible the RIA level, we have to:

- *Minimize the global thickness of the entire optical system.*
- *Use glasses with lowest possible RIA.*

There is a special class of glasses, called Radiation Hardened Glasses, which is designed to fulfill this need. These glasses have the particularity to match the refractive index and Abbe number usual of glasses but are codoped with Cerium. The next sections will present the SCHOTT [91] radiation hardened glasses and some radiation defects linked to silica, bore and sodium. Then we will explain how Cerium prevents the apparition of radiation induced point defects in the glass matrix and discuss the limitation of this hardening technique.

C.1.4. Available radiation hardened commercial glasses and attenuation related to some dopants

C.1.4.1 SCHOTT radiation hardened glasses

For the best compromise between radiation hardness and the achievements of the optical performance requirements, we decided to focus our study on existing and commercially-available radiation-hardened glasses developed for space and high energy physics applications. These radiation-hardened glasses are doped with Cerium, a rare earth allowing to efficiently reduce the defect generation.

Table 16 lists radiation-hardened glasses present in the SCHOTT catalog at the time of the PhD thesis (2016 – 2020) and details their compositions as given in the manufacturer datasheets. The number after the "G" letter in the glass name gives the weight percentage (%wt) of Cerium. Composition of commercial glasses includes many other chemical elements allowing to obtain, by tuning their relative concentrations, a great diversity of Abbe numbers and refractive indices needed to optimize the performances of optical systems.

Table 16: Composition of SCHOTT Rad-Hard glasses in weight %, data from Scott "Technical Safety Information revisited in 2015. [92]–[97]

	$_{5}$B Oxide	$_{11}$Na Oxide	Silica	$_{19}$K Oxide	$_{20}$Ca Oxide	$_{25}$Mn Oxide	$_{30}$Zn Oxide	$_{40}$Zr Oxide	$_{56}$Ba Oxide	$_{57}$La Oxide	$_{58}$Ce Oxide	$_{82}$Pb Oxide
BK7G18	10 - 20	1 - 10	60 - 70	1 - 10			< 1		1 -1 0		1 - 10	
F2G12		1 - 10	40 - 50	1 - 10							1 - 10	40 - 50
K5G20	1 - 10	1 - 10	60 - 70	10 - 20	1 - 10		1 - 10				1 - 10	1 - 10
LAK9G15	30 - 40		1 - 10		10 - 20	1 - 10	1 - 10	1 - 10	1 - 10	20 - 30	1 - 10	
LF5G19		1 - 10	50 - 60	1 - 10							1 - 10	30 - 40
SF6G05		< 1	20 - 30	1 -10							< 1	70 - 80

Glass manufacturers are not interested in reaching a full understanding of the processes defining the radiation response of their glasses, the complexity being too high while the marked size being too small to justify the investments. On another side, the

researchers cannot reproduce these glasses with small modification to measure the effect of each component because the details of the manufacturing process are confidential. Moreover this work may be pointless because even for the same glass reference there are differences in their radiation responses between different batches [98]. This issue is well known in electronics, difficult to mitigate except by qualifying a batch and using the same batch of production for the application. This work is not devoted to the identification of all the types of potential optically-active defects that can occur in those commercial materials, this is clearly outside our scope. On the other hand, we can guide the reader on the origin of particular centers which can be created in some glasses of specific interest such as: pure silica or bore/sodium doped glasses.

C.1.4.2 Attenuation related to Silica defects

The structural unit of silicon dioxide is a tetrahedral formed by a silicon atom having covalent bonds with four oxygen atoms in both crystalline and amorphous state, see Fig. 71.a) [99]. Fig. 71.b) is a simplified 2D representation of an ideal pure silica glass structure (only silicon, oxygen and no defect), it can be viewed as a random structure of tetrahedral linked by the corner. The amorphous state has no symmetry at long distances, and parameters such as angles and bond lengths are characterized by a distribution around a mean value [100]. This section will be centered on the intrinsic defects in amorphous silica (SiO_2). Silica is a well-known material and many reviews deal with the modification of its optical, structural properties with radiation. In this paragraph, we will give some overviews on the main Si-related defects that affect the visible. Fig. 72 gives an example of some of these defects possibly involved in the silica response, more details can be found in [99] [101] [102].

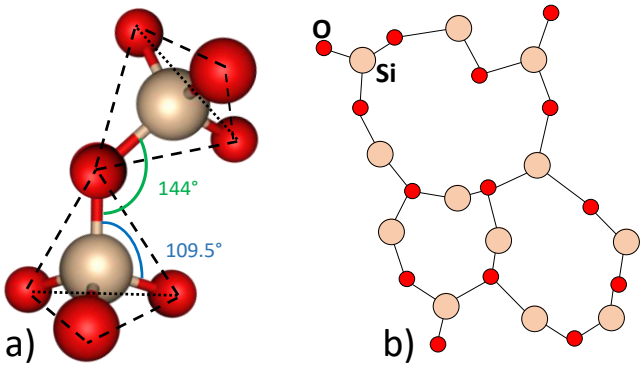

Fig. 71: a) Tetrahedral structure of silica, b) Ideal pure-silica glass structure (simplified 2D representation)

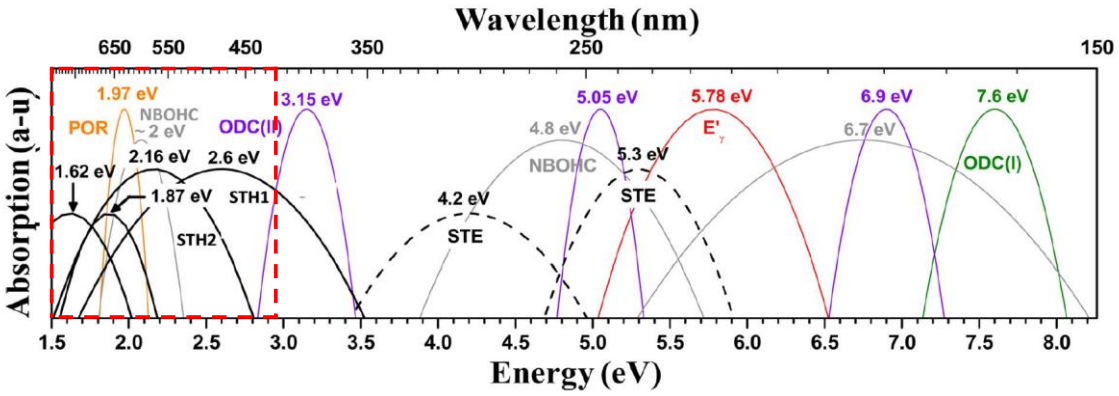

Fig. 72: Absorption bands associated with different Si-related point defect structures. Red square highlights the part of the spectrum of interest for the CAMRAD camera. Figure adapted from [100]

Despite all the precautions taken by manufacturers, intrinsic defects, also called precursor sites, are present in the glass matrix. Then the irradiation will generate additional point defects either at those precursor sites or at regular bonds.

E' defect

There are three different defects related to oxygen vacancies, we will focus on the well-known E' center. It corresponds to a silicon dangling bond with unpaired localized electrons [103] [99], its structure is illustrated in Fig. 73. Its first observation was reported in [104]. This defect is paramagnetic, it possesses an absorption band at ≈5.8 eV (FWHM ≈0.8 eV) and it is not yet associated with any luminescence band.

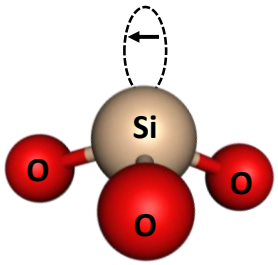

Fig. 73: The structure of E' (Si) defect

NBOH Center

The Non-Bridging Oxygen Hole Center (NBOHC) is a paramagnetic defect with the configuration presented in Fig. 74, [105] [106] [107]. It is characterized by an

absorption band at 1.97 eV (FWHM 0.17 eV) [99] [108] and two other absorption bands between 4 and 8 eV [108] [109] [110]. It also has an emission band at around 1.91 eV (FWHM 0.17 eV, τ=10-20 µs) [108] [111]. Three mechanisms can lead to its generation:

- Breaking of the ≡ Si ─ O ─ Si ≡ strained bond [112]
- Radiolysis of the OH group [113] [114] [115]
- Breaking a peroxy linkage [116]

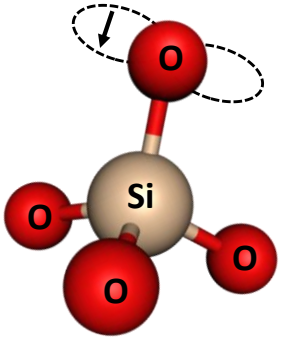

Fig. 74 The structure of NBOH Center

C.1.4.3 Attenuation in borosilicate

Glasses such as BK7G18, K5G20 and LAK9G15 contain between 1 and 40 wt. % of boron. There are only a few studies centered on borosilicate materials and none of these focused on the basic mechanisms of radiation induced effects on these glasses. We first review the knowledge about the RIA in borosilicate glasses then study borate glass to more deeply explore the specific defects observed in this class of glass. One of the oldest study of RIA in borosilicate glass was performed by Levy [117]. The sample was provided by Corning (no information about the composition) and irradiated with gamma rays for RIA measurements. The obtained results are reported in Fig. 75[4].

[4] The conversion from Roentgen (R) to Gray is detailed in Appendix C

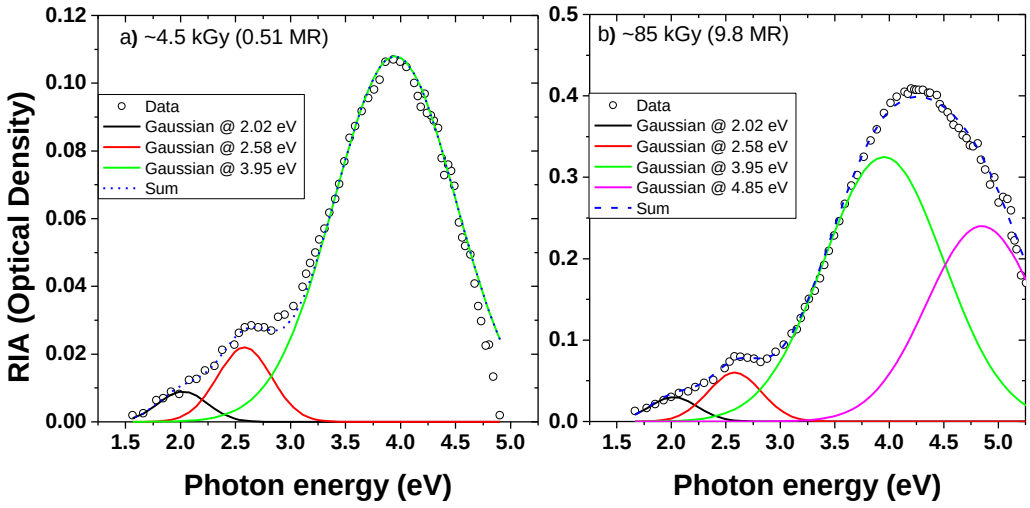

Fig. 75: RIA spectra measured after 4.5 kGy (≈0.51 MegaRoentgen) and 85 kGy (≈9.8 MR) in a borosilicate glass [117]. Gaussian bands are defined as $\alpha(E) = \alpha_m e^{-(4ln(2)/U^2)(E-E_0)^2}$ with E_0 the energy at the peak, U the full with at half maximum (by increasing energies 0.52, 0.58, 1.3, 1.19 eV respectively), α_m is the absorption at the maximum and $\alpha(E)$ the absorption for photons of energy E. Figure adapted from [117]

At 4.5 kGy three absorption bands are observed at 2.02, 2.58 and 3.95 eV then at 85 kGy an additional band is measured at 4.85 eV.

A huge study on borosilicate was made by the ESA [118] on five glasses which are optical analogs to BK7 (all borosilicate, same refractive index and Abbe number, but different manufacturers). Their main result is reported in Fig. 76. The goal was to highlight that even glasses with close compositions such as N-BK7 and BK7 (only difference is the replacement of the As_2O_3 by Sb_2O_3) have different RIA spectra at the same gamma dose and after the same recovery time (not shown here).

As an example, Table 17 presents the difference in term of composition between N-BK7 (SCHOTT) and S-BSL7 (Ohara). Both glasses have a $n_d \cong 1.517$ and $\nu_d \cong 64$.

Table 17: Composition comparison between N-BK7 and S-BSL7

Name of glasse	$_5$B Oxide	$_{11}$Na Oxide	Silice	$_{17}$Cl Oxide	$_{19}$K Oxide	$_{20}$Ca Oxide	$_{22}$Ti Oxide	$_{30}$Zn Oxide	$_{51}$Sb Trioxide	$_{56}$Ba Oxide
N-BK7	10 - 20	10 - 20	60 - 70	< 1	1 - 10	< 1	< 1		< 1	1 - 10
S-BSL7	10 - 20		60 - 70				0 - 2	0 - 2	0 - 2	0 - 2

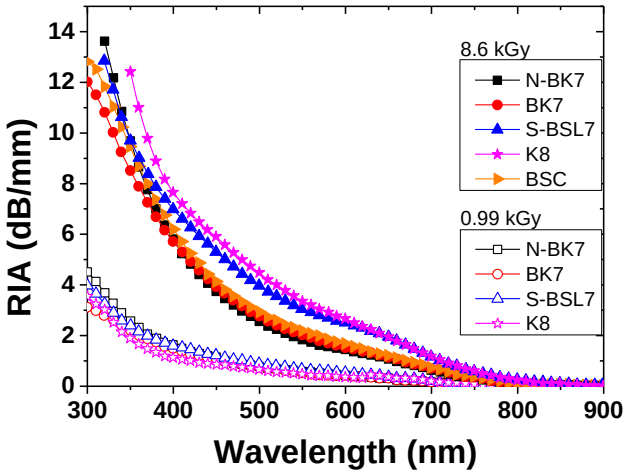

Fig. 76: Radiation induced attenuation of 5mm thick samples of different borosilicate glasses after 990 Gy and 8.6 kGy doses of gamma ray (dose rate of 6 mGy/s).Figure adapted from [118]

RIA spectra of the different glasses are close at the first irradiation step (0.99 kGy) while some differences appear at the largest dose (8.6 kGy). It is interesting to notice, that K8 glass presents the smallest RIA at 0.99 kGy and the highest at 8.6 kGy. Table 18 gives the fit parameters used to reproduce the experimental results of the N-BK7.

Table 18: Parameters of the Gaussian bands allowing to reproduce the RIA spectrum for the N-BK7,data from [118]

Band center E_0 (eV)	1.95	2.37	3.11	4.01	4.57	5.47
Full Width at Half Maximum (FWHM) σ (eV)	0.21	0.31	0.49	0.51	0.40	0.23

Even though this decomposition made with the method described in [76], the corresponding active centers are not identified yet. To have some insight, even limited, it is necessary to use simpler glasses with better-defined composition and process elaboration as it was the case in [119]. In this study, the samples have a constant molar fraction of B_2O_3 and different concentrations of CaO and Al_2O_3, while the irradiations were performed with gamma rays. The reported RIA spectra are given in Fig. 77.

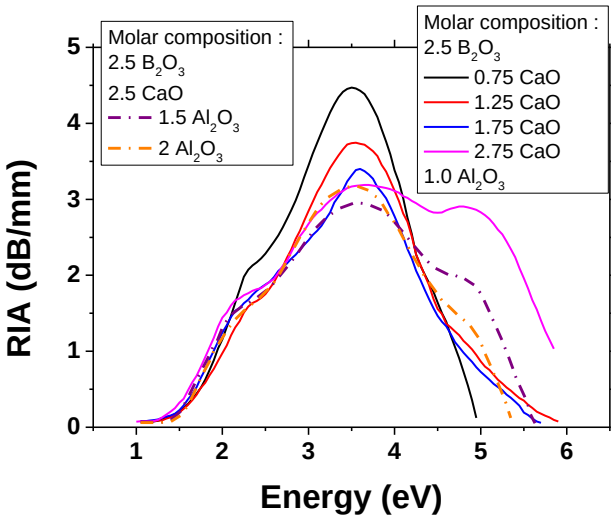

Fig. 77: Effect of the CaO concentration on RIA @ 11.5 MR (≈100 kGy). Glass composition are in mole: 2.5 B_2O_3, 2.5 CaO and X Al_2O_3 with X is the value indicated in the left caption or 1 Al_2O_3, 2.5 B_2O_3 and Y CaO. Y is the value indicated in the right caption. Figure adapted from [119]

The measured RIA spectra can be reproduced using a set of 3 OA bands at ≈2.3 eV, ≈3.5 eV and ≈5.15 eV. As a conclusion we can observe:

- At low energies (< 2.3 eV) the different compositions exhibit a similar behavior with no major change;
- The 3.5 eV band intensity gradually decreases at increasing [CaO] *(this notation means "concentration"*) and when [Al_2O_3] decreases;
- The losses associated with the 5.15 eV OA band are enhanced by the increase of [CaO] and the decrease of [Al_2O_3].

In Fig. 78 we summarize the identified OA bands in those glasses.

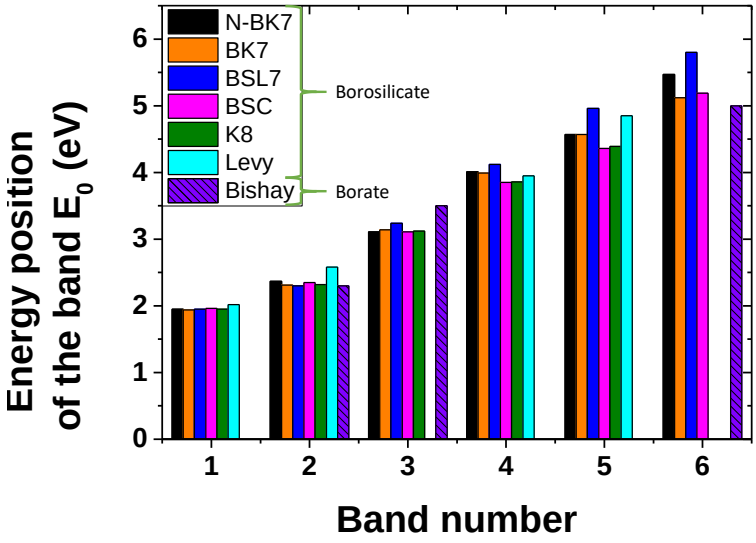

Fig. 78: Energy positions of the different bands for the 7 boron doped irradiated glasses. The 5 first glasses refer to the ones presented in [118], "Levy" refers to the glass presented in [117] and "Bishay" refers to the glass presented in [120]

Band n°1 is interesting as it seems present in all borosilicate glasses. Its properties are very close to those of the well know NBOHC defect with an OA peak around 2 eV (between 0.18 and 0.21 eV) [118]. Band n°2 is the most likely related to bore. This attribution it based on two clues: this band does not have any correspondence with (known) silica's bands and it is the only one present in all glasses with only small differences in the E0 position. In [121] authors propose that this band is related to hole trapping. For the other bands no attribution has been yet suggested.

C.1.4.4 Attenuation related to sodium

Sodium is well known to act as a glass modifier, it is also used to decrease the glass fusion temperature. For this element we have to deal with a limited literature. One of the major papers about absorbance of sodium-containing glass is [122] in which Yokota prepared several canonical samples made with SiO_2 and Na_2O then he irradiated them with X-rays (45 kV, 10 mA, tungsten target for 2 hours, no information about dose rate or dose). The corresponding results are reported in Fig. 79.

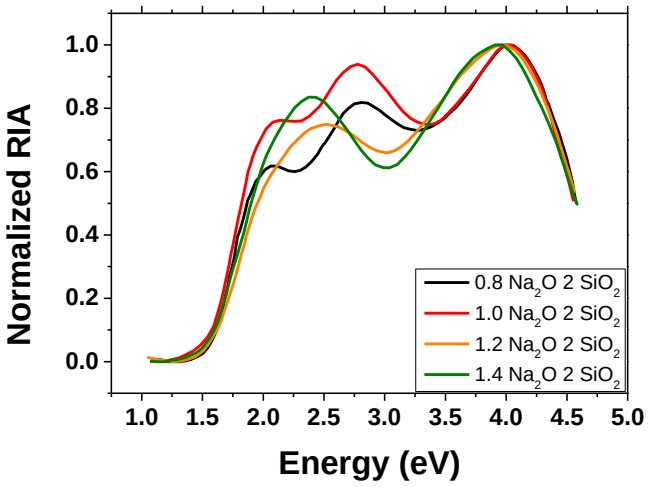

Fig. 79: Normalized RIA in silicate glass for different [Na_2O]. Figure created from [122]

Spectral shapes evolve with the evolution of [Na]. Some other papers studied glasses with sodium, such as [123] [124] [125]. After the digitalization of the curves, we fitted all the available RIA of these glasses and the corresponding analysis is summarized in Fig. 80.

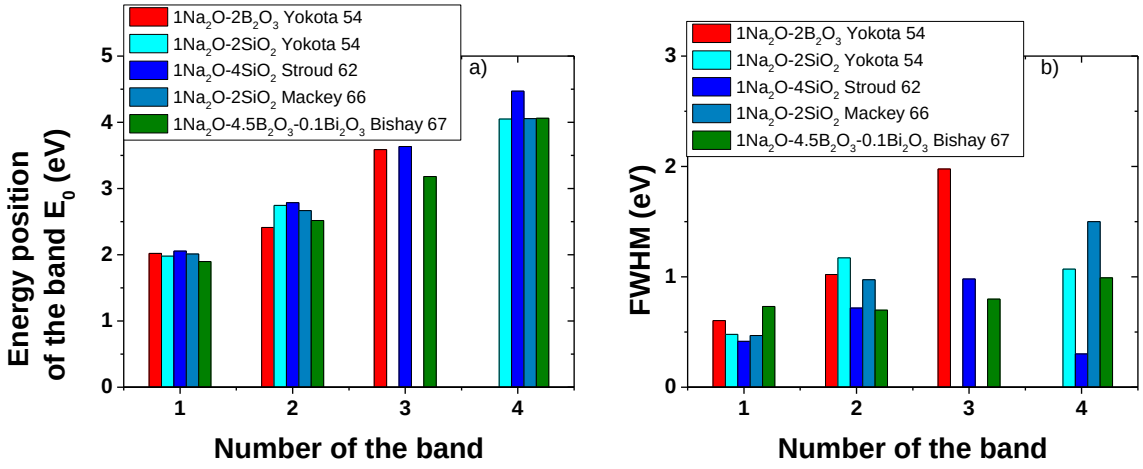

Fig. 80: Gaussian fit parameters used to adjust the RIA band locations in Na-doped glasses. "Stroud" refers to [123], "Yokota" 54 refers to [122], "Mackey" refers to [124] and "Bishay" refers to [125]

This analysis reveals that the 2 eV band has its peak position nearly independent of the glass composition. As it is present in glass without silica it may be related to sodium. For the second band, its peak position is quite stable but very different FWHM values are reported depending on the composition. For the two last bands both peak values and FWHM are not constant from one glass to another.

This review of the literature on defects related to silica, boron and sodium highlights the difficulty to clearly attribute absorption bands to particular defects or atoms in multicomponent glasses and how numerous bands are. Now we will explain how Cerium doping acts to reduce the RIA in glasses independently of their compositions.

C.1.5. Reduction of RIA by Cerium doping

We treated some of the major elements present in SCHOTT radiation hardened glasses (that is the set of glasses retained for this study), but there are many others components, which are not addressed in the literature. All these doping elements will create some defects and absorption bands, not investigated yet (at least all together), but causing the glass darkening. However, Cerium codoping of those glasses is able to prevent the generation of most of these radiation induced defects.

This section will first give some information about Cerium spectroscopy and its electronic states. Then we will discuss which type of defects are inhibited when Cerium is added to a glass matrix. The third part will discuss the effect of Cerium concentration in glasses. Finally, studies about the responses of commercial radiation hardened glasses will be reviewed as well as the limits of this hardening technique.

C.1.5.1 Cerium atom and spectroscopy

In the literature, several elements were used and tested as glass dopants in order to prevent RIA. In [126], authors used a potassium-barium-aluminum phosphate based glass and alternately doped it with Chromium, Cobalt, Copper Nickel, Molybdenum, Manganese, Iron, Titanium (trivalent), Titanium (Quadrivalent), Tungsten and, Vanadium. None of them was as efficient as Cerium to prevent RIA. Either the dopant created an absorption in the visible before irradiation (see Fig. 81.a) or/and it did not efficiently prevent the RIA (see Fig. 81.b)

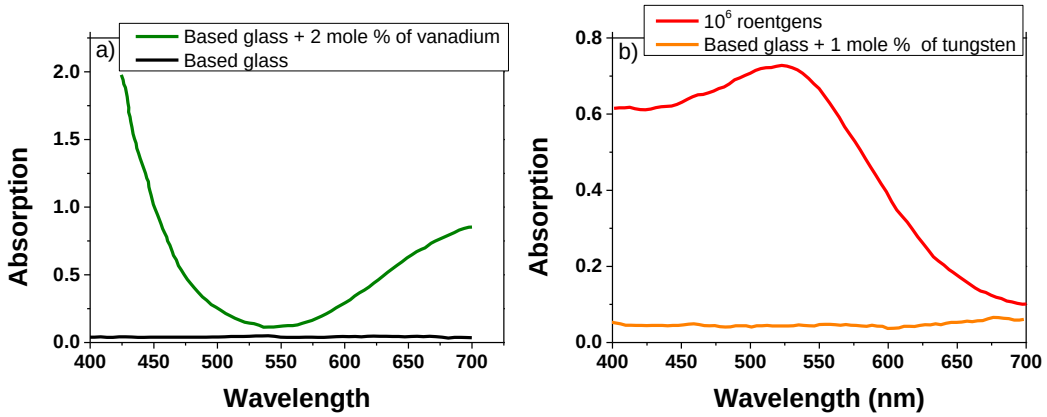

Fig. 81: a) Effect of 2 mole % of vanadium on the absorption of the based glass, before irradiation. b) Effect of 10^6 roentgens (≈ 8.7 kGy) on the based glass doped with 1 mole % of tungsten. Based glass is a potassium-barium-aluminum phosphate glass of 0.2 mm thick. Figure adapted from [126]

The efficiency of Ce to prevent the RIA in the visible domain, even at low concentration, make it a good candidate to design radiation hardened glasses. Cerium in glasses may exist in two ionic forms:

- Ce^{3+} has as electronic configuration [Xe] $4f^1$ and a 4f→4f transition in the infrared and a 4f→5d in the ultraviolet (absorption band near 320 nm) [127],

- Ce^{4+} has as electronic configuration [Xe] $4f^0$, in silicate glasses, the OA band is located around 240 nm [127].

As it was previously explained, RIA is due to defect generation caused by ionization processes. These mechanisms will be countered by the Cerium. Ce^{4+} ions will capture free electrons to become a Ce^{3+} and Ce^{3+} will capture free holes to become a Ce^{3++}. This notation[5] is used to design a Ce^{4+} in a Ce^{3+} site. So [Ce^{3+}] and [Ce^{4+}] will evolve during the irradiation. This explains the capacity of Cerium to prevent both electrons and holes to create other absorption bands. Existence of Ce^{3++} was first suggested by Stroud in 1961 [129] and confirmed with spectroscopic studies as [130] [131]. Its presence was highlighted by using the following procedure.

Stroud prepared different silica glasses doped with Cerium, the glass composition was 75% SiO_2, 25% Na_2O and 0.060% Ce. The absorption of these glasses was low enough to allow measurements down to 200 nm. In these glasses, the Cerium

[5] Ce^{3++} may also be note as $(Ce^{3+})^+$ as in [128]

concentration was kept constant and the elaboration process varies to control the oxidation and modify the ratio between Ce^{3+} and Ce^{4+} ions.

First, by comparing the Glass 1 with reduced Cerium (only Ce^{3+}) with the glass without Cerium, Stroud provided evidence for the Ce^{3+} absorption band, illustrated in Fig. 82, which is an asymmetrical signature centered at 3.95 eV (314 nm). Then the author compared Glass 1 with Glass 2 that contained both Ce^{3+} and Ce^{4+} ions, the result is presented in Fig. 83.

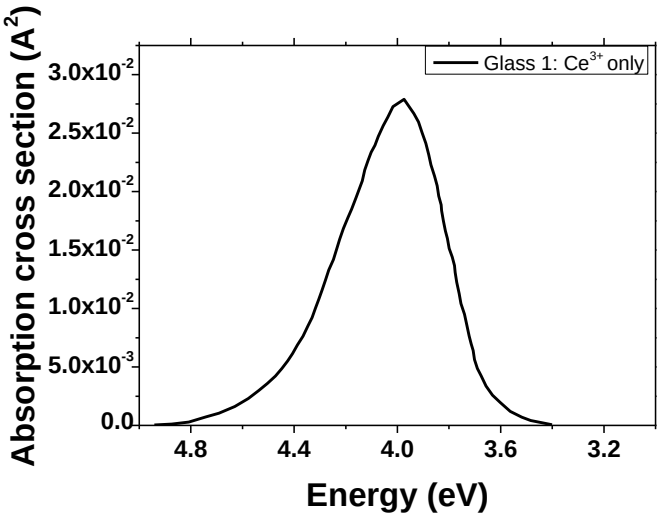

Fig. 82: Absorption spectrum of Ce^{3+} doped silicate glass. The curve is obtained by subtracting the absorption of the undoped glass. Figure adapted from [129]

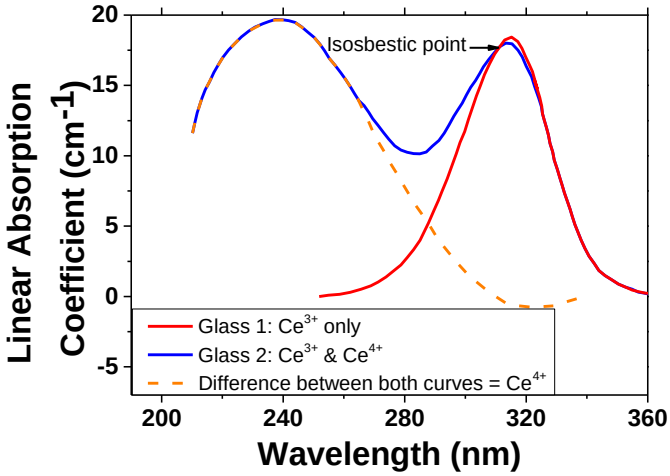

Fig. 83: Absorption spectrum of silicate glass (75% SiO_2, 25% Na_2O and 0.060% Ce) with 5.33×10^{18} Cerium ions/cm^3. Glass 1: absorption of 5.3310^{18} Ce^{3+}. Glass 2: absorption of Ce^{3+} and Ce^{4+}. Difference between both glasses corresponds to the Ce^{+4}contribution. Curves are obtained by subtracting the absorption of the

undoped glass. This figure also highlights an isosbestic between Glass 1 and Glass 2. Figure adapted from [129]

In both glasses, the Ce concentration is constant, so the [Ce^{4+}] in Glass 2 is equal to the [Ce^{3+}] decrease of Glass 1. Ce^{4+} band is centered at 240 nm overlapping Ce^{3+} band. The negative absorbance in Fig. 83 (difference between both curves) is due to the diminution of Ce^{3+} concentration in Glass 2. It's important to note that there is an isosbectic point near 310 nm. An isosbestic point is a specific wavelength at which the total absorbance is constant during a chemical reaction or a physical change. In fact, if an ion can be in two different configurations, with two different absorption bands, the total absorption coefficient is:

$$\alpha = n_3\sigma_3 + n_4\sigma_4 \quad (17)$$

Where n_3 & n_4 are the ion concentrations in both configurations and σ_3 & σ_4 are their respective absorption cross sections. The indices $_3$ and $_4$ represent the Ce^{3+} and the Ce^{4+}. The total number of ions n is:

$$n = n_3 + n_4 \quad (18)$$

Substituting (17) in (18) give:

$$\alpha = n\sigma_3 + n_4(\sigma_4 - \sigma_3) \quad (19)$$

If there is an overlap between the two bands, it is possible to have for one or more wavelengths a case such as $\sigma_4 = \sigma_3$ so $\alpha = n\sigma_3$. In this case α only depends on the total number of ions and not on the ratio between both states. The absorption curves obtained by keeping n constant and varying $^{n_3}/_{n_4}$ all pass through the isosbestic point.

Two other samples, Glasses 3 and 4, containing different Ce^{3+} and Ce^{4+} ratios, were UV irradiated and their RIA are reported in Fig. 84. This irradiation did not modify Cerium-free glass absorption (not shown in the paper), so all the difference between pristine and irradiated Cerium doped glasses can be attributed to Cerium. Both glasses have an unresolved band on their long-wavelength tail near 330 nm. Glass 3 presents a broad absorption centered at around 250 nm. Glass 4 also presents a broad absorption but with two maxima, one at 227.5 nm and another at 260 nm. The difference between the two RIA spectra shows only one OA band with a maximum at 242.5 nm and a spectral shape close to the one of the Ce^{4+} band.

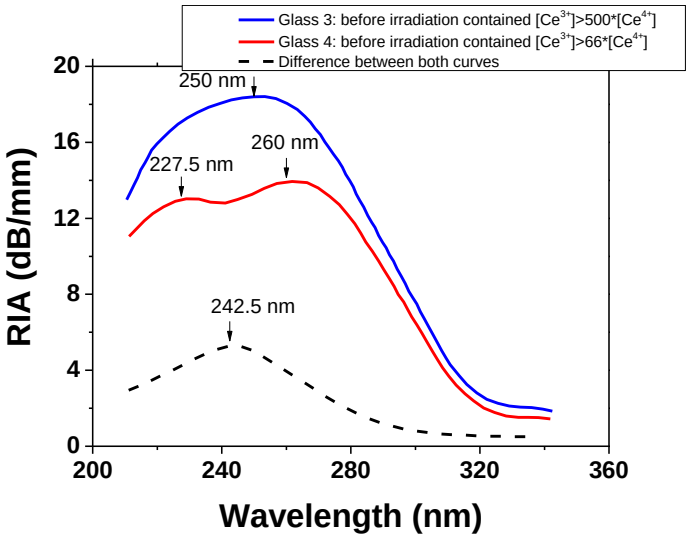

*Fig. 84: Radiation Induced Attenuation of two Ce doped silicate glasses constraining 5.33×10^{18} Ce/cm^3, after UV irradiation. Glass 3: before irradiation contained 5.33×10^{18}Ce^{3+}/cm^3 and less than 10^{16} Ce^{4+}/cm^3. Glass 4: before irradiation contained 4.6*10^{18}Ce^{3+}/cm^3 and 7*10^{17} Ce^{4+}/cm^3. Figure adapted from [129]*

In Fig. 84 there is no more any isosbectic point, so another reaction than the conversion between Ce^{3+} and Ce^{4+} ion took place. Moreover, the RIA of Glass 3 shows an absorption band with a maximum at 250 nm which is close (but not equal) to the absorption peak of Ce^{4+}. Finally, as the difference curve corresponds to the Ce^{4+} band, it suggests that the [Ce^{4+}] decreases in the glass 4 and no generation of Ce^{4+} occurs in the Glass 3. These arguments led the author to suggest the existence of a Ce^{3++} state. The Ce^{3++} is basically a Ce^{4+} in a Ce^{3+} site and originates from the ionization of Ce^{3+}. Because the Ce^{3++} environments (neighbors) is not similar to the Ce^{4+} one, its properties differ from those of the Ce^{4+} ions which result in different absorption spectra.

Table 19 summarizes the difference between Ce^{4+} and Ce^{3++} ion properties (computed by the author).

Table 19: Optical absorption bands associated with Ce^{4+} and Ce^{3++} ions, from [129]

	Ce^{4+}	Ce^{3++}
Position of the OA band (nm)	240	250
FWHM (eV)	0.65	0.72
Absorption cross section at the maximum (A^2)	0.2	0.3

C.1.5.2 Type of defects inhibited by Cerium

Additional studies, performed by Stroud [123], provided some evidence that Ce^{4+} can contribute to a decrease of the glass RIA. The corresponding irradiation tests were done with X-rays (tungsten-target tube operated at 250 kV filtered by a 0.22 mm thick copper filter). Samples with the same composition as in [129], were irradiated with X-rays to highlight the inhibition of the radiation-induced point defects generation. The RIA of Glass 6 (no Ce), Glass 7 (Ce^{3+} only) are reported in Fig. 85.

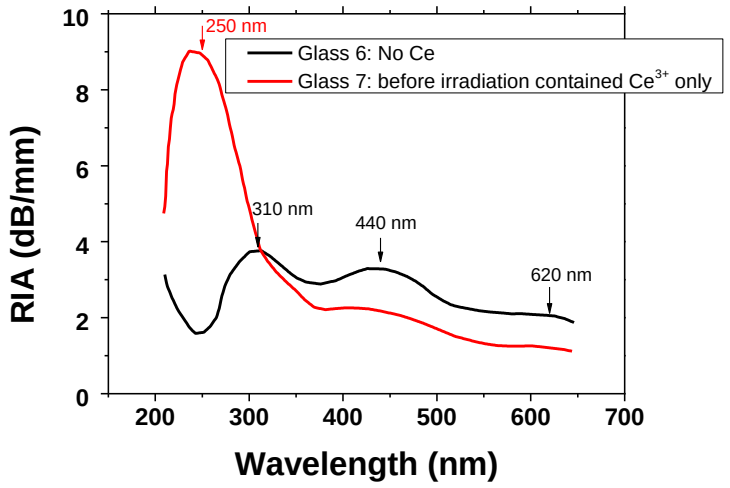

Fig. 85: RIA responses after 150 kilo-roentgen X-ray of Glass 6: Ce free, Glass 7 (Ce doped: $5.3\times10^{18}Ce^{3+}/cm^3$) before irradiation. Figure adapted from [123]

For the glass without Cerium (Glass 6), X-rays generated three OA bands peaking at 310, 440 and 620 nm. While UV irradiation has no influence on this sample [129], X-ray irradiation highlights different optical responses. Regarding the Ce^{3+} doped glass (Glass 7), the RIA is lower in the visible spectral domain with a strong OA band at 250 nm attributed to the Ce^{3++}. Due to the overlap of the Ce^{3++} and the Ce^{3+} optical responses, it's not possible to discern the band at 310 nm in glass 7.

The only possible reaction for the Ce^{3+} is to be converted in Ce^{3++} by capturing a hole. As a consequence, defects around 440 and 620 nm are due to holes. To confirm the attribution of these two bands to trapped holes, complementary X-ray irradiations were performed on a specific set of glasses with different Cerium concentrations (varying the Ce^{3+} and Ce^{4+} ratio) [123]. The obtained results are reported in Fig. 86.

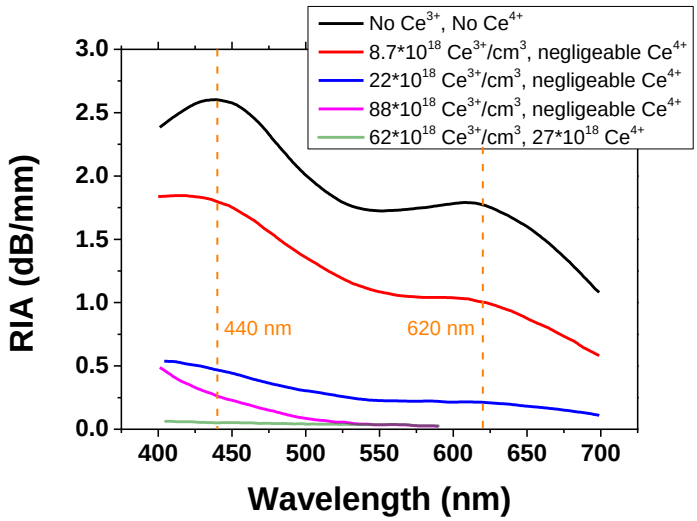

Fig. 86: Radiation Induced attenuation after 220 kilo-roentgen X-ray of silicate glasses doped with different Cerium concentrations and stoichiometric ratios between Ce^{3+} and Ce^{4+}. Figure adapted from [123]

In the undoped sample, the two expected bands (440 and 620 nm) are observed. Increasing the [Ce^{3+}] inhibits more efficiently the generation of these defects as shown by the amplitude decrease of the associated bands. This may be explained by the increasing probability of capture for larger concentrations, up to a total bleaching with 88×10^{18} Ce^{3+}/cm^3. Ce^{3+} ions capture holes, so it's another argument for the attribution of these bands to hole traps. At the higher Ce^{3+} concentration (pink curve), it's possible to see a new absorption band with a maximum in the UV and extending up to 600 nm. The addition of Ce^{4+} ions inhibits this new band, as Ce^{4+} is able to capture electrons we can suggest that this new band is due to electron traps. As a consequence, with an appropriate balance between Ce^{3+} and Ce^{4+} in the pristine glass, Cerium can prevent defect caused by both traps and electrons.

C.1.5.3 Effect of Cerium concentration

As shown in section C.1.5.1, Cerium has specific absorption bands that will modify the glass host matrix optical response. Fig. 87 reports an example of this additional absorption impact on the transmission properties of a commercial glass. It also highlights that, after irradiation, the transmission spectra of the Cerium doped glass (BK7G18) is better than the one of the undoped sample (BK7).

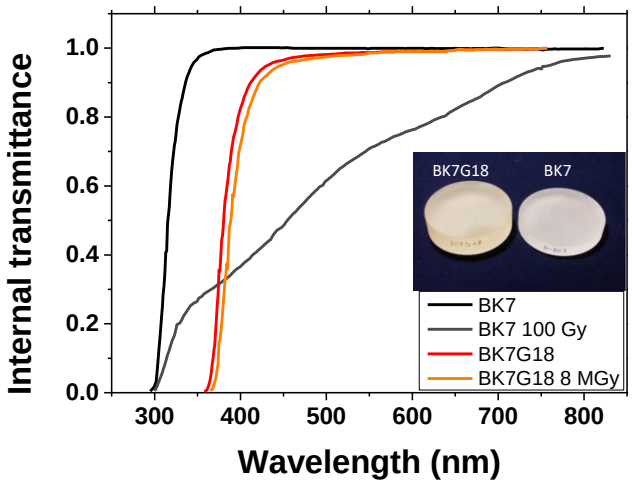

Fig. 87: Transmittance spectra pristine and gamma irradiated samples of BK7 & BK7G18. Picture shows pristine BK7G18 & BK7 windows before irradiation, the yellow coloration of BK7G18 is due to Cerium doping. Figure adapted from [132].

The primary goal of Cerium doping is to keep a low absorbance during irradiation. We should balance the [Ce] doping concentration that decreases the glass intrinsic transmission (pre-irradiation loss) and the prevention of RIA. In order to optimize the quantity of Cerium in the glass, a modeling study was made by Stroud [123]. We will explain the idea behind this model by using holes traps (the same one can be used for electrons after redefinition of symbols). If a Ce-doped glass is irradiated, holes will be formed by ionization. If a new hole is formed in a capture volume v_3 surrounding a Ce^{3+} ion, it will be captured and the Ce^{3+} will be converted in Ce^{3++}. If the hole is generated elsewhere, it will be captured by another trap and create an absorption band. The probability for a hole to escape the capture is $(1 - {}^{c_3}/_{\rho})^{v_3\rho}$ [123] where c_3 is the Ce^{3+} concentration and ρ the density of sites that can be occupied by Ce^{3+}. As it will be shown in Fig. 88, Fig. 89 and in [133] the effect of Cerium on the RIA saturates after a certain concentration, typically some percent. It is confirmed by the fact that in commercial radiation hardened glasses, even in old glasses, SCHOTT did not used more than 4 %wt [Ce] (see Fig. 92). It is consistent with the Stroud's explanation that after a certain Ce concentration all atoms in the glass will be inside the influence zone of Cerium ions (v_3). The total attenuation [123] can be written as:

$$\alpha = \alpha_h \exp(-v_3 c_3) + \alpha_e \exp(-v_4 c_4) \qquad (20)$$

With α_h is the absorption of the trapped holes when $c_3 = 0$ and α_e the absorption of the trapped electrons when $c_4 = 0$ (equivalent to [Ce^{4+}]=0). v_4 is the capture volume of the Ce^{4+} ion for an electron and v_3 is the capture volume of the Ce^{3+} ion for an hole. To validate this model, we study the case of (20) when c_4 is small (a glass with a large majority of c_3 or Ce^{3+}) as presented in Fig. 88. The fit on the experimental data was adjusted by using (21):

$$\alpha = \alpha_h \exp(-v_3 c_3) + \alpha_e \qquad (21)$$

If $\alpha_h \gg \alpha_e$ then α decreases exponentially with increasing c_3 at low c_3 and tends to α_e as high c_3.

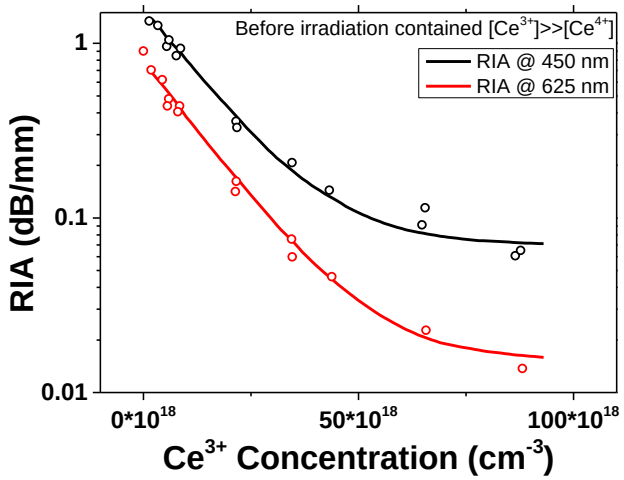

Fig. 88: Evolution of the RIA (at 450 nm and 625 nm) as a function of [Ce^{3+}] concentration. The irradiation X-ray dose is 9.6 kilo-roentgen. Glasses were made in similar conditions than the ones of sections C.1.5.1 & C.1.5.2. Fitted by equation (21). Figure adapted from [134]

The proposed model fits quite well the experimental results. When [Ce^{3+}] increases, the RIA exponentially decreases because of the increasing probability of hole to be captured by a Ce^{3+} ion. Then at a sufficient concentration the positive effect of Ce^{3+} saturates because there is nearly no more holes to be captured. Here, this appears at Ce-concentration of about 5×10^{19} Ce^{3+}/cm^{-3}. Similar result was shown in [133] (see Fig. 89), a concentration higher than 2 %wt seems to not improve the glass radiation response after an equivalent dose but even a small increase of [Ce] may decrease its intrinsic transmission in the blue part of the spectrum, this is highlighted by Fig. 90. The two types of glasses have quite different compositions, we cannot extrapolate this result

for all glasses but the behavior trend can be applied to all samples. This effect is enhanced in the SF6G05 sample, even with a low Cerium concentration (0.5 %wt) its transmission is strongly shifted compared to N-SF6 (Ce free) as shown in Fig. 91. According to [135] [136] the transmission shift due to Cerium is stronger for glasses which contain constituents heavy metal oxide such as Pb, Ba and La (SF6G05 contains 70 - 80 %wt of Pb). This pre-irradiation shift could be related to covalence degree of the glass [136], [137].

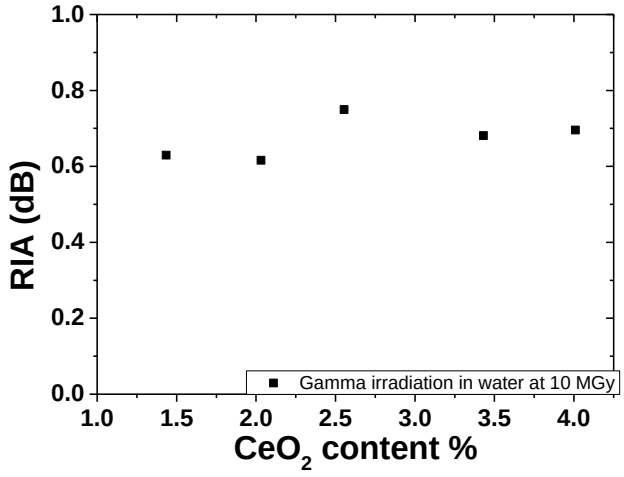

Fig. 89: RIA @ 410 nm vs CeO_2 content in a glass. Figure created from [133] in the hypothesis that the 5 irradiated glasses have the same thickness. This publication did not give the glass type and its thickness, but at the best of our knowledge it is the only article that present attenuation measurements in function of the CeO_2 content in a glass.

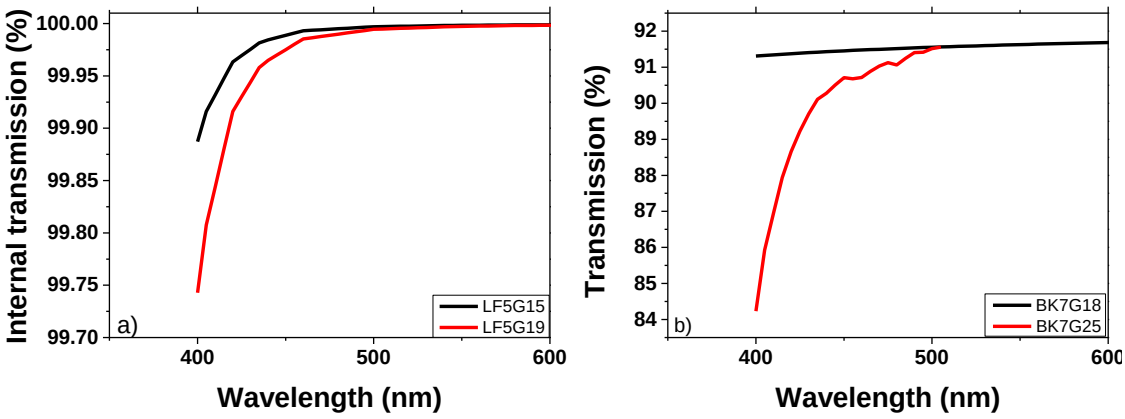

Fig. 90: a) Comparison between the internal transmissions (no Fresnel reflection losses) of 20 mm of LF5G15 (1.5 wt % of Ce) and LF5G19 (1.9 %wt of Ce). Figure created from: [138], [139] b) Comparison between the transmissions of 2.5 mm of BK7G18 (1.8 %wt of Ce) and BK7G25 (2.5 %wt of Ce). Figure created from [126], [133]

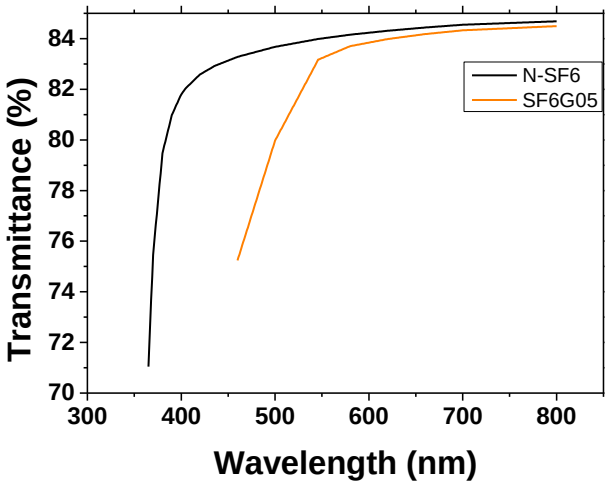

Fig. 91: Comparison of the N-SF6 (Ce free) and SF6G05 (0.5 wt % of Ce) transmission before irradiation. Figure created from [62], [140]

C.1.5.4 RIA of Cerium doped commercial glasses after gamma irradiation

CAMRAD optical system will be based on commercial radiation hardened glasses, so we will review the available data for these glasses type. For radiation resistant glasses the possible set of samples elaborated by SCHOTT was larger in the past than today with more than twenty radiation resistant glasses across the Abbe diagram (see Fig. 92). At the best of our knowledge, at the time of CAMRAD project, there remains:

- Only five glasses left by SCHOTT in their catalog,
- One by Ohara [141] (five were announced in December 2015 [142] but only one reference is accessible on their website),
- Forty five by CDGMGD (but with no data about their compositions, no post irradiation spectrum and doses in roentgen [143]).
- At least six from LZOS company [144] (we only found one study that tested them under neutron irradiation), we did not succeed to found a full list.

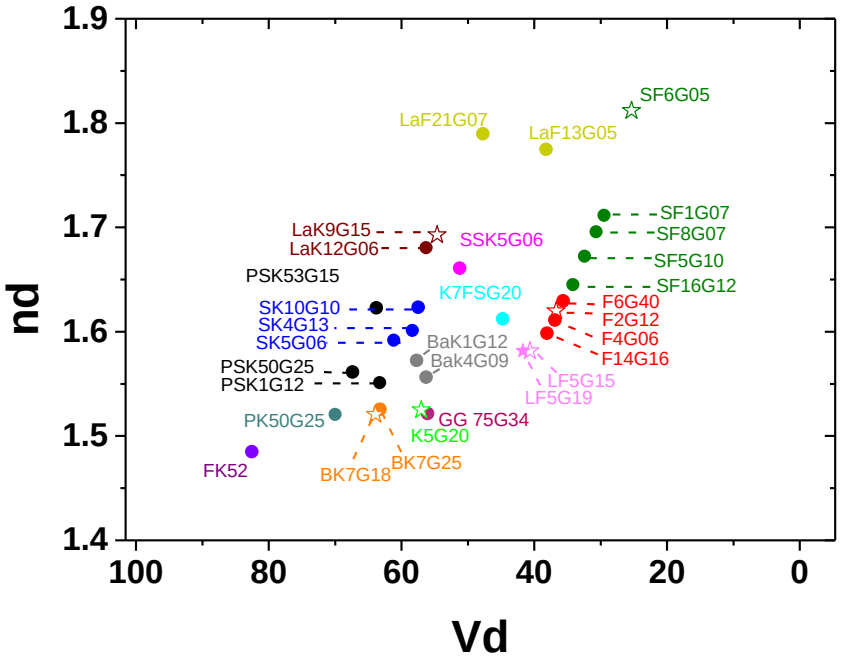

Fig. 92: Abbe diagram of SCHOTT radiation resistant glasses in 1992. Each glass family has a different color (see Fig. 59 to the full name of each family). Stars are used for glasses still commercially available in 2019, during this time the F2G12 was added to SCHOTT catalog. Figure redrawn from [135]

There are practically no data available in the open literature about the transmission of these glasses after radiation. The radiation resistance of some of them was discussed in [133], but all the tested references were no longer available for CAMRAD. Some data provided by SCHOTT [145] on their glasses after gamma irradiation are shown in Fig. 93.

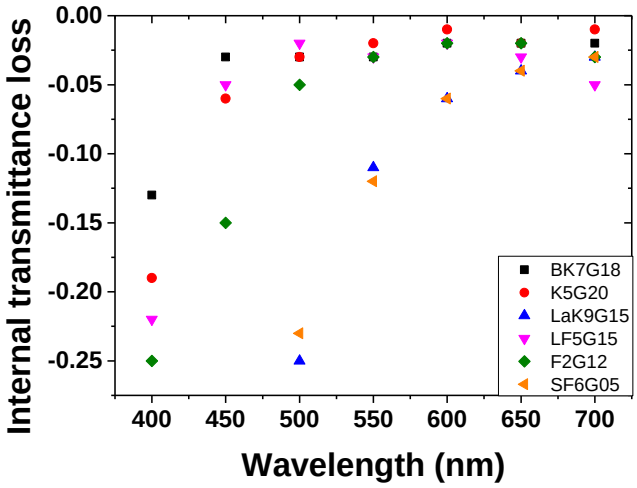

Fig. 93: Internal transmission loss for the rad-hard SCHOTT glasses, after 1 MGy (gamma) for 10 mm thick samples. Figure redrawn from [145].

These data have some issues:

- No guarantee exists that the glass composition (and then the radiation response) remains constant throughout the years, because as it is writen in [145] “data dates back to the first radiation resistance glass catalog were performed in the 1980s”.
- Some data points are surprising, such as those showing a decrease of the RIA at shorter wavelengths.
- The number of measurement points is limited, but gives the global tendency response.
- Internal transmittance is a computed quantity. Its calculation uses the refractive index (not reported in the corresponding paper).

One publication [130] deals with the K509 Cerium doped glass made by CDGM Glass Co.,Ltd a Chinese glass maker. Its composition (measured by the authors by inductively coupled plasma-optical emission spectrometry) is given in Table 20. The Ce-doped K509 sample and its Ce-free counterpart K9 were gamma irradiated (^{60}Co source) up to a cumulated dose of 1 MGy [130], the measured post-mortem RIA spectra are shown in Fig. 94. Thanks to the small thickness of their samples (0.2 mm) they succeed to measure the attenuation far enough in the UV range highlighting the presence of Cerium’s OA bands, see Fig. 94 a). Fig. 94 b) compared both glasses at 1 MGy and demonstrates the efficiency of Ce-doping to prevent the RIA.

Table 20: Composition of two optical analogs K9 (Ce free) and K509 (Ce doped) glasses elaborated by CDGM Glass Co., Ltd, data from [130]

Glass name	$_{11}$Na Oxide	$_{13}$Al Oxide	Silica	$_{19}$K Oxide	$_{20}$Ca Oxide	$_{26}$Fe Oxide	$_{30}$Zn Oxide	$_{56}$Ba Oxide	$_{58}$Ce Oxide
K9	10.78	0.14	76.39	10.76	0.017	0.002	0.20	1.71	Ø
K509	10.6	0.13	77.6	9.1	0.011	0.002	0.2	1.8	0.43

The last publication [146] deals only with the radiation response of the BK7G18 radiation hardened glass under gamma radiation. The authors performed spectral RIA and kinetic measurements for different dose rates (16, 140 and 550 mGy/s) up to a cumulated dose of 300 kGy (gamma). Fig. 95.a) shows the RIA spectra for different doses.

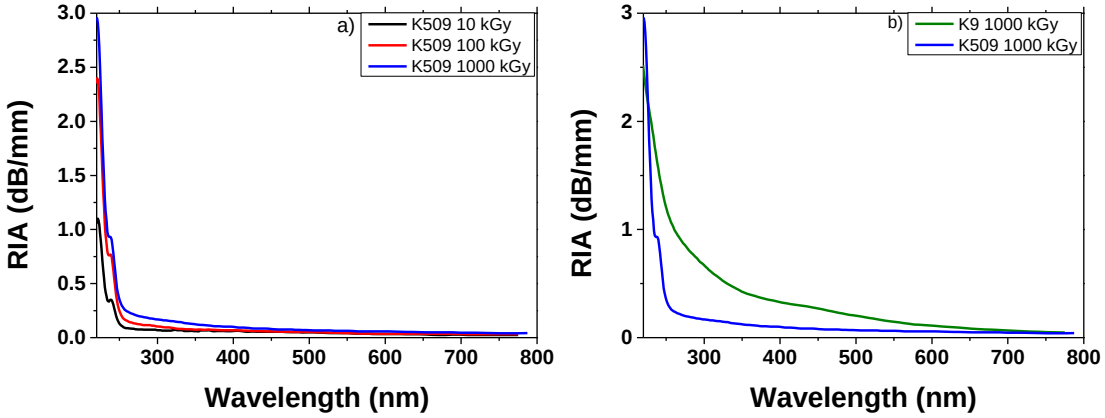

Fig. 94: a) Spectral radiation induced attenuation of K509 glass at different doses (gamma irradiated). b) RIA of K9 versus K509 at 1 MGy. Figure adapted from [130]

Samples were 3 mm thick which allows measurement down to 360 nm (tail of the Cerium absorption band) with no detectable RIA presence after 450 nm see Fig. 95.b). The authors also highlighted that for this glass, the higher the dose rate is, the higher the saturation value. This is illustrated in Fig. 96. The recovery phase (post-irradiation RIA measurements) was recorded periodically during one year highlighting the instability of the generated defects. During this period, samples were kept in the dark at room temperature. It is interesting to note that the recovery is faster for a higher dose rate. It comes from the fact that the irradiation duration is shorter as a consequence the created defects have less time to recover during the irradiation and are more bleached after the irradiation stops.

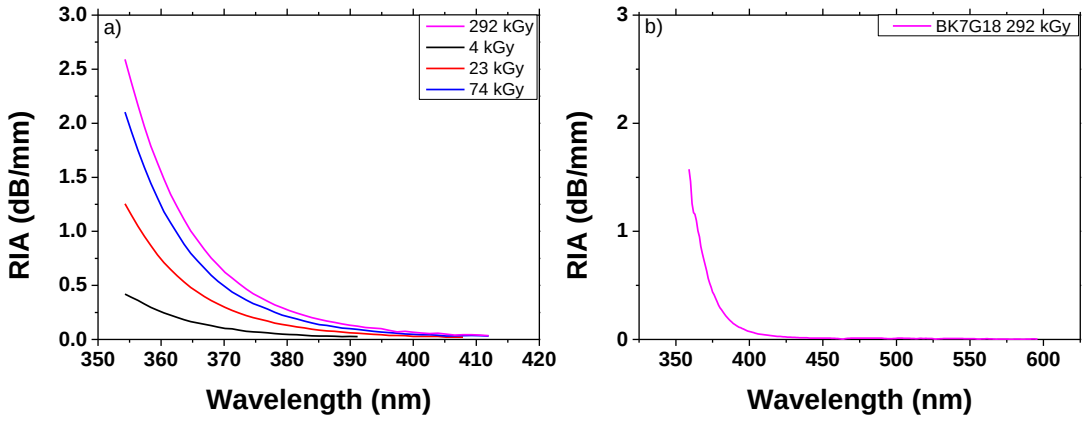

Fig. 95: a) Calculated RIA of BK7G18 after different doses (gamma) in the blue and UV region range adapted from [146]. b) RIA after 292 kGy in the visible range. Figure created from [146].

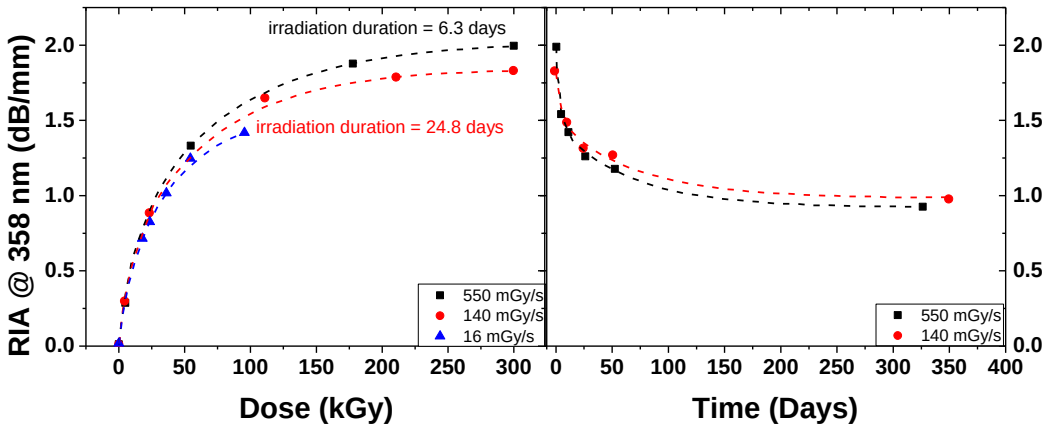

Fig. 96: RIA growth kinetic @ 358 nm, of BK7G18 at different dose rates and different times after the end of the irradiation. Figure adapted from [146]

We can also quote [98] that tested radiation hardened glasses but only up to 0.1 MGy. Nevertheless it found that the LaK9G15 exhibit large induced losses in the [400 - 500 nm] spectral range after exposure to only 3 kGy.

One of the issues for the project is the non-guaranteed availability of the radiation hardened glasses needed to develop the camera optical system. As it is mentioned by SCHOTT in [145] “Radiation resistant glasses are inquiry glasses which we do not purposely keep on stock”. Indeed, for this optical system, it is mandatory to have access to glasses with well-defined characteristics (refractive index and Abbe number) to optimize its optical performances. As Ohara announced the conception of five radiation hardened four years ago and had only released one, we cannot be confident in their capacity to provide a replacement glass if SCHOTT decided for example to stop the production of one mandatory glass for the optical system. CDGMGD do not provide sufficient data to allow the use of their glasses without complementary tests (they are time consuming and expensive) and at the best of our knowledge, LZOS glasses do not fit the characteristics of SCHOTT ones. This question may become a real issue for the production of CAMRAD cameras in the future. A way that may lead us to avoid this issue is developed in section C.3.4. As a comparison, ITER seems to focus its glass studies (for lenses) on high-purity quartz especially KU1 and KS-4V that are provided by Kurchatov Institute (Russian Federation) [6], [80].

C.1.5.5 Limitation of Cerium hardening against radiation effects

We described how Cerium is able to prevent most of the RIA in the visible domain. But from data available in [71], Cerium doped glasses show different and sometimes higher RIRIC than the non-doped counterpart ones. As an example, BK7 and BK7G18 (Ce doped) samples were gamma irradiated at a cumulative dose of 4 kGy on their plate's peripheries and at a dose level of 8 kGy on their centers. Wavefront measurement maps (by Fizeau interferometry at 633 nm) highlight the RIRICs according to the irradiated areas – the corresponding results are reported in Fig. 97.

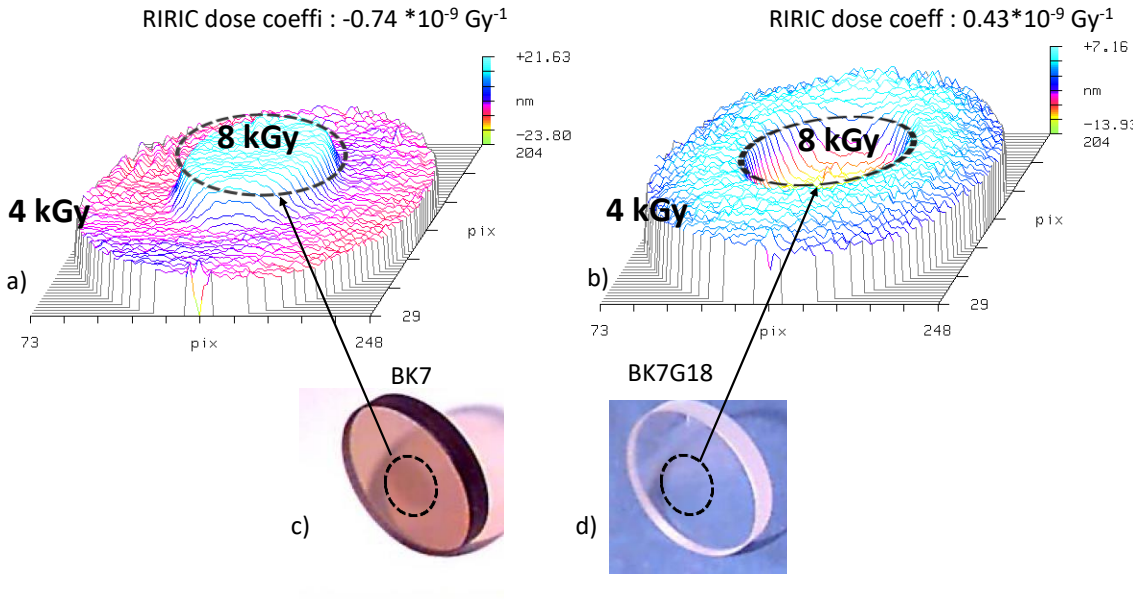

Fig. 97: Evaluation of RIRIC by the wavefront technique (with a Fizeau interferometer at 633 nm) in a) BK7 and b) BK7G18 samples. Glass central parts were irradiated at a cumulative gamma dose of 8 kGy while their periphery areas were irradiated at a dose of 4 kGy. c) and d) are pictures of both glasses after irradiation. Figure adapted from [59].

While the BK7 RIRIC is negative, the one of the BK7G18 is positive. That may be explained by the two formulas given in C.1.3.3, the Cerium may change the dilatation / compaction of the glass and absorbance bands in the UV that affect RIRIC in the visible range. The Cerium doping can change the RIRIC sign (BK7/BK7G18) or not (LaK9/LaK9G15) and increase its value (LaK9/LaK9G15) or not (BK7/BK7G18).

Even if the RIE may not affect the image, the glass hardening modify it. In term of RIE, the Cerium presence will contribute via its specific emission centered at around 450 nm [147] [127]. This effect is highlighted in F2 (Ce-free) and F2G12 (Ce-doped) samples irradiated at the electron accelerator ELSA (France) with 18 MeV neutrons in Fig. 98.

Even if the intensity of the overall integrated signal is relatively low (around 63 and 130 nW/cm^3/Rad respectively for F2 and F2G12 samples). All in all, this level is still too low to affect the image.

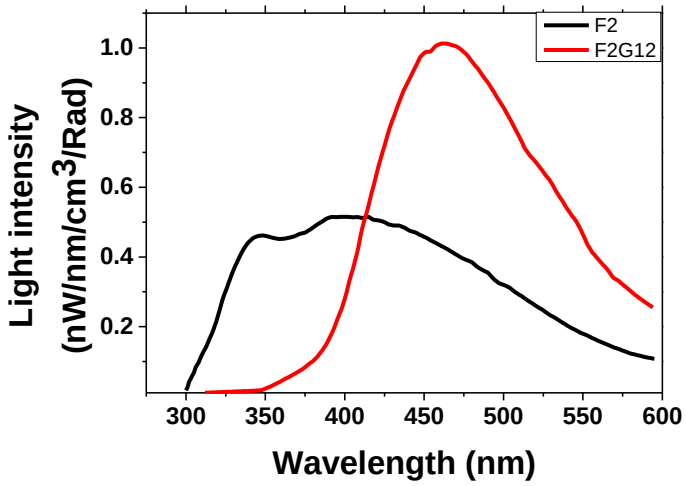

Fig. 98: RIE spectra of F2 and F2G12 samples irradiated at the ELSA facility with 18 MeV X-ray and normalized to dose and glass volume. Figure adapted from [84].

Conclusion Section C.1

First, we used the chromatic aberration case to explain why our study has to include several glasses with different optical parameters and so different compositions. Then we described radiation effects on optical glasses (RIA, RIE & RIRIC) and their consequences for the camera. The main one is the RIA because if the light level on the image sensor is too low, all other parameters of the image are no longer relevant.

To minimize the RIA, we decided to study a special class of optical glasses named “radiation resistant glasses”. They have the particularity to contain Cerium as a codopant. The conversion of Ce^{3+} to Ce^{3++} and Ce^{4+} to Ce^{3+} under irradiation prevents the RIA growth in the visible part of the spectrum. We also show with a model proposed by Stroud and confirmed by measurement that only some wt % of Cerium are enough to prevent the RIA. We reviewed the few RIA data available (after gamma irradiation) in the open literature for commercial radiation hardened glasses and the question of their commercial availability. We showed that there is an effect of Cerium on the amplitude of RIRIC but without clear dependence on the glass composition probably due to the absence of sufficient data. Finally, even if Cerium creates a RIE band at higher

wavelength than the usual glass, its amplitude remains low so it should not be too much impacting for the CAMRAD project.

C.2. Materials and methods for measurement on glasses

This chapter is focused on the description of the samples selected for our application and the characterization techniques used to measure the RIA during the irradiation.

C.2.1. Samples preparation and description

As it was previously explained, we will focus our study on the RIA measurements generated in a selection of SCHOTT Rad-Hard (Cerium doped) glasses under X-rays. Their generic information is reported in Table 21 while their chemical compositions were reported in Table 16.

Table 21: Tested samples for online RIA measurements

Glass Name	Bath number	Samples Thickness [min max] (mm)
BK7G18	D105 903 4A	[8.47 – 9.72]
K5G20	Y117171001	[8.40 – 8.44]
F2G12	ZF9634Z001	[8.89 - 9.92]
LAK9G15	PAP05924	[9.89 – 10.93]
LF5G19	Y240509005	[9.86 – 9.90]
SF6G12	THA29482	[8.75 - 8.79]

All glasses were cut and polished at the laboratory. As our system does not allow us to obtain so-called “optical polishing” our measurements are often nearly 2.5 % lower than in the literature as show in Fig. 99. However, our study is not devoted to the absolute values but to the radiation induced changes.

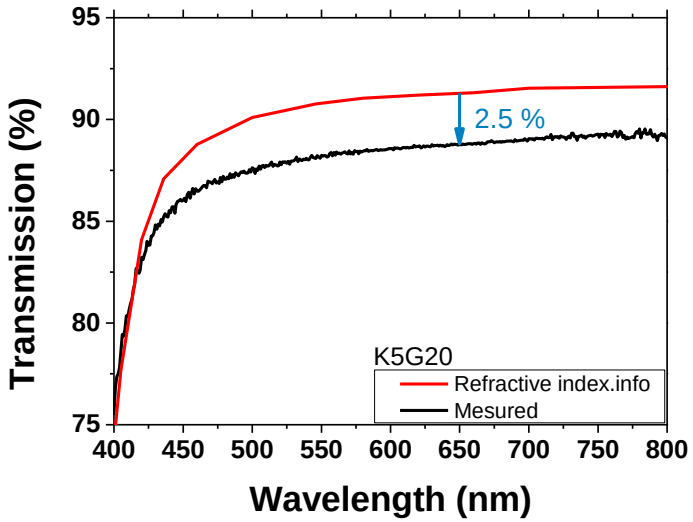

Fig. 99 : Comparison of the transmission of pristine K5G20 from the literature (Refractive index.info [148]) and the one cut, polished and measured at the laboratory

C.2.2. Irradiation conditions

The *MoperiX* facility was already described in section B.2.2. Our goal is to evaluate the effect of dose rate and temperature on the RIA optical responses of rad-hard glasses. Regarding the irradiation conditions, they can be summarized as:

- To keep the same distance between the X-ray tube and the bulk sample under test for every measurement in order to enhance the repeatability,
- To have one dose rate close to IRMA Co60 facility one's (near 1 Gy/s),
- To have one measurement up to a cumulated dose of 1 MGy(SiO_2),
- For equipment availability constraints all the measurements had to be done in 3 weeks.

So, the experimental design of experiments is summarized in Table 22.

Irradiations up to 0.1 MGy are used to analyze dose rate and temperature influences. The irradiation up to 1 MGy is needed for photometric budget simulation and to evaluate the measurement repeatability.

Table 22: Online irradiation conditions, curve colors will be the same in all figures comparing dose rates or temperatures in C.3.

Irradiation name in text and caption	Dose rate	Total dose	Irradiation duration	Temperature
1.2 Gy/s	**1.2 Gy/s**	0.1 MGy	23h9min	30°C
10 Gy/s	**10 Gy/s**	0.1 MGy	2h46min	**30°C**
50°C	10 Gy/s	0.1 MGy	2h46min	**50°C**
80°C	10 Gy/s	0.1 MGy	2h46min	**80°C**
50Short	**50 Gy/s**	**0.1 MGy**	33min	30°C
50Long	**50 Gy/s**	**1 MGy**	5h33min	30°C

C.2.3. Refractometer

To measure refractive indices, we used an Abbe refractometer by Antoon Paar. A small-size sample is placed on the polished surface of the prism which is made from synthetic YAG (Yttrium Aluminum Garnet) material. The sample is enlightened by a LED white light source through an optical filter (bandwidth of ± 0.2 nm), a converging lens and prism as shown in Fig. 100

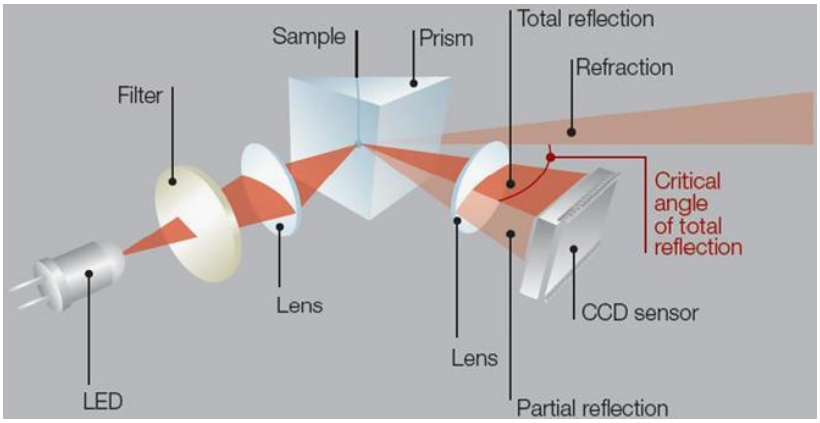

Fig. 100: Abbe refractometer diagram. Figure from [149]

Refractive indices are deduced from the critical angle of the beam total reflection method at a selected wavelength. The sample and prism are temperature-controlled by

in-built solid-state Peltier support. All our measurements were performed at 20°C. The uncertainty on the refractive index value is stated to be ± 5×10^{-5} by the manufacturer. We selected the probe wavelengths to be able to calculate the change in the Abbe number.

C.2.4. Spectrophotometry

For the offline absorption measurements on the bulk glasses, we used a *Carry 5000* spectrophotometer from Agilent. Its schematic diagram is reported in Fig. 101.

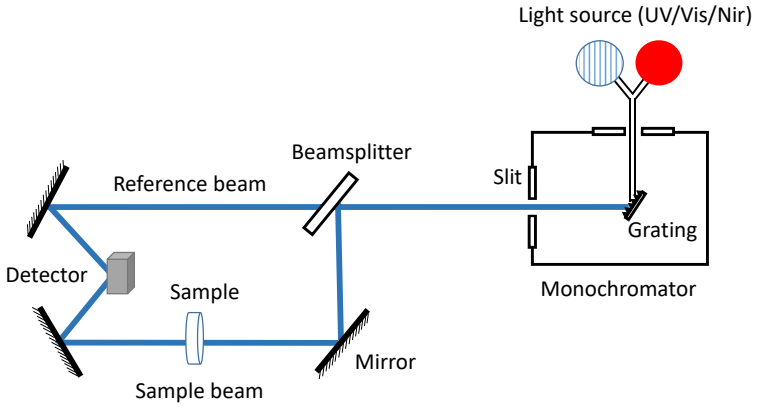

Fig. 101: Schematic diagram of the used spectrophotometer (Carry 5000 spectrophotometer from Agilent)

The instrument is equipped with a halogen lamp for studies in the visible spectral domain as well as a deuterium lamp for UV investigations. After the adjustment of the instrument's parameters (gain, acquisition time, spectral resolution...), we set a baseline. The sample is then, inserted, at normal incidence to the probe beam and many scans can be repeated (and integrated) to reduce noise/signal ratio. With this instrument, RIA is computed as:

$$RIA\ (dB/mm) = \frac{A_{irradiated}}{L_{irradiated}} - \frac{A_{Pristine}}{L_{pristine}} \qquad (22)$$

With $A_{irradiated}$ the measured attenuation of the irradiated glass, $A_{Pristine}$ the attenuation of the pristine glass, $L_{irradiated}$ the length of the irradiated sample in mm and $L_{pristine}$ the length of the pristine sample in mm. As often as possible we compared the absorption after irradiation to the absorption of the same sample before irradiation, in this case $L_{irradiated} = L_{pristine}$

C.2.5. Online RIA in glass measurement set-up

This section will describe the online measurement set-up specifically developed for this study. We used N-BK7 material as a textbook case for this section.

C.2.5.1 Description

The following test bench[6] has been developed for the RIA measurements during and after the X-ray exposures. The light incident beam from a deuterium-halogen source (*DH2000BAL* from Ocean Optics) is injected into a multimode fiber (*Draka MM SuperRadHard*) pigtail connected to an UV-Enhanced Aluminum Reflective Collimator (*Thorlabs RC02SMA-F01*) tool. This device is well adapted to extract the signal from the input fiber in the form of a 2 mm diameter parallel light beam thanks to a parabolic mirror. By adjusting the distance between the fiber and the mirror, it is possible to decrease the size of the spot close to a diameter of 1 mm.

This incoming beam is directed onto the sample under test. After propagation in air over tens of cm, it arises on the top of the glass sample (typically just below its surface exposed to radiation) that will be submitted to X-rays coming from the tube placed above it. After its propagation in the sample (between a few mm to more than one cm), the emerging beam, is collected by another *Thorlabs RC02SMA-F01* element and is injected into a multimode transport fiber connected to a spectrometer (*Hamamatsu UV/VIS C10082CA*) operating in the [163 – 845 nm] wavelength range.

At shorter wavelengths (< 350 nm), the measurements are limited by the metal-coated mirrors reflectance of the *Thorlabs RC02SMA-F01* and pigtails absorption. Fig. 102 presents two schematics views of the setup and Fig. 103 shows a picture of the developed setup incorporated in the *MOPERIX* machine. Thanks to the limited size of the X-ray beam, the setup (fibers and collimators) is irradiated at lower dose than the glass sample (this effect is studied in C.2.5.5). The RIA is then obtained by comparing the

[6] We would like to acknowledge Dr. Jochen Kuhnhenn and his team from the Fraunhofer Institute for Technological Trend Analysis INT, Euskirchen (Germany) for very fruitful discussion and precious advice on the building of the setup.

measured transmission spectra at any time during or after irradiation with a reference spectrum acquired before the irradiation starts.

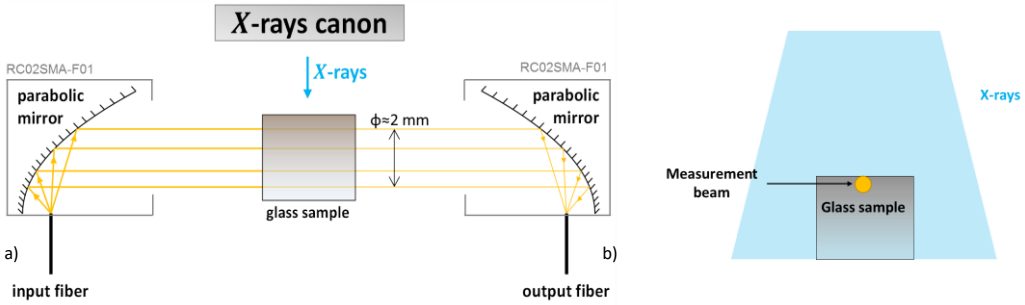

Fig. 102: Schematic representation of the irradiation set-up, a) front view, b) side view.

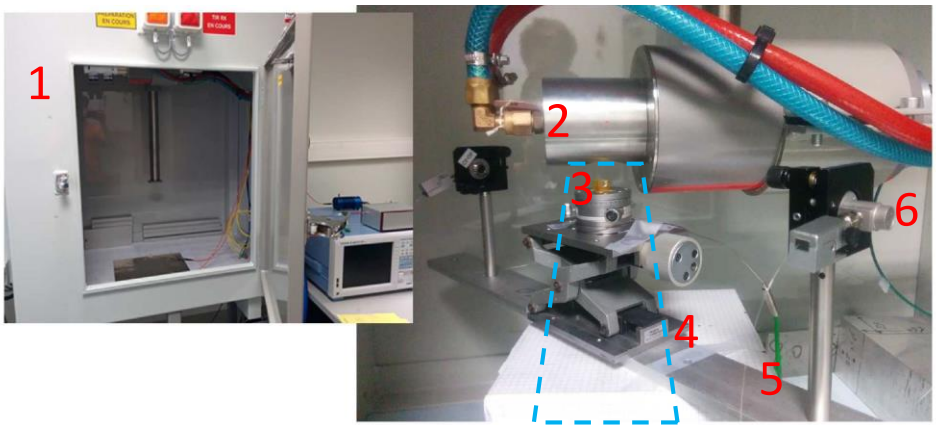

Fig. 103: Illustration of the MOPERIX Facility (1) and of the developed setup for the online RIA measurement during and after irradiation on bulk glasses. (2) X-ray canon, (3) sample under test, (4) the blue trapezoid illustration of the X-ray beam, (5) multimode fiber, (6) Collimator

With our setup, RIA is computed as:

$$RIA\left(\frac{dB}{mm}\right) = -\frac{10}{L} \times log_{10}\left(\frac{I_{irrad} - noise}{I_0 - noise}\right) \quad (23)$$

With L the sample length in mm, I_0 the intensity before the irradiation in count, I_{irrad} the intensity during the irradiation or the recovery in count, $noise$ the spectrometer dark signal in count.

C.2.5.2 Temperature management

The temperature is adjusted thanks to a controlled heating plate. While the measurement is carried out by type K thermocouple placed on the heating plate and on

the sample. As all the glasses samples are quite high (around 8 mm ± 0.3 mm) we can easily highlight the temperature gradient over the glass under test. As detailed in Fig. 105.a), the white light probe beam is as close as possible to the top of the sample. So, we define the setpoint temperature as the temperature on the top of the sample. For the temperature measurements, we associated with each sample under test another N-BK7 sample of a similar height and on which we placed a thermocouple (right sample in Fig. 104). In order to avoid variations in ambient temperature, we used the hot plate for all the measurements and we set the low temperature to 30°C. We made irradiations up to 80°C because it is the highest temperature level than the CAMRAD's camera may have to handle. The temperature was set at least 30 minutes before the irradiation start to avoid temperature variation during the irradiation. An example of the temperature evolution overall an irradiation run is reported in Fig. 105. During the 5 hours of the experiment, the temperature at top surface of the reference sample fluctuates by no more than 2°C see Fig. 105.a). One part is probably caused by the heating of the irradiation chamber during the irradiation Fig. 105.b) and one smaller part by the irradiation itself.

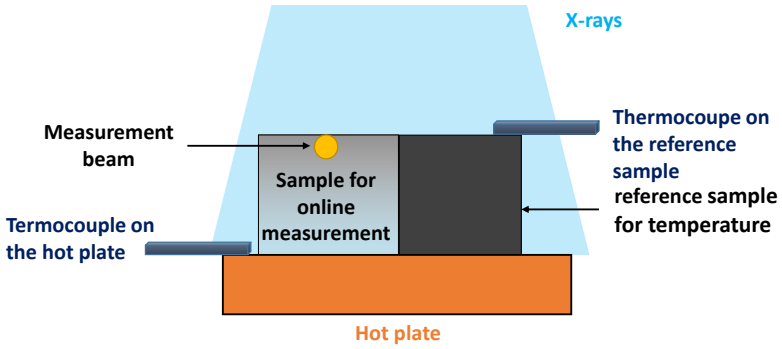

Fig. 104: Schematic representation of the side view of the irradiation set-up, with the hotplate and the temperature control set-up. All experiments were made in this configuration

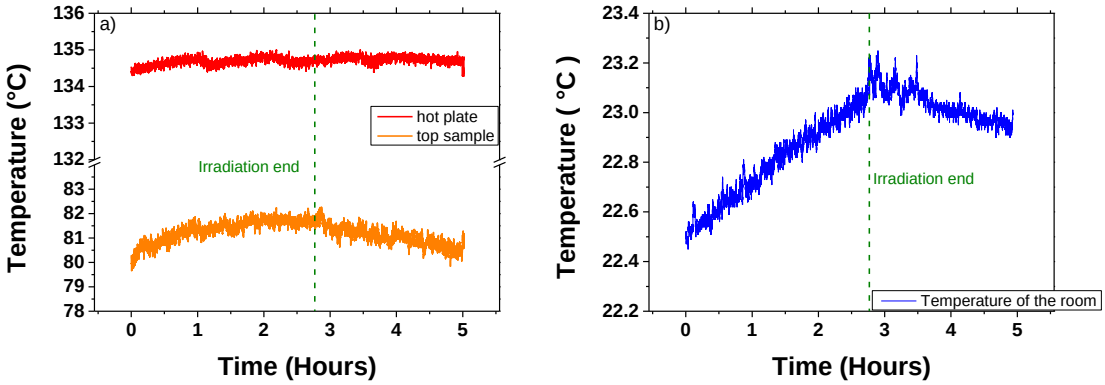

Fig. 105: a) Temperature of the hotplate and on the top of the reference sample, b) Temperature of the room, during the irradiation of N-BK7 at 80°C (dose rate 10 Gy/s)

C.2.5.3 X-Ray penetration depth and dose

Our irradiation machine produces low energy X-rays. So, penetration depth in silica-based materials could be a real issue. There will therefore be a gradient of the deposited dose over time. In order to highlight this effect, we recorded the response, at different doses, on N-BK7. Consequently, the RIA spectra will be affected. If we define a zone, on the top part of the sample, via a circle spot with a diameter of 2 mm (which corresponds to the maximum size of the probe light beam) as shown in the Fig. 106, we easily highlight the RIA evolution over the time therefore during irradiation.

For our measurements it implies that measured kinetics are growing slightly slower than real ones because the measurement is an average between glass layers irradiated at different doses with a different X-ray spectrum (the spectrum is modified by the glass absorption). So, all the following doses are the one deposed in the top of the sample measured with a dosimeter (*soft X-ray chamber TN23344W*) from PTW. Nevertheless, at high doses (depending on the recovery rate) this measurement is still much more representative of the application needs than gamma irradiation followed by post mortem measurements (see C.2.5.7).

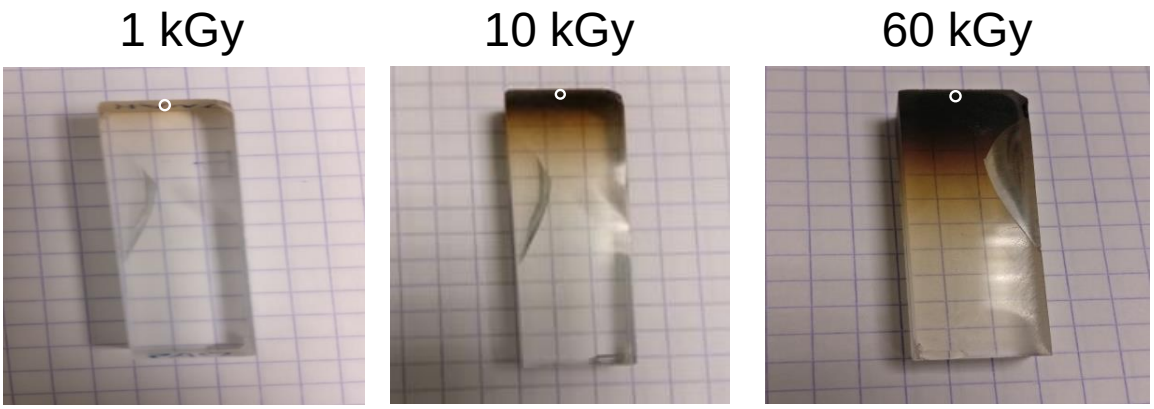

Fig. 106: Evolution of the RIA at different doses in N-BK7. White circles are the probe beam positions at 1:1 scale (for a diameter of 0.1 mm).

C.2.5.4 Validation of the RIA measurement

In order to validate this RIA measurement, we irradiated a N-BK7 sample and monitored its RIA both during irradiation up to 100 kGy cumulated dose and for 1.5 hours after the irradiation stops. After that, we removed the sample from the irradiation chamber and performed RIA measurements (at the same position as the online one) following the usual procedure with a *Carry 5000* spectrophotometer. The comparison between the two RIA spectra, reported in Fig. 107, shows that the two setups give very similar RIA spectral responses. The small discrepancy could be explained by a larger time (18 h for the post-mortem measurement instead of 1.5 h) for recovery allowed to the sample before the *Carry 5000* measurement. Similar results have been obtained for other glasses and one with a longer recovery time is reported in [19]. These comparisons validate both our procedure and setup.

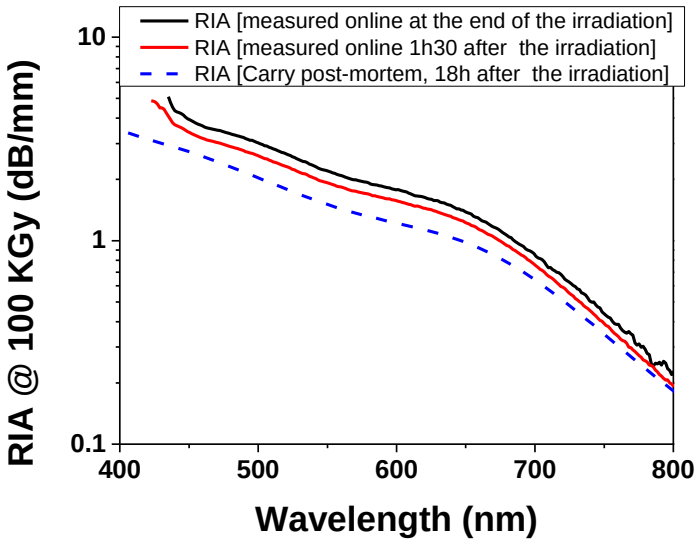

Fig. 107: Comparison between the spectral dependence of the RIA measured for N-BK7 glass by the setup at the end of the irradiation, 1h30 after the end of the X-ray irradiation and with the Carry 5000 spectrophotometer from Agilent

To check the repeatability, we performed 2 irradiation runs in the same conditions (30°C and 50 Gy/s) for each sample, one up to 0.1 MGy and the other up to 1 MGy cumulated doses respectively. We show in Fig. 108 the results obtained for the two N-BK7 samples. Both on kinetics and spectral dependence we have a good repeatability. This completes the validation process for the RIA measurements.

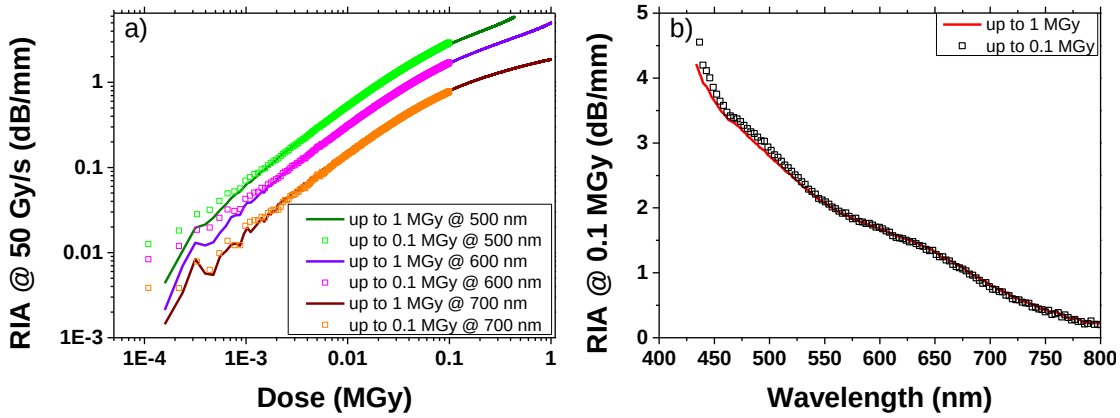

Fig. 108: a) Comparison between RIA growth kinetics at selected wavelengths of two N-BK7 samples, one X-ray irradiated up to 0.1 MGy and another irradiated up to 1 MGy (dose rate is set to 50 Gy/s and temperature 30°C). b) Comparison between RIA spectral dependence @ 0.1 MGy from one N-BK7 X-ray irradiation up to 0.1 MGy and one up to 1 MGy (dose rate of 50 Gy/s and temperature 30°C)

C.2.5.5 Effect of radiation on the set up

To deport the optical signal from the irradiation chamber to the measuring instruments (located outside the irradiation zone), we used so-called transport optical fibers, the part of which placed in the irradiation chamber is located outside the X-ray field. Even if they are hardened optical fibers and they are not directly exposed to X-rays, they will be affected by RIA. To quantify radiation effects on this part of the set-up, we proceeded to sample-free RIA measurements to assess the instrumental responses of our experience. Doses given below are those located at the sample top-position. The corresponding results are reported in Fig. 109.

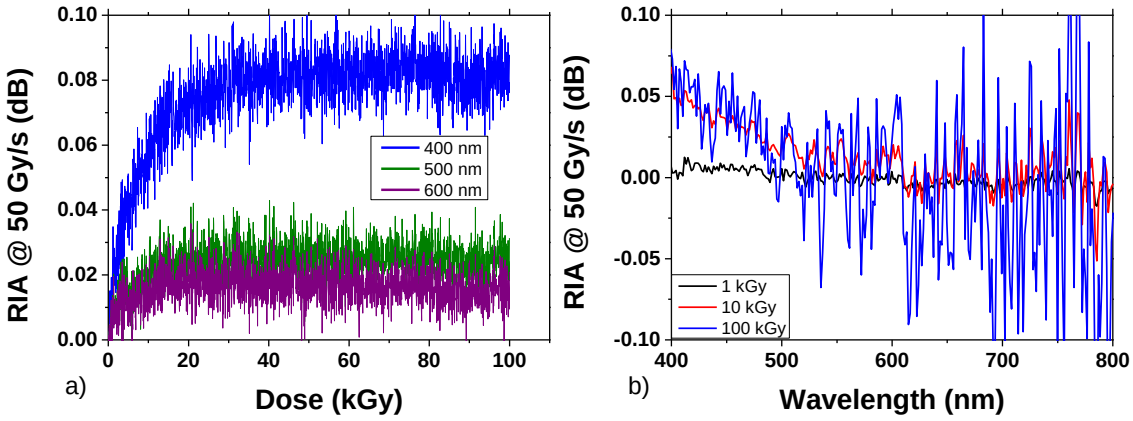

Fig. 109: a) RIA growth kinetics of the setup at some selected wavelengths during a X-ray irradiation run at a dose rate of ~50 Gy/s up to a cumulative dose of 0.1 MGy(SiO2). b) RIA spectral dependence of the setup only at some irradiation doses (dose rate of ~50 Gy/s, 30°C

Between 400 and 500 nm there is a measurable RIA which saturates after 40 kGy. At higher wavelength the attenuation is in the noise level. Fig. 110 shows the dose rate effect on the setup attenuation after its saturation. At a dose rate of 10 Gy/s the residual RIA is relatively low over the entire studied spectral range.

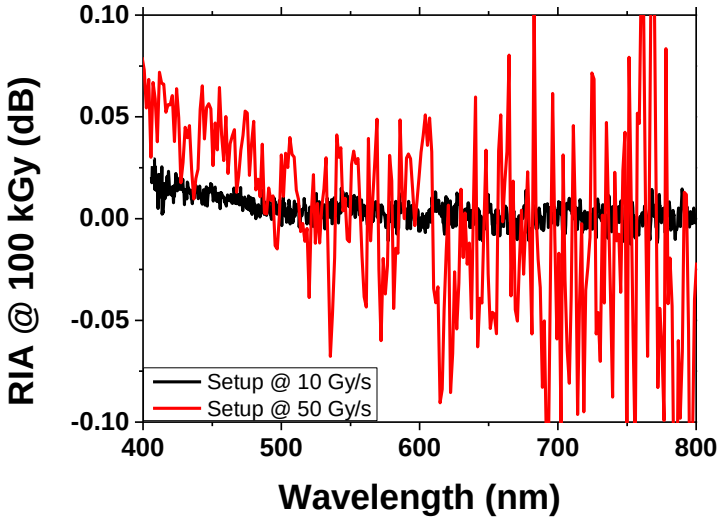

Fig. 110: RIA spectral dependence of the setup at an irradiation dose of 100 kGy(SiO_2) (for two different dose rates: 10 Gy/s and 50 Gy/s).

The RIA levels without sample can be compared to the measurements obtained, under the same irradiation conditions on a sample, here the BK7G18 rad-hard glass. We did this measurement at 10 and 50 Gy/s, see Fig. 111. This case is not representative of all the glasses, but it demonstrates that even for a glass with a low RIA and a thickness ≈ 9.3 mm, the so called 'set-up RIA response' is quite low.

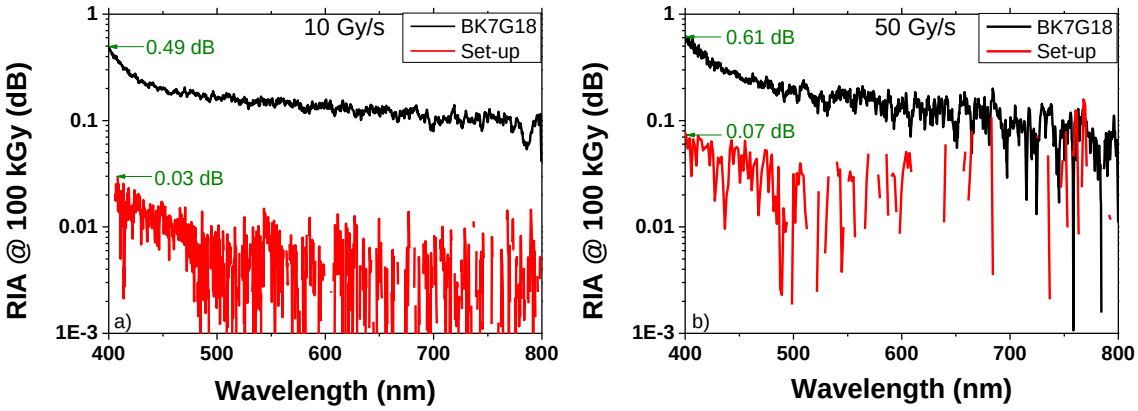

Fig. 111: Spectral RIA responses at a cumulative X-ray dose of 100 kGy on set-up (with no sample) and BK7G18 glass. A) dose rate: 10Gy/s b) dose rate:50 Gy/s

C.2.5.6 Effect of the probing light on the RIA

To evaluate if our measurement causes any photobleaching (continuous presence of probe optical beam during the entire irradiation duration) we used a third sample as shown in Fig. 112. The sample in the middle is not enlightened and it is exposed to the same dose than the one under test. At the end of the experiment we did a post-mortem measure of both samples. If the probe had bleached the sample under test, its RIA will be lower than the non-enlightened one. Result is shown in Fig. 113, there is no difference between both RIA responses, so our probe optical signal does not induce a photobleaching effect.

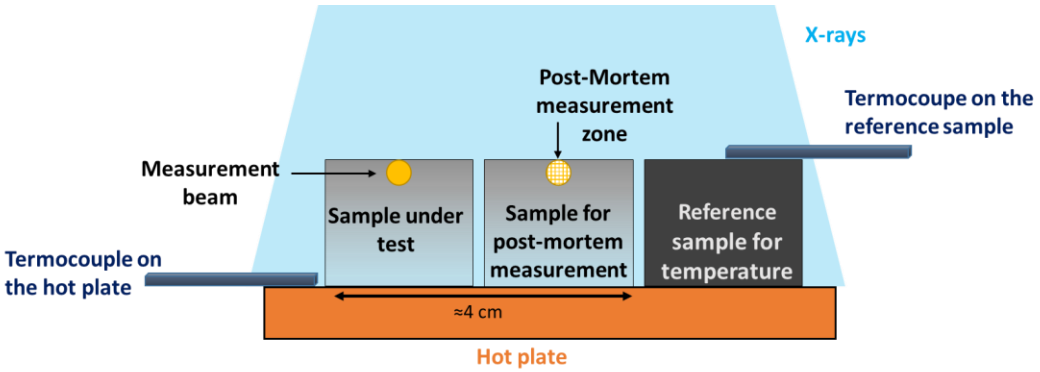

Fig. 112: Irradiation set-up to measure the influence of optical bleaching on the RIA, view at the exit faces of the samples.

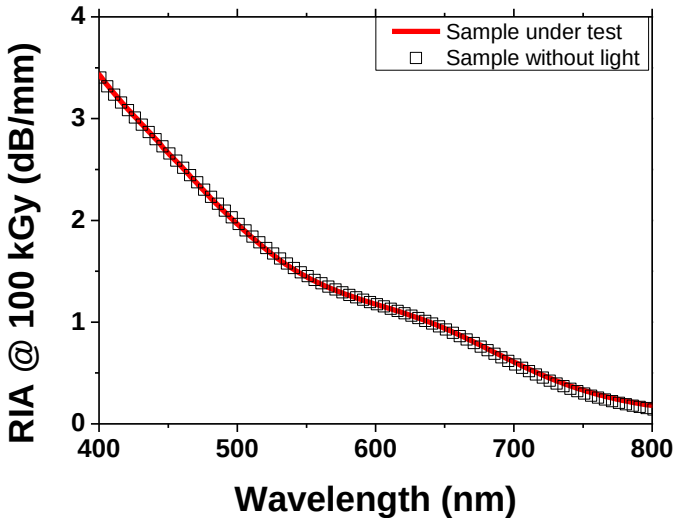

Fig. 113: Comparison of the post-mortem RIA between N-BK7 sample under test (enlightened during the entire irradaition run) and the one for post mortem measurement (not enlightened) @ 100 kGy (dose rate: 10 Gy/s).

C.2.5.7 Gamma irradiation responses and comparison with the X-Rays

However, the final objective of this study is to develop a hardened camera which will be subjected to different harsh environments and in particular to gamma irradiations which are not affected by the penetration depth issue that I have highlighted previously. So, we carried out some gamma-irradiation experiments on our samples and we compare online X-ray and post-mortem γ-ray RIA results. As both tests were performed at different conditions with mainly different dose rates, we wanted to verify the global tendency responses.

Fig. 114.a) show RIA spectrum measured at the same doses for N-BK7 irradiated with gamma ray at the SCK-CEN [150] and online measurement under X-ray. At 0.1 MGy, the RIA level measured in the X-ray irradiated sample is 0.7 time (Fig. 114.b) the one of the same glass under gamma irradiation. At the two higher doses, the online measurement gives RIA levels respectively ≈1.4 and ≈1.6 times higher than the gamma irradiated ones (Fig. 114.b). Because of the spot size we need a certain dose before being able to correctly measure the RIA but after this dose (that differs probably for each glass type) our method is better than the post-mortem one because we are not affected by the post irradiation recovery.

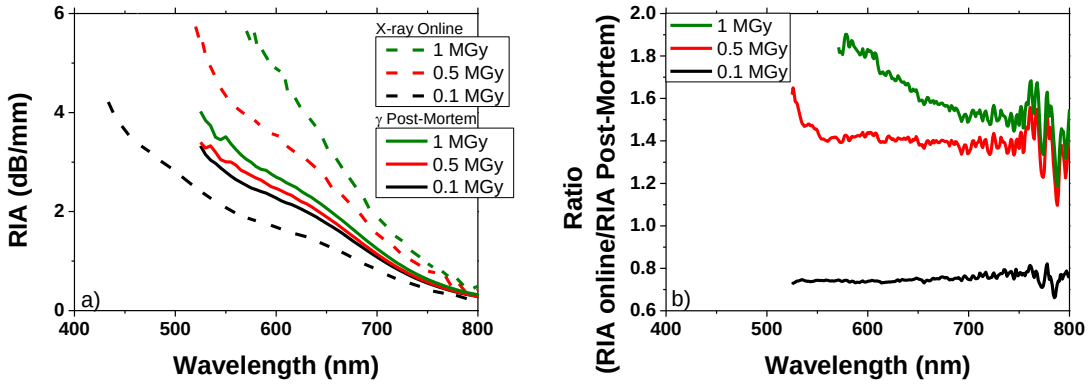

Fig. 114: a) Comparison between the RIA responses of N-BK7 irradiated at the same doses with gamma rays (Post-mortem measurement) or with X-rays (online measurement) b) Ratio between both RIA (RIAX/RIAγ)

As it was done for optical fibers [151], it is important to see if the same absorption bands are generated independently of the photons energies. So Fig. 115 compares the normalized RIA spectra of N-BK7 acquired on samples irradiated at similar doses with

either X-rays or gamma rays. Both spectra have nearly the same profile, only a small difference is noticed around ≈650 nm. This supports that as for optical fibers, the two radiation types cause similar defects and RIA levels [151].

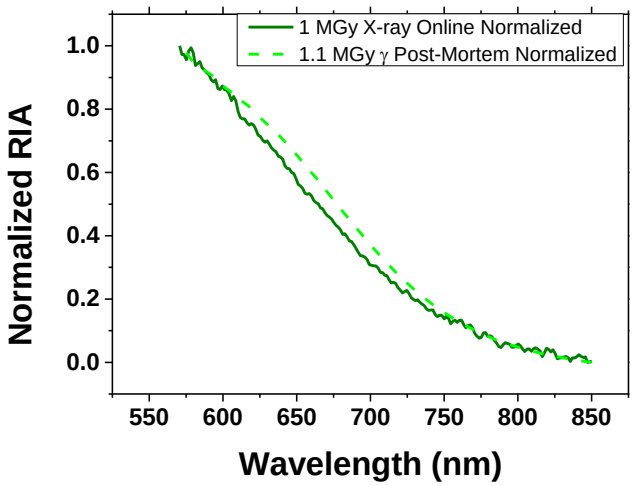

Fig. 115: Comparison between RIA N-BK7 normalized spectrum irradiated with X-ray or gamma rays.

C.2.5.8 Limitations & possible improvements

We describe the setup, discussed the limitations associated with the use of X-rays (especially their penetration depth at low energy) and explain how we evaluate the dose deposited in the sample under test. We demonstrate that the setup only slightly degrade the measurement and we validated the experimental procedure by comparing it with the most conventional based-spectrophotometer technique. Finally, we verified that our system (permanent illumination of the sample during the entire irradiation run) do not induce any photobleaching effect and we showed that RIA caused by X-rays or gamma rays are similar.

Now we will discuss the limitation and the possible improvement of this technique. This technique is valid as long as the analysis is done close to the upper surface of the sample. The higher error risk comes from the beam position relatively to the sample top. It may cause an error which depends on the experimenter, the sample quality and cannot be estimated with only one measurement. With the chosen set of experiments, we can estimate it only with the repetition of the measurement in the same conditions (as runs 50*short* and 50*long*). The worst measured case was for the SF6G05, see in Fig. 116 the

error on both kinetics and spectrum. The fact that this glass had more than 70% of lead in its composition, made every beam positioning difference visible.

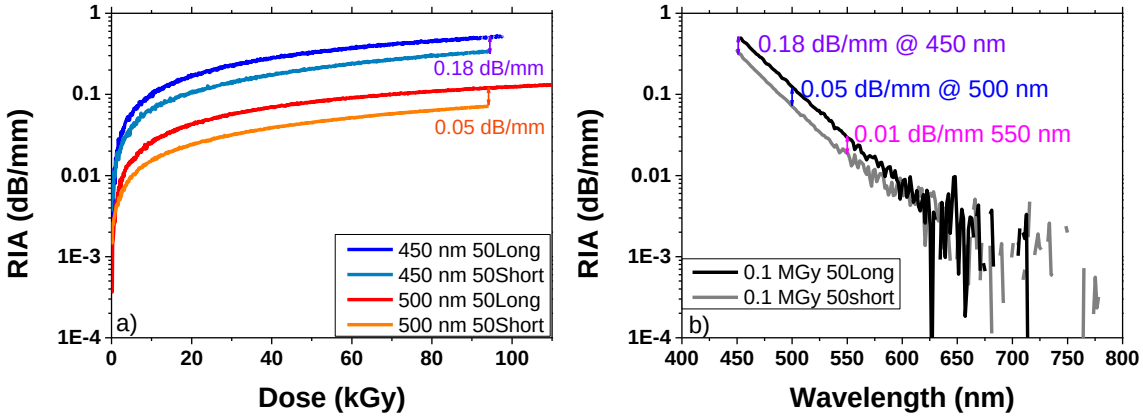

Fig. 116: a) RIA kinetic vs the cumulative X-ray dose for SF6G05 for the two irradiations at 50 Gy/s. b) RIA spectrum of SF6G05 for the two irradiations at 50 Gy/s after 0.1 MGy.

So from our test set on radiation hardened glasses we can tell that no measurement shows a difference higher than 0.18 dB/mm. To finish this section, we want to propose some improvements that we did not have the time to realize during this PhD thesis:

- A monitoring line to remove both source fluctuation and setup RIA of the result. A possibility will be to use a bifurcated optical fiber (as the Qbif from Ocean Insight [152]).
- A sample holder that will allow better control of the beam position relatively to the sample's top. It may let the beam pass through a hole smaller than the beam (like a line of 500 µm high) to exchange a part of the measurement dynamic with a better dose accuracy.

Conclusion Section C.2

In this chapter, we gave all information about samples and irradiation conditions. Then we explain the three optical techniques used to measure both RIRIC and RIA.

We made a focus on the designed setup for online RIA measurement in bulk glasses. After a description of the setup, we validated it by comparison with post-mortem measurements that are the usual method for RIA measurement in glasses. Then we demonstrated that the RIA in the optical lead-in and read-out part of the setup are

negligible. Even with the lower penetration depth of X-rays compared to gamma rays, this method allows measuring more accurately the RIA because it is not affected by the recovery time. Our setup has limitations especially because of the probe size and its position. These limitations can be overcome with a future improvement of the setup.

C.3. Radiation responses of optical glasses

This chapter will present first our preliminary results of the Radiation-Induced Refractive-Index Change (RIRIC) in three glasses. Then we will detail the effect of dose, dose rate and temperature on the RIA growth and decay kinetics in each of the investigated SCHOTT radiation hardened glasses in the framework of CAMRAD. Finally, the last part of this chapter will be devoted to an original study (*that leads to one UJM/ANDRA/Optsys patent in 2019* [14]) about the feasibility to conceive high dose radiation tolerant color optical systems using only standard not Ce-doped optical glasses.

C.3.1. Radiation-induced refractive-index change results

We measured the RIRIC in three different optical glasses after two irradiation runs performed at the SCK-CEN[7] in Mol [150] up to the dose of 1.1 MGy(SiO_2). Main obtained results are summarized in Fig. 117 that illustrates how the RIRIC depends on the operation wavelength. The two radiation-hardened glasses (SUPRASIL and K5G20) exhibit RIRIC higher than 6×10^{-4} at this dose level. For the SUPRASIL glass, the RIRIC is larger than -5×10^{-4} in the lower part of the visible range. For the N-BK7, the radiation sensitive glass (in terms of RIA), there is nearly no more RIRIC increase after a total dose of 0.4 MGy, in agreement with the behavior observed for the RIA of standard glasses that also tends to saturate at larger irradiation doses [19]. For K5G20, the RIRIC modification at the two doses appears larger. For the SUPRASIL pure silica characterized by very low RIA, this modification of the refractive index could be attributed to a slight modification of the glass density rather than to the excess of attenuation caused by radiations as it happened in [88] or a huge band in the UV. Indeed, RIRIC is usually considered as the result of two modifications: density change and RIA (through Kramer–Krönig relation). These two modifications are somehow linked and there is no

[7] This work was supported by Fusion for Energy under specific Contract F4E-OMF-272-01-18 and Contract F4E-OFC-358-2-01-01.

consensus about the relative contributions of these effects in our dose range. Furthermore, the resulting RIRIC may be either positive or negative [88], [153]. To better understand the RIRIC origins, those experiments should be complemented with density change measurements and ideally high-precision spectral measurements of RIA in the UV domain. For the Cerium-doped glasses such measurement is prevented by the Cerium-induced attenuation below 500 nm and for the N-BK7 case, the numerous impurities also prevent it, causing too high intrinsic attenuation levels. Gusarov et al. [73] attributed the observed positive variation of the refractive index to a side effect of Cerium codoping of the glass. Compositions of N-BK7 and other doped silica glasses are only partially known and remain too complex to allow identifying the point defects responsible for the RIA and RIRIC. During the PhD, we did not succeed in measuring RIRIC in the other radiation hardened glasses with the refractometer available at LabHC due to the limitations of this commercial setup. This effect and its impact have then been systematically investigated through Zemax optical simulations in the framework of the PhD of Cyprien Muller [15].

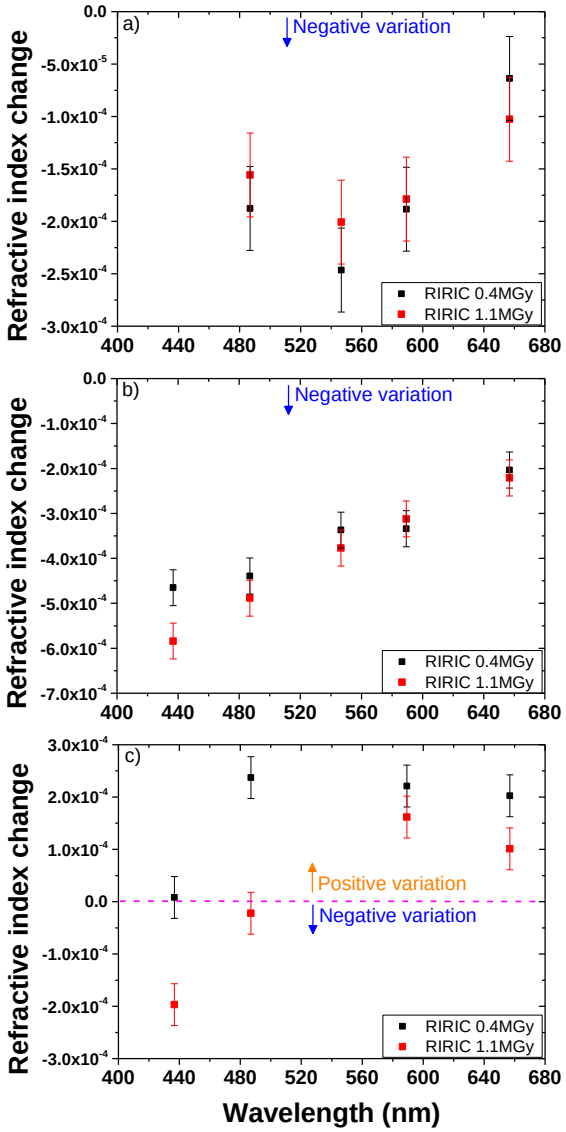

Fig. 117: RIRIC spectral dependence in gamma-irradiated glasses at 0.4 and 1.1 MGy, a) N-BK7, b) Suprasil, c) K5G20

C.3.2. Online RIA of radiation hardened glasses up to 1 MGy and its dose rate & temperature dependence

For the characterization of each investigated glass, we followed the same testing procedure to perform an investigation as systematic as possible:

- **Spectral RIA growth up to a cumulative dose of 1 MGy(SiO_2) (**at a dose rate of **50 Gy/s** under a fixed temperature of **30°C)** followed by a one-hour post irradiation phase**.** These accelerated tests give a worst-case evaluation of the RIA growth with

dose as well as the potential recovery of the glasses that could occur during maintenance phase (radiations OFF) of the CAMRAD camera.

- **Investigation of the dose rate effects (1.2, 10 & 50 Gy/s) on the RIA growth and recovery kinetics**. These tests allow estimating how the accelerated tests represent a worst case for the CAMRAD applications that will be probably associated to lower dose rate than **1.2 Gy/s**

- **Temperature effect (30, 50, 80°C) on the RIA growth and recovery kinetics.** As the CAMRAD camera should be able to operate in relatively hot environments (up to **80°C**), it is interesting to verify the temperature dependence of the RIA. Furthermore, it gives information on the potential recovery that could be achieved on the optical system by applying a thermal treatment at moderate temperatures.

We will focus our presentation of the results on the RIA kinetics at 425 nm as this wavelength is usually affected by the largest RIA level and corresponds to the lowest wavelength of interest for white LEDs (blue domain). Consequently, the presented results give a worse case estimation of the RIA for the optical glasses used for the CAMRAD optical system, the RIA at higher wavelengths will then be lower than the ones presented here. In the particular case of the SF6G05 glass, because of its very high intrinsic attenuation at 425 nm, we consider its RIA at 550 nm. Its intrinsic absorbance leads to a yellowish color compared to the yellow shade of other Cerium doped glasses (see Fig. 118). The results for each glass are briefly described and then discussed.

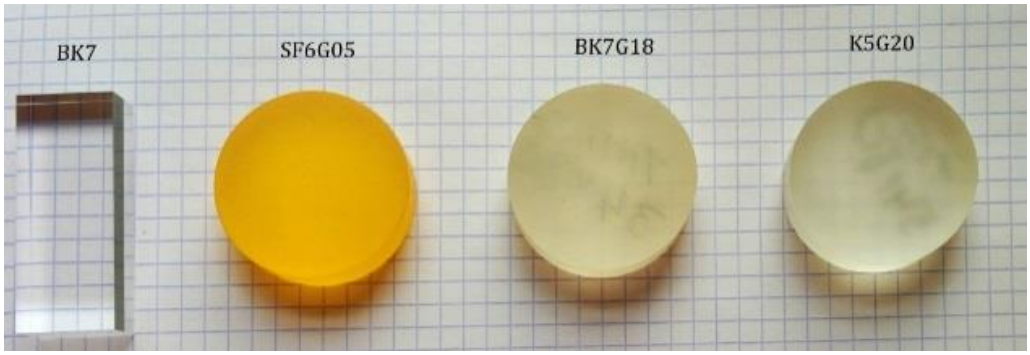

Fig. 118: Picture of some pristine optical glasses

Some of the experiments were not usable, which are then excluded from this manuscript. It was not possible to reproduce them before the PhD thesis end but the experiments should be reconducted in the future. Those bias are attributed to experimental setup malfunction or either to error in the setting of the glass sample for an experimental run. For these reasons, the following results are missing: BK7G18 **1.2** Gy/s / **50**°C / **80**°C as well as K5G20 **50**°C measurements. It may present some differences between spectral data at **50** Gy/s such as Fig. 119 (**50Long** up to 1 MGy) and RIA kinetics at **50** Gy/s (**50Long** up to 0.1 kGy) as Fig. 120 because they did not come from the same data set as it is detailed in C.2.5.8.

C.3.2.1 BK7G18

The online RIA experimental results obtained for the BK7G18 glass from SCHOTT are summarized in Fig. 119 and Fig. 120. Fig. 119.a) gives the RIA spectra at various doses from 1 to 1000 kGy(SiO_2) while Fig. 119.b) shows the recovery of the RIA spectra during the post-irradiation hour. Fig. 120 illustrates the RIA growth and decay kinetics at 425 nm in this glass and compares the kinetics at three different dose rates: **2.5** Gy/s, **10** Gy/s and **50** Gy/s.

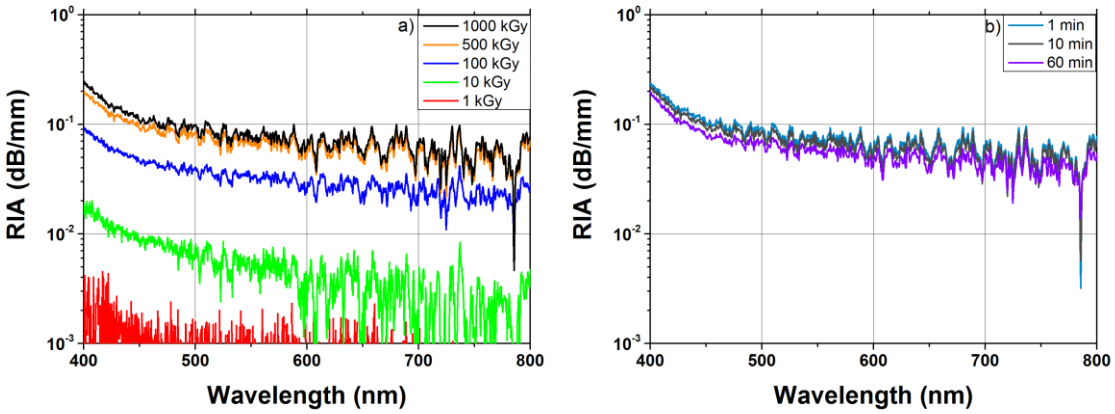

Fig. 119: BK7G18 sample, a) RIA spectral dependence versus the accumulated dose and b) its spectral recovery response after X-ray irradiation up to 1 MGy (50 Gy/s)

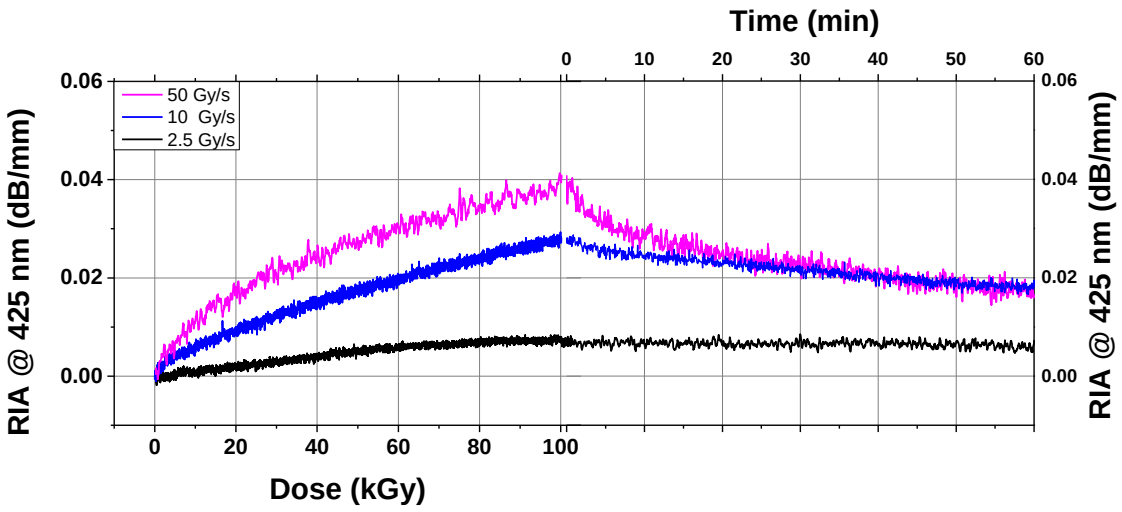

Fig. 120: BK7G18, RIA kinetics (growth and recovery) for three dose rates (2.5, 10 and 50 Gy/s) up to 0.1 MGy to 0.1 MGy

Several points should be highlighted about our characterization of this glass. First the kinetic measured at **1.2** Gy/s was affected by too strong fluctuations of the white light source, so we replaced it with the one at **2.5** Gy/s that is coherent with the two higher dose rates. Second, the BK7G18 was the first glass that we tested in temperature in this set of experiments. We faced some troubles of noise and an experimental failure due to the temperature. That made the results of both experiments at **50** and **80**°C useless and they should be repeated in the future. From the acquired data we can say that:

- **Fig. 119**: For the higher dose rate, the BK7G18 spectral RIA at 425 nm saturates after 500 kGy, typically below 0.2 dB/mm
- **Fig. 120**: Increasing the dose rate increases the RIA level at 425 nm as well as the glass recovery rate after 1 hour: **2.5** Gy/s: 14 % / **10** Gy/s: 30 % / **50** Gy/s: 43 %.
- **Fig. 120**: At the three dose rates, the RIA seems to converge during the recovery phase same RIA permanent level, around 0.01 dB/mm at room temperature.

An important point regarding this characterization is that the RIA remains low for this batch of BK7G18[8] with typical levels below 0.05 dB/mm (0.5 dB/cm) at low wavelengths for doses up to 100 kGy. However, we cannot recommend the use of this glass as it seems that its radiation response greatly changed from one production batch to another

[8] During the PhD thesis, two different batches of BK7G18 have been acquired from SCHOTT (refs D105 903 4A and TNA 3400 8C) and tested under irradiation. By comparing the radiation responses of these two glasses, very different radiation responses have been observed (see [19] for results on the other batch) showing a bad radiation hardness assurance quality for this reference.

as presented in Fig. 121. This figure compare the online RIA of the BK7G18 tested in this thesis again the one of the BK7G18 used in [19].

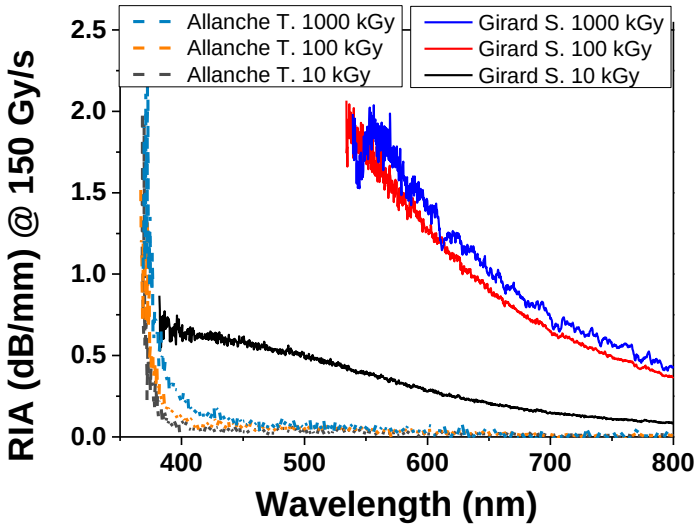

Fig. 121 : RIA spectral dependence versus the accumulated dose for two different batches of BK7G18. "Allanche T." refer to the BK7G18 batch number D105 903 (@ 30°C), "Girard S." refer to the BK7G18 batch number TNA 3400 8C tested in [19] (@ room temperature).

C.3.2.2 F2G12

The online RIA experimental results for the F2G12 glass from SCHOTT are summarized in Fig. 122 to Fig. 124. Fig. 122.a) gives the RIA spectra at various doses from 1 to 1000 kGy(SiO_2) while Fig. 122.b) shows the recovery of the RIA spectra during the first post-irradiation hour. Fig. 123 illustrates the RIA growth and decay kinetics at 425 nm in this glass and compares that kinetics at three different dose rates: **1.2** Gy/s, **10** Gy/s and **50** Gy/s. Fig. 124 shows the influence of the temperature on the RIA growth and decay kinetics at the same wavelength.

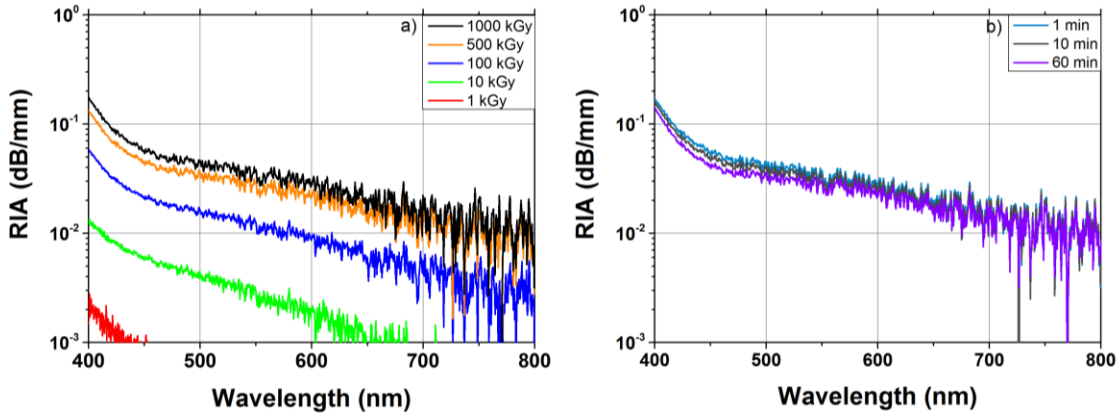

Fig. 122: F2G12 sample, a) RIA spectral dependence versus the accumulated dose and b) its spectral recovery response after X-ray irradiation up to 1 MGy (50 Gy/s)

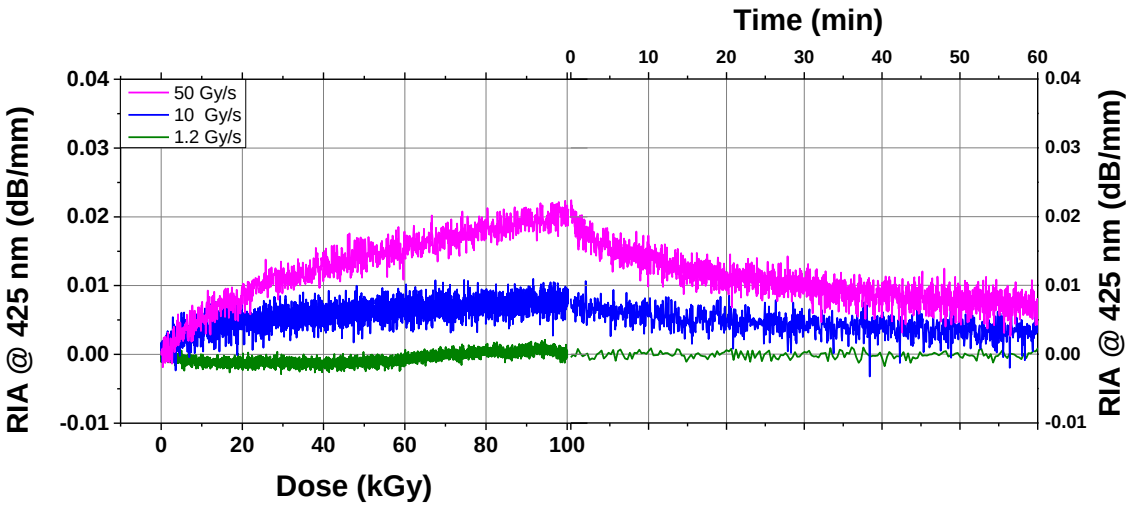

Fig. 123: F2G12, RIA kinetics (growth and recovery) for three dose rates (1.2, 10, 50 Gy/s) up to 0.1 MGy at room temperature

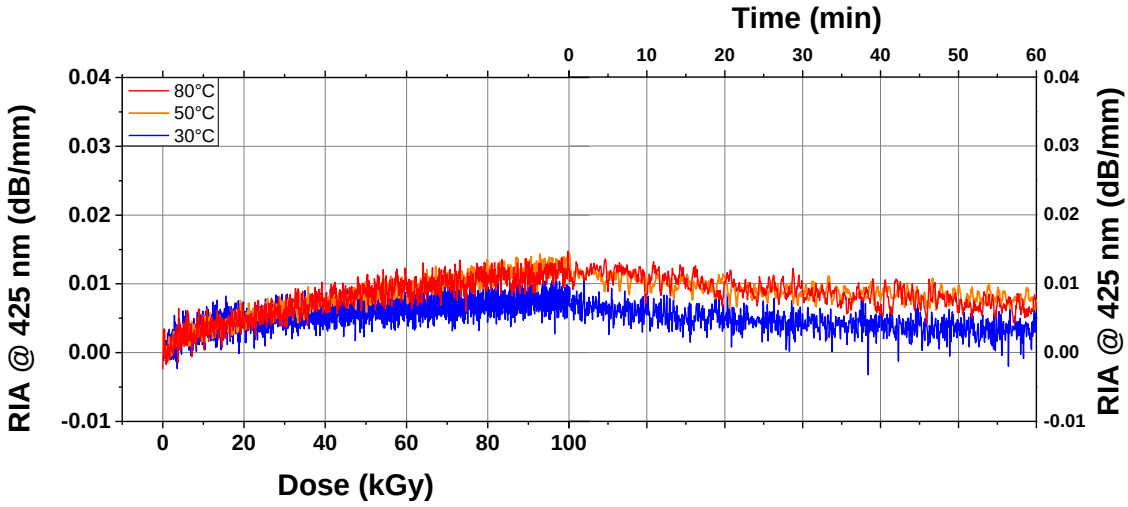

Fig. 124: F2G12, RIA kinetics (growth and recovery) for three temperatures (30°C, 50°C and 80°C) up to 0.1 MGy at 10 Gy/s

From the acquired data we can deduce:

- **Fig. 122**: For the higher dose rate, the F2G12 spectral RIA tends to saturate above 500 kGy, typically below 0.1 dB/mm that represents a very low RIA value.
- **Fig. 123**: Increasing the dose rate increases the RIA level at 425 nm in the investigated dose range. As a consequence, the obtained RIA values are worst case for application associated with dose rates below 1 Gy/s. At such low dose rate, the RIA is indeed too low to be accurately evaluated with our experimental setup
- **Fig. 123**: At the three dose rates, RIA seem to converge during the recovery phase to the same very low level of permanent RIA. As a consequence, increasing the dose rate increases the recovery rate after 1 hour: **1.2** Gy/s: 0 % / **10** Gy/s: 51 % / **50** Gy/s: 67 %; this is coherent with the observed RIA increase with dose rate during irradiation.
- **Fig. 124**: The temperature in the **30** to **80**°C range does not affect significantly the RIA growth and decay kinetics. As a consequence, for this glass, the RT tests are representative for the whole temperature range targeted for the CAMRAD application.

An important point regarding this characterization is that the RIA remains very low in this batch of F2G12 with RIA levels typically below 0.02 dB/mm (0.2 dB/cm) at low wavelengths for doses up to 1 MGy. It is then also a radiation hardened glass (in terms of RIA) for MGy dose applications.

C.3.2.3 K5G20

The online RIA experimental results obtained for the K5G20 glass from SCHOTT are summarized in Fig. 125 to Fig. 127. Fig. 125.a) gives the RIA spectra at various doses from 1 to 1000 kGy(SiO_2) while Fig. 125.b) shows the recovery of the RIA spectra during the first post-irradiation hour. Fig. 126 illustrates the RIA growth and decay kinetics at 425 nm in this glass and compares that kinetics at three different dose rates: **1.2** Gy/s, **10** Gy/s and **50** Gy/s. Fig. 127 shows the influence of the temperature (RT, **80**°C) on the RIA growth and decay kinetics at the same wavelength.

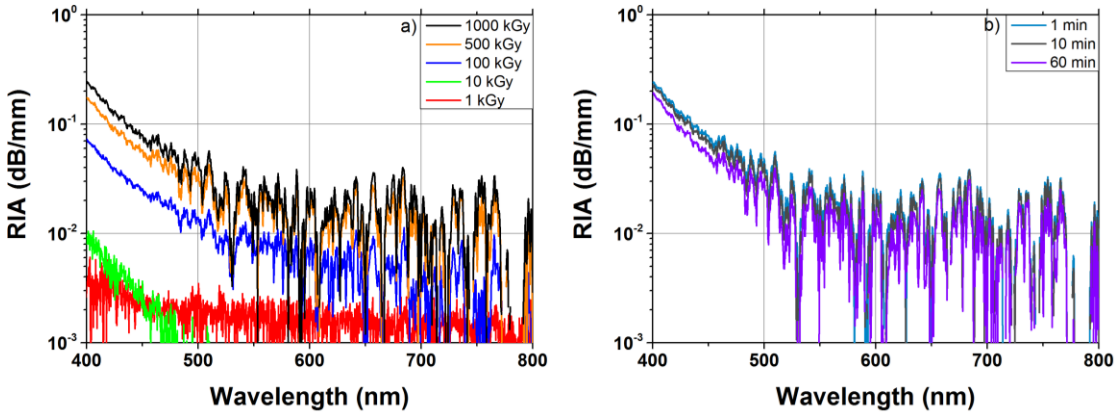

Fig. 125: K5G20 sample, a) RIA spectral dependence versus the accumulated dose and b) its spectral recovery response after X-ray irradiation up to 1 MGy (50 Gy/s)

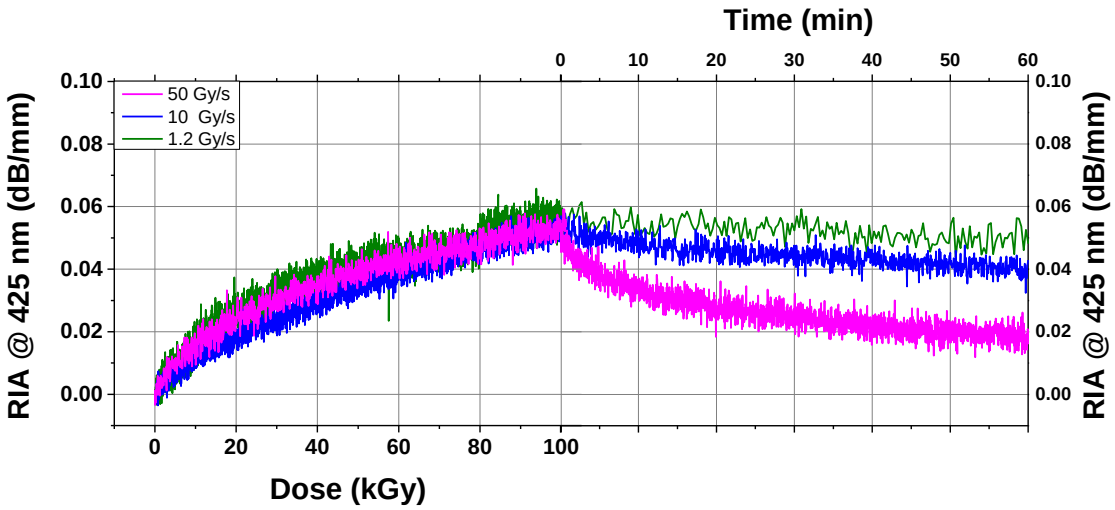

Fig. 126: K5G20, RIA kinetics (growth and recovery) for three dose rates (1.2, 10 and 50 Gy/s) up to 0.1 MGy at room temperature

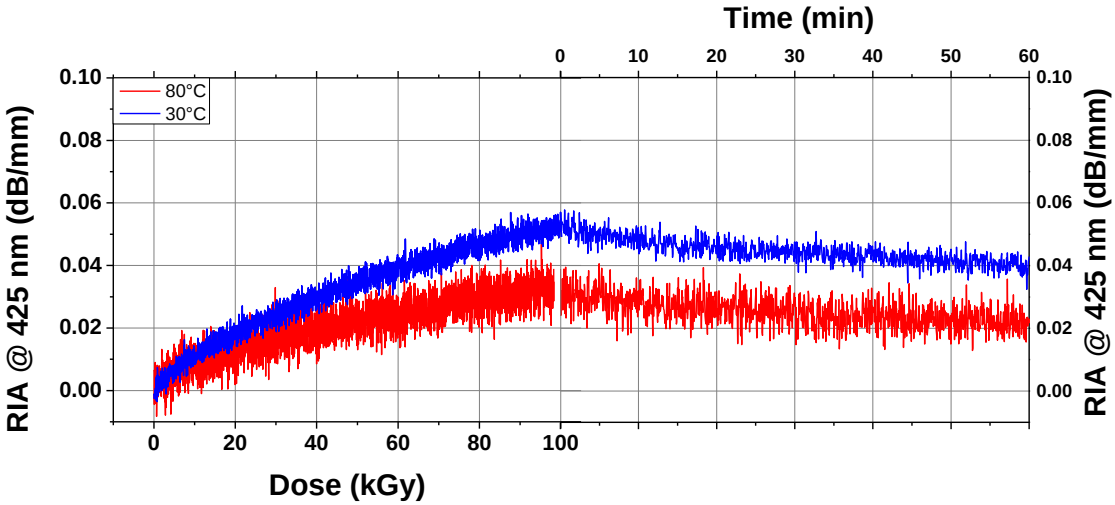

Fig. 127: K5G20, RIA kinetics (growth and recovery) for two temperatures (30°C and 80°C) up to 0.1 MGy at 10 Gy/s

From the acquired data we can deduce:

- **Fig. 125**: For the higher dose rate, the K5G20 spectral RIA saturates after 500 kGy, typically below 0.2 dB/mm that represents a very low RIA value.
- **Fig. 126**: The dose rate seems to marginally affect the RIA growth kinetics while it causes an increase of the recovery rate after 1 hour: **1.2** Gy/s: 14 % / **10** Gy/s: 27 % / **50** Gy/s: 65 %. This is a rare tendency, difficult to explain at this stage and we cannot exclude that our measurement uncertainties partially explain this behavior. As a consequence, for the 3 dose rates, RIA does not seem to converge during the recovery phase.
- **Fig. 127**: Increasing the temperature from **30**°C to **80**°C seems to decrease the RIA by a factor ×2 but a measurement at a third temperature is needed in the future to confirm this positive impact of temperature. The recovery rates after 1 hour are similar for the two tested temperatures: **80**°C: 30 % / **30**°C: 27 %.

An important point regarding this characterization is that the RIA is limited but non-negligible in this K5G20 batch with RIA levels typically below 0.2 dB/mm (2 dB/cm) at low wavelengths for doses up to 1 MGy.

C.3.2.4 LaK9G15

The online RIA experimental results obtained for the LaKG19 glass from SCHOTT are summarized in Fig. 128 to Fig. 130. Fig. 128.a) gives the RIA spectra at various doses from 1 to 1000 kGy(SiO_2) while Fig. 128.b) shows the recovery of the RIA spectra during the first post-irradiation hour. Fig. 129 illustrates the RIA growth and decay kinetics at 425 nm in this glass and compares that kinetics at three different dose rates: **1.2** Gy/s, **10** Gy/s and **50** Gy/s. Fig. 130 shows the influence of the temperature (RT, **50**°C and **80**°C) on the RIA growth and decay kinetics at the same wavelength.

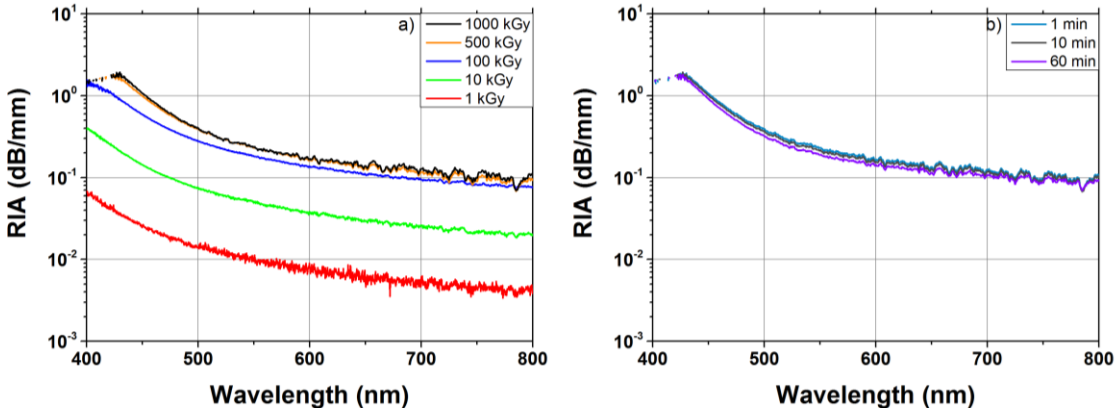

Fig. 128: LaK9G15 sample, a) RIA spectral dependence versus the accumulated dose and b) its spectral recovery response after X-ray irradiation up to 1 MGy (50 Gy/s)

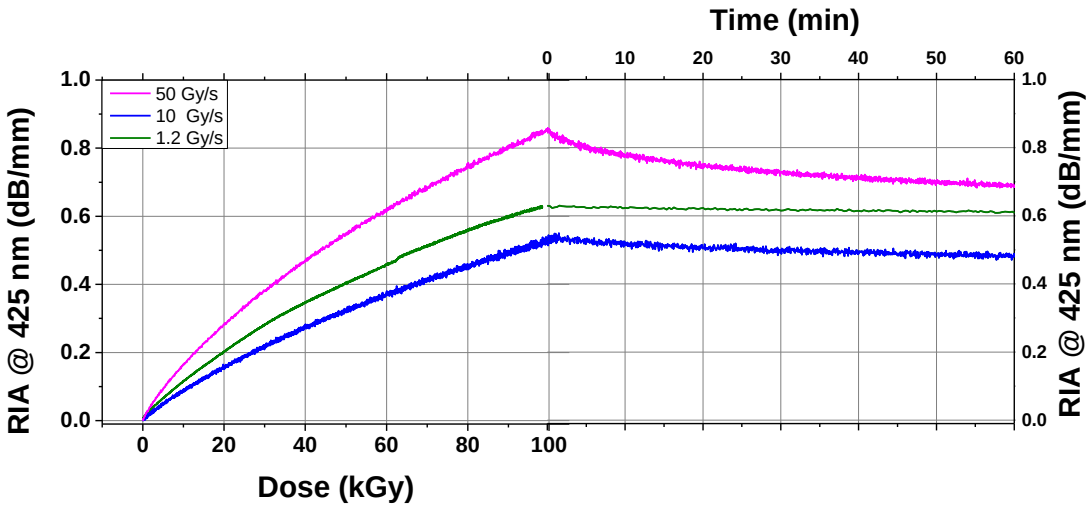

Fig. 129: LaK9G15, RIA kinetics (growth and recovery) for three dose rates (1.2 and 10, 50 Gy/s) up to 0.1 MGy at room temperature

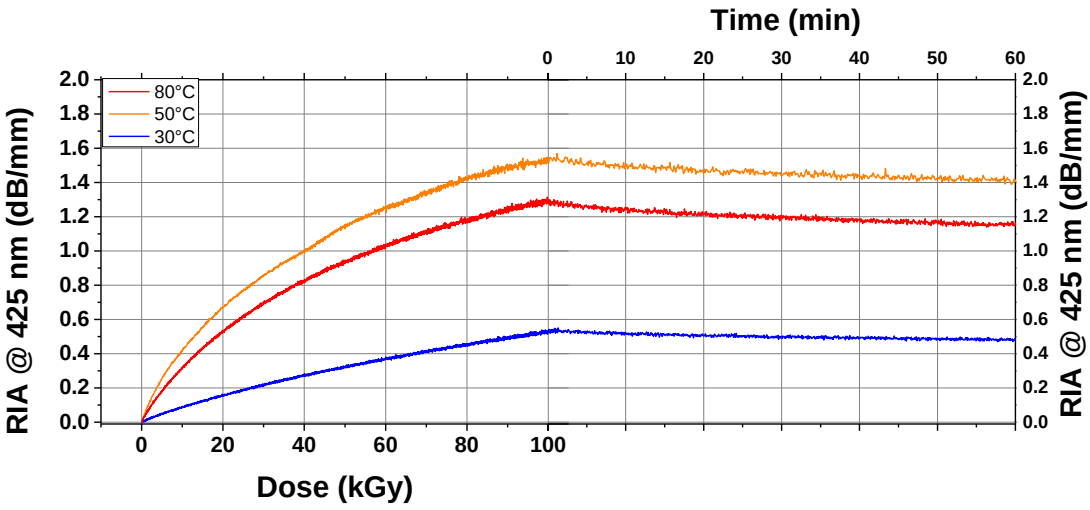

Fig. 130: LaK9G15, RIA kinetics (growth and recovery) for three temperatures (30°C, 50°C and 80°C up to 0.1 MGy at 10 Gy/s

The acquired data show that:

- **Fig. 128**: For the higher dose rate, the LaK9G15 RIA tends to saturate between 500 and 1000 kGy over the whole spectral range, but at high RIA values (typically 1 dB/mm).
- **Fig. 129**: The RIA at **10** Gy/s has the lowest growth in the dose rate experimental set but its recovery rate after 1 hour (9 %) is intermediate between the ones at **50** Gy/s (20 %) and **1.2** Gy/s (1 %). We may attribute this to dosimetry uncertainties (20%) that could lead to an underestimated RIA at **10** Gy/s. The induced losses should more probably range between the curves of the two extreme dose rates. For the three dose rates, the RIA does not seem to converge during the recovery phase.
- **Fig. 130**: So as a consequence, the **30**°C RIA kinetic (which is the same curve as the **10** Gy/s one) may also be slightly underestimated. Nevertheless, we can expect the **10** Gy/s RIA level to be between the **1.2** Gy/s and **50** Gy/s ones. Both RIA at higher temperature are stronger than the **50** Gy/s one. So, we can suggest that the temperature increases the RIA for the LaK9G15 glass. In fact, radiation tests at RT may not give the worst-case scenario in terms of RIA in this case.
- **Fig. 130**: The recovery rate after 1 hour is close for the different temperatures: **80**°C:9 % / **50**°C: 9 % / **30**°C: 9 %

An important point regarding this characterization is that the RIA is very high in this LaKG19 batch glass with typical levels up to 1 dB/mm (10 dB/cm) at low wavelengths for doses up to 1 MGy. Moreover a high RIA level was measured (at 100 kGy) in [98], so it is probably not a batch issue. This glass is then not a good candidate for the design of MGy radiation tolerant optical system of the CAMRAD camera.

C.3.2.5 LF5G19

The online RIA experimental results obtained for the LF5G19 glass from SCHOTT are summarized in Fig. 131 to Fig. 133. Fig. 131.a) gives the RIA spectra at various doses from 1 to 1000 kGy(SiO_2) while Fig. 131.b) shows the recovery of the RIA spectra during the first post-irradiation hour. Fig. 132 illustrates the RIA growth and decay kinetics at 425 nm in this glass and compares that kinetics at three different dose

rates: **1.2** Gy/s, **10** Gy/s and **50** Gy/s. Fig. 133 shows the influence of the temperature (RT, **50**°C and **80**°C) on the RIA growth and decay kinetics at the same wavelength.

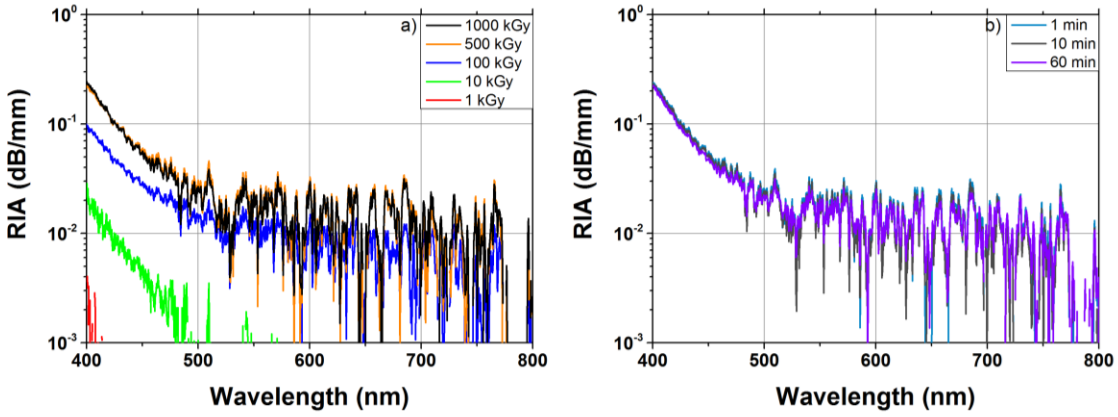

Fig. 131: LF5G19 sample, a) RIA spectral dependence versus the accumulated dose and b) its spectral recovery response after X-ray irradiation up to 1 MGy (50 Gy/s)

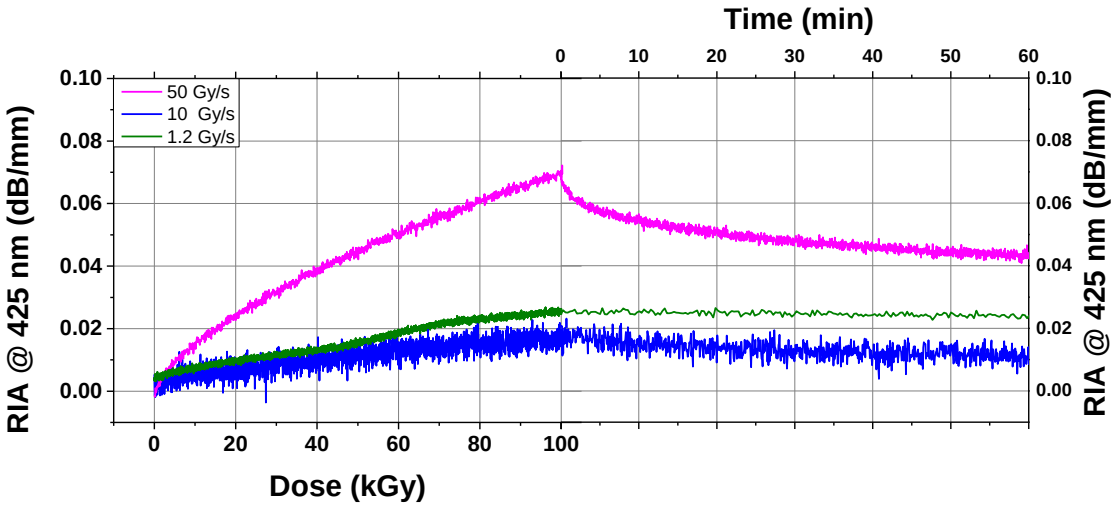

Fig. 132: LF5G19, RIA kinetics (growth and recovery) for three dose rates (1.2, 10 and 50 Gy/s) up to 0.1 MGy at room temperature

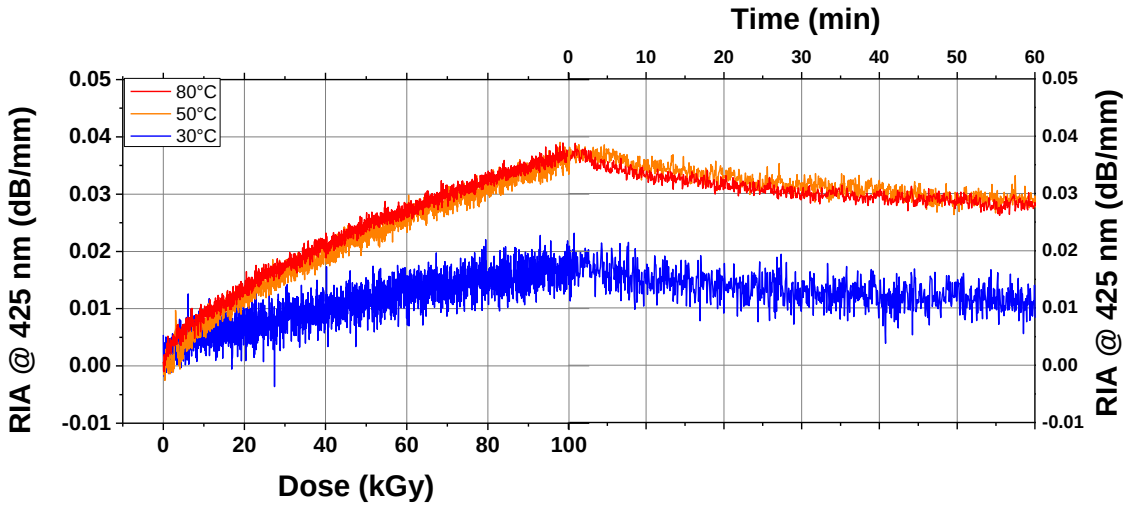

Fig. 133: LF5G19, RIA kinetics (growth and recovery) for three temperatures (30°C, 50°C and 80°C) up to 0.1 MGy at 10 Gy/s

These results highlight that:

- **Fig. 131**: For the higher dose rate, the LF5G19 spectral RIA tends to saturate between 500 and 1000 kGy with RIA levels below 0.2 dB/mm at all wavelengths at room temperature.

- **Fig. 132**: The RIA at **10** Gy/s shows the lowest growth but its recovery rate after 1 hour (38 %) is between the ones measured at **50** Gy/s (37 %) and **1.2** Gy/s (8 %). We may attribute this to the beam position (farther from the surface than for the two other experiments) leading to underestimate the **10** Gy/s RIA. So, we could consider that as usually increasing the dose rate increases the RIA level, our tests are then a worst case for applications having to operate in lower dose rate environments.

- **Fig. 133**: As a consequence, the **30**°C kinetic is probably also under evaluated for the comparison between the run results at the three temperatures of irradiation. Nevertheless, we can expect the **10** Gy/s RIA level to be between the **1.2** Gy/s and **50** Gy/s ones. In any case, the temperature effect on the RIA growth and decay kinetics seems limited.

C.3.2.6 SF6G05

The online RIA experimental results for the SG6G05 glass from SCHOTT are summarized in Fig. 134 to Fig. 136. Fig. 134.a) gives the RIA spectra at various doses

from 1 to 1000 kGy(SiO_2) while Fig. 134.b) shows the recovery of the RIA spectra during the first post-irradiation hour. Fig. 135 illustrates the RIA growth and decay kinetics at 550 nm in this glass and compares that kinetics at three different dose rates: **1.2** Gy/s, **10** Gy/s and **50** Gy/s. Fig. 136 shows the influence of the temperature (RT, **50**°C and **80**°C) on the RIA growth and decay kinetics at the same wavelength.

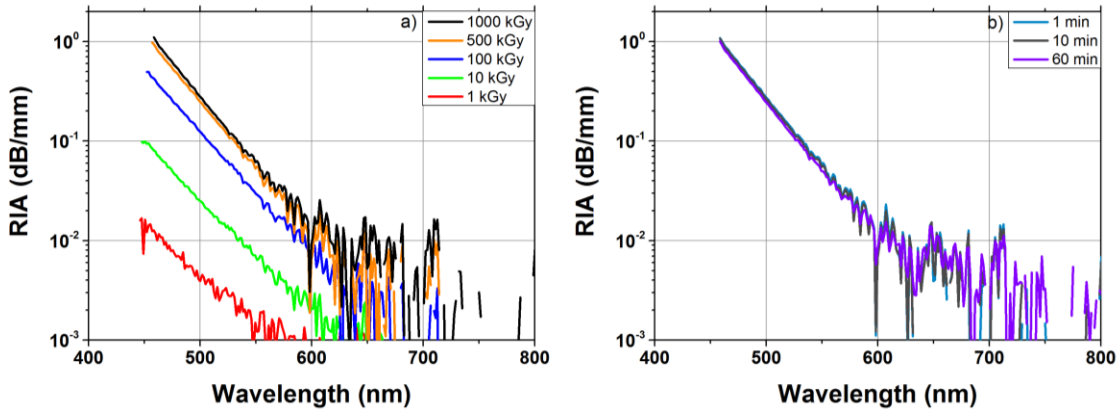

Fig. 134: SF6G05 sample, a) RIA spectral dependence versus the accumulated dose and b) its spectral recovery response after X-ray irradiation up to 1 MGy (50 Gy/s)

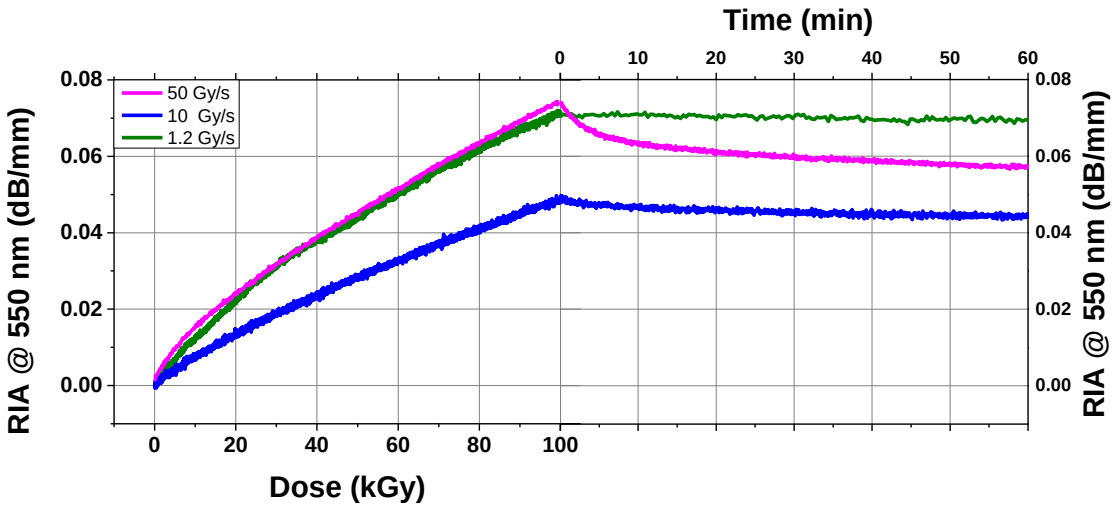

Fig. 135: SF6G05, RIA kinetics (growth and recovery) for three dose rates (1.2, 10 and 50 Gy/s) up to 0.1 MGy at room temperature at 10 Gy/s

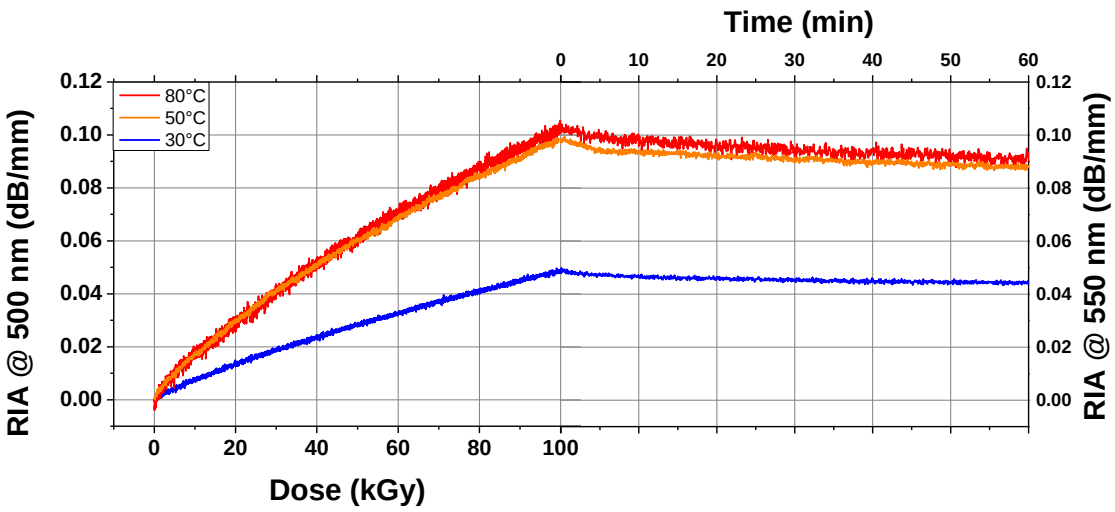

Fig. 136: SF6G05, RIA kinetics (growth and recovery) for three temperatures (30°C, 50°C and 80°C) up to 0.1 MGy

As for the other glasses, we observe that for the higher dose rate, the SF6G05 spectral RIA saturates between 500 and 1000 kGy at level as high as 1 dB/mm at 450 nm.

Fig. 135: The **10** Gy/s set of data has the lowest RIA growth in the dose rates set but its recovery rate after 1 hour (8 %) is between the one to the **50** Gy/s (22 %) and the one of the **1.2** Gy/s (3 %). In this case the beam was probably farther from the surface than for the two other experiments and we are under evaluating the **10** Gy/s RIA. For the SF6G05 it is then also probable that an increase of the dose rate increases the RIA level, but not strongly. As a consequence, the **30**°C kinetic at the same dose rate is also under evaluated. Nevertheless, we can expect the **10** Gy/s RIA level to be between the **1.2** Gy/s and **50** Gy/s ones. Both RIAs at higher temperature are stronger than the **50** Gy/s one. We can then suggest that the temperature increases the RIA for the SF6G05 as already observed for some of rad-hard glasses from SCHOTT.

C.3.2.7 Summary of online measurements

From our measurements on the six investigated SCHOTT radiation hardened glasses, we can draw the following conclusions about their potential for the CAMRAD project:

- For four of these six glasses: BK7G18, F2G12, K5G20 and LF5G19 glasses; their maximal RIA in the visible are lower than 0.25 dB/mm after 1 MGy. As a reminder

the N-BK7 has nearly 4 dB/mm @ 450 nm after the same dose. These glasses may be suitable for optical system design depending on the total thickness of their respective lenses and the camera photometry budget.

- It seems probable that for all glasses, the increase of the dose rate increases the RIA growth. From a practical point of view, as the CAMRAD tests are accelerated (higher dose rate) with respect to the expected environments for the camera, one could expect lower RIA degradation in real application cases.

- The effect of the irradiation temperature varies according to the considered glass, in a way that is impossible to predict without doing tests. From an applicative point of view, this temperature dependence needs to be considered by additional margins can during the tolerance study of the OS if no data are available.

C.3.3. Comparison between radiation hardened glasses and standard ones

As for radiation hardened glasses, the radiation response of standard (without Ce-doping) optical glasses at MGy dose level is not well documented in the open literature. As a consequence, we decided to check the validity of the hypothesis that choosing the radiation hardened glasses for the CAMRAD optical system is the best choice to limit their radiation induced darkening. We should in particular consider that the non-Cerium doped glasses (classical references) have lower intrinsic absorbance in the visible range (see Fig. 118) compared to Ce-doped glasses.

For this, we also performed online measurement on the non-radiation hardened glasses. The chosen dose rate is really important in this case, because it strongly affects the RIA of standard glasses as presented in Fig. 137 (*this result is valid for other SCHOTT Ce-free glasses*). Consequently, we performed this study at the closest dose rates (compared to the one of the final test ≈0.8 Gy/s) available for each glass: **10** Gy/s for the N-BK7 & BK7G18 and **1.2** Gy/s for the other glasses.

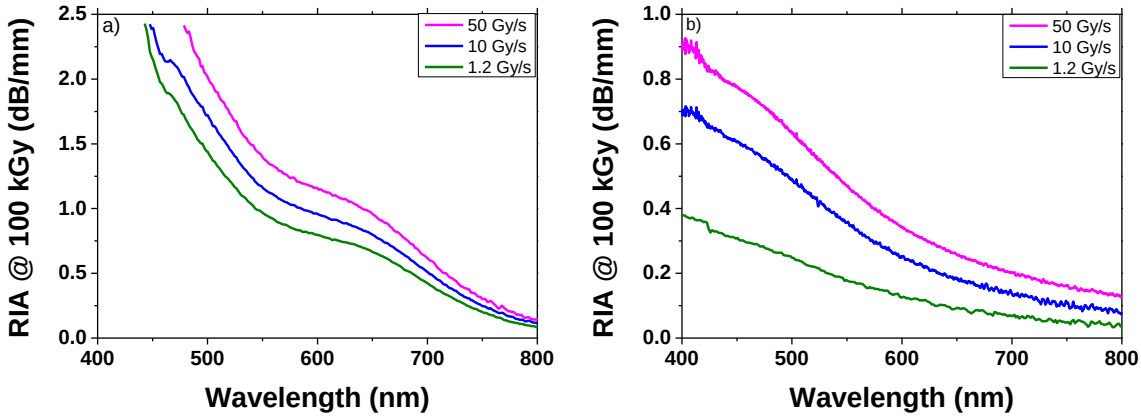

Fig. 137: Effect of the dose rate on the spectral RIA (30°C) of a) N-K5, b) N-SF6

In Fig. 138 we present the difference between the total losses (intrinsic + RIA) of standard glasses (Ce-free) minus the total losses of radiation hardened glasses at different doses. If the curve is under zero that means that the standard glass has a lower attenuation after exposure than its rad-hard counterpart, positive value is for the opposite trend. For all glasses, at the studied dose rates there is nearly no difference between both categories of glasses before 1 kGy. Standard glasses are even more transparent in the blue part of the spectrum than the Cerium doped counterpart thanks to their lower intrinsic absorbance. Then more the dose increases, more the radiation hardened glasses demonstrate their interest in limiting the visible RIA level.

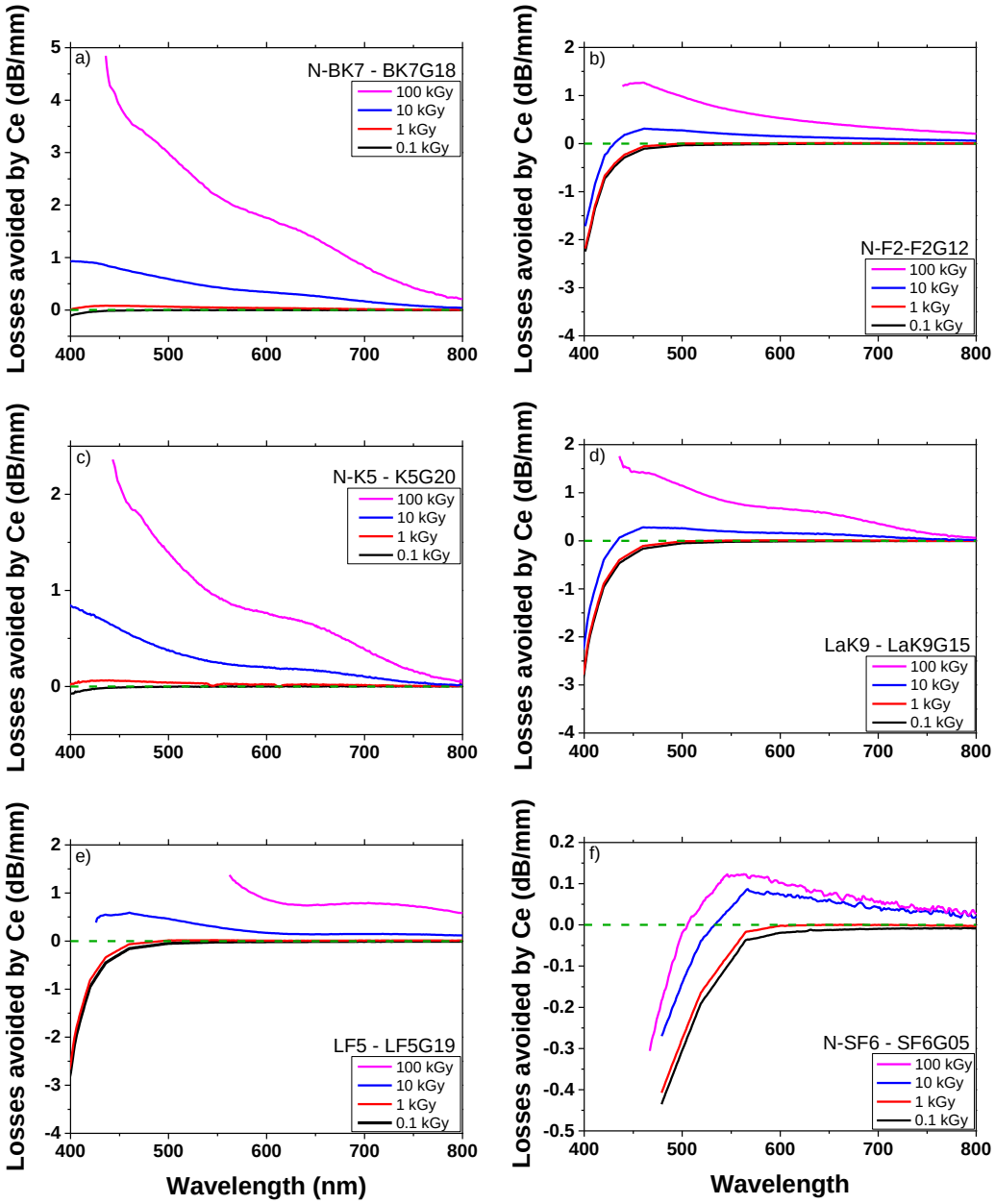

Fig. 138: Difference between the RIA spectra of the standard glass (no Ce doped) and hardened one at different doses & 30°C. a) N-BK7 – BK7G18 @ 10 Gy/s) , b) N-F2- F2G12 @ 1.2 Gy/s, c) N-K5 - K5G20 @ 1.2 Gy/s, d) LaK9 – LaK9G15 @ 1.2 Gy/s, e) LF5 – LF5G19 @ 1.2 Gy/s, f) N-SF6 – SF6G05 @ 1.2 Gy/s

Nevertheless, it is interesting to note that the attenuation of the N-SF6 @ 100 kGy is quite close to the SF6G05 attenuation from 800 to 500 nm and the Cerium codoping is efficient only for doses above 100 kGy. Moreover, as shown in Fig. 139 the RIA of N-SF6 saturates at all wavelengths after 100 kGy @ 50 Gy/s, so we could expect stable RIA levels at higher doses.

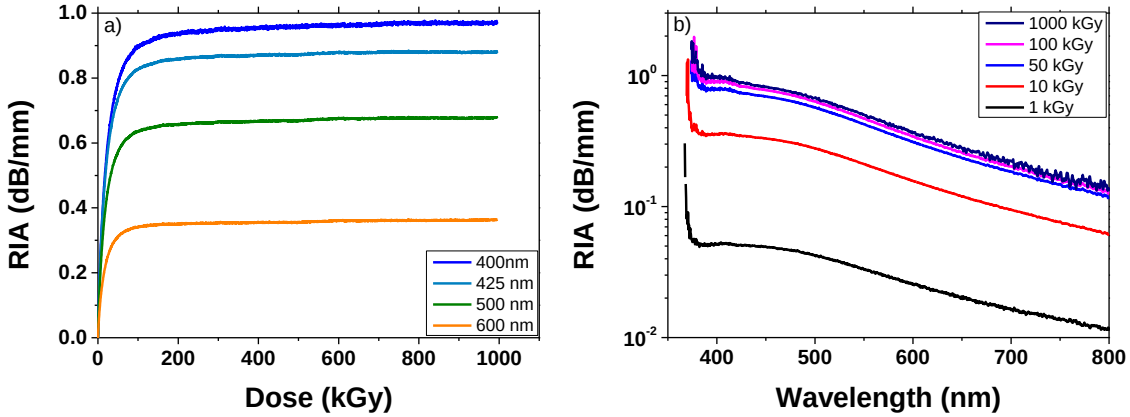

Fig. 139: N-SF6 (1.2 Gy/s & 30°C) a) RIA kinetics at different wavelengths up to 1000 kGy b) RIA spectral dependence

It seems probable than the RIA of the N-SF6 will be smaller at lower dose rates, so depending on this parameter, it may be interesting to use some non-radiation hardened glasses in harsh environment. In the case of the serial production of lens, as in CAMRAD, it will be a strong advantage to use standard glasses as N-SF6 because there are easier to buy and cheaper than radiation hardened glasses. In this case, the variability of the radiation responses of different glass batches should be investigated.

C.3.4. Standard glasses at high doses

As it was developed in section C.1, it is mandatory to use glasses with different Abbe numbers to limit the appearance of chromatic aberrations. The only radiation hardened glass with a low Abbe number is the SF6G05 and it is also the one with the higher intrinsic absorption in the blue part of the spectrum (Fig. 140.a) and the higher RIA below 500 nm (Fig. 140.b). Then, its replacement by another glass is not only useful in terms of cost but also to design a camera with a better color restitution and less constrains on the illumination system.

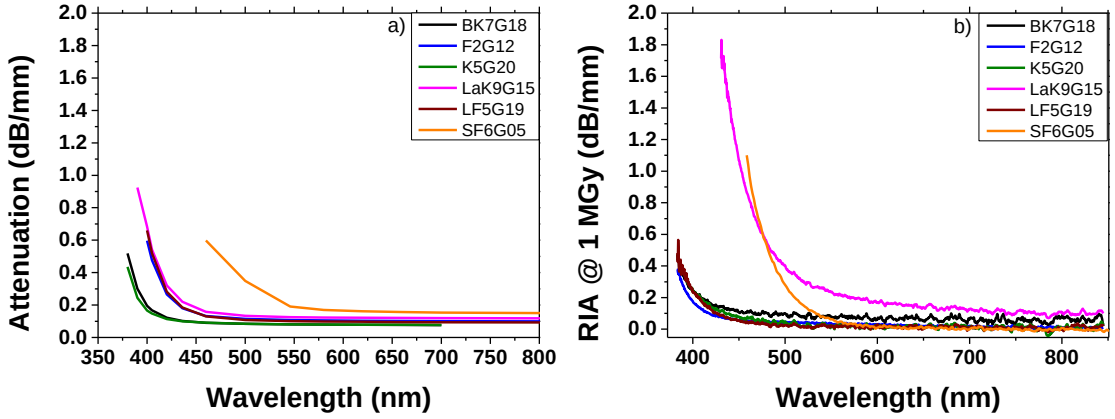

Fig. 140: a) Intrinsic absorbance, b) RIA spectral dependance, of SCHOTT radiation hardened glasses.

We focus our analysis on the comparison between the SF6G05 and the N-SF6 glasses for which we have a full data set. As presented in Fig. 141, the intrinsic absorption of the N-SF6 is negligible in the visible (as for the other standard glasses) whereas the one of the SF6G05 is large below 500 nm and cuts all the blue signal of both blue and white LEDs (that is consistent with its yellow color as shown in Fig. 118). In Fig. 142, we see that after 100 kGy (1.2 Gy/s) @ 465 nm the N-SF6 absorption is 3 times lower than the one of the SF6G05 (we don't have the RIA of the SF6G05 at lower wavelengths) that correspond to a transmission of 93 % for the N-SF6 and 76 % for the SF6G05. It's equivalent to trade a reasonable increase in absorption from 625 to 500 nm with a huge decrease under 500 nm. The Fig. 143 highlights this trade by comparing the impact of irradiated N-SF6 and SF6G05 on the CXA2590 LED spectrum.

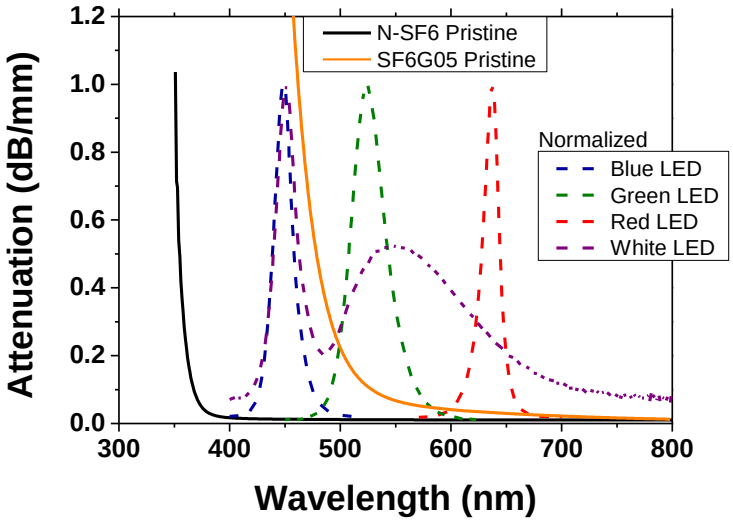

Fig. 141: Effect of the Cerium doping of the N-SF6 (pristine) and its impact on the color transmission of a RGB LED.

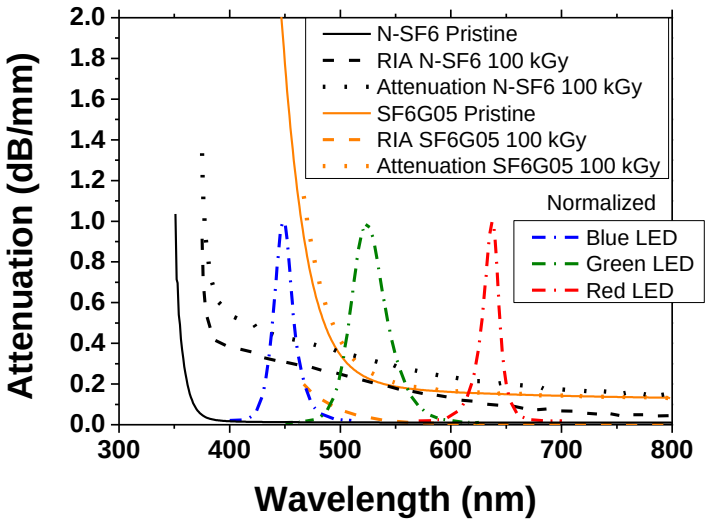

Fig. 142: Comparison between the total attenuation (intrinsic attenuation + RIA) for the N-SF6 and the SF6G05 irradiated at 100 kGy (1.2 Gy/s & 30°C).

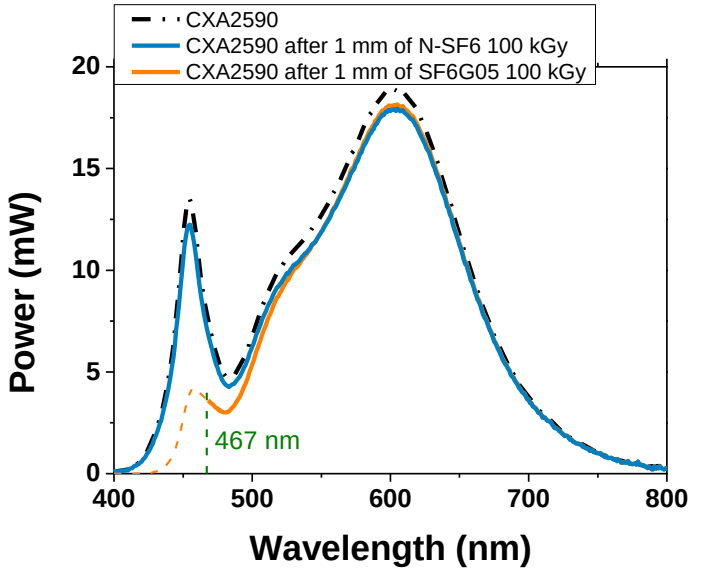

Fig. 143: Comparison between the CXA2590 LED spectra through 1mm of N-SF6 or SF6G05 irradiated at 100 kGy (1.2 Gy/s & 30°C) Data for the SF6G05 (dashed line) were extrapolated under 467 nm.

Based on this result that at least one standard optical glass can sustain high doses with moderate RIA, we decided to create a database of SCHOTT standard glasses RIA. Glasses were irradiated with gamma-rays at IRMA at doses of 0.1, 0.5 and 1 MGy at respectively 0.84, 0.42 and 0.084 Gy/s. After the irradiation we performed a *post-mortem* RIA measurement (as described in section C.2.4) to estimate the glass permanent RIA. In Fig. 145 we report a synthesis of our results. We decided to use as

criteria the average RIA in the range from 425 to 500 nm which is the emission range of the blue LED spectrum. It is a simple way to compare their impact on the image quality.

We found that many glasses on the top right side of the Abbe diagram are quite radiation resistant and have a low permanent attenuation in the blue domain such as the N-SF14 which is as good as a radiation hardened glass regarding this criterion. This is particularly significant for optical system designers because this part of the diagram contains the most efficient glasses to compensate the chromatic aberration of glasses such as pure silica (SUPRASIL). We do not have enough information on their composition to give any hypothesis in order to explain their good radiation resistance in terms of RIA. But because this will allow an easier conception of radiation-hardened optical systems at a lower price, the Laboratoire Hubert Curien, Optsys and ANDRA are patenting this approach [14]. It is important to note that these measurements were made at ~20°C (air-conditioned room) and concerns only the permanent part of the RIA at this temperature as the transient losses are then bleached. During this time of several months before measurements, the samples were stocked at 20°C in the dark. In addition, all samples were cut and polished at LabHC so the sample quality may affect some of the results as the ones of Fig. 144.d. Each sample was measured at least 4 times allowing determination of the error bars. We chose to present the detailed results only for some relevant glasses:

- With high refractive index and low Abbe number, Fig. 144.a to.c
- One glass with high refractive index and medium Abbe number because there is no radiation hardened glass in this area of the diagram, Fig. 144.e
- Glasses that may replace radiation hardened glasses. Fig. 144.f to.g

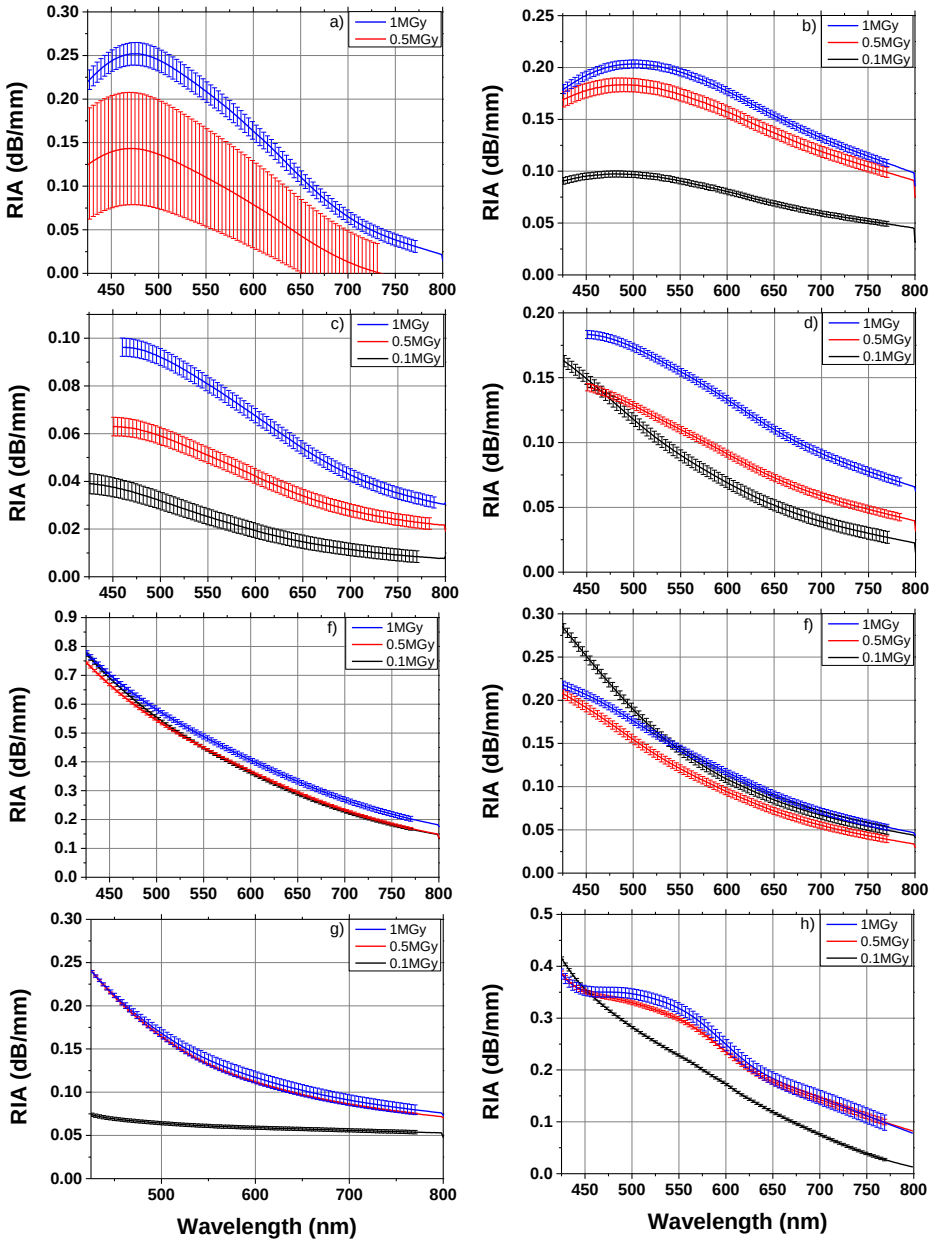

Fig. 144: RIA spectral dependence of a) N-SF66, b) N-LASF46B, c) SF14, d) N-LASF7, e) N-LASF41, f) N-SF2, g) N-BAF4, h) N-KF9, these curves represent the permanent RIA at RT

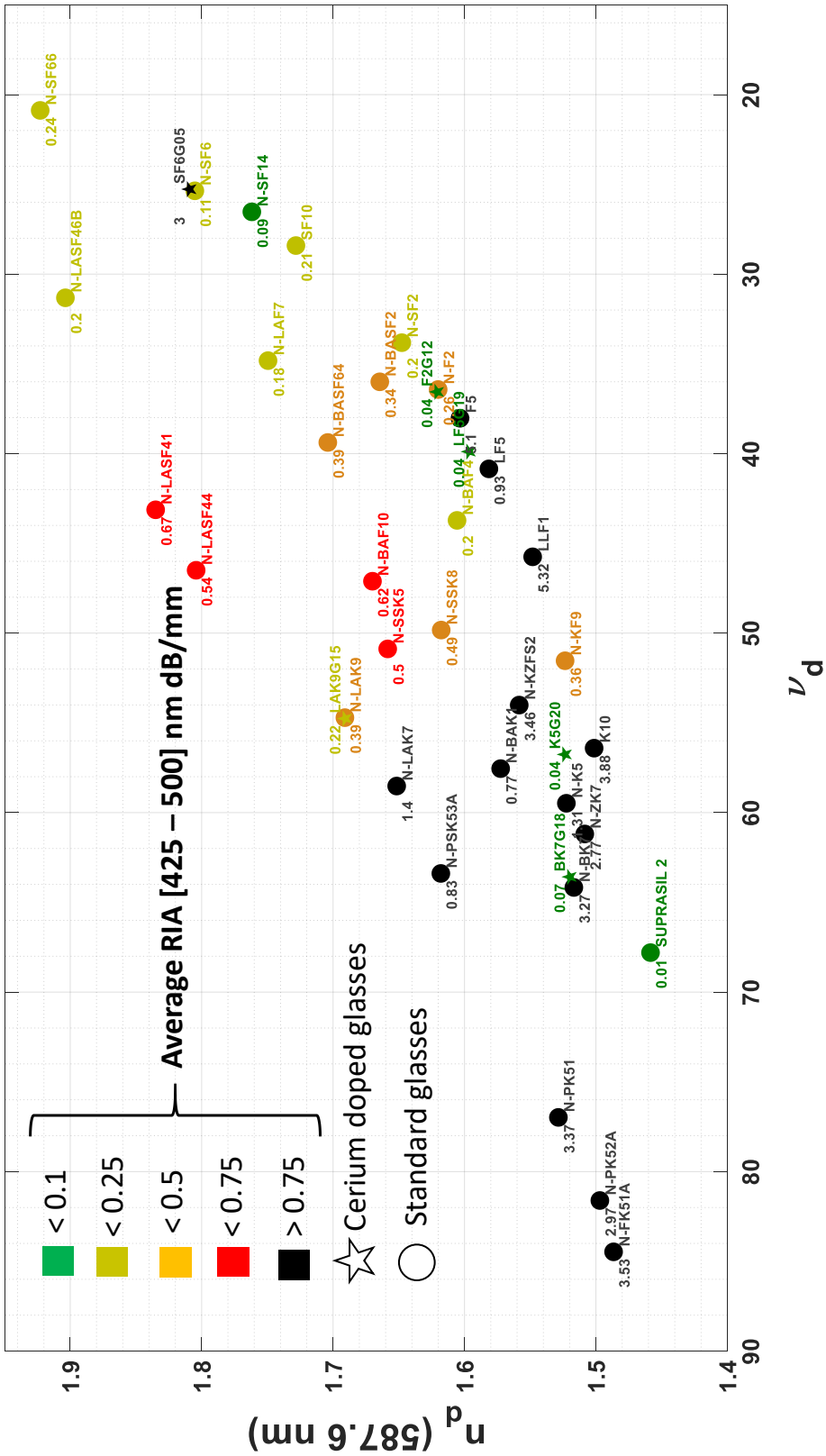

Fig. 145: Average RIA (post-mortem) of some SCHOTT standard glasses after 1 MGy dose (gamma).

At low dose rates, the recovery is slower and limited, as shown in [154] and by our measurements. Depending on the glass nature, it could be not negligible. These RIA levels are strongly affected by the duration of the recovery, so they cannot be seen as the RIA level during the irradiation, especially at 0.1 MGy also because of the low dose rate as shown in Fig. 146. But these tests help in identifying which of the standard glasses deserve future online RIA measurements.

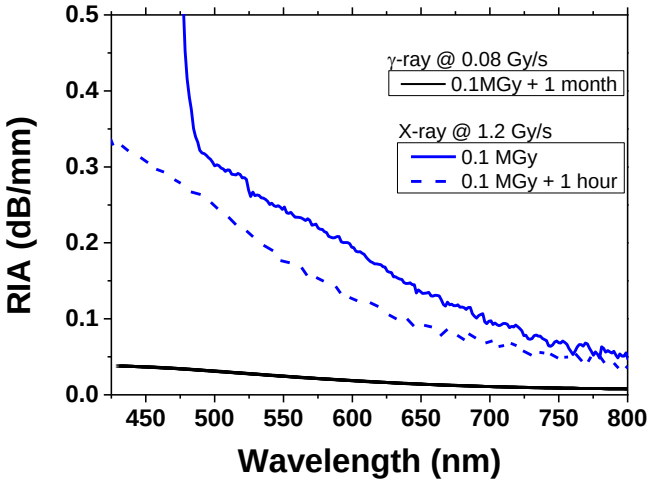

Fig. 146: RIA spectral dependence of N-SF6 online and post-mortem measured

Depending on the parameters (dose rate and the temperature) of the application, we found between 9 and 13 standard glasses that present sufficiently interesting properties to be benchmarked with radiation hardened glasses. The addition of other glass compositions will for sure strongly release design constraints for the optical systems. Moreover, as presented in Fig. 148, the temperature had a strong effect on RIA kinetics and level. We found the same type of results for the N-BK7, N-F2, N-LaK9, LF5 and N-SF6. The two main probable applications of CAMRAD camera will be to inspect the container before their storage in CIGEO and to allow the monitoring of the storage center during its exploitation. Containers will present a maximum dose rate of ≈0.014 Gy/s (50 Gy/h) [155] and a maximum temperature of ≈90°C [156]. In CIGEO, the temperature near the cells will be comprised between 30 and 40°C [157], and the maximum dose rate in the installation will by ≈0.0028 Gy/s (10 Gy/h) [158]. Then, at a lower dose rate than the ones of this study and at medium temperature, all conditions are met to potentially allow using optical systems based on well-chosen standard glasses. As

highlighted in Fig. 147 nearly all radiation environments are associated with a dose rate below 1 Gy/s, so the use of standard glasses may have numerous applications.

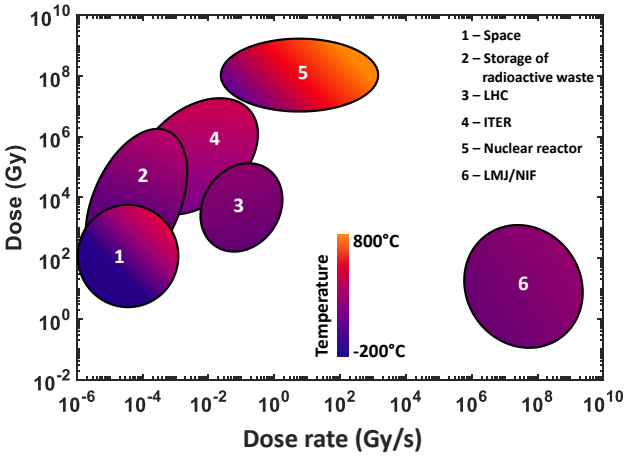

Fig. 147: Diagram summarizing the dose rate, dose and temperature characteristics of the radiation environments described in [101] and adapted from [15].

Nevertheless, the composition of standard glasses may undergo some variation from one batch to another so it will be more secure to carry online measurement before the start of a serial production of optical systems. A radiation hardened assurance strategy will have to be developed.

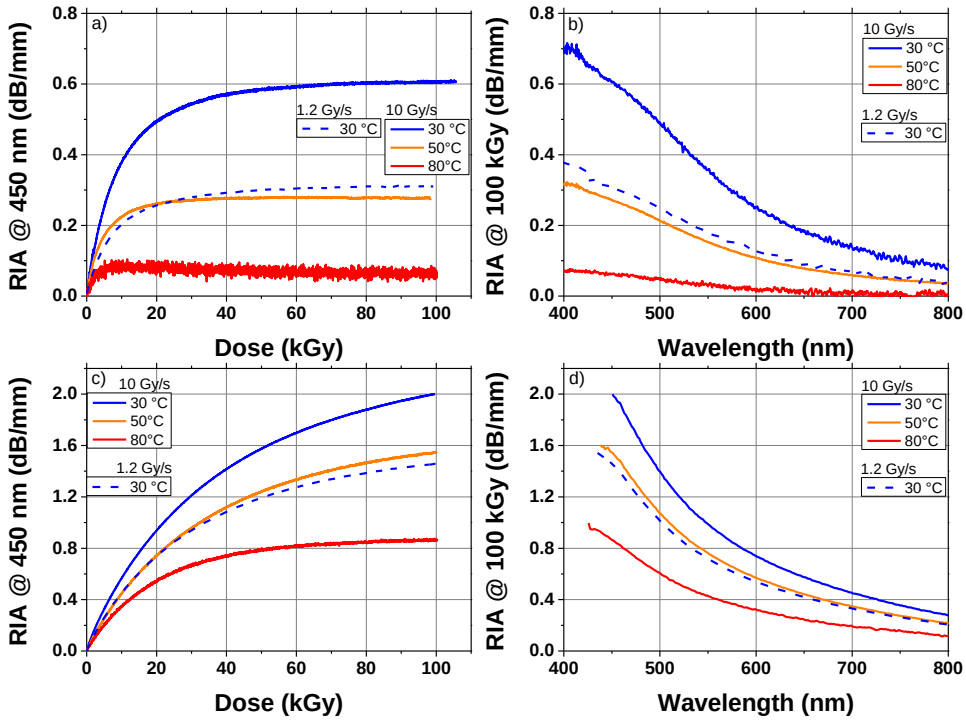

Fig. 148: Combined effects of temperature and dose rate on RIA kinetics and spectral dependence for a & b) N-SF6, c & d) N-F2.

Conclusion Section C.3

In this last chapter, results obtained during the different irradiation campaigns have been presented and are discussed in the framework of the CAMRAD project.

Even with a dedicated measurement device, it is not easy to obtain usable RIRIC data. At least we confirmed that RIRIC seems to saturate at larger doses for some glasses. Today, it seems more realistic to perform simulations to conceive by design optical systems robust to RIRIC of a few 10^{-4}.

We presented with a critical analysis the effect of dose, dose rate and temperature on the RIA in SCHOTT radiation hardened glasses. The low RIA levels of these materials in the visible domain makes the measurement hard to perform online, even if this approach is richer than the usual post mortem measurements. Even if the setup's precision can be upgraded, our data allow optical designers to perform transmission simulations of optical systems up to MGy dose levels and to have an insight about the impact of the temperature and dose rate on their systems.

The last two sections of this PhD thesis present the possibility to design an optical system based on standard glasses for implementation in a radiation environment. We found at least 9 glasses that are interesting in this context and we have deposited a patent targeting their use to conceive color optical systems for harsh environments. This discovery has the potential to decrease the optical systems cost, decrease the glasses order time, simplify the optical designers work and enhance the image quality. Further experiments are necessary to fully characterize these glasses and the variability of their responses lot by lot.

Main conclusion and Perspectives

This PhD thesis was dedicated to the study of the LEDs and optical glasses technologies. Those technologies are needed in the CAMRAD project founded by ANDRA to conceive and manufacture a radiation hardened camera that will fulfill their needs in the context of CIGEO project, in particular a resistance to a cumulative ionizing dose of 1 MGy. This prototype will become COTS product after industrialization by Optsys and will find applications in other domains; for example, in power plants to increase the safety or in fusion devoted facilities such as ITER for the remote handling operations.

Regarding LEDs, there was not available data on the tolerance of high-power LEDs at the MGy level, in particular regarding the impact of radiation on LEDs emission angle and no online measurement. Our systematic measurements show that the temperature management of high-power LEDs is mandatory to obtain trustful output power. We show that most of the white LEDs are tolerant to γ-rays with limited power losses up to 1 MGy. From our measurements and modeling we propose to adapt the LEDs choice to radiation environment by the use of a lower number of LEDs working at high current, rather than many LEDs at low current as is commonly used in lighting systems. We also demonstrated that their emission angles remain unaffected by these radiation dose levels, this point validating an important hypothesis in the photometry simulation of the camera (cf. Cyprien Muller PhD thesis). Finally, thanks to the home-made setup for online measurement under X-rays, we show that even if the electric behavior of LEDs undergoes some fluctuations during the irradiation they are too small to significantly affect their output power. These tests also showed that under irradiation, LEDs operating temperature seems to be slightly increased. Compared to post mortem γ-ray characterizations, X-rays tests show a smaller degradation in agreement with the A. Johnston hypothesis that the LEDs degradation is due to displacement damages [36]. However, X-ray testing may be used to approximate γ-rays effect at lower cost.

Tests with more energetic X-ray have to be carried out in order to enhance the approximation of γ-rays. Moreover, we have to use an active cooler to accurately separate temperature and radiation effects during online measurement.

For optical glasses, there was also a lack of RIA data at the MGy level for both standard and radiation hardened glasses and no reported technique to perform online measurement. We then built, characterized and validated a portable test bench for online RIA measurement allowing us to measure the effect of dose, dose rate and temperature on SCHOTT radiation hardened glasses up to 1 MGy. We know that our measurement method could still be improved but it is already a huge improvement compared to the literature. Moreover, they also confirmed that 5 of the 6 tested radiation hardened glasses are better than their standard counterpart after one to tens of kGy. But the 6th radiation hardened glasses is SF6G5 that is really useful in optical design to compensate chromatic aberration have a strong absorption in the blue part of the spectrum. So; we realized a systematic investigation of the RIA of a large set on SCHOTT standard glasses. We found at least 9 glasses that present a sufficiently low degradation to be candidates for operation in a radiation environment in particular if it is associated with low dose rate and moderate temperature as in the case of the CIGEO project. The developed innovative approach for the design of radiation hardened color optical systems with those glasses leads the Laboratoire Hubert Curien, Optsys and ANDRA to deposit a patent in 2019.

Next steps are an increase in the measurement repeatability as suggested in section C.2.5.8 and a benchmark of the standard glasses found to be intrinsically radiation resistant. We will also show the interest of our set-up with other radiation sources, in particular neutrons and protons that may activate glasses and prevent any post-mortem measurement with a reasonable delay.

Appendix A. Redrawn graphics

In order to increase the readability of the curves from the literature and to provide the reader with a visual consistency in the entire PhD thesis, all of them were redrawn thanks to WebPlotDigitizer [159]*. This software allows obtaining value from curves after axis calibration.*

*We usd the mention "**redrawn from**" in the caption followed by a citation of the reference that contains data to mean the figure is the same as the original but fits with the design of other graphics and/or was translated into English.*

As an example:

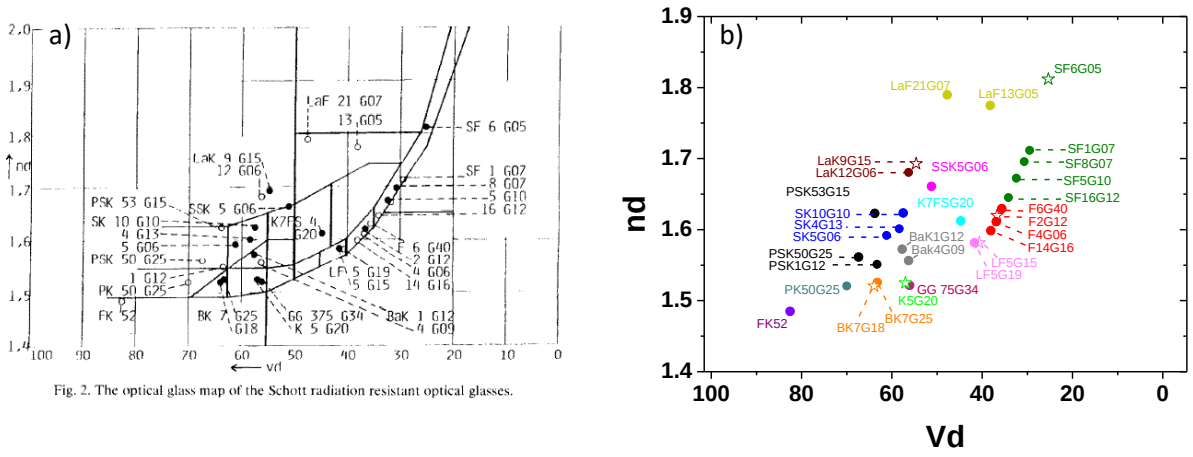

Fig. 2. The optical glass map of the Schott radiation resistant optical glasses.

Fig. 149 a) original Fig. 92, b) Redrawn *Fig. 92*

*In addition, this software also allows us to modify figures by using modified curve names (to make reading easier), or by adding information in the figure or drawing fewer curves than in the original figure. We used the mention "**adapted from**" in the caption following by a citation of the reference that contain data to mean that we modified the figure in at least one of the following ways:*

- *We changed the axis name as "Induced absorbance" to "RIA"*
- *We converted Rad into Gray.*
- *We changed the name of the curves to make them easier to understand in the context of this PhD thesis.*

- *We cut a part of the figure (as the wavelength scale) or there are fewer curves than on the original ones.*
- *We had information on the figure such as arrows or error bars.*
- *We merged curves from different figures belonging to the same paper.*

*We also used the "**adapted from**" mention when we had information on a picture from a reference.*

As an example:

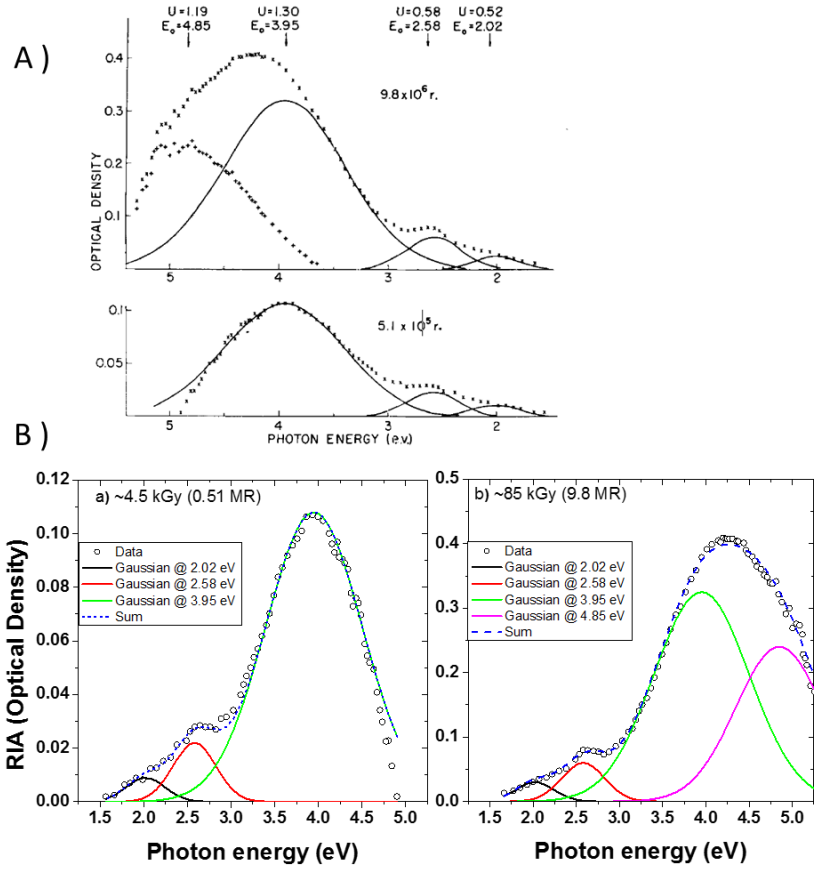

Fig. 150 A) Original Fig. 75, B) Adapted Fig. 75

*We also used it to create original figures either by combination of figures from different figures/papers or by do calculation based on literature data. We used the mention "**created from**" in the caption following by a citation of the reference that contains data to mean that we used the data in at least one of the following ways:*

- *We converted absorbance in RIA*
- *We converted Roentgens in Gray following the procedure described In Appendix C*
- *We plot together data from different references*
- *We converted Transmission data to Absorbance*

As an example:

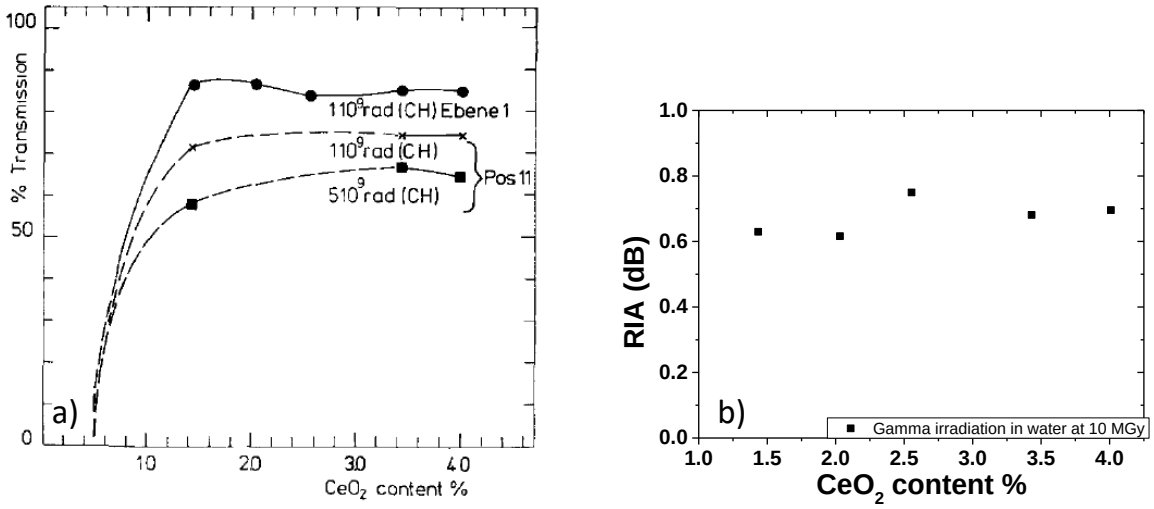

Fig. 10. Change of optical transmission as a function of CeO_2 content Reference medium: unirradiated glass. Wavelength: 410 nm

Fig. 151: a) Original Fig. 89, b) Created Fig. 89

Appendix B. List of LED references

Colored LEDs

In the following tables colors of the text indicate the color of the LED. If the name is black that means that all three colored LEDs are on the same chip.

Name in the thesis	Full reference	Manufacturer
RTDUW	LE RTDUW S2W	OSRAM
F50360	RGB: F50360	Seoul Semiconductor Inc
Seoul Z power	R42180 G42180 B42180	Seoul Semiconductor Inc
SML LX1610	SML-LX1610SIC/A SML-LX1610UPGC/A SML-LX1610SBC/A	Lumex

White LED

Name in the thesis	Full reference	Manufacturer
CXA2590	CXA2590-0000-000R00Z430F	CREE
CXA3590	CXA3590-0000-000R00AD27F	CREE
MKRBWT	MKRBWT-02-0000-0N0HG430H	CREE
MKRAWT	MKRAWT-02-0000-0B0HG407E7	CREE
MCE4WT	MCE4WT-A2-0000-000GA9	CREE
XMLAWT	Star-W2700-10-00-00	CREE
XPEBWT	XPEBWT--H1-R250-00BE5	CREE
XPEWHT	XPEBWT-H1-0000-00BE5	CREE
LHC1-3090	LHC1-3090-1211CRSP	LUMILED
SDW84F1C	LED High-power SDW84F1C-J1/J2-GA	Seoul Semiconductor Inc

Appendix C. Roentgens to Gray relation

Some old papers gave doses in Roentgens, so, to allow a better comparison, we converted doses in Gray when it was possible. We only did it for gamma irradiation and not for X-ray irradiation because the X-ray spectrum was not given in the paper.

We used the method given in Radiation Physics Division, “IRRADIATION OF PASSIVE DOSIMETERS,” NIST, Procedure05v400, Jul. 2015. [Online]. Available: https://www.nist.gov/system/files/documents/2016/10/18/procedure05v400.pdf.

In this reference, authors said: “*To obtain exposure in roentgens, divide air kerma in grays by 8.79E-3 for* ^{60}*Co*” So we can obtain air kerma in grays by multiplying roentgens value by 8.79E3 for ^{60}Co. A close factor (8.87E-3) is also given by radprocalculator, “radprocalculator :FAQ,” May 14, 2020. http://www.radprocalculator.com/FAQ.aspx.

We decided to use a coefficient of 8.79E-3 from roentgens to grays. In this case, Gray are Gray in air.

References

[1] IRSN, “Installations nucléaires en démantèlement en France,” *IRSN*, Nov. 06, 2019. https://umap.openstreetmap.fr/fr/map/installations-nucleaires-en-demantelement-en-franc_214517#18/47.68440/1.56555 (accessed Nov. 06, 2019).

[2] IRSN, “Les démantèlements des réacteurs nucléaires dans le monde Démantèlements de réacteurs en Europe et aux États-Unis : état des lieux et expérience acquise,” *IRSN*, Nov. 06, 2019. https://www.irsn.fr/FR/connaissances/Installations_nucleaires/demantelement/demantelement-reacteurs-nucleaires-monde/Pages/2-acquis-demantelement-reacteurs-nucleaires-monde.aspx?dId=8a40a529-13f8-4aa6-a925-a71c51dc5420&dwId=7c7f58c2-3410-42ae-895b-e2247aecfdd1 (accessed Nov. 06, 2019).

[3] MINISTERE DE LA TRANSITION ECOLOGIQUE ET SOLIDAIRE, “Synthèse : Programmations pluriannuelles de l’énergie 2019-2023 / 2024-2028,” Jan. 2020. [Online]. Available: https://www.ecologique-solidaire.gouv.fr/sites/default/files/20200422%20Synthe%CC%80se%20de%20la%20PPE.pdf.

[4] Andra, “Le planning du projet [CIGEO],” *Le projet CIGEO*, Nov. 06, 2019. https://meusehautemarne.andra.fr/le-projet-cigeo/les-installations-et-le-fonctionnement-du-centre/les-differentes-phases (accessed Nov. 06, 2019).

[5] Fusion for Energy, “Developing tiny Big Brother cameras for ITER.” https://fusionforenergy.europa.eu/mediacorner/newsview.aspx?content=1015 (accessed Jan. 16, 2020).

[6] S. M. González de Vicente, E. R. Hodgson, and T. Shikama, “Functional materials for tokamak in-vessel systems—status and developments,” *Nucl. Fusion*, vol. 57, no. 9, p. 092009, Sep. 2017, doi: 10.1088/1741-4326/aa6a5d.

[7] V. Goiffon *et al.*, “CAMRAD: Development of a Multi-Megagray Radiation Hard CMOS Camera for Dismantling Operations,” p. 10, 2018.

[8] J. W. Cho, Y. S. Choi, and K. M. Jeong, “Monitoring performance of the cameras under the high dose-rate gamma ray environments,” *Health Phys.*, vol. 106, no. 5, pp. S47–S58, 2014.

[9] S. Girard, “Multi-MGy Radiation Hardened Camera for Nuclear Facilities,” presented at the Advancements in Nuclear Instrumentation Measurement Methods and their Applications (ANIMMA 2015), Lisbon, Apr. 2015, [Online]. Available: https://hal-ujm.archives-ouvertes.fr/ujm-01185893.

[10] Nexter, “Optsys,” May 11, 2020. https://www.nexter-group.fr/filiales/optsys.html.

[11] S. Rizzolo *et al.*, “Radiation Hardness Comparison of CMOS Image Sensor Technologies at High Total Ionizing Dose Levels,” *IEEE Trans. Nucl. Sci.*, vol. 66, no. 1, pp. 111–119, Jan. 2019, doi: 10.1109/TNS.2018.2884037.

[12] C. Muller *et al.*, “Investigations of the MGy dose level radiation effects on the photometric budget of a radiation-hardened CMOS-based camera,” *Appl. Opt.*, vol. 58, no. 22, p. 6165, Aug. 2019, doi: 10.1364/AO.58.006165.

[13] S. Rizzolo *et al.*, “Partially Pinned Photodiode Performances for Emerging Space and Nuclear Applications,” *IISW2019_Proceeding*, 2019.

[14] S. Girard, T. Allanche, and A. Boukenter, “Procédé de fabrication d’un dispositif de mesure optique apte à fonctionner sous rayonnement ionisant et dispositif de mesure optique apte à fonctionner sous rayonnement ionisant,” FR1908146.

[15] C. Muller, “Conception optique pour les environnements radiatifs et application à une caméra résistante à des doses élevées (MGy),” CAMRAD.

[16] IRNS, “Installation IRMA,” Apr. 01, 2015. https://www.irsn.fr/FR/Actualites_presse/Communiques_et_dossiers_de_presse/Documents/IRSN_Installation-IRMA.pdf (accessed Jan. 14, 2020).
[17] IRSN, “Modern2020,” *IRSN*, Sep. 03, 2020. https://www.irsn.fr/dechets/recherche/projets-europeens/modern2020/Pages/Modern2020.aspx.
[18] D. A. Baiko, S. K. Bhaskaran, and S. W. Czebiniak, “CID25: radiation hardened color video camera,” San Jose, CA, Feb. 2006, p. 61190D, doi: 10.1117/12.646384.
[19] S. Girard *et al.*, “Growth and Decay Kinetics of Radiation-Induced Attenuation in Bulk Optical Materials,” *IEEE Trans. Nucl. Sci.*, pp. 1–1, 2017, doi: 10.1109/TNS.2017.2778318.
[20] V. Goiffon, C. Virmontois, P. Magnan, S. Girard, and P. Paillet, “Analysis of Total Dose-Induced Dark Current in CMOS Image Sensors From Interface State and Trapped Charge Density Measurements,” *IEEE Trans. Nucl. Sci.*, p. 5618600, Dec. 2010, doi: 10.1109/TNS.2010.2077653.
[21] G. R. Hopkinson, “Radiation effects in a CMOS active pixel sensor,” *IEEE Trans. Nucl. Sci.*, vol. 47, no. 6, pp. 2480–2484, Dec. 2000, doi: 10.1109/23.903796.
[22] T. Allanche *et al.*, “Analysis of X-Ray Photo-Charge Induced Speckles in a Radiation Hardened CMOS Image Sensor,” in *2017 17th European Conference on Radiation and Its Effects on Components and Systems (RADECS)*, Geneva, Switzerland, Oct. 2017, pp. 1–4, doi: 10.1109/RADECS.2017.8696152.
[23] Z. Wang *et al.*, “Comparison of transient response characteristics in the CIS detector irradiated by gamma rays and X rays,” *Nucl. Instrum. Methods Phys. Res. Sect. Accel. Spectrometers Detect. Assoc. Equip.*, Jul. 2018, doi: 10.1016/j.nima.2018.06.071.
[24] C. Wang, S. Hu, C. Gao, and C. Feng, “Nuclear Radiation Degradation Study on HD Camera Based on CMOS Image Sensor at Different Dose Rates,” *Sensors*, vol. 18, no. 2, p. 514, Feb. 2018, doi: 10.3390/s18020514.
[25] L. Massol, *Les LED pour l’éclairage*, LED engineering development. Dunod, 2012.
[26] Q. Dai *et al.*, “On the symmetry of efficiency-versus-carrier-concentration curves in GaInN/GaN light-emitting diodes and relation to droop-causing mechanisms,” *Appl. Phys. Lett.*, vol. 98, no. 3, pp. 033506-1 033506-3, 2011, doi: 10.1063/1.3544584.
[27] E. F. Schubert, *Light-emitting diodes*. Cambridge; New York: Cambridge University Press, 2006.
[28] M.-H. Kim *et al.*, “Origin of efficiency droop in GaN-based light-emitting diodes,” *Appl. Phys. Lett.*, vol. 91, no. 18, pp. 183507-1 183507-3, Oct. 2007, doi: 10.1063/1.2800290.
[29] M. H. Crawford, “LEDs for Solid-State Lighting: Performance Challenges and Recent Advances,” *IEEE J. Sel. Top. Quantum Electron.*, vol. 15, no. 4, pp. 1028–1040, Jul. 2009, doi: 10.1109/JSTQE.2009.2013476.
[30] A. Daami and F. Olivier, “InGaN/GaN µLED SPICE modelling with size-dependent ABC model integration,” in *Physics and Simulation of Optoelectronic Devices XXVII*, San Francisco, United States, Feb. 2019, p. 13, doi: 10.1117/12.2509382.
[31] A. H. Johnston, “Radiation damage of electronic and optoelectronic devices in space,” *Proceedings of the 4th International Workshop on Radiation Effects on Semiconductor Devices for Space Application*, 2000. http://nepp.nasa.gov/docuploads/D41D389D-04D4-4710-BBCFF24F4529B3B3/Dmg_Space-00.pdf.
[32] G. M. Swift, G. C. Levanas, J. M. Ratliff, and A. H. Johnston, “In-flight annealing of displacement damage in gaas leds: a galileo story,” *IEEE Trans. Nucl. Sci.*, vol. 50, no. 6, pp. 1991–1997, Dec. 2003, doi: 10.1109/TNS.2003.821374.
[33] J. D. Devine and A. Floriduz, “Radiation hardening of LED luminaires for accelerator tunnels,” in *2016 16th European Conference on Radiation and Its Effects on Components and Systems (RADECS)*, Bremen, Sep. 2016, pp. 1–6, doi: 10.1109/RADECS.2016.8093210.

[34] A. Floriduz and J. D. Devine, “Modelling of proton irradiated GaN-based high-power white light-emitting diodes,” *Jpn. J. Appl. Phys.*, vol. 57, no. 8, p. 080304, Aug. 2018, doi: 10.7567/JJAP.57.080304.
[35] A. H. Johnston, “Radiation effects in light-emitting and laser diodes,” *IEEE Trans. Nucl. Sci.*, vol. 50, no. 3, pp. 689–703, Jun. 2003, doi: 10.1109/TNS.2003.812926.
[36] A. H. Johnston, “Radiation Effects in Optoelectronic Devices,” *IEEE Trans. Nucl. Sci.*, vol. 60, no. 3, pp. 2054–2073, Jun. 2013, doi: 10.1109/TNS.2013.2259504.
[37] L. Wang *et al.*, “Multiple Angle Analysis of 30-MeV Silicon Ion Beam Radiation Effects on InGaN/GaN Multiple Quantum Wells Blue Light-Emitting Diodes,” *IEEE Trans. Nucl. Sci.*, vol. 65, no. 11, pp. 2784–2792, Nov. 2018, doi: 10.1109/TNS.2018.2872582.
[38] I.-H. Lee *et al.*, “Electron irradiation of near-UV GaN/InGaN light emitting diodes: Electron irradiation of near-UV GaN/InGaN light emitting diodes,” *Phys. Status Solidi A*, vol. 214, no. 10, p. 1700372, Oct. 2017, doi: 10.1002/pssa.201700372.
[39] I.-H. Lee *et al.*, “Point defects controlling non-radiative recombination in GaN blue light emitting diodes: Insights from radiation damage experiments,” *J. Appl. Phys.*, vol. 122, no. 11, p. 115704, Sep. 2017, doi: 10.1063/1.5000956.
[40] A. S. Hedzir, N. N. Sallehuddin, N. Saidin, and N. F. Hasbullah, “Influence of electron irradiation on the electroluminescence spectra of white InGaN light emitting diodes,” *Ukr J Phys Opt*, vol. 19, no. 3, p. 6, 2018.
[41] S. J. Pearton, R. Deist, F. Ren, L. Liu, A. Y. Polyakov, and J. Kim, “Review of radiation damage in GaN-based materials and devices,” *J. Vac. Sci. Technol. Vac. Surf. Films*, vol. 31, no. 5, pp. 050801-1 050801-15, Sep. 2013, doi: 10.1116/1.4799504.
[42] G. A. Umana-Membreno *et al.*, “60Co gamma-irradiation-induced defects in n-GaN,” *Appl. Phys. Lett.*, vol. 80, no. 23, pp. 4354–4356, Jun. 2002, doi: 10.1063/1.1483390.
[43] R. Khanna, S. Y. Han, S. J. Pearton, D. Schoenfeld, W. V. Schoenfeld, and F. Ren, “High dose Co-60 gamma irradiation of InGaN quantum well light-emitting diodes,” *Appl. Phys. Lett.*, vol. 87, no. 21, pp. 212107-1 212107-3, Nov. 2005, doi: 10.1063/1.2132085.
[44] K. N. Orlova, A. V. Gradoboev, and I. A. Asanov, “Gamma degradation of light-emitting diodes based on heterostructures AlGaInP,” in *Strategic Technology (IFOST), 2012 7th International Forum on*, 2012, pp. 201–204, Accessed: Jan. 07, 2017. [Online]. Available: http://ieeexplore.ieee.org/xpls/abs_all.jsp?arnumber=6357528.
[45] T. Takeuchi *et al.*, “Development of Radiation-Resistant In-Water Wireless Transmission System Using Light Emitting Diodes and Photo Diodes,” *IEEE Trans. Nucl. Sci.*, vol. 63, no. 5, pp. 2698–2702, Oct. 2016, doi: 10.1109/TNS.2016.2582299.
[46] T. Allanche *et al.*, “Vulnerability and Hardening Studies of Optical and Illumination Systems at MGy Dose Levels,” *IEEE Trans. Nucl. Sci.*, vol. 65, no. 1, pp. 132–140, Jan. 2018, doi: 10.1109/TNS.2017.2783187.
[47] J.-L. Meyzonnette and T. Lépine, *Bases de radiométrie optique*. Toulouse: Cépaduès Éd, 1999.
[48] F. deBlois, G. Landry, and F. Verhaegen, “spekcalc.” http://spekcalc.weebly.com/ (accessed Jan. 15, 2020).
[49] G. Poludniowski, G. Landry, F. DeBlois, P. M. Evans, and F. Verhaegen, “*SpekCalc* : a program to calculate photon spectra from tungsten anode x-ray tubes,” *Phys. Med. Biol.*, vol. 54, no. 19, pp. N433–N438, Oct. 2009, doi: 10.1088/0031-9155/54/19/N01.
[50] G. G. Poludniowski and P. M. Evans, “Calculation of x-ray spectra emerging from an x-ray tube. Part I. Electron penetration characteristics in x-ray targets: Calculation of x-ray spectra. Part I,” *Med. Phys.*, vol. 34, no. 6Part1, pp. 2164–2174, May 2007, doi: 10.1118/1.2734725.
[51] G. G. Poludniowski, “Calculation of x-ray spectra emerging from an x-ray tube. Part II. X-ray production and filtration in x-ray targets: Calculation of x-ray spectra. Part II,” *Med. Phys.*, vol. 34, no. 6Part1, pp. 2175–2186, May 2007, doi: 10.1118/1.2734726.

[52] S. Seltzer, “XCOM-Photon Cross Sections Database, NIST Standard Reference Database 8.” National Institute of Standards and Technology, 1987, doi: 10.18434/T48G6X.
[53] G.-B. Lin, D. Meyaard, J. Cho, E. Fred Schubert, H. Shim, and C. Sone, “Analytic model for the efficiency droop in semiconductors with asymmetric carrier-transport properties based on drift-induced reduction of injection efficiency,” *Appl. Phys. Lett.*, vol. 100, no. 16, p. 161106, Apr. 2012, doi: 10.1063/1.4704366.
[54] A. Nardelli, E. Deuschle, L. D. de Azevedo, J. L. N. Pessoa, and E. Ghisi, “Assessment of Light Emitting Diodes technology for general lighting: A critical review,” *Renew. Sustain. Energy Rev.*, vol. 75, pp. 368–379, Aug. 2017, doi: 10.1016/j.rser.2016.11.002.
[55] K.-X. Sun, N. Leindecker, S. Higuchi, J. Goebel, S. Buchman, and R. L. Byer, “UV LED operation lifetime and radiation hardness qualification for space flights,” *J. Phys. Conf. Ser.*, vol. 154, p. 012028, Mar. 2009, doi: 10.1088/1742-6596/154/1/012028.
[56] B. Chambion, “Etude de la fiabilité de modules à base de LEDs blanches pour applications automobile,” p. 253.
[57] “Zemax,” Dec. 10, 2019. https://www.zemax.com/.
[58] I. Rajta, S. Z. Szilasi, J. Budai, Z. Tóth, P. Petrik, and E. Baradács, “Refractive index depth profile in PMMA due to proton irradiation,” *Nucl. Instrum. Methods Phys. Res. Sect. B Beam Interact. Mater. At.*, vol. 260, no. 1, pp. 400–404, Jul. 2007, doi: 10.1016/j.nimb.2007.02.052.
[59] D. Doyle, “Radiation Hardeness of Optical Materiel,” presented at the 3rd Europa Jupiter System Mission Instrument Workshop, ESA ESTEC, Noordwijk, Jan. 2010.
[60] E. R. Dowski and W. T. Cathey, “Extended depth of field through wave-front coding,” *Appl. Opt.*, vol. 34, no. 11, p. 1859, Apr. 1995, doi: 10.1364/AO.34.001859.
[61] SCHOTT, “N-SF66,” *RefractiveIndex.Info*. https://refractiveindex.info/?shelf=glass&book=SCHOTT-SF&page=N-SF66.
[62] SCHOTT, “N-SF6,” *RefractiveIndex.Info*. https://refractiveindex.info/?shelf=glass&book=SCHOTT-SF&page=SF6.
[63] SCHOTT, “N-BK7,” *RefractiveIndex.Info*. https://refractiveindex.info/?shelf=glass&book=BK7&page=SCHOTT.
[64] Johnson and Christy, “Fused Silica,” *RefractiveIndex.Info*. https://refractiveindex.info/?shelf=main&book=Ag&page=Johnson.
[65] “Abbe number,” *Wikipedia*. https://en.wikipedia.org/wiki/Abbe_number (accessed Jan. 16, 2020).
[66] E. Hecht and A. R. Ganesan, *Optics*. 2012.
[67] edmundoptics, “Chromatic and Monochromatic Optical Aberrations,” *edmundoptics*. https://www.edmundoptics.com/knowledge-center/application-notes/optics/chromatic-and-monochromatic-optical-aberrations/ (accessed Jan. 16, 2020).
[68] P. Hartmann, R. Jedamzik, S. Reichel, and B. Schreder, “Optical glass and glass ceramic historical aspects and recent developments: a Schott view,” *Appl. Opt.*, vol. 49, no. 16, p. D157, Jun. 2010, doi: 10.1364/AO.49.00D157.
[69] A. Fluegel, “Statistical regression modelling of glass properties – a tutorial,” *Glass Technol.*, vol. 50, no. 1, p. 22, 2009.
[70] P. W. Levy, “Overview Of Nuclear Radiation Damage Processes: Phenomenological Features Of Radiation Damage In Crystals And Glasses,” Dec. 1985, p. 2, doi: 10.1117/12.975356.
[71] M. Fruit, A. I. Gusarov, D. B. Doyle, and G. J. Ulbrich, “Radiation impact on spaceborne optics: the dose coefficients approach,” Dec. 1999, p. 60, doi: 10.1117/12.373286.
[72] M. Fruit, A. I. Gusarov, and D. B. Doyle, “Measuring space radiation impact on the characteristics of optical glasses: measurement results and recommendations from testing a selected set of materials,” Nov. 2002, p. 132, doi: 10.1117/12.452255.

[73] A. I. Gusarov *et al.*, “Refractive-index changes caused by proton radiation in silicate optical glasses,” *Appl. Opt.*, vol. 41, no. 4, pp. 678–684, 2002.
[74] A. I. Gusarov and D. B. Doyle, “Radiation-induced wave-front aberrations: a new approach,” *Appl. Opt.*, vol. 37, no. 4, pp. 643–648, 1998.
[75] D. B. Doyle *et al.*, “Radiation qualification and testing of a large number of optical glasses used in the ESA Fluid Science Laboratory onboard the Columbus Orbital Facility of the International Space Station,” Seattle, WA, Nov. 2002, p. 124, doi: 10.1117/12.452227.
[76] A. I. Gusarov and D. B. Doyle, “Modeling of gamma-radiation impact on transmission characteristics of optical glasses,” Toulouse, France, Jan. 2002, pp. 78–85, doi: 10.1117/12.454388.
[77] A. I. Gusarov, D. B. Doyle, M. Fruit, and D. P. Kinet, “Prediction of long-term radiation kinetics of transmission spectra of commerical optical glasses,” Nov. 2002, p. 142, doi: 10.1117/12.452233.
[78] M. FRUIT, A. GUSAROV, D. DOYLE, G. ULBRICH, and A. HERMANNE, “Space radiation sensitivity of glasses: first results towards a comprehensive dose coefficients database,” vol. 4134, p. 7.
[79] M. García-Matos, A. Moroño, and E. R. Hodgson, “KU1 quartz glass for remote handling and LIDAR diagnostic optical transmission systems,” *J. Nucl. Mater.*, vol. 283–287, pp. 890–893, Dec. 2000, doi: 10.1016/S0022-3115(00)00195-1.
[80] A. Moroño, R. Vila, and E. R. Hodgson, “KU1 and KS-4V quartz glass lenses for remote handling and diagnostic optical transmission systems,” *J. Nucl. Mater.*, vol. 329–333, pp. 1438–1441, Aug. 2004, doi: 10.1016/j.jnucmat.2004.04.163.
[81] D. L. Griscom, “Nature of defects and defect generation in optical glasses,” *SPIE Vol 541 - Radiat. Eff. Opt. Mater. PW Levy Ed*, vol. 541, pp. 38–59, Dec. 1985.
[82] E. Lell, N. J. Kreidl, and J. R. Hensler, “RADIATION EFFECTS IN QUARTZ, SILICA, AND GLASSES,” *Prog. Ceram. Sci. Vol. 4 Burke J E Ed N. Y. Pergamon Press Inc1966*, pp. 1–93, 1968.
[83] J. V. Jelley, “Cerenkov radiation and its applications,” *Br J Appl Phys*, vol. 227, no. 6, pp. 227–232, 1955.
[84] A. Rousseau *et al.*, “Nuclear background effects on plasma diagnostics for megajoule class laser facility,” Aug. 2013.
[85] A. S. Chauchat *et al.*, “Construction of a Compton source for X-rays in the ELSA facility,” *Nucl. Instrum. Methods Phys. Res. Sect. Accel. Spectrometers Detect. Assoc. Equip.*, vol. 608, no. 1, pp. S99–S102, Sep. 2009, doi: 10.1016/j.nima.2009.05.134.
[86] “Hale et Querry - 1973 - Optical Constants of Water in the 200-nm to 200-µm.pdf.” .
[87] A. Gusarov and S. K. Hoeffgen, “Radiation Effects on Fiber Gratings,” *IEEE Trans. Nucl. Sci.*, vol. 60, no. 3, pp. 2037–2053, Jun. 2013, doi: 10.1109/TNS.2013.2252366.
[88] J. A. Ruller and E. J. Friebele, “The effect of gamma-irradiation on the density of various types of silica,” *J. Non-Cryst. Solids*, vol. 136, no. 1–2, pp. 163–172, 1991.
[89] D. R. Olson, H. D. Dieselman, and J. B. Schroeder, “Radiation-induced Changes in Refractive Index and Absorption Coefficient for Several Optical Materials,” *Appl. Opt.*, vol. 10, no. 1, p. 81, Jan. 1971, doi: 10.1364/AO.10.000081.
[90] C. Muller *et al.*, “Potential performance loss and compensation techniques of a lens under ionizing radiations,” in *Optical Design and Engineering VII*, Frankfurt, Germany, Jun. 2018, p. 24, doi: 10.1117/12.2313245.
[91] SCHOTT, “SCHOOT,” May 12, 2020. https://www.schott.com/france/french/index.html.
[92] Schott Ltd, “BK7G18 Technical Safety Information,” 5, Mar. 2015. [Online]. Available: http://www.schott.com/d/advanced_optics/248e1947-ddc0-4245-907b-4cb890a44439/BK7G18_SDS_EN_V5_201505.pdf?tenant=ao-cert.

[93] Schott Ltd, “F2G12 Technical Safety Information,” 5.2, Nov. 2016. [Online]. Available: https://www.schott.com/d/advanced_optics/6c48fb54-0fa6-4944-8581-8e64251501db/F2G12_SDS_EN_V5.2_201903.pdf?tenant=ao-cert.
[94] Schott Ltd, “K5G20 Technical Safety Information,” 5, Mar. 2015. [Online]. Available: http://www.schott.com/d/advanced_optics/1803dcea-fbad-4ede-8976-186674ae2d5d/K5G20_SDS_EN_V5_201505.pdf?tenant=ao-cert.
[95] Schott Ltd, “LAK9G15 Technical Safety Information,” 5, Mar. 2015. [Online]. Available: https://www.schott.com/d/advanced_optics/abc889f9-8b3d-4d91-951b-dd617a3f827e/LAK9G15_SDS_EN_V5_201505.pdf?tenant=ao-cert.
[96] Schott Ltd, “LF5G15 Technical Safety Information,” Schott, 5.2, Nov. 2016. [Online]. Available: https://www.schott.com/d/advanced_optics/2d2a0468-8950-4d24-acbe-01e22b351190/LF5G15_SDS_EN_V5.2_201903.pdf?tenant=ao-cert.
[97] Schott Ltd, “SF6G05 Technical Safety Information,” 5, Mar. 2015. [Online]. Available: http://www.schott.com/d/advanced_optics/b7b59039-1ca0-40c3-ad34-ab3ac5aafd64/SF6G05_SDS_EN_V5_201505.pdf?tenant=ao-cert.
[98] T. D. Henson and G. K. Torrington, “Space radiation testing of radiation-resistant glasses and crystals,” San Diego, CA, Nov. 2001, pp. 54–65, doi: 10.1117/12.446894.
[99] G. Pacchioni, L. Skuja, and D. L. Griscom, *Defects in SiOb2s and related dielectrics: science and technology*. Dordrecht: Springer Science, 2000.
[100] S. Girard *et al.*, “Radiation Effects on Silica-Based Optical Fibers: Recent Advances and Future Challenges,” *IEEE Trans. Nucl. Sci.*, vol. 60, no. 3, pp. 2015–2036, Jun. 2013, doi: 10.1109/TNS.2012.2235464.
[101] S. Girard *et al.*, “Recent advances in radiation-hardened fiber-based technologies for space applications,” *J. Opt.*, vol. 20, no. 9, p. 093001, Sep. 2018, doi: 10.1088/2040-8986/aad271.
[102] S. Girard *et al.*, “Overview of radiation induced point defects in silica-based optical fibers,” *Rev. Phys.*, vol. 4, p. 100032, Nov. 2019, doi: 10.1016/j.revip.2019.100032.
[103] L. Skuja, “Optically active oxygen-deficiency-related centers in amorphous silicon dioxide,” *J. Non-Cryst. Solids*, vol. 239, no. 1–3, pp. 16–48, Oct. 1998, doi: 10.1016/S0022-3093(98)00720-0.
[104] R. A. Weeks, “Paramagnetic Resonance of Lattice Defects in Irradiated Quartz,” *J. Appl. Phys.*, vol. 27, no. 11, pp. 1376–1381, Nov. 1956, doi: 10.1063/1.1722267.
[105] L. Skuja and A. Naber, “Site-selective luminescence study of defects. in gamma-irradiated glassy germanium dioxide,” *Nucl. Instrum. Methods Phys. Res. Sect. B Beam Interact. Mater. At.*, vol. 116, no. 1–4, pp. 549–553, Aug. 1996, doi: 10.1016/0168-583X(96)00106-1.
[106] L. Skuja, H. Hosono, and M. Hirano, “Laser-induced color centers in silica,” Boulder, CO, Apr. 2001, p. 155, doi: 10.1117/12.425020.
[107] H. Hosono, K. Kajihara, T. Suzuki, Y. Ikuta, L. Skuja, and M. Hirano, “Vacuum ultraviolet optical absorption band of non-bridging oxygen hole centers in SiO2 glass,” *Solid State Commun.*, vol. 122, no. 3–4, pp. 117–120, Apr. 2002, doi: 10.1016/S0038-1098(02)00118-7.
[108] M. Cannas and F. M. Gelardi, “Vacuum ultraviolet excitation of the 1.9-eV emission band related to nonbridging oxygen hole centers in silica,” *Phys. Rev. B*, vol. 69, no. 15, p. 153201, Apr. 2004, doi: 10.1103/PhysRevB.69.153201.
[109] L. Skuja, K. Kajihara, M. Hirano, and H. Hosono, “Visible to vacuum-UV range optical absorption of oxygen dangling bonds in amorphous SiO 2,” *Phys. Rev. B*, vol. 84, no. 20, p. 205206, Nov. 2011, doi: 10.1103/PhysRevB.84.205206.
[110] M. Cannas, L. Vaccaro, and B. Boizot, “Spectroscopic parameters related to non-bridging oxygen hole centers in amorphous-SiO2,” *J. Non-Cryst. Solids*, vol. 352, no. 3, pp. 203–208, Mar. 2006, doi: 10.1016/j.jnoncrysol.2005.12.001.

[111]L. Vaccaro, M. Cannas, and R. Boscaino, “Luminescence features of nonbridging oxygen hole centres in silica probed by site-selective excitation with tunable laser,” *Solid State Commun.*, vol. 146, no. 3–4, pp. 148–151, Apr. 2008, doi: 10.1016/j.ssc.2008.02.001.
[112]R. A. B. Devine and J. Arndt, “Defect pair creation through ultraviolet radiation in dense, amorphous SiO 2,” *Phys. Rev. B*, vol. 42, no. 4, pp. 2617–2620, Aug. 1990, doi: 10.1103/PhysRevB.42.2617.
[113]D. L. Griscom, “Thermal bleaching of x-ray-induced defect centers in high purity fused silica by diffusion of radiolytic molecular hydrogen,” *J. Non-Cryst. Solids*, vol. 68, no. 2–3, pp. 301–325, Nov. 1984, doi: 10.1016/0022-3093(84)90013-9.
[114]S. Munekuni, N. Dohguchi, H. Nishikawa, Y. Ohki, K. Nagasawa, and Y. Hama, “Si—O—Si strained bond and paramagnetic defect centers induced by mechanical fracturing in amorphous SiO_2,” *J. Appl. Phys.*, vol. 70, no. 9, pp. 5054–5062, Nov. 1991, doi: 10.1063/1.349012.
[115]T. Bakos, S. N. Rashkeev, and S. T. Pantelides, “Optically active defects in Si O 2 : The nonbridging oxygen center and the interstitial OH molecule,” *Phys. Rev. B*, vol. 70, no. 7, p. 075203, Aug. 2004, doi: 10.1103/PhysRevB.70.075203.
[116]S. Munekuni *et al.*, “Various types of nonbridging oxygen hole center in high-purity silica glass,” *J. Appl. Phys.*, vol. 68, no. 3, pp. 1212–1217, Aug. 1990, doi: 10.1063/1.346719.
[117]P. W. Levy, “The Kinetics of Gamma-Ray Induced Coloring of Glass,” *J. Am. Ceram. Soc.*, vol. 43, no. 8, pp. 389–395, 1960.
[118]D. Doyle, “Radiation-induced transmission degradation of borosilicate crown optical glass from four different manufacturers,” *Opt. Eng.*, vol. 46, no. 4, p. 043004, Apr. 2007, doi: 10.1117/1.2722322.
[119]A. Bishay, “Gamma Irradiation Studies of Some Borate Glasses,” *J. Am. Ceram. Soc.*, vol. 44, no. 6, pp. 289–296, Jun. 1961, doi: 10.1111/j.1151-2916.1961.tb15380.x.
[120]A. M. Bishay, “Gamma-Ray Induced Coloring of Some Phosphate Glasses,” *J. Am. Ceram. Soc.*, vol. 44, no. 11, pp. 545–552, Nov. 1961, doi: 10.1111/j.1151-2916.1961.tb11655.x.
[121]A. M. Bishay, “Role of Cerium in Suppression of Gamma-Ray Induced Coloring of Borate Glasses,” *J. Am. Ceram. Soc.*, vol. 45, no. 8, pp. 389–393, Aug. 1962, doi: 10.1111/j.1151-2916.1962.tb11176.x.
[122]R. Yokota, “Color Centers in Alkali Silicate and Borate Glasses,” *Phys. Rev.*, vol. 95, no. 5, pp. 1145–1148, Sep. 1954, doi: 10.1103/PhysRev.95.1145.
[123]J. S. Stroud, “Color Centers in a Cerium-Containing Silicate Glass,” *J. Chem. Phys.*, vol. 37, no. 4, pp. 836–841, Aug. 1962, doi: 10.1063/1.1733170.
[124]J. H. Mackey, H. L. Smith, and A. Halperin, “Optical studies in x-irradiated high purity sodium silicate glasses,” *J. Phys. Chem. Solids*, vol. 27, no. 11–12, pp. 1759–1772, Nov. 1966, doi: 10.1016/0022-3697(66)90107-7.
[125]A. M. Bishay and M. S. Maklad, “Gamma-Induced Absorption Bands Associated with Tl+, Pb2+, or Bi3+ in Potassium Borate Glasses,” *J. Am. Ceram. Soc.*, vol. 50, no. 10, pp. 503–508, Oct. 1967, doi: 10.1111/j.1151-2916.1967.tb14981.x.
[126]N. J. Kreidl and J. R. Hensler, “Formation of color centers in glasses exposed to gamma radiation,” *J. Am. Ceram. Soc.*, vol. 38, no. 12, pp. 423–432, 1955.
[127]A. Nissrine, “Etude de verres pour la dosimétrie fibrée de rayonnements ionisants,” Lille, 2018.
[128]D. D. Francesca, “Role of Dopants, Interstitial O2 and Temperature in the Effects of Irradiation on Silica-based Optical Fibers,” UNIVERSITÉ JEAN MONNET & UNIVERSITÀ DEGLI STUDI DI PALERMO, Saint Etienne, 2015.
[129]J. S. Stroud, “Photoionization of Ce^{3+} in Glass,” *J. Chem. Phys.*, vol. 35, no. 3, pp. 844–850, Sep. 1961, doi: 10.1063/1.1701227.

[130] X. Fu, L. Song, and J. Li, “Radiation induced color centers in cerium-doped and cerium-free multicomponent silicate glasses,” *J. Rare Earths*, vol. 32, no. 11, pp. 1037–1042, Nov. 2014, doi: 10.1016/S1002-0721(14)60180-0.
[131] M.-L. Brandily-Anne, J. Lumeau, L. Glebova, and L. B. Glebov, “Specific absorption spectra of cerium in multicomponent silicate glasses,” *J. Non-Cryst. Solids*, vol. 356, no. 44–49, pp. 2337–2343, Oct. 2010, doi: 10.1016/j.jnoncrysol.2010.02.020.
[132] Schott Ltd, “Technical note: Radiation Resistant Optical Glasses,” Feb. 2007. [Online]. Available: http://www.couriertronics.com/docs/notes/General_Machine_Vision_Appnotes/TIE-42_Radiation_resistant_glasses_%281%29.pdfhttp://www.couriertronics.com/docs/notes/General_Machine_Vision_Appnot es/TIE-42_Radiation_resistant_glasses_%281%29.pdf.
[133] B. McGrath, H. Schönbacher, and M. Van de Voorde, “Effects of nuclear radiation on the optical properties of cerium-doped glass,” *Nucl. Instrum. Methods*, vol. 135, no. 1, pp. 93–97, 1976.
[134] J. S. Stroud, “Color-Center Kinetics in Cerium-Containing Glass,” *J. Chem. Phys.*, vol. 43, no. 7, pp. 2442–2450, Oct. 1965, doi: 10.1063/1.1697143.
[135] B. Speit, E. Rädlein, G. H. Frischat, A. J. Marker, and J. S. Hayden, “Radiation resistant optical glasses,” *Nucl. Instrum. Methods Phys. Res. Sect. B Beam Interact. Mater. At.*, vol. 65, no. 1, pp. 384–386, 1992.
[136] J. Bei, G. Qian, X. Liang, S. Yuan, Y. Yang, and G. Chen, “Optical properties of Ce3+-doped oxide glasses and correlations with optical basicity,” *Mater. Res. Bull.*, vol. 42, no. 7, pp. 1195–1200, Jul. 2007, doi: 10.1016/j.materresbull.2006.10.020.
[137] G. Chen, S. Baccaro, M. Nikl, A. Cecilia, Y. Y. Du, and E. Mihokova, “The Red-Shift of Ultraviolet Spectra and the Relation to Optical Basicity of Ce-Doped Alkali Rare-Earth Phosphate Glasses,” *J. Am. Ceram. Soc.*, vol. 87, no. 7, pp. 1378–1380, Jul. 2004, doi: 10.1111/j.1151-2916.2004.tb07741.x.
[138] SCHOTT, “LF5G15,” *RefractiveIndex.Info*. https://refractiveindex.info/?shelf=glass&book=SCHOTT-LF&page=LF5G15.
[139] SCHOTT, “LF5G19,” *RefractiveIndex.Info*. https://refractiveindex.info/?shelf=glass&book=SCHOTT-LF&page=LF5G19.
[140] SCHOTT, “SF6G05,” *RefractiveIndex.Info*. https://refractiveindex.info/?shelf=glass&book=SCHOTT-SF&page=SF6G05.
[141] Ohara, “Radiation Resistant Glass,” *Oharacorp*, May 13, 2020. https://www.oharacorp.com/radiation-resistant-glass.html.
[142] Ohara, “Press Release : Non-Browning Optical Glass Has Released,” 2015 12AD. Accessed: May 13, 2020. [Online]. Available: https://www.ohara-inc.co.jp/en/news/images/151222_NonBrowingGlass_PressRelease_Final_Eng.pdf.
[143] CDGMGD, “Optical Glass(PDF)201904new.” Accessed: Jan. 27, 2020. [Online]. Available: http://www.cdgmgd.com/downloadFile.htm?id=12981.
[144] I. I. Orlovskiy, K. Yu. Vukolov, E. N. Andreenko, and M. N. Gulyukin, “Neutron irradiation of flint glasses for optics in ITER,” *Nucl. Mater. Energy*, vol. 15, pp. 249–253, May 2018, doi: 10.1016/j.nme.2018.05.009.
[145] “TIE-42: Radiation Resistant Optical Glasses.” SCHOTT, Apr. 2018, Accessed: Oct. 30, 2019. [Online]. Available: https://www.us.schott.com/advanced_optics/english/knowledge-center/technical-articles-and-tools/tie.html.
[146] S. Baccaro, A. Cemmi, I. Di Sarcina, and F. Menchini, “Gamma Rays Effects on the Optical Properties of Cerium-Doped Glasses,” *Int. J. Appl. Glass Sci.*, vol. 6, no. 3, pp. 295–301, Sep. 2015, doi: 10.1111/ijag.12131.
[147] A. Moroño, P. Martín, A. Gusarov, and E. R. Hodgson, “Radiation induced absorption and luminescence of selected alternative radiation resistant glasses,” *J. Nucl. Mater.*, vol. 386–388, pp. 1030–1033, Apr. 2009, doi: 10.1016/j.jnucmat.2008.12.229.

[148] SCHOTT, “K5G20,” *RefractiveIndex.Info*. https://refractiveindex.info/?shelf=glass&book=SCHOTT-K&page=K5G20.
[149] “Antonpaarbrochure,Abbematrefractometerseries.s.l.:Antonpaar,2012.”
[150] A. F. Fernandez *et al.*, “SCK·CEN gamma irradiation facilities for radiation tolerance assessment,” 2002, pp. 171–176, doi: 10.1109/REDW.2002.1045549.
[151] A. Alessi *et al.*, “Gamma and x-ray irradiation effects on different Ge and Ge/F doped optical fibers,” *J. Appl. Phys.*, vol. 118, no. 8, p. 085901, Aug. 2015, doi: 10.1063/1.4929458.
[152] Ocean Insight, “UV-Visible Bifurcated Fibers,” *oceaninsight*, May 03, 2020. https://www.oceaninsight.com/products/fibers-and-probes/fibers/bifurcated-fibers/uv-vis-bifurcated-fiber/ (accessed May 03, 2020).
[153] A. Bishay, “Radiation induced color centers in multicomponent glasses,” *J. Non-Cryst. Solids*, vol. 3, no. 1, pp. 54–114, Jan. 1970, doi: 10.1016/0022-3093(70)90106-7.
[154] I. Manolis *et al.*, “The ESA RADGLASS activity: a radiation study of non rad-hard glasses,” Toulouse, Oct. 2015, vol. 9639, pp. 96391N-1 96391N-15, doi: 10.1117/12.2193913.
[155] Andra, “DOSSIER D’OPTIONS TECHNIQUES DE RÉCUPÉRABILITÉ,” Andra, DOCUMENT TECHNIQUE CG-TE-D-NTE-AMOA-RV0-0000-15-0059/A, Apr. 2016. Accessed: Apr. 30, 2020. [Online]. Available: https://www.andra.fr/sites/default/files/2018-11/CG-TE-D-NTE-AMOA-RV0-0000-15-0059-A%20DOREC.pdf.
[156] ANDRA, “Classification.” https://www.andra.fr/les-dechets-radioactifs/tout-comprendre-sur-la-radioactivite/classification (accessed Apr. 30, 2020).
[157] ANDRA, “La R&D en support à la conception puis à l’exploitation de Cigéo,” Dec. 08, 2014, Accessed: Apr. 30, 2020. [Online]. Available: https://meusehautemarne.andra.fr/sites/meuse/files/2018-04/clis-la-r-d-en-support-a-la-conception-puis-a-l-exploitation-de-cigeo.pdf.
[158] X. Phéron, “Durabilité des capteurs à fibres optiques sous environnement radiatif,” p. 132.
[159] A. Rohatgi, “WebPlotDigitizer.” https://automeris.io/WebPlotDigitizer.

List of related papers and communication

List of papers

1. S. Rizzolo, A. Boukenter, **T. Allanche**, J. Perisse, G. Bouwmans, H. El Hamzaoui, L. Bigot, Y. Ouerdane, M. Cannas, M. Bouazaoui, J.-R. Mace, S. Bauer, and S. Girard, “Optical Frequency *Domain Reflectometer Distributed Sensing Using Microstructured Pure Silica Optical Fibers Under Radiations,* **IEEE TRANSACTIONS ON NUCLEAR SCIENCE**, vol. 63, no. 4, pp. 2038-2045, 2016.
   DOI: 10.1109/TNS.2016.2519238

2. V. Goiffon, S. Rolando, F. Corbiere, S. Rizzolo, A. Chabane, S. Girard, J. Baer, M. Estribeau, P. Magnan, P. Paillet, M. Van Uffelen, L. Mont Casellas, R. Scott, M. Gaillardin, C. Marcandella, O. Marcelot, and **T. Allanche** , *Radiation Hardening of Digital Color CMOS Camera-on-a-Chip Building Blocks for Multi-MGy Total Ionizing Dose Environments* **IEEE TRANSACTIONS ON NUCLEAR SCIENCE**, vol. 64, no. 1, pp. 45-53, 2017.
   DOI: 10.1109/TNS.2016.2636566

3. C. Muller; T. Lépine; **T. Allanche** ; A. Boukenter; P. Paillet; S. Girard; Y. Ouerdane
   “Potential performance loss and compensation techniques of a lens under ionizing radiations"
   IEEE Transactions on Nuclear Science, vol. 64, no. 1, pp. 45-53, 2017.
   DOI: 10.1109/TNS.2016.2636566

4. **T. Allanche** , V. Goiffon, S. Rizzolo, P. Paillet, O. Duhamel, A. Chabane, C. Muller, P. Magnan, F. Corbiere, S. Rolando, R. Clerc, E. Marin, A. Boukenter, Y. Ouerdane, and S. Girard, “*Analysis of X-Ray Photo-Charge Induced Speckles in a Radiation Hardened CMOS Image Sensor*,” **17th European Conference on Radiation and Its Effects on Components and Systems (RADECS)**, Geneva, Switzerland, pp. 1-4 2017.
   DOI: 10.1109/RADECS.2017.8696152.

5. **T. Allanche** , P. Paillet, V. Goiffon, C. Muller, M. Van Uffelen, L. Mont-Casellas, O. Duhamel, C. Marcandella, S. Rizzolo, P. Magnan, R. Clerc, T. Lepine, M. Hebert, A. Boukenter, Y. Ouerdane, R. Scott, W. De Cock, and S. Girard, *“Vulnerability and Hardening Studies of Optical and Illumination Systems at MGy Dose Levels”* **IEEE Transactions on Nuclear Science,** vol. 65, no. 1, pp. 132-140, 2018.
   DOI: 10.1109/TNS.2017.2783187

6. V. Goiffon, S. Rizzolo, F. Corbiere, S. Rolando, S. Bounasser, M. Sergent, A. Chabane, O. Marcelot, M. Estribeau, P. Magnan, P. Paillet, S. Girard, M. Gaillardin, C. Marcandella, **T. Allanche** , M. Van Uffelen, L. M. Casellas, R. Scott, and W. De Cock, "*Total Ionizing Dose Effects on a Radiation-Hardened CMOS Image Sensor Demonstrator for ITER Remote Handling*," **IEEE Transactions on Nuclear Science**, vol. 65, no. 1, pp. 101-110. 2018.
   DOI: 10.1109/TNS.2017.2765481

7. S. Girard, **T. Allanche** , P. Paillet, V. Goiffon, M. Van Uffelen, L. Mont-Casellas, C. Muller, A. Boukenter, Y. Ouerdane, and W. De Cock, *"Growth and Decay Kinetics of Radiation-Induced Attenuation in Bulk Optical Materials"* **IEEE Transactions on Nuclear Science**, vol. 65, no. 8, pp. 1612-1618, 2018.
DOI: 10.1109/TNS.2017.2778318

8. T. Blanchet, A. Morana, **T. Allanche** , C. Sabatier, I. Reghioua, E. Marin, A. Boukenter, Y. Ouerdane, P. Paillet, M. Gaillardin, O. Duhamel, C. Marcandella, M. C. Trinczek, G. Assaillit, G. Auriel, D. Aubert, G. Laffont, and S. Girard, "*X-Ray, Proton, and Electron Radiation Effects on Type I Fiber Bragg Gratings*," **IEEE Transactions on Nuclear Science**, vol. 65, no. 8, pp. 1632-1638, 2018.
DOI: 10.1109/TNS.2018.2823771

9. C. Sabatier, S. Rizzolo, A. Morana, **T. Allanche** , T. Robin, B. Cadier, P. Paillet, M. Gaillardin, O. Duhamel, C. Marcandella, D. Aubert, G. Assaillit, G. Auriel, A. Boukenter, Y. Ouerdane, L. Mescia, E. Marin, and S. Girard, "*6-MeV Electron Exposure Effects on OFDR-Based Distributed Fiber-Based Sensors*" **IEEE Transactions on Nuclear Science**, vol. 65, no. 8, pp. 1598-1603, 2018.
DOI: 10.1109/TNS.2018.2804663

10. S. Rizzolo, V. Goiffon, F. Corbiere, R. Molina, A. Chabane, S. Girard, P. Paillet, P. Magnan, A. Boukenter, **T. Allanche** , C. Muller, C. Monsanglant-Louvet, M. Osmond, H. Desjonqueres, J.-R. Mace, P. Burnichon, J.-P. Baudu, and S. Plumeri, "Radiation Hardness Comparison of CMOS Image Sensor Technologies at High Total Ionizing Dose Levels" **IEEE Transactions on Nuclear Science**, vol. 66, no. 1, pp. 111-119, 2018.
DOI: 10.1109/TNS.2018.2884037

11. C. Muller, **T. Allanche** , P. Paillet, O. Duhamel, V. Goiffon, S. Rizzolo, T. Lépine, J. Rousson, J.-P. Baudu, J.-R. Macé, H. Desjonqueres, C. Monsanglant Louvet, Y. Ouerdane, A. Boukenter, and S. Girard, "Investigations of the MGy dose level radiation effects on the photometric budget of a radiation-hardened CMOS-based camera" **Appl. Opt.**, vol. 58, no. 22, pp. 61-65, 2019
DOI: 1117/12.2313245

12. H. Dewitte, S. Rizzolo, P. Paillet, P. Magnan, A. Le Roch, F. Corbiere, R. Molina, S. Girard, **T. Allanche** , C. Muller, H. Desjonqueres, J-R. Mace, J-P Baudu, A. Saravia Flores, and V. Goiffon, "*Annealing Effects on Radiation Hardened CMOS Image Sensors Exposed to Ultra High Total Ionizing Doses*"**IEEE Transactions on Nuclear Science**, submitted, 2019

List of communications

International conferences

13. **T. Allanche**, P. Paillet, V. Goiffon, C. Muller, M. Van Uffelen, L. Mont-Casellas, O. Duhamel, C. Marcandella, S. Rizzolo, P. Magnan, R. Clerc, T. Lepine, M. Hebert, A. Boukenter, Y. Ouerdane, R. Scott, W. De Cock, and S. Girard, « *Vulnerability and Hardening Studies of*

Optical and Illumination Systems at MGy dose levels », **NSREC** (*Nuclear and Space Radiation Effects Conference*), New Orleans, LA, USA, 2017.

14. V. Goiffon, S. Rizzolo, F. Corbiere, S. Rolando, S. Bounasser, M. Sergent, A. Chabane, O. Marcelot, M. Estribeau, P. Magnan, P. Paillet, S. Girard, M. Gaillardin, C. Marcandella, **T. Allanche** , M. Van Uffelen, L. M. Casellas, R. Scott, and W. De Cock, « *Total Ionizing Dose Effects on a Radiation Hardened CMOS Image Sensor Demonstrator for ITER Remote Handling* », **NSREC**, New Orleans, LA, USA, 2017.

15. **T. Allanche** , V. Goiffon, S. Rizzolo, P. Paillet, O. Duhamel, A. Chabane, C. Muller, P. Magnan, F. Corbiere, S. Rolando, R. Clerc, E. Marin, A. Boukenter, Y. Ouerdane, and S. Girard, "Analysis of X-Ray Photo-Charge Induced Speckles in a Radiation Hardened CMOS Image Sensor, « *Analysis of X-Ray Photo-Charge Induced Speckles in a Radiation Hardened CMOS Image Sensor* », **RADECS** (*Radiation and its Effects on Components and Systems*), Geneva, Switzerland, 2017.

16. C. Muller, T. Lépine, **T. Allanche** , P. Paillet, V. Goiffon, Y. Ouerdane, A. Boukenter, and S. Girard, « *Extrapolated degradation of optical systems at MGy levels due to radiation-induced refractive index change* » **RADECS**, Geneva, Switzerland, 2017.

17. S. Girard, **T. Allanche** , P. Paillet, V. Goiffon, M. Van Uffelen, L. Mont-Casellas, C. Muller, A. Boukenter, Y. Ouerdane, and W. De Cock, « *Growth and Decay Kinetics of Radiation-Induced Attenuation in Bulk Optical Materials* » **RADECS**, Geneva, Switzerland, 2017.

18. T. Blanchet, A. Morana, **T. Allanche** , C. Sabatier, I. Reghioua, E. Marin, A. Boukenter, Y. Ouerdane, P. Paillet, M. Gaillardin, O. Duhamel, C. Marcandella, M. C. Trinczek, G. Assaillit, G. Auriel, D. Aubert, G. Laffont, and S. Girard « *X-rays, Protons and Electrons Radiation Effects on Type I Fiber Bragg Gratings* » **RADECS**, Geneva, Switzerland, 2017.

19. C. Sabatier, S. Rizzolo, A. Morana, **T. Allanche** , T. Robin, B. Cadier, P. Paillet, M. Gaillardin, O. Duhamel, C. Marcandella, D. Aubert, G. Assaillit, G. Auriel, A. Boukenter, Y. Ouerdane, L. Mescia, E. Marin, and S. Girard, "*6-MeV Electron Exposure Effects on OFDR-Based Distributed Fiber-Based Sensors*" **RADECS**, Geneva, Switzerland, 2017.

20. **T. Allanche** , A. Alessi, R. Clerc, Y. Ouerdane, A. Boukenter, and S. Girard, *« In Situ measurements of Radiation Induced Absorbance in glasses and preforms*», **FMR** (*Fibres optiques en Milieu Radiatif*), Mol, Belgium, 2017.

21. **T. Allanche** and S. Girard *« A snapshot of radiations effects on LEDs and glasses devoted for cameras for applications in harsh environments*», **Radfact**, Montpellier, France, 2018.

22. V. Goiffon, S. Rizzolo, F. Corbiere, S. Rolando, S. Bounasser, M. Sergent, A. Chabane, O. Marcelot, M. Estribeau, P. Magnan, P. Paillet, S. Girard, M. Gaillardin, C. Marcandella, **T. Allanche** , M. Van Uffelen, L. M. Casellas, R. Scott, and W. De Cock, « *Total Ionizing Dose Effects on a Radiation Hardened CMOS Image Sensor Demonstrator for ITER Remote Handling* », **NSREC,** Hawaii, USA, 2018.

23. C. Muller, T. Lépine, **T. Allanche** , P. Paillet, O. Duhamel, V. Goiffon, Y. Ouerdane, A. Boukenter, S. Girard « *Extrapolated degradation of optical systems at MGy levels due to radiation-induced refractive index change* » **RADECS**, Gotherburg, Sweden, 2018.

24. C. Muller, T. Lépine, **T. Allanche** , A. Boukenter, P. Paillet, S. Girard, Y. Ouerdane "*Potential performance loss and compensation techniques of a lens under ionizing radiations*" **Optical Design and Engineering VII**, Frankfurt, Germany, 2018.

25. V. Goiffon, **T. Allanche**, C. Muller, P. Paillet, J.-R. Macé, M. Osmond, P. Burnichon, S. Plumeri, J.-P. Baudu, A. Boukenter, P. Magnan, S. Rizzolo, F. Corbière, O. Duhamel, H. Desjonqueres, R. Molina, Y. Ouerdane, T. Lépine, R. Clerc, and S. Girard, "*CAMRAD: Development of a Multi-Megagray Radiation Hard CMOS Camera for Dismantling Operations*" **DEM** (Dismantling Challenges: Industrial Reality, Prospects and Feedback Experience), Avignon, France, 2018.

26. C. Muller, V. Goiffon, **T. Allanche** , P. Paillet, J. Macé, M. Osmond, P. Burnichon, S. Plumeri, J-P. Baudu, A. Boukenter, P. Magnan, S. Rizzolo, F. Corbière, O. Duhamel, J. Rousson, J-M. Barbier, H. Desjonqueres, C. Monsanglant-Louvet, R. Molina, Y. Ouerdane, T. Lépine, R. Clerc, S. Catherin, S. Girard, "*CAMRAD project: an eye beyond the MGy dose level*" **ANIMMA** (International conference on Advancements in Nuclear Instrumentation Measurement Methods and their Applications), Portorož, Slovenia, 2019.

27. C. Muller, **T. Allanche** , A. Morana, P. Paillet, T. Lépine, A. Boukenter, Y. Ouerdane, S. Girard. "*Optical response of antireflection coatings under X-rays at the MGy dose level*" **RADECS**, Montpellier, France, 2019.

28. S. Rizzolo, V. Goiffon, F.Corbière, R. Molina, S. Rolando, S. Girard, P. Paillet, P. Magnan, A. Boukenter, **T. Allanche** , C. Muller, C. Monsanglant Louvet, H. Desjonqueres, J-R Macé, J. Rousson, J-M Barbier, J-P Baudu, A. Saravia Flores and S. Catherin
"*Partially Pinned Photodiode Performances in for Emerging Space and Nuclear Applications*" **ISSW** (International Image Sensor Society Workshop), Snowbird, USA, 2019.

National conferences (France)

29. **T. Allanche** and Y. Ouerdane
« *Caractérisation et Réponses de composants optiques irradiés à fortes doses* » **JOURNÉE DE LA RECHERCHE,** Saint-Étienne, 2018.

30. **T. Allanche** , S. Girard, P. Paillet, V. Goiffon , C. Muller, A. Boukenter and Y. Ouerdane « *Caractérisation de verres optiques en milieu radiatif: cinétique d'évolution de l'atténuation induite* » **OPTIQUE**, Toulouse, 2018.

Abstract

The CAMRAD project responds to the PIA call for proposals from the French National Agency for Radioactive Waste Management with the aim of finding new solutions for radioactive waste management in prevision of its strong increase due to the dismantling of the current French nuclear facilities. The project aims to design a high-definition, radiation-hardened, camera capable to withstand radiation dose levels at least ten times higher than the currently available cameras. This PhD thesis deals with the effects of radiation (up to the MGy) on LEDs allowing the camera to be autonomous in terms of lightning and the optical glasses to be used for the realization of optical system. After a description of CAMRAD, the requirement in terms of lighting are detailed. The main innovations of this work are the qualification at the MGy level of numerous commercial LEDs, post-irradiation measurements of their emission angles and online X-ray measurements. The third part concerns radiation effect on optical glasses. After detailing how Cerium doping of so-called "hardened" glasses protects them from darkening under radiation, we show that there is a lack of literature on the effects of high doses. In order to fill it and to improve the radiation induced attenuation measurements, we have developed an optical set-up allowing to measure the darkening of glasses during irradiation rather than post mortem. We carried systematic measurements on hardened and standard glasses as a function of dose rate and temperature. We have shown that certain standard optical glasses are highly promising for use at MGy dose levels, the followed approach has led to the filing of a patent.

Résumé

Le projet CAMRAD répond à un appel à projets PIA de l'Agence Nationale pour la gestion des Déchets RAdioactifs (ANDRA) en vue de faciliter la gestion des déchets nucléaires, dont le volume va considérablement augmenter avec le démantèlement du parc nucléaire français. Celui-ci prévoit la conception d'une caméra à Haute Définition durcie aux radiations à des doses au moins dix fois supérieures aux caméras actuellement disponibles. Cette thèse porte sur les effets des rayonnements (jusqu'au MGy) sur les LEDs rendant la caméra autonome en termes de lumière et les verres optiques nécessaires à la réalisation de son système optique. Après une description du projet, les besoins en termes d'éclairage sont détaillés. Les principales innovations de ce travail sont la qualification au MGy de nombreuses LEDs commerciales, des mesures post-irradiation de leurs angles d'émission et des mesures en ligne sous rayon-X. La troisième partie concerne les verres optiques sous radiation. Après avoir détaillé comment le dopage au cérium des verres dits « durci » les protège contre le noircissement causé par les radiations, nous montrons qu'il existe un manque dans la littérature sur les effets des fortes doses. Pour le combler et améliorer les mesures d'atténuation induites, nous avons développé un montage optique permettant de mesurer le noircissement des verres pendant l'irradiation plutôt qu'a posteriori. Il nous a permis de réaliser des mesures systématiques sur des verres durcis et standards en fonction du débit de dose et de la température. Ainsi nous avons montré que certains verres standards

présentent un fort potentiel pour une utilisation à des doses de radiations de l'ordre du MGy. L'approche suivie a mené au dépôt d'un brevet.